Multiphase Modelling of Desiccation Cracking in Compacted Soil

Ross A. Stirling

BSc (Hons) Geology
MSc Geotechnical Engineering

A thesis submitted for the degree of Doctor of Philosophy in the
School of Civil Engineering and Geosciences
Newcastle University
Newcastle
NE1 7RU

May 2014

Abstract

The development of cracking as a result of desiccation is increasingly under investigation. This work is set within the context of climate change effects on surface processes influencing infrastructure slope stability. The inherent changes to the mechanical and hydrological behaviour of clayey soils subjected to desiccation are significant. The preferential transmission of water due to cracking is widely cited as a source of strength reduction that leads to infrastructure slope failure.

In order to gain a better understanding of the cracking mechanism in typical compacted fill conditions, finite difference continuum modelling has been undertaken using FLAC 2D. The two-phase flow add-on has enabled the unsaturated behaviour of the desiccating soil to be included within the mesh. Physical behaviour observed in laboratory experiments has informed the development of the numerical model by allowing better constraint of boundary conditions. Model development has featured the inclusion of several non-linear processes that are fundamental to the changing soil response during drying. The influence of significant parameters has been identified and by means of a varied experimental program, the design, manufacture and testing of a laboratory test apparatus and procedure to define the tensile strength of compacted fills under varying saturation conditions was undertaken and subsequently validated.

The factors affecting crack initiation and propagation have been investigated via parametric study. This demonstrated the significant influence of basal restraint on the generation of tensile stresses conducive to cracking and the fundamental importance of the tensile strength function within the proposed modelling methodology. Experimentation with the shape of the SWRC has shown the model to be very sensitive to the hydraulic properties of the material with not only the occurrence of primary cracking being affected but also the development of the desiccated crust. The findings of this work are relatable to the incorporation of desiccation effects in the development of coupled hydrological-mechanical continuum models where atmosphere-soil interactions are increasingly significant.

Acknowledgements

I would first like to thank my supervisors Dr Colin Davie and Professor Stephanie Glendinning for their continual support, advice, reassurance and patience in the production of this thesis. My thanks also go to Dr Paul Hughes for his encouragement, particularly with the laboratory component of this work and Dr Peter Helm for his generosity of time (and empathy).

I am grateful to the technical staff at the School of Civil Engineering and Geosciences. I would like to thank Stuart Patterson and Fred Beadle for always being keen to help and offer practical advice.

I would like to recognise the funding provided by Newcastle University with contribution from the EPSRC project, iSMART.

I am very grateful to my friends who have been there as a sounding board, whether that be for the frustration or the laughter. I would like to thank my parents for their unwavering belief and inspiration. Finally, I wish to express my gratitude to my loving wife, Emma. I owe a great deal to the support of my family and friends.

Table of Contents

List of Figures

List of Tables

Chapter 1 Introduction

1.1 Research rationale

Our infrastructure network is critical to social, economic and environmental wellbeing. Therefore, it is of considerable importance that the condition and capacity is maintained and that this is undertaken sustainably. Yet the state of UK infrastructure is of ever increasing concern. The challenges that face stakeholders are a combination of historic and future pressures which are recognised to be rapidly approaching a critical condition.

Engineered slopes (embankments and cuttings) form a large component of the transport infrastructure with approximately 20,000km of geotechnical structures across the UK highway and rail network. This equates to one third of the total asset value of highway infrastructure alone. The majority of these structures were not built to modern construction specification with elements in excess of 150 years old. Progressive deterioration of this legacy infrastructure leads to failure by serious instability and/or serviceability issues. Spatial distribution analysis has indicated that unstable slopes with moderate to significant hazard potential constitute up to 10% of the area of Great Britain and that 7% of the transport network is located within this area (Dijkstra & Dixon, 2010).

Slope instability is a major safety hazard, with the risk of derailment from slope failures the greatest risk faced by the operational railway. Serviceability issues lead to the imposition of rail speed restrictions and highway slope repairs often lead to lane closures estimated to be on the order of £5,000-10,000 per hour per lane (Bassam, 2007). These both cause severe travel delays which can have a major social and economic impact. The continuous maintenance and remediation of earthworks is a major engineering and cost constraint for UK infrastructure owners. A decade ago annual maintenance costs for highway embankments alone were of the order of £50M while Network Rail is reported to spend £80 million per annum on earthwork related activities. As more operational equipment is located within the geotechnical asset (signalling, telecoms, power (rail), traffic management, noise barriers (highways)), even minor slope failures cause major service disruption and incur significant repair costs. The cost of emergency repair is commonly ten times greater than the cost of planned maintenance works.

There is increasing effort being put into the ability to predict the future performance of earthworks and to target resources towards resilient, effective maintenance. This is particularly focused in the context of adaptations to our changing climate.

The implications of climate on shrink-swelling behaviour are becoming central to the effective management of infrastructure slope assets. It was reported by Jones and Jefferson (2012) that damage due to shrink-swell has cost the UK economy £3 billion in the last 10 years, surpassing that of any geo-hazard. Furthermore, an annual cost of $15 billion due to shrink-swell damage to buildings and infrastructure is estimated in the US (Jones & Jefferson, 2012).

Desiccation cracking is the product of volumetric shrinking of clays brought about by a reduction in soil-water content. Cracking is commonly understood to initiate when tensile stresses, generated by increasing suctions under the influence of some form of restraint, exceed the soil strength, which in itself, is believed to be controlled by soil-water content. Variability in soil-water content is primarily the result of seasonal fluctuation in precipitation/evaporation in addition to the transient demands of vegetation and the infiltration potential of the soil surface and is therefore largely governed by climate. Predicted climate change scenarios are recognised to have the capacity to more frequently bring about conditions conducive to the increased occurrence of this behaviour because of the increased occurrence of warmer and drier summers experiencing rainfall events of shorter duration and higher intensity (Hulme et al., 2002; Jenkins et al., 2010).

Rainfall infiltration into soil experiencing cracking increases due to the additional, preferential transmission of water (Novak et al., 2000; Albrecht & Benson, 2001; Romkens & Prasad, 2006). Hence, the presence of pervasive, deep cracking results in rapid pore-water pressure responses. Progressive failure of UK infrastructure slopes is thought to be largely governed by near-surface permeability which is in turn controlled by the micro- and macro-scale structure of the soil. Empirically reasoned bulk permeability modification is currently being employed in the modelling of embankment pore pressures (Nyambayo & Potts, 2005; Rouainia et al., 2009).

1.2 Aim and objectives

This thesis sets out to develop a two-phase, continuum modelling approach capable of capturing the onset and growth of desiccation cracking in compacted fill, typical of UK infrastructure. In order to achieve this, the following objectives have been identified:

1. Review of established understanding of desiccation cracking processes and their mathematical description
2. Identification of an appropriate modelling framework in which to incorporate the cracking mechanism
3. Development of a numerical model capable of capturing the processes involved in desiccation cracking
4. Design and validation of a method to measure cracking related physical properties for incorporation in the proposed numerical model
5. Assessment of the developed cracking model sensitivity to variation in both mechanical and hydrological parameters.
6. Critical assessment of the modelling procedure and results

1.3 Thesis structure

A brief outline of the thesis structure is provided here. Firstly, Chapter 2 illustrates the occurrence of cracking in slopes before presenting a review of the principles governing unsaturated behaviour. This is developed into an understanding of soil shrinkage and cracking. The impact of cracking on soil mass hydrology is reviewed before finally the mathematical methods previously employed to describe cracking are critically assessed.

Chapter 3 introduces the selected numerical code and details the features available through its use. Particular attention is paid to the ability to simulate fluid flow in addition to an ability to divide the mesh according to prescribed criteria by using interface elements. The second half of the chapter explains, step by step, the development process behind the creation of the cracking model.

Having established the principle behind crack initiation in Chapter 2 and the physical requirements of the adopted methodology in Chapter 3, Chapter 4 describes the work conducted to ascertain a reliable measure of compacted fill

tensile strength under the necessary variation in water content. As part of this study, the approach to validate the proposed method is presented including Digital Image Correlation and comparison to an established indirect tensile testing technique.

Chapter 5 presents the output of the model and discusses the results of simulated baseline conditions. The sensitivity of the model to variations in perceived important factors in cracking such as strength and restraint is investigated as well as the response to fundamental soil-water characteristics and drying conditions.

Finally, Chapter 6 provides a summary of the thesis findings including comment on limitations and recommendations to further develop the presented research.

Chapter 2 Literature Review

2.1 Slope desiccation cracking

The desiccation cracking phenomenon has been investigated for decades and in a variety of contexts. Examples of the many and varied situations in which desiccation cracking is observed to occur are presented by Kodikara and Costa (2013) in Table 2.1. Virtually all of these examples describe the undesirable effect cracking has on the mechanical, hydrological and even thermal properties of clayey media. Given the scope of this thesis, the role of cracking in infrastructure embankment slopes will be focused upon herein.

Table 2.1 Summary of desiccation cracking influences in field applications (after Kodikara & Costa 2013).

Discipline	Application
Geotechnical Engineering	• Slopes – There is significant evidence that cracking at the crest area of the slopes trigger the initiation of slope failure (Take, 2003). • Flood dykes – Progressive failures that take place in UK's extensive dyke system (extending up to 35,000 km with an annual maintenance budget of £450 million) are triggered commonly by desiccation cracking that takes place in the downstream slope, subsequently providing seepage paths and block uplifting during flooding (Dyer, 2009). Canal systems also suffer from desiccation cracking induced distress. • Dams – Embankment dams experience internal erosion leading to piping failures, which accounts for about 50% dam failures and accidents. Potential erosion pathways are assisted by cracks formed by desiccation above phreatic surface, differential settlement, hydraulic fracturing and earthquakes (Forster et al., 2000).
Geo-environmental Engineering	• Compacted clay landfill liners and covers and Geosynthetic clay liners – Thermally induced or evaporation induced desiccation and differential settlement induced cracking of these components in modern waste landfills is a major issue providing unwanted pathways for escape of leachate and gas (Daniel and Wu, 1993; Zhou and Rowe, 2003). • Deep nuclear waste isolation – Bentonite buffer zones can undergo thermal drying, shrinkage and cracking near the waste package (Park et al., 2001).
Transport Engineering	• Cracking in road pavements – Reactive soil induced cracking in road bases is a major problem and incur substantial annual maintenance costs worldwide (Chakrabarti et al., 2002; Lytton et al., 1976).
Mining and Resources Engineering	• Mine tailings managements – Cracking in mine tailings influences its drying rates and stability (Morris et al., 1992) and induce changes in the permeability creating environmental consequences because of the potential pollutant generation on infiltration (Rodriguez et al., 2007).
Agricultural Engineering / Soil Sciences / Geology	• Fracture of soils is important consideration in tillage and wter and chemical usage in agricultural engineering (Chertkov, 2002; Ahmad, 1996). • In irrigated lands cracks allows the water and solutes to flow rapidly through the soil bypassing the dry root zone, thus leading to water and nutrient shortage for crops (Bronswijk, 1991). • Formation of fissures and gilgai formation in soil has been a subject of research in soil and geo-sciences (Kodikara et al, 2002).
Materials Engineering	• Cracking and warping (or curling) cause problems in many coating and material elaboration processes that are based on the drying of colloidal suspensions (Pauchard et al., 1999).
Planetary Sciences	• Formation of giant polygons on Earth and Mars, and evidence of presence of water (El Marry et al., 2012).

Cracking is widely held as having considerable influence on the hydro-mechanical behaviour responsible for slope instability (Anderson et al., 1982; Simoni et al., 2004; Zhan et al., 2006). The progressive failure mechanism attributed to infrastructure slopes in clay soils is governed by the action of shrink-swell cyclicity, where volume change is in turn controlled by changes in water content (Ridley et al., 2004; Smethurst et al., 2006). Such changes are governed by environmental conditions in addition to the transient demands of vegetation and the infiltration potential of the soil surface state (e.g. desiccation). Thus, desiccation cracking is an influential factor in the ability of negative pore water pressures to be maintained in engineered slopes constructed from these expansive soils. The reduced response time between rainfall events and observed pore pressure increase is understood to be caused by the preferential transmission of water through cracks.

Slope failure triggered by crest cracking, as investigated by Take and Bolton (2002) (in Table 2.1 by Kodikara and Costa 2013), is questionably the result of desiccation alone. Upper slope cracking is brought about by movement of the slope which in turn has allowed ingress of water to depth reducing effective stress and contributing to the progressive failure mechanism. However, desiccation cracking is the result of environmental drivers and as such may be distributed over the entire slope. Hence, desiccation cracking may act over large regions of the infrastructure network subject, of course, to the locally favoured engineering fill material and climate.

The classic desiccation cracking pattern of non-orthogonal, approximately equally sized, polygonal blocks is commonly associated with the initial drying of formerly slurried clay soils and tends to originate simultaneously (Kodikara et al., 2000). This cracking style is typical of un-vegetated surfaces (Figure 2.1a), in contrast, orthogonal cracking tends to develop sequentially and is common on more densely vegetated slopes (Figure 2.1b) due to the addition of root reinforcement. The latter form is characterised by more widely spaced, linear features and is representative of UK infrastructure corridor slopes.

(a)

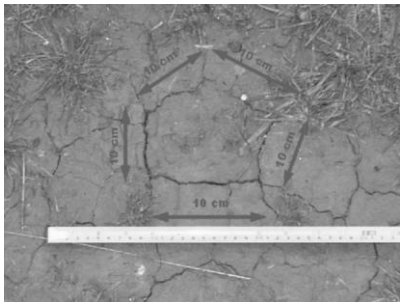

(b)

Figure 2.1 Embankment surface cracking (a) polygonal surface cracking (after Dyer et al. 2009), (b) linear cracking, Newcastle, UK (steel measure approximately 0.5m).

Crack dimensions observed in the field are common across the disciplines with reports of clay liner features being in the range of 10-25mm wide depending on the period of sampling in the shrink-swell cycle and average cracking depths of 0.25-1m (Miller & Mishra, 1989; Montgomery & Parsons, 1989; Basnett & Brungard, 1992). Dyer et al. (2009) reported crack widths in a UK flood embankment as <8mm (Figure 2.2a) and roughly uniform over the 1m depth. Similarly, Zhan et al. (2006) reported widths of 10mm with the largest reaching a maximum depth of 1.2m in a clay cutting (Figure 2.2b). Cracking observed in a trial embankment at Newcastle during excavation work was also found to extend to a depth of approximately 1m (Figure 2.2c); this is in agreement with cracking observed in a highway specification embankment by Anderson et al. (1982). It is worth noting here that the larger cracks shown in Figure 2.2a and c do not daylight through the topsoil and as such may not be apparent during surveying. These hidden, deep cracks are considered the main conduits that

facilitate bypass flow to depths in excess of the 1m trial pits. However, field infiltration tests conducted over apparent surface cracks are still consistently found to yield elevated hydraulic conductivities of up to 3 orders of magnitude (Anderson et al., 1982; Zhan et al., 2006).

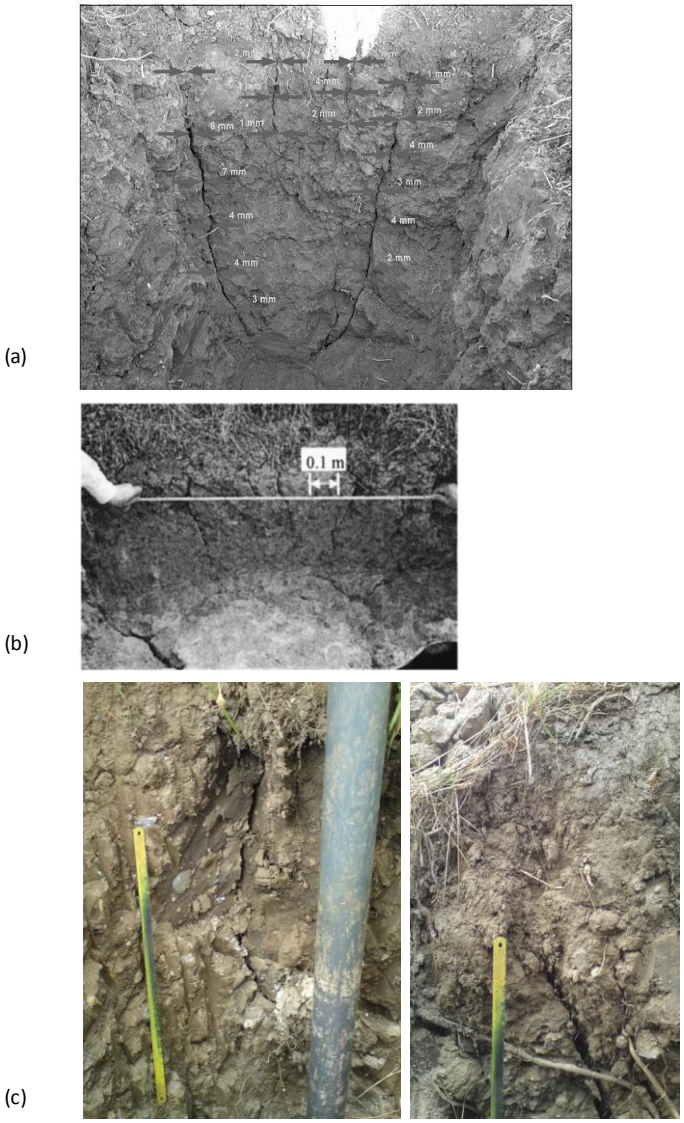

Figure 2.2 Slope cracking in cross-section (a) Dyer et al. 2009, (b) Zhan et al, 2006 and (c) Newcastle, UK (hacksaw blade 300mm).

Crack closure upon re-wetting remains under debate. Logic would suggest that upon re-saturation, previously desiccated clay soils will swell and cracks will heal. During the course of infiltration testing, it is common for recorded values to reduce though complete closure of existing crack sites is rare. Seasonal variations in crack surface widths are reported with common reoccurrence at consistent locations. Yet deep cracks, once developed, are found to persist

(Anderson et al., 1982). The reduction in shear strength caused by pervasive cracking in the top 1m of infrastructure slopes is understood to be less influential in terms of stability than the accelerated pore-water pressure response brought about by the presence of an extensive and persistent crack network. Given the occurrence of cracking within the near-surface, vadose-zone where soil behaviour is governed by unsaturated conditions, this subject is covered in the following section.

2.2 Unsaturated soils

Traditionally, soil mechanics studies are concerned with defining soil as saturated by either water or air. Flow within soils has hence been considered on the basis of saturated flow. With void space entirely filled by either water or air, deformation is considered to be governed by changes in effective stress. This relationship classically takes the form of Terzaghi's effective stress equation:

$$\sigma' = \sigma - u \qquad \textbf{2.1}$$

Where effective stress tensor, σ', is related to the total stress tensor, σ and pore pressure, u, relating to any fluid. This expression is considered accurate up to the point at which air enters the soil. With de-saturation of pore space, the soil element becomes unsaturated and the increasing air content of the soil must then be taken into account when calculating effective stress. Pore-water pressures in unsaturated soils are negative (with respect to atmospheric pressure) and are fundamental in the study of near surface soil mechanics.

In order to study the macroscopic multiphase flow in unsaturated soil, it is necessary to develop models at the microscopic level. The following sub-sections consider each phase to be composed of a single component and are under isothermal conditions. Additionally, in the following descriptions, the liquid-gas boundary will be considered as a distinct separating surface as an approximation at the molecular level.

As mentioned above, it is considered that the pore space within a porous medium is entirely occupied by two (or more) fluid phases. The quantity of each phase within a given representative elementary volume (REV) is given by the following definitions:

$$\theta_1 = \frac{Volume\ of\ phase\ 1\ in\ REV}{Volume\ of\ REV},\ 0 \leq \theta_1 \leq n,\ \sum \theta_1 = n \quad \textbf{2.2}$$

$$S_1 = \frac{Volume\ of\ phase\ 1\ in\ REV}{Volume\ of\ pore\ space\ in\ REV},\ 0 \leq S_1 \leq 1,\ \sum S_1 = 1 \quad \textbf{2.3}$$

Where θ_1 is fluid content (or water content when phase$_1$ is water) and fluid saturation is S_1 and is related to fluid content by porosity n, as defined by:

$$\theta_1 = nS_1 \quad \textbf{2.4}$$

2.2.1 Interfacial tension

A 'free interfacial energy' or 'surface free energy' exists when two immiscible phases are in contact. The energy differs from that existing toward the interior of each phase, away from their contact. For the area between the two phases to either increase or decrease, an amount of work has to be executed.

The reason for this differing interfacial free energy at the interface may be explained by the following example. Consider a surface between a liquid and its vapour. The molecules within each fluid are attracted to the other molecules of the same fluid. Therefore, where molecules toward the interior of the given fluid are surrounded by their neighbouring like molecules, they are attracted in all directions equally. However, this condition is not maintained at the surface and a net attraction toward the interior of the denser liquid interior exists. As this attraction is not balanced by the less dense vapour, the liquid contact surface will tend toward the smallest possible area.

The interface is in reality less well defined than the conceptual approximation. There exists a narrow zone of transition between the domains occupied by purely the relative phase's molecules. Their energy within this zone is different to that of the interior of each domain. The surface energy in the transition zone is defined as the difference in energy between the molecules in the zone i.e. that of the mixed phases, and those of their respective domain interiors. The interface is considered to be a two-dimensional surface i.e. negligible thickness.

For the area of the interface to increase, work must be done to oppose the cohesive forces between the molecules of the liquid to bring them from the

interior. The reverse is also true whereby energy is gained upon a reduction in surface area, this leads to a tendency for this case. The work done to increase the interface surface area by one unit is called the surface or interfacial free energy. Liquid surfaces possessing interfacial free energy tend towards the minimum possible area and behave as a thin skin under tension. It is this property that results in spherical water droplets.

It must be remembered that no thin skin actually exists and the quantity of molecules in the interface zone varies as the surface area expands and contracts.

“Free interfacial energy manifests itself as an interfacial tension” and is measured either in terms of energy per unit area or force per unit length.

The interfacial tension, $\gamma_{\alpha\beta}$ for the pair of substances α and β is the work required to separate a unit area of one from the other or increase the area by one unit. For air and water at 25°C, interfacial tension is 0.072 N/m. Surface tension, γ_{α} is the interfacial tension between a liquid and its own vapour. The work done to separate a unit area of the interface between the substances α and β into a vapour interface of each substance is given by Dupré’s formula:

$$W_{\alpha\beta} = \gamma_{\alpha} + \gamma_{\beta} - \gamma_{\alpha\beta} \qquad \textbf{2.5}$$

The term surface tension is frequently used to signify the interfacial tension between phases, often water and air.

A three phase system is presented in Figure 2.3 where two immiscible fluids are in contact with a plane solid surface (e.g. soil grain). The contact (or wetting) angle, θ is the angle between the solid surface and the fluids’ interface measured through the denser fluid along the linear triple-contact M. The angle depends on the properties of each phase and the affinity of the fluids for the solid.

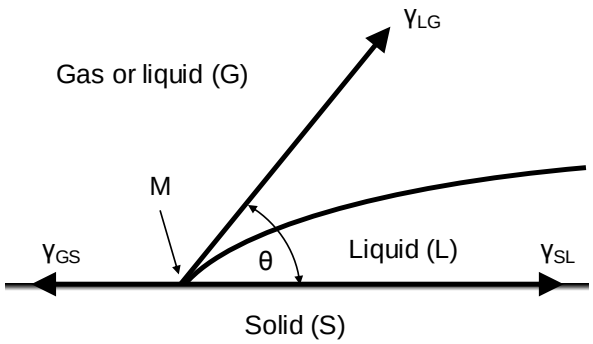

Figure 2.3 Interfacial tension (after Bear & Bachmat, 1990).

Young's equation defines the contact angle at equilibrium by the following:

$$\gamma LG \cos\theta + \gamma SL = \gamma GS \quad or \quad \cos\theta = \frac{\gamma GS - \gamma SL}{\gamma LG} \qquad \textbf{2.6}$$

Where $\cos\theta$ is the ratio between the energy released when forming a unit of area of the interface between the solid (S) and the liquid (L) to the energy needed to increase the unit area of interface between the two fluids.

The product $\gamma LG \cos\theta$ is called the adhesion tension and it indicates which of the two fluids will wet the solid, that is, which will adhere and spread over it. The fluid where θ < 90° is the wetting fluid and the fluid for which θ>90° is said to be the non-wetting fluid. It is possible for either fluid to be wetting or non-wetting and this depends upon the chemical composition of the fluids and the solid. In unsaturated soil, water is commonly the wetting fluid and air, the non-wetting.

The surface tension, $\gamma_{\alpha\beta}$ is dependent upon the temperature, pressure and composition of the fluids. The temperature on either side of an interface is assumed to be the same and equal to that of the bulk fluid. Composition is commonly expressed as chemical potential and is here assumed to be equal on both sides of the interface.

2.2.2 Capillary Pressure

Fluid pressure (fluid stress) is different on either side of an interface between two immiscible fluids. Capillary pressure, p'_c is commonly considered and is the difference between the pressure, p_n in the non-wetting fluid and the pressure, p_w in the wetting.

$$P'_c = P_n - P_w \tag{2.7}$$

The interface is considered to be a two-dimensional body with its own rheological properties and its behaviour is like that of a 'stretched membrane' under tension (meniscus). Due to this, under a force equilibrium condition, the fluids' stress must be discontinuous across the interface. If we assume the interfacial tension, γ_{wn} to be constant, the balance of forces normal to a representative element of interface at equilibrium is provided by the Laplace formula for capillary pressure:

$$P'_c = P_n - P_w = \gamma_{wn}\left(\frac{1}{r'} + \frac{1}{r''}\right) = \frac{2}{r^*}\gamma_{wn} \tag{2.8}$$

Where, r' and r'' are principle radii of curvature for the surface and r* is the mean defined by 2/r* = 1/r' + 1/r''.

At the larger scale beyond a single element of interface, consider the interface between a liquid and a gas in a capillary tube. If the liquid wets the solid such that θ=0° and the gas is non-wetting, then the gas-liquid interface is parallel to the tube wall and takes a concave form (Figure 2.4a). If the liquid fails to wet the solid such that θ=180°, then the case of capillary depression is observed where the meniscus is convex (Figure 2.4b). Generally, the liquid meets a solid with a contact angle $\theta \neq 0°$ and the pressure difference is given by Equation 2.8. For a circular capillary tube of radius *R*, the meniscus (interface) will approximate to *r** = *r'* = *r''* = *R*.

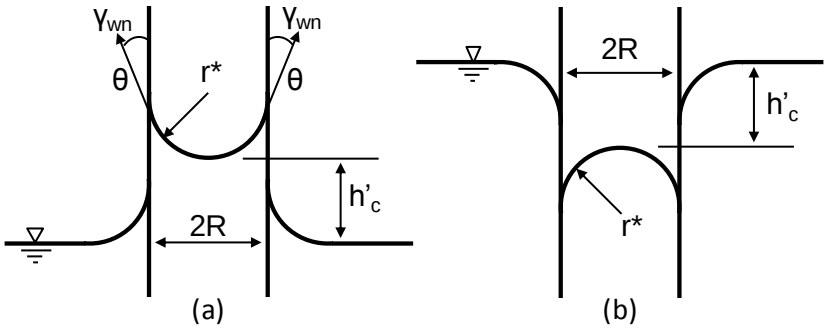

Figure 2.4 Two immiscible fluids in a capillary tube a) capillary rise and b) capillary depression (after Bear & Bachmat, 1990).

When h'_c is the height of the liquid above the external flat liquid surface, then P'_c is the hydrostatic pressure drop along the column of length h'_c (capillary rise). Therefore,

$$\pi R^2 h'_c \rho_w g = 2\pi R \gamma_{wn} \cos\theta \quad or \quad h'_c = \frac{2\gamma_{wn}\cos\theta}{\rho_w g R} \tag{2.9}$$

where γ_{wn} is surface tension. The capillary pressure head, h'_c may be calculated by Equation 2.10 with the radius of meniscus curvature of $r^* = R/\cos\theta$.

$$h'_c = \frac{2\gamma_{wn}}{\rho_w g r^*} = \frac{p'_c}{p_w g} \tag{2.10}$$

Whether a fluid-fluid interface such as a water-air meniscus is advancing or receding against a solid surface will alter the interfacial tension and ability to 'wet' – this behaviour is termed hysteresis and is discussed further in Section 2.2.5.

Air pressure is often assumed to be constant at atmospheric pressure, taken as zero and therefore,

$$p'_c = -p_w \tag{2.11}$$

This means that the water pressure, on average, in the pore space in the unsaturated zone is always negative. When modelling this case, the following definitions are commonly used:

$$h_c \equiv \varphi = \frac{p_c}{g\rho_w} = -\frac{p_w}{g\rho_w} \ (>0) \tag{2.12}$$

Where h_c and φ are capillary pressure head/tension and matric suction, respectively. Where the non-wetting fluid pressure does not equal zero, the following applies:

$$\varphi = \frac{p_a - p_w}{g\rho_w} \quad \textbf{2.13}$$

2.2.3 Adsorbed water

The plot presented in Figure 2.5 shows how the force of attraction between a solid and a wetting fluid adjacent to its surface changes with distance from that surface. Where this force is considered significant, the term adhesive fluid is used. The region immediately adjacent to the surface within the adhesive fluid is called the adsorbed fluid layer. If the fluid is water then due to its bipolar structure, the molecules are attracted perpendicularly by a very strong force leading to the properties of water to change to being much denser and much more viscous.

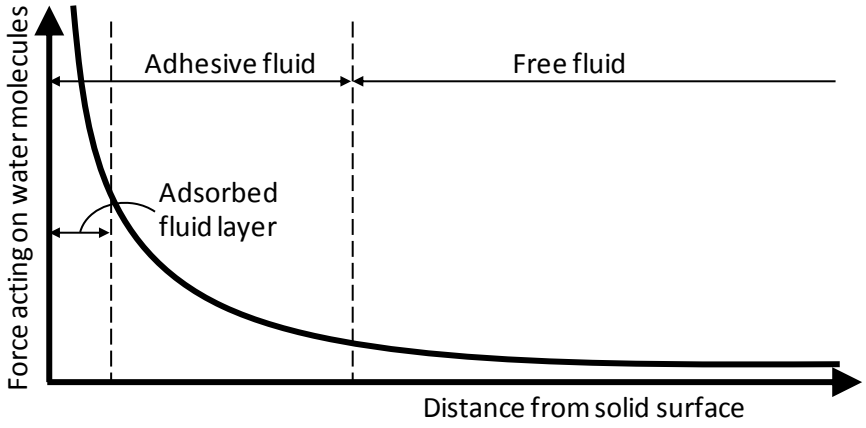

Figure 2.5 Schematic diagram of adhesive fluid near solid surface (after Bear & Bachmat, 1990).

The remaining part of the adhesive fluid outside the adsorbed fluid layer is in a transition zone where water remains immobile. However, beyond this layer, the fluid is considered mobile. If a granular medium is considered, then the distribution of these fluids (Figure 2.6) can be more accurately described purely in terms of wetting and surface tension due to the reduced influence of clay chemistry.

At low saturation, pendular rings are formed over soil grains and adjacent rings may coalesce leading to the fluid-fluid interface forming a ‘saddle’ shape. The rings do not constitute a continuous water phase besides the extremely thin adsorbed water layer. No pressure can be passed between the water rings due to the special behaviour of the water in this layer. With time, the volume of water in pendular rings may decrease due to evaporation. As saturation increases to the equilibrium water saturation, a continuous water phase will develop. Above this saturation, it is called funicular and flow is possible. With increasing saturation, air will no longer be continuous and can only move if a sufficient pressure difference is present. This state is called insular saturation. When no air is present in the pore space then complete saturation is achieved.

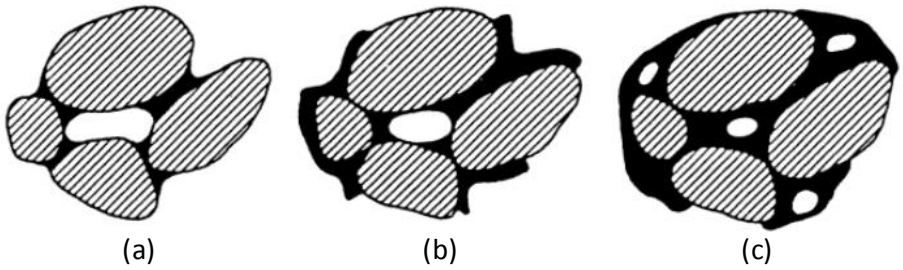

Figure 2.6 Air and water distributions at various saturations: a) Pendular saturation, b) Funicular water saturation and c) Insular air saturation (after Bear & Bachmat, 1990).

2.2.4 Capillary pressure drying/wetting

For a completely saturated soil that is then drained, allowing air to enter, the successive stages of drainage (1-5) are presented in Figure 2.7. As the removal of water progresses, menisci form whose radius depends on the capillary pressure e.g. the radius decreases as capillary pressure increases.

With progressive drainage, the menisci retreat into channels that result in lower menisci curvature (4). This process leads to a reduction in interface area which is a non-equilibrium state and so water will continue to retreat to a position where the narrow pore space will allow a meniscus of appropriately large curvature.

Therefore, for soils of a uniformly small pore-size distribution where channels are similarly sized, the simultaneous non-equilibrium for a given capillary pressure will result in rapid withdrawal of water from the soil. However, water will usually remain in the form of pendular rings.

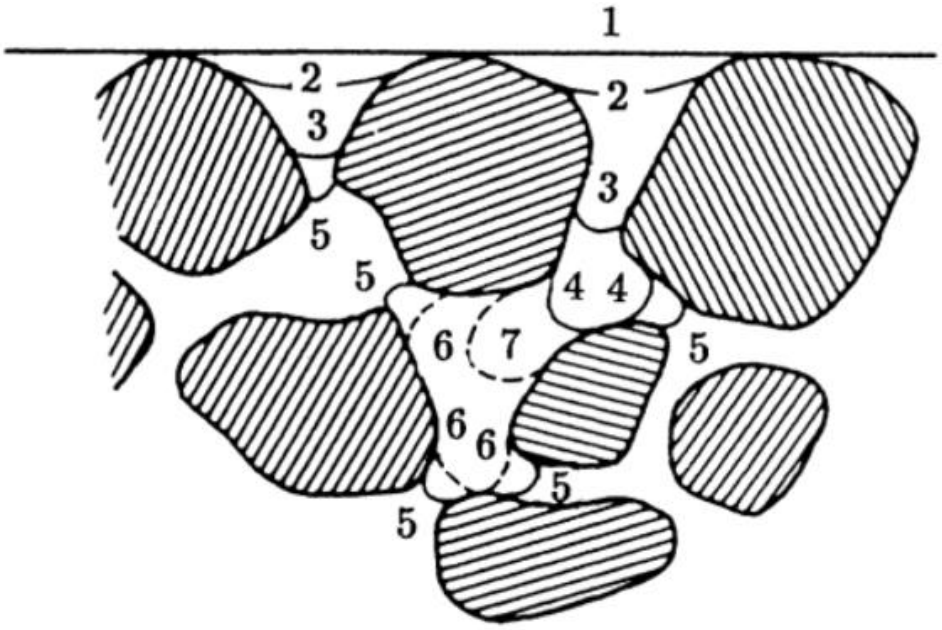

Figure 2.7 Gradual drainage and rewetting (after Bear & Bachmat, 1990).

Soils rarely comprise such a uniform pore size and as such pores de-saturate at different rates depending upon the (local) capillary pressure. Large pores will take a lower capillary pressure before desaturation will take place, whereas smaller pores are able to support menisci of smaller radii and thus require higher capillary pressures before emptying.

If drainage is ceased, an equilibrium situation will develop between surface tension and gravity where fluid motion will stop and the pressure distribution in each fluid will become hydrostatic.

In conclusion, the capillary pressure increases as the interfacial surface area decreases which is associated with a decrease in the wetting fluid content. Upon filling the soil with the wetting fluid (6-7), the menisci radii become progressively larger.

2.2.5 Soil water retention curve

A soil water retention curve (SWRC) relates the quantity of fluid present in the pores to the average capillary pressure, $P_c = P_c(S_w)$. For a soil undergoing de-saturation, the relationship is often referred to in soil physics as a desorption curve and upon wetting, a sorption curve.

At the microscopic level, the SWRC is dependent upon the factors that control the magnitude of surface tension, namely the respective temperature and chemical composition of the two fluids either side of the phase-interface. At this scale the capillary pressure in soil that experiences no grain deformation is described as: $P_c = P_c(S_w, \gamma_{wn}(T_w, T_n, c^{\gamma}_w, c^{\gamma}_n))$.

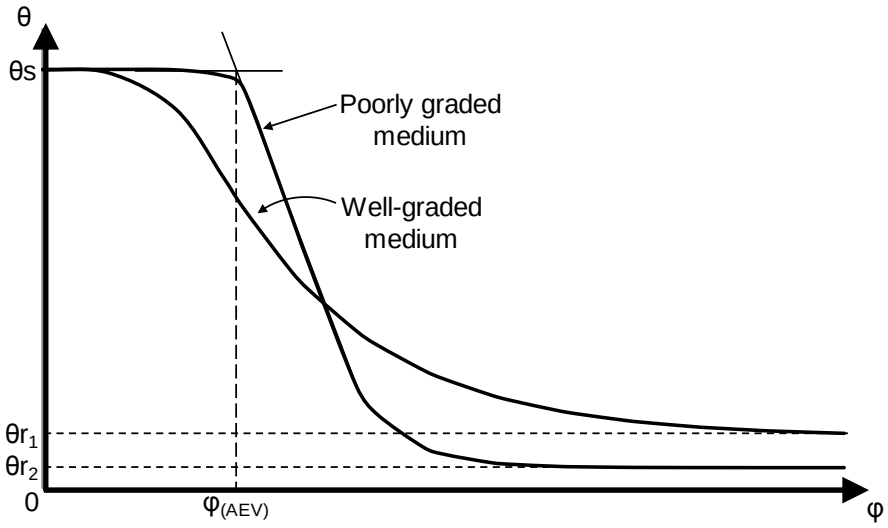

Figure 2.8 Typical desorption soil-water retention curves.

If beginning with a completely saturated soil, at saturated volumetric water content, θs, then by a very minor reduction in water content, a small magnitude of suction may be generated. Virtually no air is able to enter the soil until a critical capillary head or suction is reached, this is known as the air entry value (AEV). At this value, air will begin to enter the largest pores as they dry. For the given pair of fluids, water and air, the form which the curve takes is dependent upon the pore size and shape distribution. This gives rise to the two examples provided in Figure 2.8. When suction exceeds φ_{AEV}, water content decreases rapidly within a relatively narrow range of suction values before reducing at a more gradual rate as suction is increased beyond the residual water content, θr. At high suctions, the residual water remains in the form of immobile, pendular rings. This is the content at which a proportionally large increase in suction is required to generate a relatively minor removal of water. Beyond this stage in the desorption path, experiments have found that the total suction, which relates to zero water content, for a variety of soil types is approximately consistent at 1×10^6 kPa (Croney & Coleman, 1954; Fredlund & Rahardjo, 1993).

A number of analytical expressions have been proposed to describe the shape of the SWRC for an air-water system (Gardner, 1958; Brooks &Corey, 1964; Brutsaert, 1966; van Genuchten, 1980; Williams et al., 1983; McKee & Bumb, 1984; 1987; Fredlund & Xing, 1994; Fredlund & Pham, 2006). These are based on the assumption that air is at atmospheric pressure, taken as Pa = 0. By far, the most commonly used expression is that of van Genuchten (1980) and is presented here:

$$S_e = \frac{S_w - S_r}{1 - S_r} = \left[\frac{1}{1 + (\alpha\varphi)^n}\right]^m \quad \textbf{2.14}$$

$$\mathrm{m} = (\mathrm{n} - 1)/\mathrm{n} \quad \textbf{2.15}$$

$$\varphi = \frac{1}{\alpha}\left[\left(\frac{1}{S_e}\right)^{1/\mathrm{m}} - 1\right]^{1/\mathrm{n}} \quad \textbf{2.16}$$

The effective saturation, S_e represents the normalised saturation between complete saturation (S= 1) and the residual saturation, S_r, water present in the form of adhesive fluid forming pendular rings. The concept of residual saturation is based upon no evaporation taking place; if sufficient evaporation is allowed to take place then S_r may theoretically reduce to zero.

For the van Genuchten expression presented in Equation 2.14, α, n and m are curve fitting coefficients. The m parameter represents the asymmetry of the curve; a small m refers to a steep slope in high suction ranges and a moderate slope at low suctions. The α parameter acts to shift the curve between low and high suctions by controlling the air entry suction, and therefore does not influence the shape of the overall curve. The n parameter is related to the pore size distribution; a soil of uniform pore sizes has a large n value and results in a steeper curve in the zone of greatest de-saturation. This is due to the previously mentioned simultaneous non-equilibrium for a given capillary pressure which results in a rapid withdrawal of water. The n and m parameters may be related to each other by Equation 2.15 after Mualem (1976). The van Genuchten expression is commonly rearranged to approximate the average suction present based on the effective saturation state of the soil (Equation 2.16).

When the soil is re-wet, the SWRC differs from that upon drying and this dependence upon the history of drainage or wetting is known as hysteresis (Figure 2.9). The hysteresis phenomenon has itself been characterised in proposed SWRC models as reviewed by Pham et al. (2005).

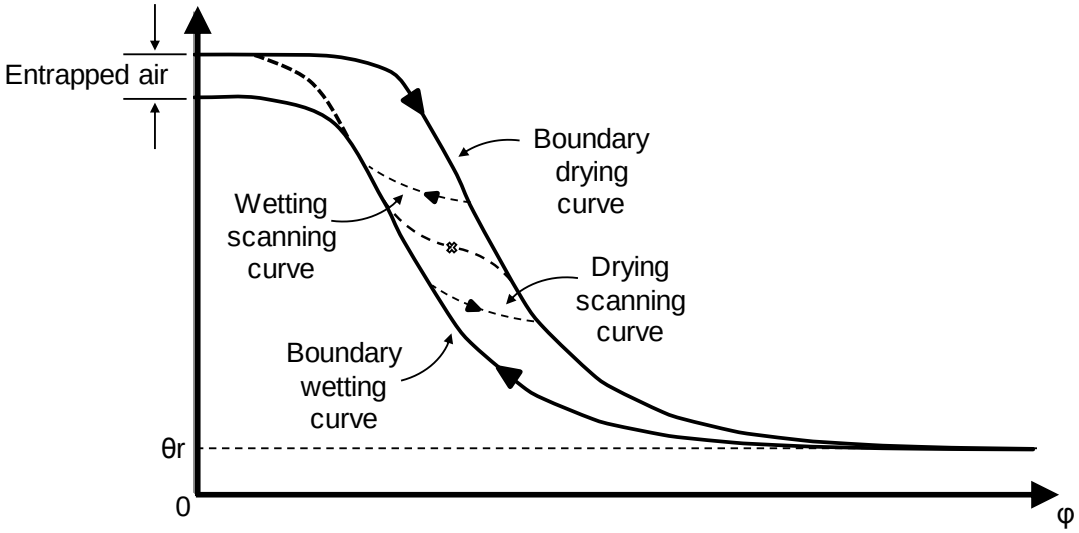

Figure 2.9 Illustration of hysteresis in SWRC.

This is brought about by the following phenomena:

Ink-bottle effect – The alternating narrow and wide structures that comprise the pore spaces allow menisci of the same radius to exist at different positions in the channels (Figure 2.10). This results in achieving different water saturations for the same capillary pressure.

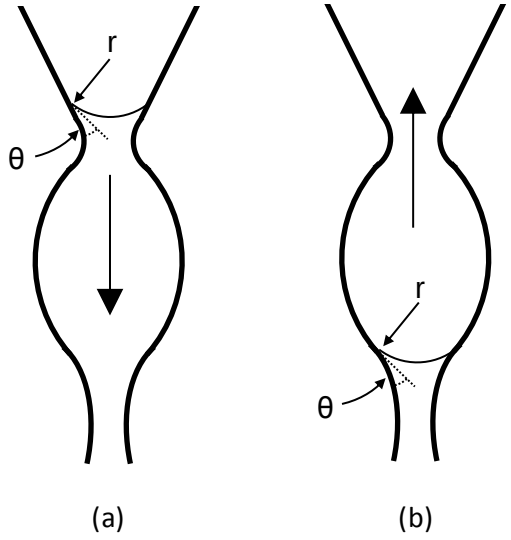

Figure 2.10 Hysteresis due to the ink-bottle effect, a) drainage, b) imbibition.

Raindrop effect – The contact angle at the receding edge of the fluid-fluid-solid interface, θ_1 differs from the contact angle at the advancing edge, θ_2 (Figure 2.11). This is because of impurities and/or variability in the composition and roughness of the solid surface.

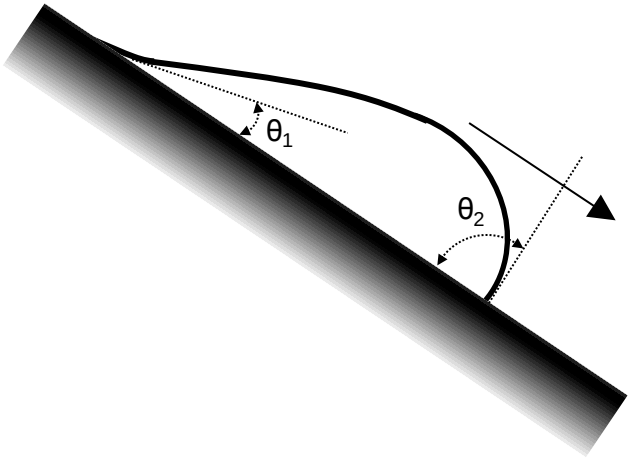

Figure 2.11 Hysteresis due to the raindrop effect.

Entrapped air – The non-wetting fluid may become entrapped meaning the total wetting fluid saturation is not achieved upon rewetting.

Shrink-swell – This particularly affects fine, non-consolidated media as it alters the geometry of the solid matrix upon drying and wetting.

The SWRC presented in Figure 2.9 shows the effect of entrapped air, where the drying and wetting curves do not form a closed loop. It is possible to follow either path from any point within the space bounded by the drying and liquid curves; this behaviour is depicted by the wetting/drying scanning curves. It is therefore shown that the suction-water content relationship is dependent upon the drying/wetting history of the soil.

If no consolidation takes place and the soil structure is stable then the hysteresis loop may be repeatedly traced. If consolidation does take place, the curve will shift to reduced water content as porosity (saturated fluid content) is reduced.

2.2.6 Relation to Phreatic Surface

The distribution of water in the unsaturated zone, above the phreatic surface ($P_w=0$), may be given by the SWRC. There exists, immediately above the phreatic surface, a capillary fringe of elevation equivalent to φ_{AEV} (m) shown in Figure 2.8, this fringe is practically saturated.

Specific yield, θ_y, is related to the volume of water drained from a soil column, in the unsaturated zone, by the lowering of the phreatic surface elevation. The specific retention, θ_r, is the water retained in the soil against gravity by capillary forces. At any instant of time, $\theta_y + \theta_r = n$ (Figure 2.12).

The water distribution in a homogenous soil profile is presented in Figure 2.12. The profile consists of two water table depths, d' at t' and d'' at t''>t'. The specific yield for this case depends on the starting and final phreatic surface elevations and on the time taken to lower the surface. The time element is important as a new moisture distribution will take time to be established following a rapid change in phreatic surface elevation. This lag is removed if the lowering of the surface elevation is sufficiently slow. If the two example water tables are at sufficient depth then the water content curves are the same shape and parallel.

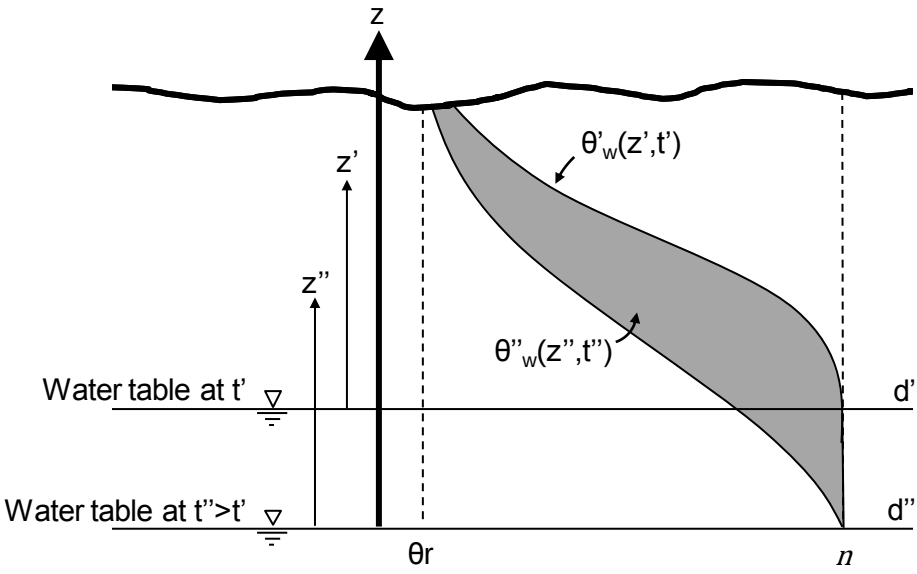

Figure 2.12 Specific yield for a shallow phreatic surface (after Bear & Bachmat, 1990).

2.2.7 Unsaturated Permeability

Intrinsic permeability, k_i, is a quantitative property of porous material and is a function of pore geometry through which fluid may be transmitted. Saturated hydraulic conductivity, K_s, however, is a measure of the ability of saturated soil to transmit a fluid of specific viscosity (η) and density (ρ) when subjected to a hydraulic gradient. Intrinsic permeability is the portion of hydraulic conductivity which is representative of the properties of the porous medium, independent of fluid viscosity and density (Equation 2.17).

$$K_s = k_i \frac{\rho g}{\eta} \quad \textbf{2.17}$$

The hydraulic conductivity for a given soil therefore becomes lower when the fluid is more viscous. In some cases, K_s is used as a synonym for permeability (and vice versa) though this application strictly requires qualification of the fluid in question and thus its assumed properties.

A fundamental aspect of multiphase flow modelling is the nonlinear calculation of fluid flow velocity based upon the dependency of permeability relative to either pressure or saturation. As the saturation of a given fluid reduces, so too does the permeability of that fluid. Richards (1931) identified the following scenario: “If there is a steady flow of liquid through a porous medium which is (un)saturated, then the larger pore spaces contain air and the effective cross-sectional area of the water conducting region is reduced” (pp323)

Due to the action of adhesive forces and pressure differences between liquid-air-solid interfaces, the formation of continuous and connected water films exists, the size of which depends on the amount of water present (Figure 2.13). It is through these films that capillary flow takes place (Richards, 1931).

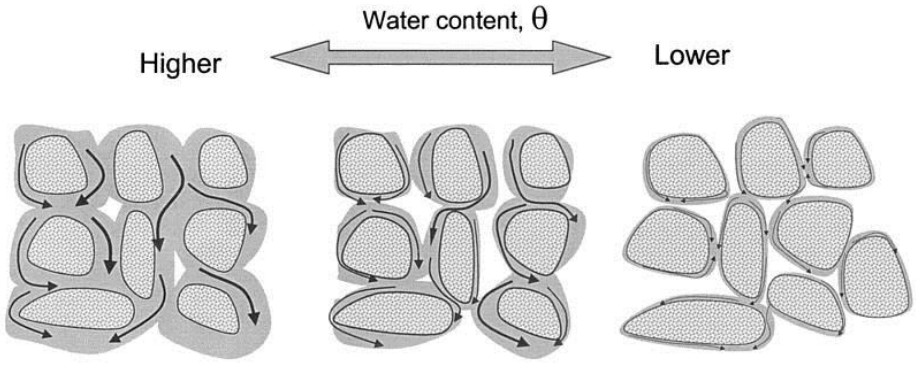

Figure 2.13 Illustration of reduced water conductivity in unsaturated soil (after Toride et al., 2003).

Additionally, it is recognised that with increasing water content, an independent, mobile water phase exists through which greater flow will be enabled. Conversely, with an increased degree of saturation, the permeability of the air phase is decreased. The unsaturated permeability of the two phases are commonly normalised to their respective saturated permeability and are termed 'relative permeabilities' (Lu & Likos, 2004). This brings about the definition of a further permeability term which describes this reduced effective transmission of water under unsaturated conditions. The relative permeability for a given fluid is given by:

$$k_r = \frac{k_i}{k_s} \leq 1 \qquad \textbf{2.18}$$

where k_i is the effective permeability and k_s is the saturated permeability. The intrinsic permeability is equivalent to the soil under saturated conditions by a single phase e.g. representative of the entire water conducting region. Here, the effective permeability is a measure of the soil's reduced ability to conduct water depending on the water content of the soil.

The relative permeability of each fluid is dependent upon the configuration of the respective fluid in the pore space. Therefore, relative permeability is a function of saturation, $k_r = k_r(S)$. A representative permeability curve for air and water is presented in Figure 2.14. The density and viscosity of each fluid are assumed to remain constant despite the influence of viscosity ratio being shown to affect the specific discharge of the unsaturated medium (Bear, 1972)

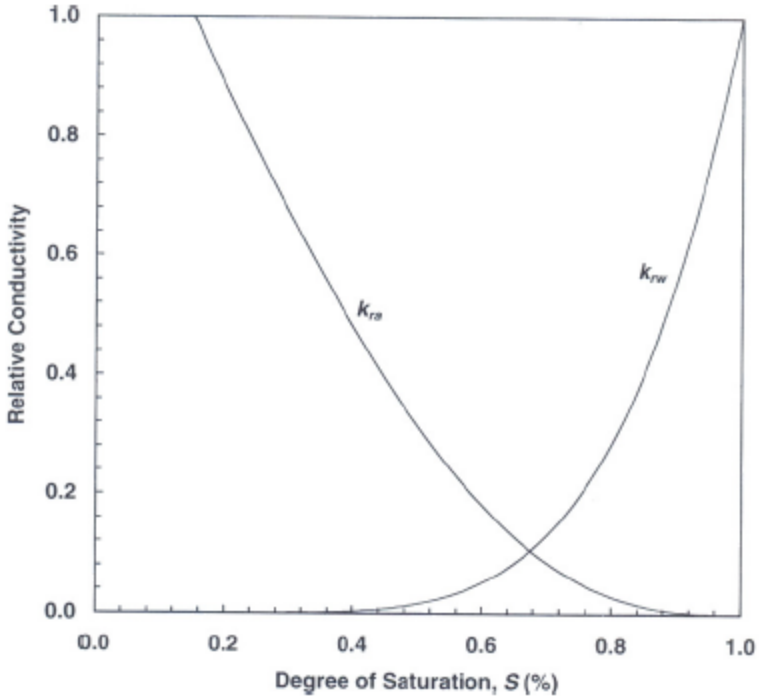

Figure 2.14 Typical relationship between air and water conductivity and degree of saturation (after Lu and Likos 2004).

The relationships illustrated in Figure 2.14 are commonly empirically derived. Empirical expressions have been proposed including Equation 2.19 for the relative permeability of water by van Genuchten (1980), based on the equations of Maulem (1976). Parker (1987) later derived Equation 2.20 for the relative permeability of air. Both of these expressions, where θ_e is the effective water content, incorporate the fitting parameter m introduced in Section 2.2.5.

$$k_{rw}(\theta_w) = {\theta_e}^{1/2}\left(1 - \left(1 - {\theta_e}^{1/m}\right)^m\right)^2 \quad \textbf{2.19}$$

$$k_{ra}(\theta_a) = (1 - \theta_e)^{1/2}\left(1 - {\theta_e}^{1/m}\right)^{2m} \quad \textbf{2.20}$$

2.3 Shrinkage

The phenomenon of cracking has been studied for decades and despite this, the definite mechanism that governs the occurrence of cracking is still widely under investigation. The currently held understanding of the mechanics by which clay soils crack was established as far back as 1960 and centres on the generation of tensile stresses as a product of restrained shrinkage due to the removal of moisture (Corte & Higashi, 1960; Towner, 1987; Towner, 1961).

Consider a bar whose ends are fixed in the longitudinal direction (Figure 2.15 left). Anisotropic shrinkage will occur in the width and depth orientations of the bar until tensile stresses induced in the longitudinal direction increase beyond the increasing tensile strength and the bar cracks.

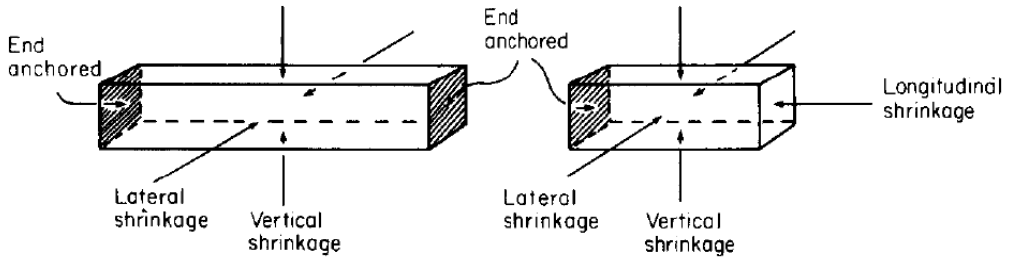

Figure 2.15 Shrinking clay bars (left) longitudinal ends anchored. (right) one end anchored (after Towner 1987).

It is hypothesised that the tensile stress due to isotropic shrinkage is equal to the change in soil-water suction (Towner, 1987)a. Consider a bar that is only anchored at one end (Figure 2.15 right). As the bar dries, water is extracted and the soil-water suction increases. It has been empirically justified that for a saturated soil, internal suction is quantitatively equivalent to an external compressive stress applied to the free surfaces (Towner, 1961). Hence, the free end is compressed towards the fixed end. If one takes the free end to represent the plane of a potential crack, for shrinkage to be opposed, an equal and opposite stress must be applied. The resulting tensile stress is equal to the soil-water suction that induced the longitudinal shrinkage (Towner, 1987)b.

Investigations into the volume-changes associated with changing soil water content were conducted by Haines (1923). The term “volume of soil” is used to describe the total volume occupied by the soil skeleton which constitutes the soil particle arrangement and the interstices whether these are filled by water,

air or a combination of the two. Haines (1923) describes the shrinkage of an initially saturated soil by two approximate straight lines, as depicted in Figure 2.16 . The primary drying stage is associated with the exclusive removal of water without the ingress of air and as such, the soil remains completely saturated during this phase. The volume change is assumed equal to the volume of water leaving the soil and this stage represents the period of greatest volumetric shrinkage. As water is removed further, the soil consolidates until eventually the soil particles contact and shrinkage begins to slow. Further drying is termed residual drying and signifies the entry of air into voids replacing water. Little change in the total volume of soil occurs during residual drying due to the contact between solid particles. The greatest portion of volume decrease occurs in saturated conditions (Fleureau et al., 1993). Hence, total shrinkage is heavily related to the relative volumes of water and solids present as drying progresses. This theory is backed up by more recent studies that link measured volumetric shrinkage strain to water content at compaction (Albrecht & Benson, 2001) and is the principle characteristic quantified by common laboratory standard tests e.g. BS 1377-2:1990 Section 6 (British Standard, 1990).

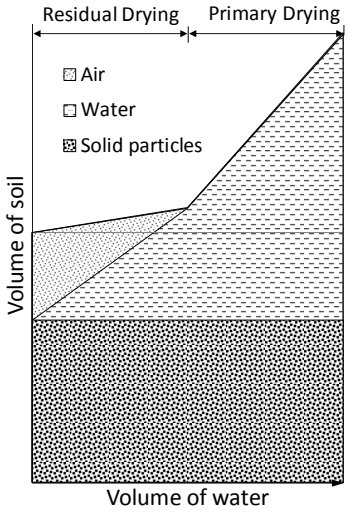

Figure 2.16 Drying stages (after Haines, 1923).

The concept that most shrinkage occurs while the soil is still saturated has been established in several previous studies (Croney & Coleman, 1954; Fleureau et al., 1993). It is therefore not too great a logical step to suggest that cracking initiates during this period of greatest shrinkage; that is to say while the soil is undergoing primary (or ‘normal’) drying in a state of full saturation.

2.4 Quantifying cracking

Laboratory scale experiments offer researchers the opportunity to better isolate the parameters that influence the initiation of desiccation cracking although just as each soil may behave differently, the means and methods of investigation are extensive. Typically, such investigations are phenomenological – empirical observations of soil desiccation, shrinkage and cracking are used in the effort of developing a consistent, fundamental theory. The geometry of desiccation cracks and their networks, for example width, depth and surface area, is highly influential in the mechanical and hydrological behaviour of cracked soil. Therefore, a convenient quantitative descriptor is required to characterise the degree to which a soil surface has undergone cracking. Works have often focused on the statistical assessment of cracking patterns from direct crack measurement to the increasingly frequently use of imaging analyses.

Corte and Higashi (1960) were among the earliest contributors providing data gathered from a comprehensive laboratory programme of approximately 60 tests. Experiment parameters were split into extrinsic and intrinsic categories. Externally controlled parameters were temperature, relative humidity, soil layer thickness and base/mould material and intrinsic parameters were initial moisture content and compaction (Corte & Higashi (1960) cited in Kodikara et al. (2000)). In order to compare the observed cracking behaviour of each test condition, the mean cell area defined as the total cell area (coherent ped between cracks) divided by the number of cells at the end of drying was considered. This approach enabled observations such as smaller cell sizes (diffuse smaller cracks) on glass than wood to be quantitatively presented alongside the effect of increasing cell sizes with soil layer thickness as illustrated in Figure 2.17.

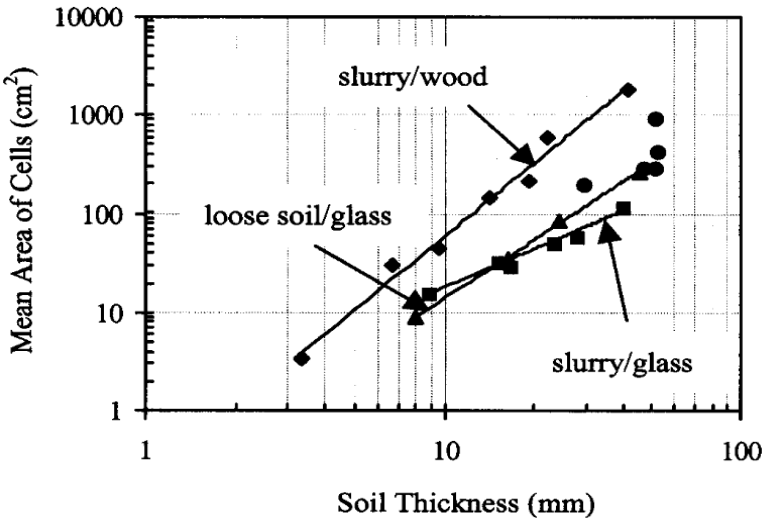

Figure 2.17 Mean cell area resulting from drying of varying soil thicknesses on different basal materials (after Kodikara et al. 2000).

Subsequently, several authors have proposed various means of describing the cracked state. Transects were favoured to provide an unbiased representation and were based upon crack interception (Ringrose-Voase & Sanidad, 1996). A cracking severity scale of 0-4 was described by Kleppe and Olsom (1985) where 0 equals no cracking at all and 4 indicating deep cracks with widths >20mm. However, with the progression in digital imaging resolution and processing, these tools are increasingly favoured and are described in the following sub-section.

2.4.1 Crack Intensity Factor

The Crack Intensity Factor (CIF) was introduced and defined by Miller et al. (1998) as the ratio of the total surface crack area to the total surface area of the clay. This ratio may be calculated as a time-variable and thus used to describe the progressive development of cracking.

Physical measurement of the CIF is difficult given the inherent tortuosity of cracks leading to potentially imprecise calculation. However, several researchers have adopted computer based image analysis procedures to determine the various properties of the crack network (Yesiller et al., 2000; Vogel et al., 2005; Tang et al., 2008; Tang et al., 2010; Tang et al., 2011).

The image analysis procedure for a 2D crack pattern may be broadly described by the following steps. A colour photograph of the soil state representing a

given time is changed to a grey level image (Figure 2.18a) before increasing the image contrast. In a process known as binarisation, this is then reduced to a binary black and white image where black pixels represent the opened crack surface and white, the coherent clods (Figure 2.18b). The relative areas may then be used to calculate the CIF while further stages may be employed to establish other network properties such as crack intersections and length by image skeletonising (Figure 2.18c). Although much of this procedure may be conducted automatically using image processing software, optical artefacts may still need identifying and removing for an accurate analysis. Such adverse phenomena include the generation of shadow effects caused by the angle of test lighting and the reflecting nature of the test substrate which may become visible through exceptionally wide crack apertures (Vogel et al., 2005; Tang et al., 2008).

Figure 2.18 Procedure of digital image processing (a) initial grey level image, (b) binary black and white image and (c) skeleton of crack network (after Tang et al. 2008).

2.5 Tensile strength

Given the widely held understanding that cracks occur when the tensile strength is exceeded by shrinkage induced tensile stress, the determination of this property as a function of water content and/or suction is essential to understanding soil response to desiccation. The following section introduces soil tensile strength theory before providing an overview of published tensile testing methods.

As described in section 2.2, fluids are configured within the pore space according to the degree of saturation which leads to a gradation between the dominant mechanisms that act to withstand tensile load on the grain-grain scale. While the soil remains within the capillary regime, prior to desaturation, capillary pressure can directly contribute to the increase in effective stress. Upon desaturation, the soil enters the funicular regime where air gradually enters the soil. Fully saturated pores remain alongside drained pores related to the formation of menisci; this leads to the combined capillary forces associated with water filled pores and interfacial tension. Finally, with continued de-saturation within the pendular regime, the capillary force is governed by the tension force at the water-solid contact and the pressure deficit between the meniscus water and pore air pressure. The macroscopic tensile strength of soil is given by the net tensile forces that exist under each given saturation regime.

Many analytical expressions to predict the tensile strength of idealised soil grain arrays have been proposed. These typically concern soils comprising perfectly spherical grains of uniform diameter packed in regular arrays or more focused solutions on two-grain systems. One such study is that of Lu and Likos (2004) who expressed the tensile strength due to water bridging between two identical contacting spheres in the pendular regime (Figure 2.6 Section 2.2.3) in the form:

$$\sigma_t = \frac{r_2}{R^2}\frac{r_1 + r_2}{r_1}\gamma_s \qquad \textbf{2.21}$$

where R represents the radius of the grain, γ_s is the surface tension of the wetting fluid and the radii r_1 and r_2 describe the water bridge geometry. An illustration of the two-grain conceptual scenario is given in Figure 2.19. The

filling angle, θ, describes the size of the meniscus and is directly relatable to the degree of saturation. Presented in the diagram is the scenario of a non-zero solid-wetting fluid contact angle, α. This parameter is dependent upon the fluid properties, solid surface and the wetting/drying direction (see section 2.2.5). From this idealised geometry, the radii $r_1$and $r_2$may be defined as:

$$r_1 = R\frac{1-\cos\theta}{\cos(\theta+\alpha)} \quad \textbf{2.22}$$

$$r_2 = R\tan\theta - r_1 \quad , \quad \alpha = 0 \quad \textbf{2.23}$$

$$r_2 = R\tan\theta - r_1\left(1-\frac{\sin\alpha}{\cos\theta}\right) \quad , \quad \alpha > 0 \quad \textbf{2.24}$$

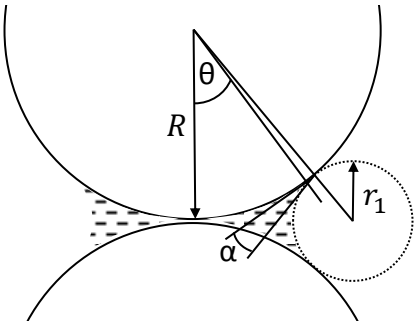

Figure 2.19 Meniscus geometry between two identical grains with a non-zero contact angle (after Lu and Likos, 2004).

Rumpf (1961) also proposed a theoretical solution for the pendular regime. Although the proposed theory was presented for the scenario of non-contacting identical spherical grains, the theory may be scaled up to predict the macroscopic tensile strength by assuming the bonding forces to be distributed in all directions between grain surfaces and using a mean value. Hence, from the case illustrated in Figure 2.20, the following expression is defined:

$$\sigma_t = \frac{(1-n)}{n}\frac{\pi\gamma_s}{2R}\sin\theta\left[\sin(\theta+\alpha) + \frac{\sin\theta}{4}\left(\frac{1}{r^*}-\frac{1}{h^*}\right)\right] \quad \textbf{2.25}$$

where,

$$h^* = \frac{h}{2R} = \frac{\sin\theta}{2} + \frac{r}{2R}[\sin(\theta+\alpha)-1] \quad \textbf{2.26}$$

$$r^* = \frac{r}{2R} = \frac{(1-\cos\theta) + \frac{a}{2R}}{2\cos(\theta+\alpha)} \quad \textbf{2.27}$$

The parameters γ_s, R, θ and α are, as before, surface tension, common grain radius, filling angle and the contact angle respectively. In addition to these terms is the bulk porosity, n and the dimensionless grain separation distance, $a/2R$. It may be seen that the tensile strength term is inversely proportional to the size of the grains.

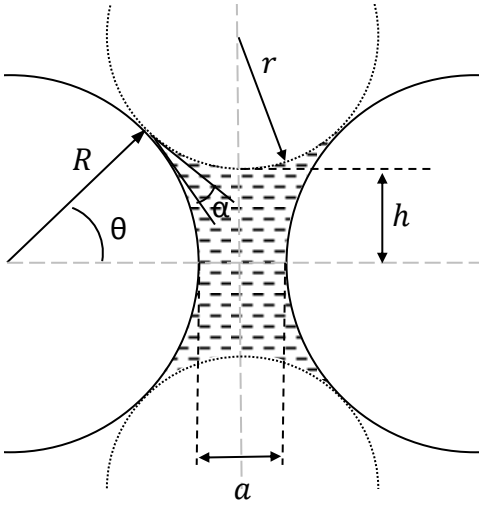

Figure 2.20 Meniscus geometry between two non-contacting grains with a non-zero contact angle (after Kim and Hwang, 2003).

In the case of non-contacting grains, the filling angle may be related to the water content by the following expression by Pietsch and Rumpf (1967) (cited in (Pietsch, 1968)):

$$w = \frac{6k}{G_s}\frac{V_{bridge}}{2\pi d^3}$$

$$= \frac{6k}{G_s}\left\{[r^{*2} + (r^* + h^*)^2]r^*\cos(\theta-\alpha) - \frac{r^{*3}cos^3(\theta+\alpha)}{3}\right.$$

$$- r^{*2}(r^* + h^*)\left[\cos(\theta+\alpha)\sin(\theta+\alpha)\left(\frac{\pi}{2} - \theta - \alpha\right)\right] \quad \textbf{2.28}$$

$$\left. - \frac{1}{24}(2+\cos\theta)(1-\cos\theta)^2\right\}$$

This assumes that the specific gravity of the soil is known and that the mean number of grain-grain contacts per grain may be estimated as a direct relation to the mode of grain packing e.g. simple cubic $(k = 6)$, tetrahedral $(k = 12)$. Hence, not only is the size and separation of the grains important in the tensile strength in the pendular regime but so too is the grain assembly/packing.

By using the contact angle of the solid-wetting fluid, Goulding (2006)was able to infer the effect of wetting verses drying on the magnitude of the theoretical tensile strength assuming a simple cubic packing order. The contact angle during drainage and imbibition are typically different depending upon the wettability of the surface with a contact angle approaching zero common during drying and larger angles typical of wetting. Therefore, the data illustrated in Figure 2.21 indicates that tensile strength during drying may be relatively greater than that experienced by the same configuration during wetting.

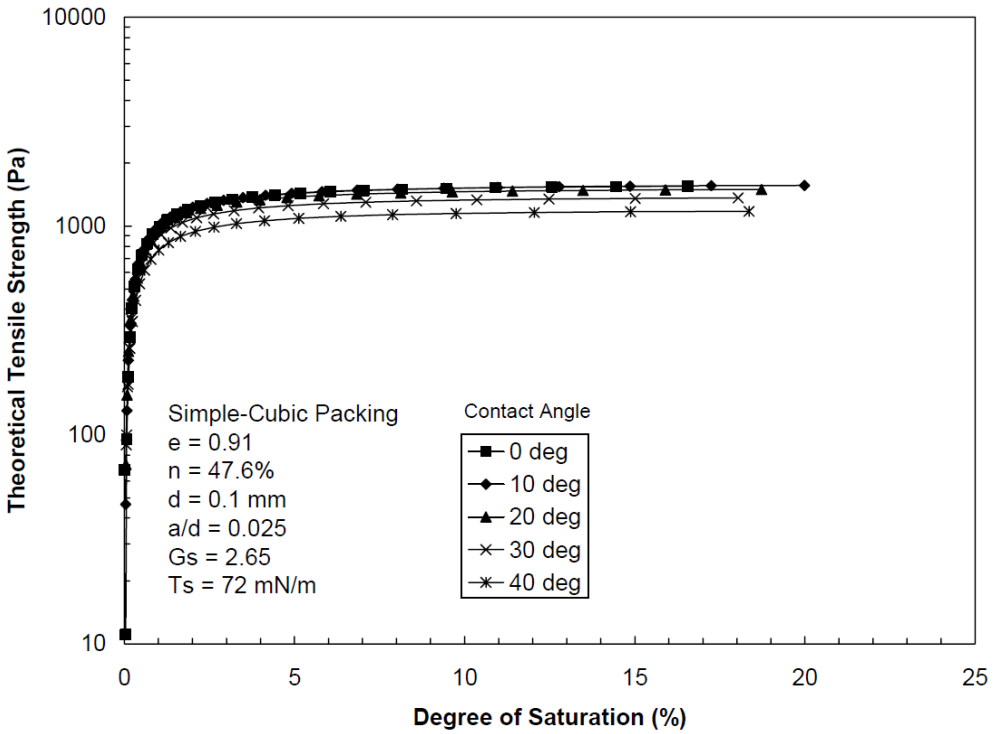

Figure 2.21 Theoretical tensile strength as a function of contact angle (after Goulding, 2006).

A theoretical expression for the tensile strength of soils closer to saturation, yet under negative pore-water pressure (capillary regime) was proposed by Schubert (1975) [Equation 2.29]. Hence, when the soil is saturated, while the capillary pressure (matric suction) is below the air entry value, the theoretical

tensile strength is equal to the matric suction as was proposed by (Towner, 1987)b.

$$\sigma_t = SP_c \quad \textbf{2.29}$$

By combining Equations 2.25 and 2.29, Schubert (1984) proposed a model for tensile strength in the funicular state:

$$\sigma_{t_f} = \sigma_{t_p} \frac{S_c - S}{S_c - S_f} + \sigma_{t_c} \frac{S - S_f}{S_c - S_f} \quad \textbf{2.30}$$

where, subscripts $_p$ and $_c$ refer to the pendular and capillary regimes, respectively. The tensile strength terms are normalised by saturation with reference to the boundary saturations between the capillary, funicular and pendular states. For example, the boundary saturation between funicular and capillary saturations is given by S_c and between pendular and funicular by S_f. These boundaries may be deduced from the shape of the SWRC in relation to the AEV and the residual water content. Hence, peak tensile strengths are attributed to near the AEV in the capillary regime and the residual water content in the pendular regime.

It is important at this stage to remember that these theoretical expressions apply to idealised packing of spheres. Waldron et al. (1961) asserted that it is adsorption as opposed to capillary effects that determine the retention of water, especially in clayey soils. A combined understanding is proffered by Snyder and Miller (1985) where it is recognised that adsorption effects will become significant at very low water contents when appreciable adsorption forces will dominate. Additionally, such theoretical expressions are not applicable to soils which exhibit considerable cementation as these will fail differently subject to the properties of the cementing agent. Work by Bishop and Garga (1969) has shown that although cementation may be important in dried or undisturbed soils, its effect is minor in disturbed and moist soils.

2.5.1 Tensile strength testing

There exists no unified approach to the testing of tensile strength of soils as there is for standard soil mechanics such as shear or compression. Methods have traditionally been created using adaptations of standard tests or adopted from the testing of other materials i.e. rock or metals. The published methods may be categorised on the principle of loading as illustrated in Figure 2.22.

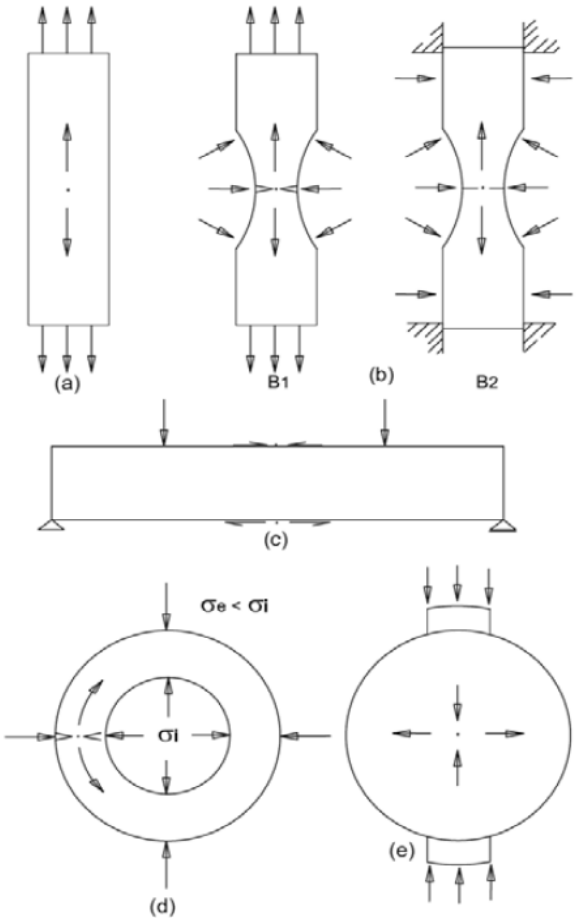

Figure 2.22 Tensile tests according to the manner of loading (a) axial tensile test, (b) triaxial tensile test, (c) bending test, (d) hollow cylinder and (e) indirect tensile test (after Vanicek, 2013).

The axially loaded test (Figure 2.22a) offers the most direct measurement of tensile soil behaviour although suffers from uncertainty regarding the uniformity of stress distribution about the cross section, difficulty in gripping the specimen without inducing problematic stress concentration and the inherent undrained nature of the test. This type of test is further described in Section 2.5.1.3.

Figure 2.22b B1 and B2 are versions of traditional drained triaxial tests where the axial effective stress at the centre of the specimen becomes negative (i.e. tensile) via the reduction in back pressure. Such tests were conducted by

Bishop and Garga (1969) who noted a brittle style of failure with a relatively large variability in the maximum strain. The bending test shown in Figure 2.22c will be familiar to structural engineers as it is an established method in the testing of beams. The hollow cylinder technique (Figure 2.22d) is based on the application of varying internal and external hydrostatic pressure. This method is considered the most involved approach illustrated in terms of specimen production and testing but provides the ability to more precisely investigate the deformability and strength of anisotropic materials under drained conditions.

Lastly, the indirect, Brazilian test is illustrated (Figure 2.22e) and is the standard test for determination of tensile strength in brittle materials such as rock and concrete. The prolific use of this technique in geotechnical engineering and engineering geology makes this an attractive option for measuring tensile strength although its use in soil testing is subject to some major limitations. This approach is further discussed in Section 2.5.1.2.

2.5.1.1 Extrapolation method

An alternative to bespoke testing of tensile soil properties is the extrapolation of standard triaxial testing data assuming constitutive behaviour. One of the most recent examples of the triaxial approach is presented by Venkaramana et al. (2009). A total of 14 different clay soils were prepared by sieving to 425μm and wetting up to their optimum water content. This material was allowed to homogenise for over 2 days before being compacted into a triaxial mould ($\emptyset = 34mm$, $L = 76mm$). Five identical samples were formed from each soil type corresponding to its OMC and hence, maximum dry density. These samples were subjected to undrained shearing at a rate of 1.25mm/min and five different confining pressures (25, 50, 100, 200 and 300kPa).

From the plotting of results in the form shown in Figure 2.23, a common tangent defines the Mohr-Coulomb failure envelope. By extending this envelope linearly to determine the intercept on the σ axis, this $-\sigma$ value is taken to equal the tensile strength.

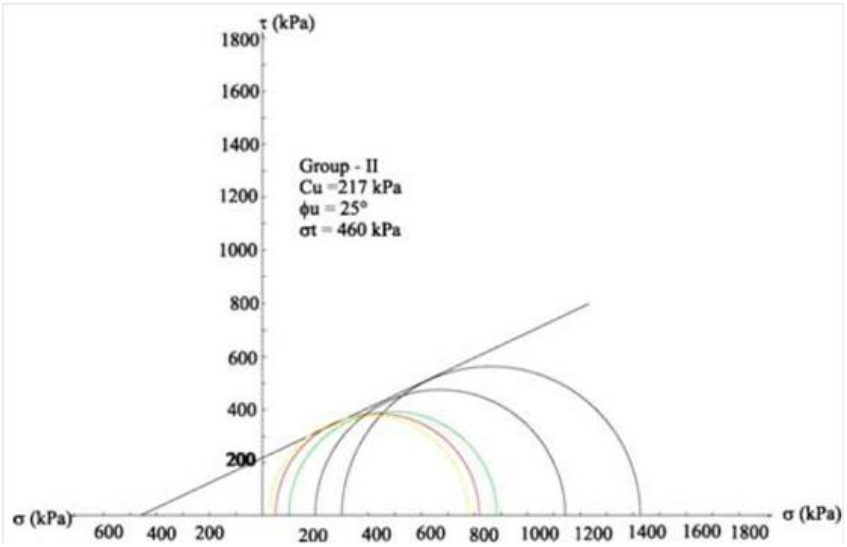

Figure 2.23 Typical Mohr-Coulomb strength envelope for a study soil (after Venkataramana et al., 2009).

The authors have shown tensile strengths obtained using this method to range between 350-500kPa. In comparison to published tensile strengths, this order of magnitude is not unreasonable for a clay soil at maximum dry density and OMC i.e. optimum strength condition. However, this indirect extrapolation of tensile strength from the assumed linear $\tau - \sigma$ relationship is inherectly prone to the overestimation associated with the back-casting of the Mohr-Coulomb envelope.

As an aside, Venkataramana et al. (2009) goes on to explore a comparison between these experimentally obtained values and those gained by applying soil classification terms to varous analytical expressions gathered from the literature. They describe that in seeking a widely applicable expression for determining the tensile strength of fine-grained soils, a dependancy on their physical, chemical and mineralogical properties exists yet current expressions often restrict the relation to a singular property variable. The authors conclude that tensile strength may most effectively (when validated against their experimental data) be related to clay content, cation exchange capacity and suction.

2.5.1.2 Indirect tensile strength tests

The Brazilian test was developed simultaneously yet independently by Carneiro and Barcellos (1953) and Akazawa (1953). The test assumes biaxial linear elasticity in two-dimensions and the sample is considered to fail at the centre of the disc, where the tangential stress ($\sigma_{\theta y}$) will overcome the uniaxial tensile strength under the application of a radially compressive stress (σ_{ry}) (Figure 2.24), (Fairhurst, 1964).

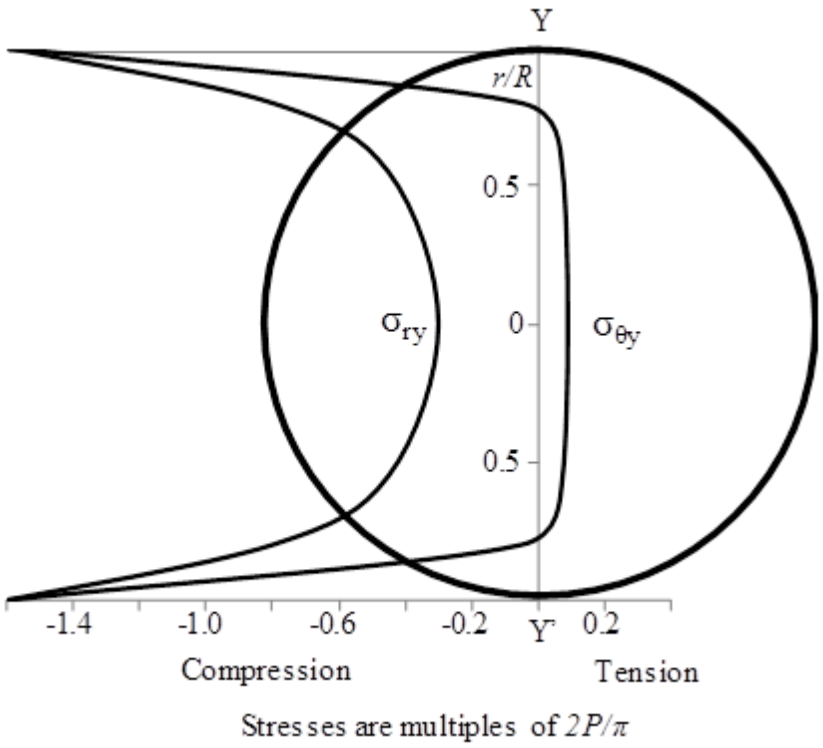

Figure 2.24 Stress distribution along line YY' in the Brazilian test where, r=radial distance, R=disc radius and P=applied load (after Fairhurst, 1964).

The method has most commonly been used in rock mechanics and is comprehensively described in rock testing standards, namely ISRM (1978) and ASTM (1984). These standards differ in a number of ways with respect to recommended sample dimensions and load/strain rate control. However, the principle difference is the manner in which the loading platens make contact upon the circumference of the sample as illustrated in Figure 2.25.

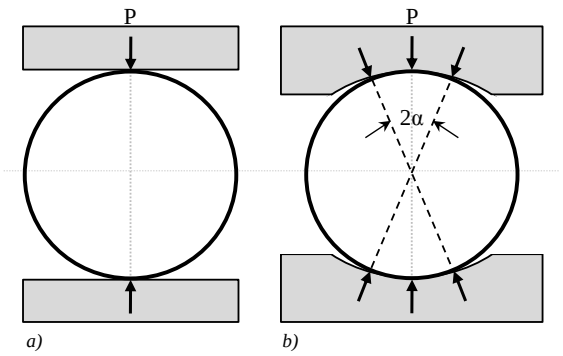

Figure 2.25 Standard Brazilian test loading geometries (a) (ASTM, 1984) and (b) (ISRM, 1978) (after Stirling et al., 2013).

These geometries are the product of an effort to avoid the localised crushing of the sample at the point of loading contact. This behaviour is largely dependent upon the type of material being tested with soils posing a particular challenge in the occurrence of undesirable sample deformation. However, there have been a number of studies that have identified the Brazilian test potential in the testing of stiff soils.

Frydman (1964) investigated the validity of Brazilian tests where heavy plastic deformation is expected. The author showed that in testing soils and stabilised soils, the quantified deformation, in most cases, does not invalidate the theoretical basis upon which the test is conducted and proposed a critical cut-off at which the standard theory would no longer apply. Later, Krishnayya and Eisenstein (1974) examined the biaxial stress condition at the centre of the soil disc. Where brittle materials are commonly tested in the Brazilian test, the difference between moduli in compression and tension is considered negligible i.e. $E_c/E_t = 1$. However, for more plastic materials such as soils where the tensile strength is much lower, the modulus in tension is considerably lower than in compression e.g. $2 < E_c/E_t < 15$ (Krishnayya, 1973).

A series of comparative tests were undertaken on relatively stiff mica till via conventional unconfined compression apparatus for assessment of compressive stress-strain behaviour and Brazilian tests for tensile behaviour. The experimental setup presented in Figure 2.26 shows the use of a traditional strain gauges mounted across the central region and in the orientation in which tension is induced. Compressive strain was measured using an LVDT positioned against the upper platen (as shown) and was used to gather data to

in order to refine the apparent strain recorded by the clip gauge down to that purely induced by tensile stress.

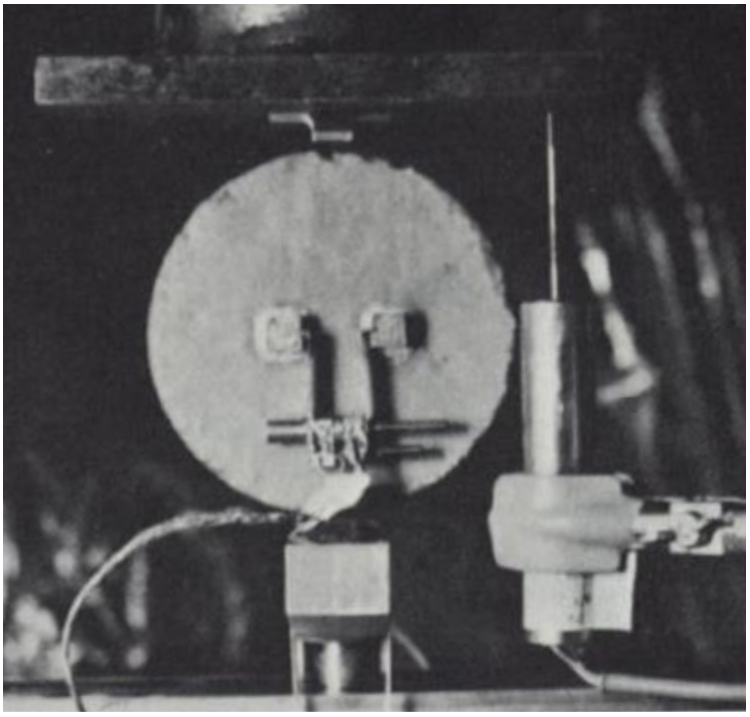

Figure 2.26 Disc sample with clip gauge (after Krishnayya & Eisenstein, 1974).

It was shown that although the Brazilian test is a simple method for gaining tensile strength measurements of low plasticity materials that fail in a brittle manner, when there is a marked difference in the compressive and extensional stress-strain relationship, error is introduced by the use of traditional tensile strength calculation. Hence, Krishnayya and Eisenstein (1974) describe a Finite Element method for the calculation of tensile and compressive stresses at the sample centre for varying E_c/E_t ratios which they suggest allow for an appropriate estimation of tensile strength.

The practicalities of the Brazilian test sample preparation are the greatest limitation in its use in soil tensile strength testing. The sample is required to be self-supporting in the first instance. This restricts the applicability of the test to a soil condition that is considerably well below saturation. Depending upon the plasticity of the cohesive component of the soil, the water content at testing is commonly very low e.g. <10%. This makes the test inapplicable to research concerned with the progressive desaturation of clay soils.

2.5.1.3 Direct tensile strength tests

Direct methods of tensile strength determination are often preferred for their theoretical simplicity; however, they are difficult to design and conduct with a high degree of confidence and are restricted to undrained conditions. Of primary concern is the means by which the load is applied to the soil sample at the apparatus-soil interface. At the centre of this problem are the induction of shear stress and the introduction of secondary substances (i.e. glues and resins) which interfere with the measurement of pure tension in the soil under investigation. The following section outlines various proposed laboratory approaches to the direct tensile loading problem.

A uniaxial tensile load is often applied to the soil sample in one of two ways, either by gripping the sample via end caps/internally or by laterally restraining the sample via loading jaws. Earlier work adopted the former of these methods while the latter approach has been favoured more recently, primarily differing in the geometry of the jaw design.

One of the earliest ‘gripping’ methods was proposed by Heibrock et al. (2003) who used a 90 mm x 24 mm hollow-cylinder form. Cylinders were trimmed from a standard Proctor sample of manufactured kaolin compacted wet of optimum at 25% water content. The relationship between water content and tensile strength was investigated by air drying or wetting up the sample surface as required from determined water content from sample trimmings. Samples were then wax coated to prevent further drying and stored in a climatic chamber for ~48hours to ensure a homogeneous water distribution. Finally, an 8mm diameter hole was drilled through the centre of the sample before adding a filter textile and epoxy resin to fix dowels to which two hooks were mounted. Having removed the wax coating, the sample was mounted in the apparatus shown in Figure 2.27 and pulled apart at a rate of 0.06mm/min. The authors describe how lower velocities were shown to have little effect on the measured tensile strength values.

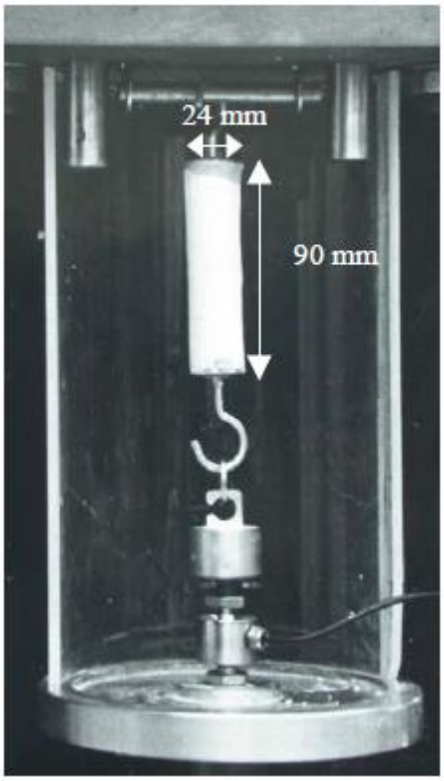

Figure 2.27 Tensile strength test device (after Heibrock et al., 2003).

This method relies upon the sample being of competent consistency such that when unconfined, the sample is able to withstand the internal spreading upon loading. This inherently limits the methods applicable to stiff materials or soils at sufficiently low water content, a similar limitation to that identified in discussion of the Brazilian test.

Nahlawi et al. (2004) proposed a method for measuring the direct tensile strength that provided a required degree of confinement to test weak, high water content clays in addition to strong cement stabilised crushed rock material and was based on the concrete testing method developed by Hannant et al (1999). The apparatus is based on a conventional direct shear test frame though the assembled loading cell component of the rig is highly modified from that of the shearbox.

The loading jaws developed by Nahlawi et al. (2004) are presented in Figure 2.28 and consist of a broadly rectangular 200x100x100mm enclosure. Upon displacement of the moving half, restraint against tensile loading is provided in the specimen by 8 shear keys per specimen half. To ensure failure is induced at the centre of the specimen, the central cross-sectional area is reduced to

70x100mm (formerly 100mm^2). Reduction of the area over which loading is applied is a commonly used approach to localise increasing maximum tensile stress (e.g. Rodriguez (2002); Kim & Hwang (2003); Ibarra et al. (2005); Tamrakar et al. (2005); Trabelsi et al. (2010)). The use of embedded shear keys is relatively novel in tensile strength testing. However, the inclusion of 'glued' structures has previously been employed (e.g. Heibrock et al. (2003); Zeh & Witt (2005)). It is impossible to fully assess the behaviour of the specimen around these structures given their embedded location and this makes it difficult to neglect the influence of internal shearing on the generation of tensile stress/strain. Nonetheless, Nahlawi et al. (2004) considers all sides to be free of shear and normal stresses about the neck area, hence normal tensile stresses are assumed to be uniformly distributed.

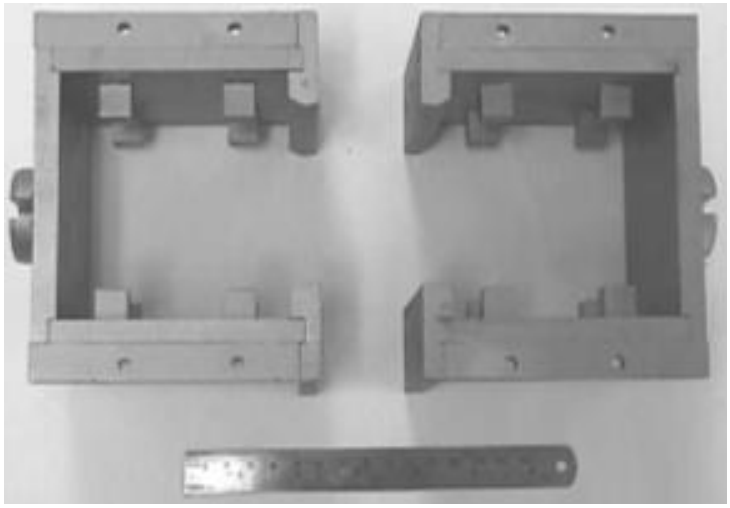

Figure 2.28 Loading jaws with embedded shear keys (after Nahlawi et al., 2004).

Monitoring of tests was conducted using a load cell positioned between the mould and motor as well as tensile displacement measured using LVDTs either attached to the two mould halves or placed in the specimen directly (Figure 2.29). Again, the embedding of such structures is believed to impact the generation of tensile stress/strain to an undeterminable extent as well as provide only a very broad trend in local strain behaviour.

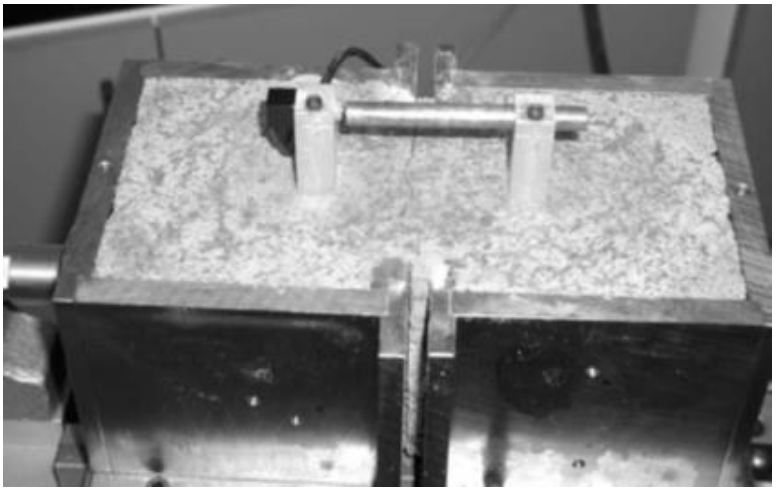

Figure 2.29 Stabilised crushed rock test including strain gauge (after Nahlawi et al., 2004).

Clay samples were prepared (dried and sieved (425μm)) and mixed to required water contents before being left to hydrate uniformly over 12h in sealed plastic bags. Compaction was conducted directly into the split mould (jaws) using “a special hammer” to achieve the desired dry density. As compacted at approximately optimum water content, the dry density was found to be reasonably constant (Nahlawi et al., 2004). The mould together with the compacted specimen was then kept in controlled environmental conditions until testing. Direct compaction into the mould minimises sample positioning damage and allows material of high water content to be prepared where transporting these would be difficult. However, in compacting the specimen into the mould and then storing before testing, for any given environmental condition, the specimen will undergo a degree of undetermined drying prior to testing. Although the water content may be determined immediately after testing, drying prior to testing will be experienced at the upper, exposed surface giving rise to a vertical saturation gradient that is believed to influence the generation of tensile stress across the loaded area of interest. Nahlawi et al. (2004) noted difficulties in testing soils of very high water content (>liquid limit) using their design (i.e. seepage of slurried material) and that it was necessary to cover gaps using adhesive tape. This highlights the suitability of the apparatus to stiffer soil consistencies (e.g. ≤plastic limit). The specimen procedure is also recognised to be material/time intensive as the loading jaws are occupied from specimen formation through to testing. This makes batch preparation and testing difficult without numerous duplicates of the mould/jaws.

Nahlawi et al (2004) conducted strain controlled testing on a clayey soil of extreme plasticity: liquid limit = 127%, plastic limit = 26% with a linear shrinkage = 22%. Tests were carried out at a constant displacement rate of 1.285 mm/min via a conventional Wykeham Farrance motor. However, the actual rate recorded via the specimen mounted LVDT gauge showed a dependency upon soil stiffness with rates ranging between 0.12mm/min and 0.9mm/min up to peak stress. At this stress, observable failure commonly occurred as approximately vertical cracking which developed rapidly over the full depth of the specimen.

The work demonstrated the ability of the method to identify the tensile strength increase with decreasing moisture content trend; conversely, tensile strain at failure was shown to decrease with decreasing moisture content (Figure 2.30). The effect of drying on increasing stiffness was also shown using the secant moduli at failure.

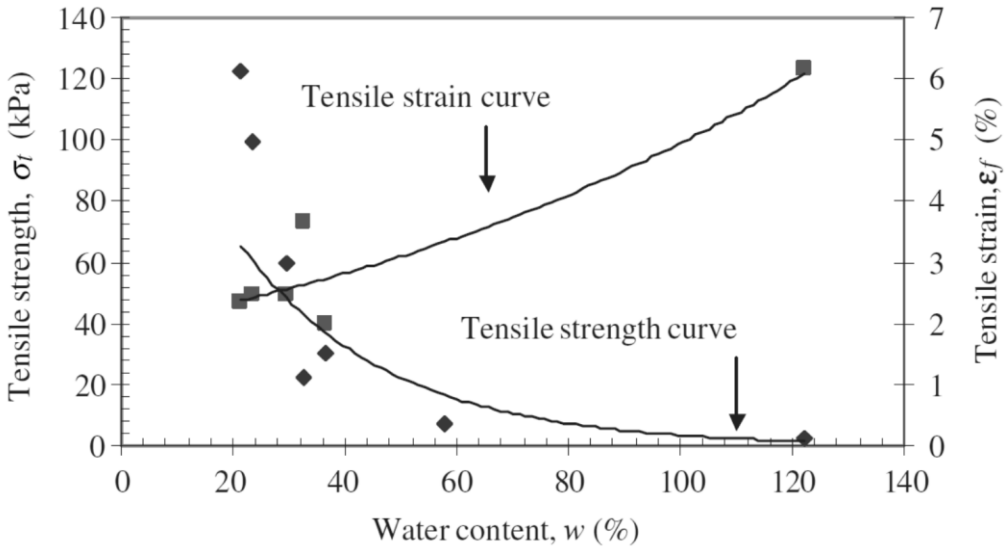

Figure 2.30 Tensile strength and strain at failure versus water content for Werribee clay (after Nahlawi et al. 2004)

Later developments upon the same principle include the work of Tamrakar et al. (2005)a; (2005)b; (2007). The proposed apparatus was designed and tested to establish the tensile strength of both compacted and saturated soft to medium soils. Similar to the design of Nahlawi et al. (2004), the loading jaws consisted of a box split into two halves with one half of the box fixed while the other is allowed to move upon a horizontal platform of rollers to reduce friction.

However, unlike Nahlawi et al. (2004), the jaws were made of two opposing “C” structures as shown in Figure 2.31. This design uses the central cross-sectional area restriction approach along with lateral restraint in order to concentrate tensile stress at the centre of the sample yet leaves the sample free of any internally restricting structures.

To assess the influence of stress concentration at the constricted middle section during testing, Tamrakar et al. (2005)b used two mould/jaw types. The first (type-A) consisted of the two meeting “C” structures (Figure 2.31) while the second (type-B) include a bridging structure (Figure 2.32). Before testing using type-B, the bridging structure is removed. The tensile strengths of tests conducted using mould types-A and -B are found to be identical but for a very small shift in stress-displacement behaviour whereby the displacement at failure of type-B was greater than type-A. The authors concluded the removal of the bridging component makes mould type-A better due to its simplicity and so all subsequent testing was conducted using mould type-A.

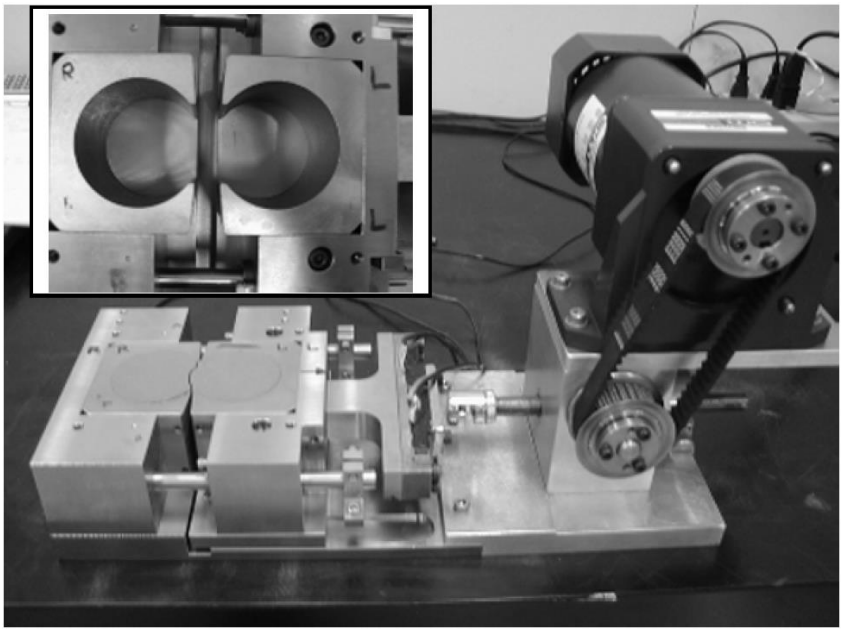

Figure 2.31 Tensile strength “C” shaped apparatus (type-A) (after Tamrakar et al., 2007).

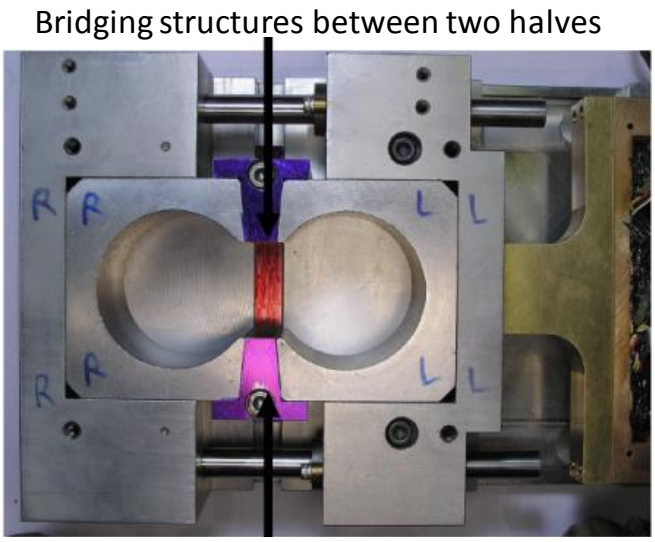

Figure 2.32 Tensile strength apparatus incorporating bridging structures (type-B) (after Tamrakar et al., 2005).

The subject material was prepared in the laboratory from commercially available clays and silts in order to examine the effect of particle distribution in addition to a locally sourced loam. Compacted samples were made by mixing with distilled water to desired moisture content before being sealed in an air tight plastic bag and being left for one week to homogenise. This period is recognised to be considerably longer than that employed by Nahlawi et al. (2004). For samples where the proportion of clay-sand and silt-sand were under investigation, a moisture content of 10% was maintained. The inner surface of the mould/jaws was greased prior to filling to reduce the friction between the soil and metal surfaces. It is understood that this will aid the reduction of shearing at the edge of the sample and hence, not interfere with the generation of tension. Compacted samples were prepared directly into the testing mould in a single layer using a prescribed quantity of material to achieve a fixed dry density. Pre-consolidated (saturated) samples were transferred directly from the consolidation apparatus to the mould using the consolidation shaft after aligning the two devices. Following insertion, the sample was trimmed using a ‘cheese wire’.

Tamrakar et al. (2005)a reported preliminary testing at three constant displacement rates: 0.174, 0.342 and 0.882mm/min. The dependency of tensile strength on displacement rate was found to be within a 1/10 kPa order and a rate of 0.342mm/min was used for reported testing. Later, Tamrakar et al.

(2007) went on to show that both increasing and decreasing the displacement rate about a given value (assumed to be soil specific) produced an increase in strength (Figure 2.33). Increased peak stress with increased deformation rate is a commonly observed behaviour in triaxial testing but increased strength at lower rates was attributed to the effect of drying associated with prolonged exposure during the longer testing run (Tamrakar et al., 2007).

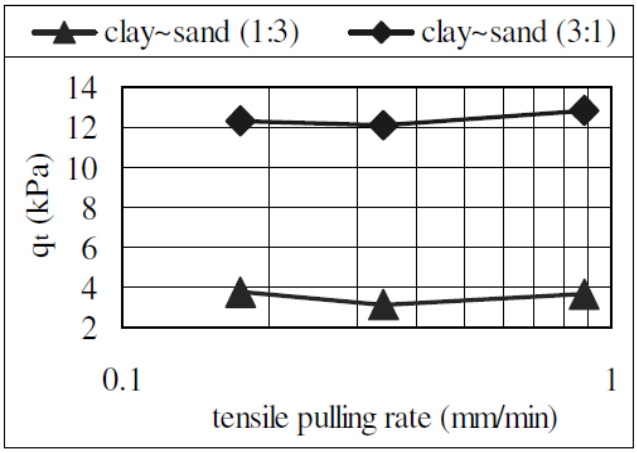

Figure 2.33 Effect of tensile pulling rate on tensile strength (soil mixtures at 10% water content prepared under 200kPa consolidation pressure) (after Tamrakar et al., 2007).

Tensile crack development was observed on the exposed, upper surface of the specimens. Compacted specimens exhibited instantaneous crack development across the constricted section while pre-consolidated, saturated samples showed cracks to initiate at the sides of the central portion before continuing to propagate inward until the specimen halves had separated. The detachment (crack) surfaces are found to be smooth; this indicates an even distribution of tensile force (Tamrakar et al., 2005a). However, upon microscopic inspection, some variability in the surface is seen and is suggested to be the result of the distribution of soil particles and their relative adhesion forces. Tensile strength is defined as the maximum tensile stress necessary to break most of the soil particle bonds. A reducing tensile stress trend is observed post tensile stress maximum and is thought to be the product of remaining bond breakage ((Ohkubo et al., 2002; Ono et al., 2003) cited in Tamrakar et al., 2005a).

The effect of three different dry densities on tensile strength (q_t) established by Tamrakar et al. (2005a) is presented in Figure 2.34. The general relationship of strength verses water content is similar for all curves in this study. Strength is

found to increase with increasing water content up to ~60% beyond which strength is found to decrease with any further increase in water content. Although not expressly explained by the authors, this trend may be evidence of the tensile strength peak at the capillary-funicular saturation boundary as described by Schubert (1975). Broadly, with an increase in dry density, there is an increase in tensile strength. The difference in strength due to dry density is greater to the dry side of the strength maximum whereas the difference due to dry density in the wetter direction of the strength maximum decreased with increasing water content where strengths are very closely matched towards saturation/high water content.

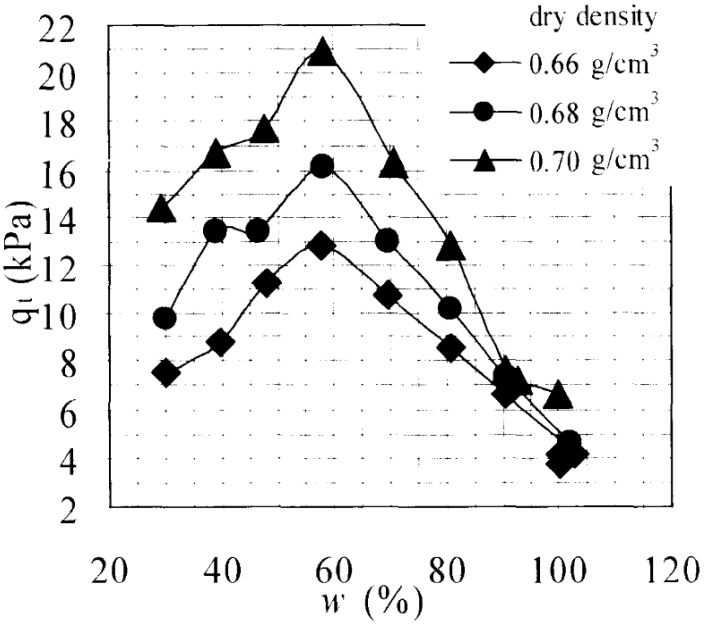

Figure 2.34 Relationship between tensile strength and water content for compacted Kanto loam at different dry densities (after Tamrakar et al., 2005a).

This water content dependent tensile strength trend differs to that of Nahlawi et al. (2004) and Trabelsi et al. (2010) were an approximately increasing strength with decreasing water content relationship was observed. However, a similar staged trend has been observed by other investigators (e.g. Lu et al. (2007), Villar et al. (2009)).

An additional component of the work by Tamrakar et al. (2005a); (2005b); (2007) was a comparison between tensile strength and unconfined compressive strength. The results presented in Figure 2.35 show that the two strengths may be related linearly by a proportionality coefficient that ranges between 10.6 and

13.1 for the three dry densities tested. A similar comparison between unconfined compressive strength and tensile strength for a compacted till was conducted by Krishnayya et al. (1974) using an indirect tensile testing method where a proportionality coefficient range of 12 to 32 was established. The relationship between unconfined compressive and tensile strength with water content is presented in Figure 2.36 where it is shown that water content has a greater influence on the strength ratio at the drier end of the tests conducted (<50% water content). Therefore, it is important that water content be considered if determining q_t from q_u (Tamrakar et al., 2005a; 2005b).

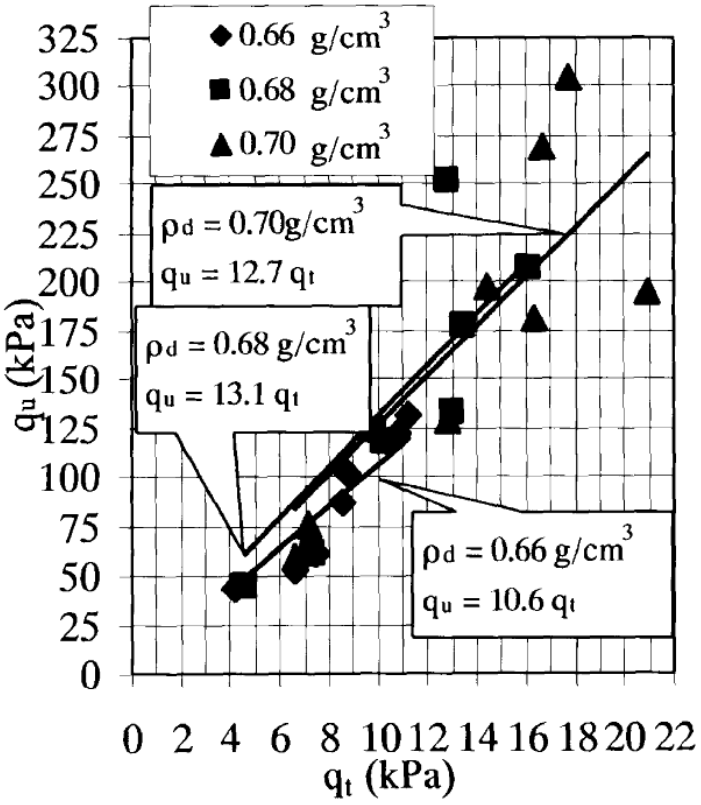

Figure 2.35 Relationship between tensile and unconfined compressive strength for compacted Kanto loam (after Tamrakar et al. 2005a).

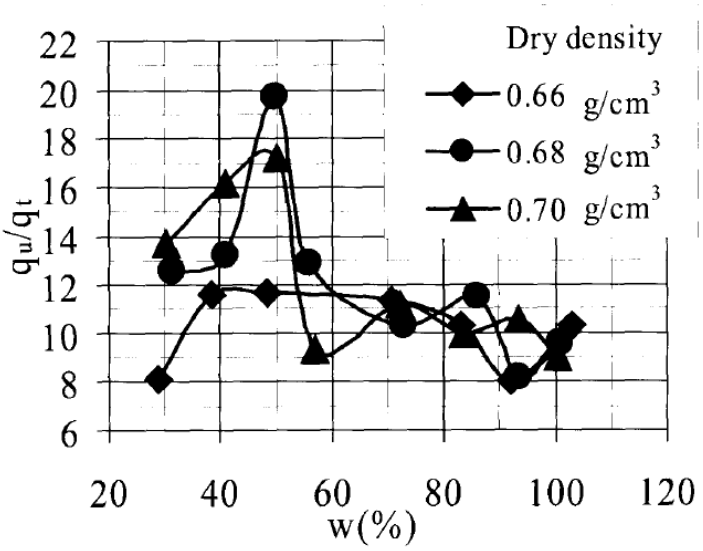

Figure 2.36 Effect of water content on the compressive/tensile strength ratio (after Tamrakar et al. 2005a).

More recently, apparatus was designed and tested by Trabelsi et al. (2010) (2012) on a natural, highly plastic clay. Soil samples were tested to investigate the effect of the water content variable from three initial states. The following preparation methods were used: remoulded (saturated and desiccated); compacted at a constant water content and desiccated; compacted at different initial water contents. Only tests conducted on soil desiccated from saturation were used by Trablesi et al. (2012) to form the basis of numerical simulation. However, the apparatus used in these two studies differs and is shown to result in differing characterisation of the same material.

The presented method by Trablesi et al (2010) uses opposing, truncated triangular shaped loading jaws mounted upon a modified direct shear testing frame (Figure 2.37). As with the loading jaws/mould described by Nahlawi et al. (2004) and Tamrakar et al. (2005)a, one half of the apparatus is fixed while the other is made to move providing an essentially uniaxial loading condition. Load is induced by the motor fixed to the free jaw which is set to a constant displacement rate (strain controlled testing). Once again, a reduced central cross-section is incorporated into the design to produce a localised tensile stress concentration. Restraint is provided against the external loading by tapered inner sides of the loading jaws. However, unlike Tamrakar et al. (2005)a, the inside edge is perfectly straight and does not provide a surface

perpendicular to the orientation of loading which is believed to be more likely to shear the edges of the sample proximal to the vertices at the restricted centre.

The apparatus shown in Figure 2.38 was later adopted by Trabelsi et al. (2012). This device was based upon that proposed by Rodriguez et al. (2002), shown in Figure 2.39 and is similar to that presented by Kim and Hwang (2003) in Figure 2.40. The loading jaws are elongated in comparison to those employed by Trabelsi et al. (2010) and feature a greater degree of reduced central cross-section. The test is considered stress controlled due to the method of load application, this is done by the discrete addition of weights to a cable suspended from the free triangular half of the apparatus. However, Kim and Hwang (2003) used a continuous method where water is poured at a known rate into the loading containers. The continuous method is recognised to provide a gradual increase in load and is less likely to induce tensile failure from system shock.

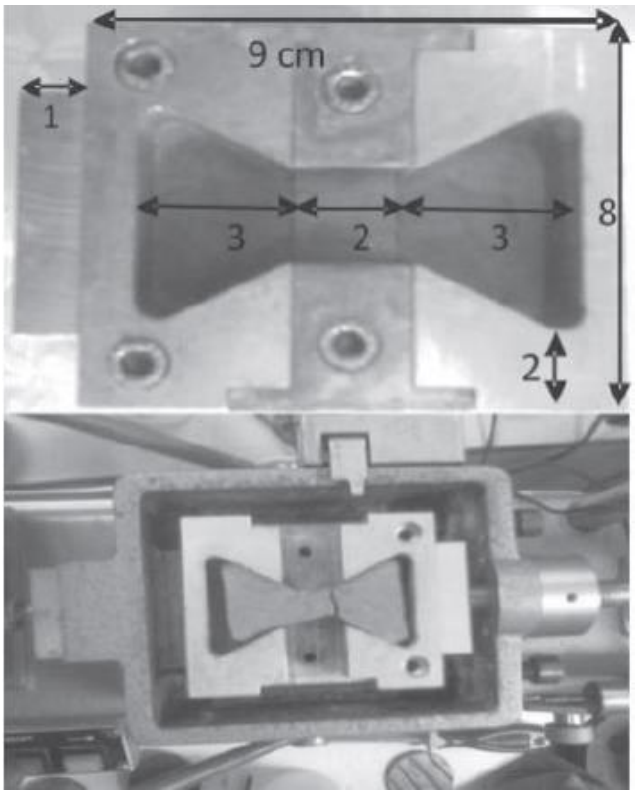

Figure 2.37 Strain controlled tensile test device (after Trabelsi et al. 2010).

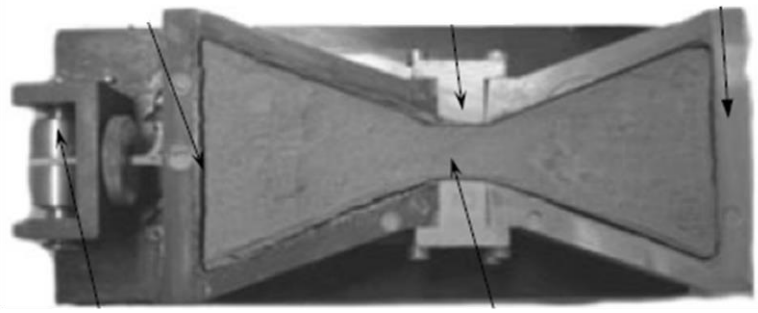

Figure 2.38 Stress controlled tensile test device (after Trabelsi et al. 2012).

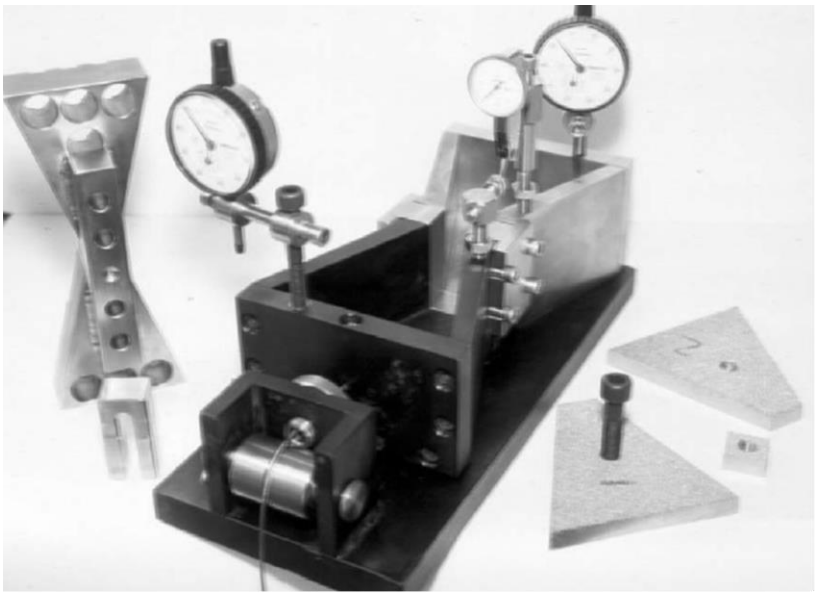

Figure 2.39 Traction equipment to measure direct tensile strength (after Rodriguez 2002).

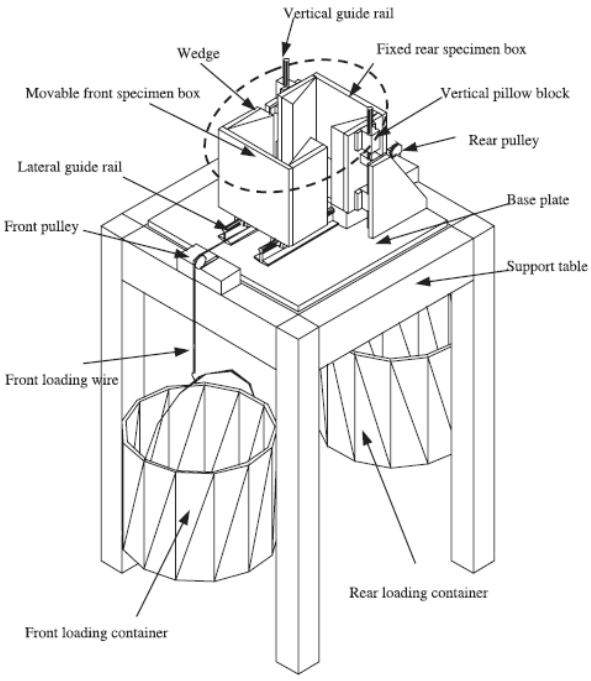

Figure 2.40 Direct tension apparatus (after Kim & Hwang 2003).

In testing using the later design of Trabelsi et al. (2012), the interior of the jaws were lubricated to reduce friction by removing adhesion between the sample and the jaw. Preliminary tests were described where lubricant was not used. It is reported that during desiccation within the jaws, non-lubricated samples would crack due to basal restraint generating excessive tensile stress and were therefore abandoned as sample integrity was lost making results unrepeatable. Lubricating allowed for free shrinkage (without cracking) of the specimen during drying to the desired testing moisture content. It was checked that the 'zone of interest' was undamaged by the drying process prior to mechanical loading. Conversely, Kim and Hwang (2003) lined their apparatus with sand paper in an effort to ensure no slip was facilitated between the sample and the mould/loading jaws. Since only a limited number of water contents were tested in the study conducted by Kim and Hwang (2003) and these were tested in the as-compacted state with no drying period, no shrinkage and so no loss in sample integrity was anticipated.

The soil used by Trabelsi et al (2010) and Trabelsi et al (2012) was placed directly into the testing mould/jaws in either a saturated (WC 65-120%) or compacted state and exposed to fixed environmental conditions. Given the saturated nature of some samples tested, a central bridging structure similar to that evaluated by Tamrakar et al. (2005)a although this was only kept in place during drying until the sample was sufficiently dry and stiff enough to support itself during testing. In both test styles, displacement of the free jaw was measured directly using an LVDT (Trabelsi et al., 2010) or dial gauge (Trabelsi, et al., 2012). However, it was noted that "the main difficulty is to measure the displacement in the central zone of the specimen (interest zone) because of the low consistency of the slurry clayey soil" (Trabelsi et al., 2012, p.1413).

Load was applied incrementally by adding weights of 1g. Following failure in the zone of interest, small specimens were taken to measure their suction, water content and dry density. Suction was measured directly using the psychometric method. A small difference between water content at the top and bottom of the ZOI was observed and these values were averaged for analyses. This vertical moisture gradient is brought about by drying of the exposed surface and will introduce a differential stiffness between the top and bottom of the sample.

Such a stiffness gradient will influence the initiation of tensile fracture according to the depth at which the tensile strength is exceeded. However, given the shallow depth of tested samples, this gradient is believed to be negligible. Also observed was a gap between specimen and mould which is believed to be the product of shrinkage during drying to the testing water content (Figure 2.38), the required displacement to seat the sample within the jaws was identified and corrected for in presented data.

The peak tensile stress (strength) as a function of water content is presented for both displacement and stress controlled studies in Figure 2.41 and Figure 2.42 respectively. The data presented by Trabelsi et al. (2010) (Figure 2.41) shows tensile strength to change as an exponential function of water content when the soil is dried from a saturated and compacted state with the compacted and dried trend showing a higher exponential coefficient. A similar, yet on average weaker exponential relationship is observed in data gathered from the testing of the same material using the more recent stress controlled apparatus (Figure 2.42). The tensile strength tests conducted on samples tested at as-compacted water content show a very different trend (Figure 2.41). This relationship is noted to be comparable to that of dry density with a decreasing tensile strength wet and dry of a peak value achieved at an optimal water content of approximately 14% in the study. The trend is similar to that established by Tamrakar et al. (2005)a where, like the tested at as-compacted test series, no desiccation from a common initial water content was employed.

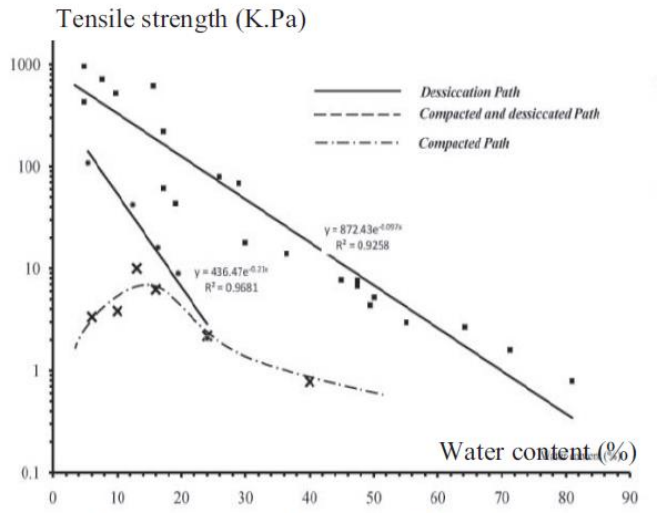

Figure 2.41 Variation of tensile strength with water content from a variety of initial states according to Trabelsi et al. (2010).

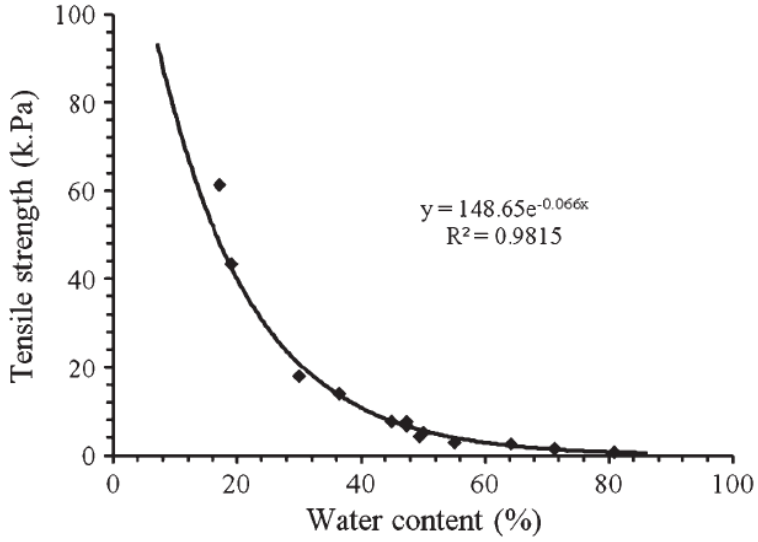

Figure 2.42 Variation of tensile strength with water content from saturation (after Trabelsi et al., 2012).

An exponential relationship was also found by Ibarra et al. (2005) in the testing of a sandy loam soil using a stress controlled method similar to Rodriguez (2002) and Trabelsi et al. (2012) but using clamped cylindrical samples.

Cylindrical samples were prepared using a hydraulic press at a range of initial moisture contents, bulk densities and compaction pressures. Prior to compaction, the soil was sieved and wetted-up by the desired amount before being sealed to allow the water content to homogenise before drying to varying degree. Compacted sample diameter was reduced in the central portion using a manually rotated soil lathe (Figure 2.43a) with the aim of inducing tensile failure

in this area, similar to the constricted centre in the previously described direct tension methods. The use of the lathe limits the water content range that is practicable to that that allows the soil to be self-supporting. Therefore, this method is inappropriate for soils at high water contents. Cylindrical specimens were chosen to eliminate corner stress concentrations, a known phenomenon in material testing although largely neglected in the angular sample forms adopted by Nahlawi et al (2004) and Trabelsi et al. (2010).

Direct tensile strength testing was conducted using the setup shown in Figure 2.43b. A tensile force was applied to the ends of each sample via metal clamps that were tightened around the sample circumference; these were padded using rubber foam to ensure an even contact. The lower clamp was fixed to the apparatus base while the upper clamp was attached to the loaded wire which ran vertically above the sample over a pulley rig, as depicted in the above figure. A constant loading rate of 0.02 Ns^{-1} was applied by the addition of weights to the loading wire in the same manner as Rodriguez (2002) and later adopted by Trabelsi et al. (2012). 'Friction losses' in the apparatus were measured by lifting known weights and were identified within the lifting wire and pulley setup as 0.02 – 0.05N. This pulley loss was subtracted from the tensile force required for each soil failure. The weight of the top portion of the specimen above the failure plane was subtracted from the weights used to induce failure when calculating the failure load. It was considered by the authors that because tensile failure occurred invariably at the centre of the samples, the clamps did not generate problematic stress concentrations at the sample ends. The method described does not propose any measurement of displacement and hence, no quantification of tensile strain may be calculated. Were this data recorded, a better evaluation of the transmission of load from clamp to sample would be possible as currently no appreciation of contact slippage is considered.

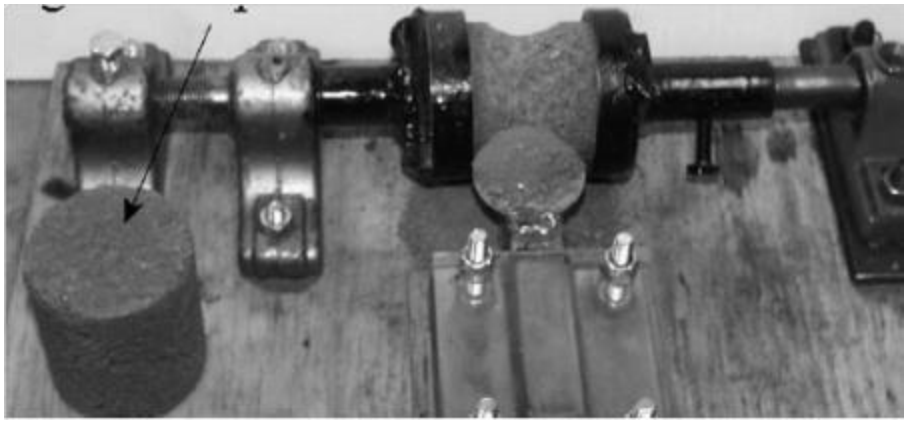

a)

b)

Figure 2.43 Tensile strength measurement method (a) sample preparation in soil lathe and (b) clamp and pulley apparatus (after Ibarra et al. 2005).

The following experiment conditions were analysed. Firstly, the water content variable was investigated with effort made to keep soil bulk density constant at approximately 1.41Mg m^{-3}. Samples were prepared from a soil-water mix that had been allowed to equilibrate for 5 days. Compacted samples were then dried in an oven at 105°C for between 0 and 4.5 hours at 30min intervals. Samples were then sealed and allowed to re-equilibrate for a further 3 days. It was found that despite efforts to control factors besides final water contents, drying caused some shrinkage meaning bulk density increased with decreasing water content at testing. Tensile strength was found to increase exponentially with decreasing water content as shown in Figure 2.44. Ibarra et al (2005) likens this trend to that observed by Vomocil et al. (1961) and Farrell et al. (1967).

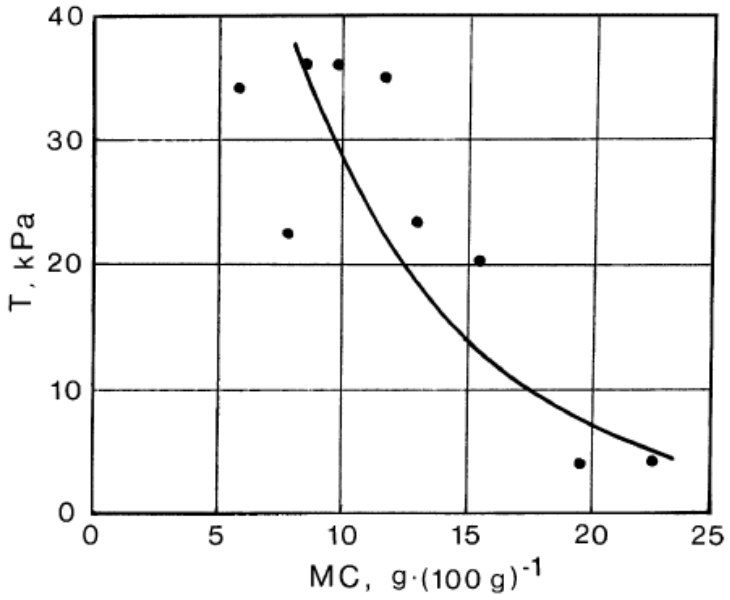

Figure 2.44 Tensile strength relationship with water content for a sandy loam (Ibarra et al., 2005).

This experiment considered the effect of soil bulk density on tensile strength at consistent moisture content where samples were produced using 5 different consolidation pressures. Tensile strength is found to increase with increased bulk density due to a more dense arrangement of particles with an inherent greater degree of inter-particle bonding. This behaviour is independent of high or low water content at sample compaction

A similar clamping method was employed by Wang et al. (2007) and is shown in Figure 2.45. However, this approach used a perfectly cylindrical sample form ($\emptyset = 62mm$, $L = 115mm$) which was loaded using an automated strain controlled mechanism at a constant deformation rate of 0.01mm/min irrespective of the sample competency. Once again, the effect of water content and bulk density was studied, the results of which are presented in Figure 2.46. Samples were compacted directly and tested at the desire water contents ranging from 16% to 19%.These data show a linear decrease in tensile strength with increasing water content although the size of the data set does not allow a thorough characterisation of strength over a wide range of water content. Given the sample preparation approach (i.e. testing at varying as-compacted water content), it would be expected that a peak strength value be identified as in the work of Trabelsi et al. (2010) and Tamrakar et al. (2005)a. However, the

restricted range of water contents tested has not captured the inferred reduced strengths at very low water contents.

Since no central cross-section constriction was used, the location of the eventual fracture is unknown and the initial cross-sectional area (is assumed in the calculation of tensile strength at the peak failure load. At the upper end of this range, a degree of ductile deformation upon loading would be expected and would lead to a reduction in the area over which load was transmitted at the moment of failure. Hence, the reported strengths may be considered as conservative values. Lastly, the influence of the sample clamp was not discussed. The tightening of the clamps is recognised to have possibly influenced the failure of the cylinder as the contrast between the confined and unconfined regions and any constriction of the sample diameter may lead to strain localisation.

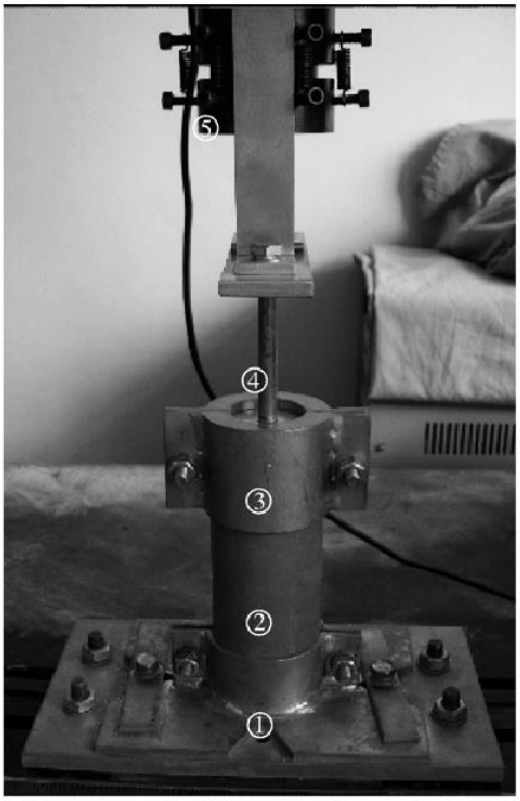

①: Lower clamp; ②: Specimen; ③Upper clamp;
④: Loading pole; ⑤: Load sensor and displacement sensor

Figure 2.45 Apparatus to determine tensile strength (after Wang et al. 2007).

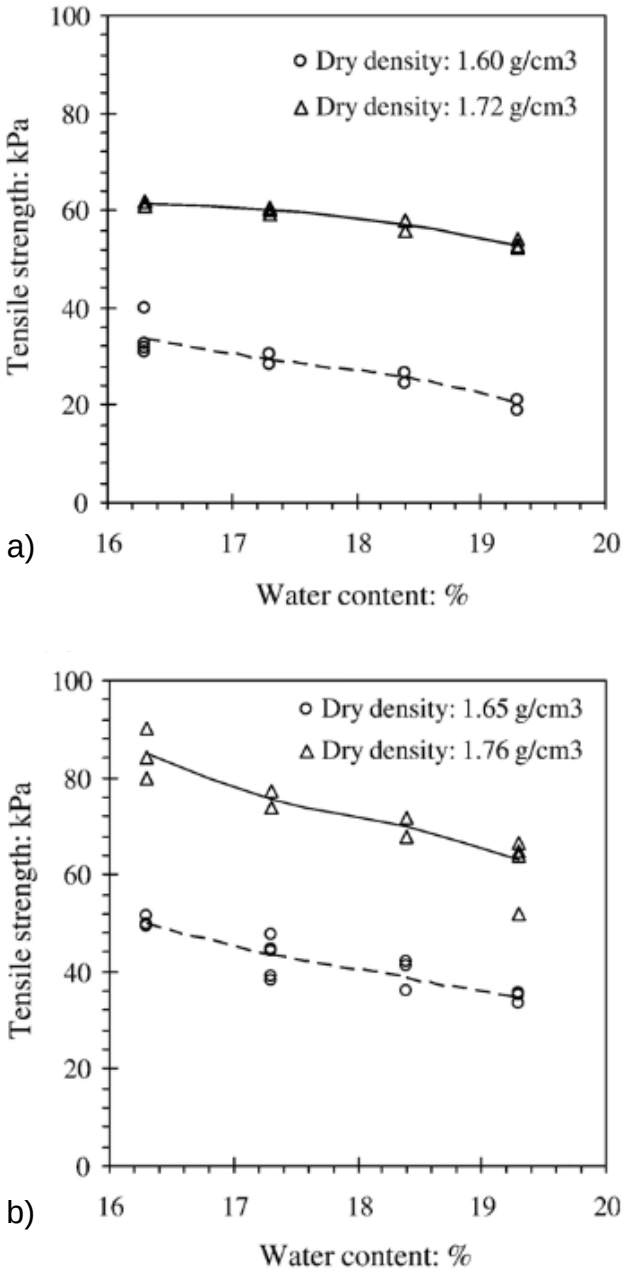

Figure 2.46 Relationship between water content and tensile strength for clay at varying dry densities (after Wang et al. 2007).

In comparison to the above test methods, Lu et al. (2005) presented an apparatus applicable to cohesionless soils. Sands are a difficult medium in the testing of tensile strength where, adhesive methods require the soil to be strong enough to be bonded to an additional substrate (e.g. Heibrock et al. (2003)) and pinched-stretching methods offer negligible confining stress (e.g. Nahlawi et al. (2004); Tamrakar et al. (2005); Trabelsi et al. (2010)). The proposed solution by Lu et al. (2005) is based upon the design of Sture and Kim (2002) where the sample is split under its own weight upon inclination. Figure 2.47a shows the

sample tubing within which the soil is directly compacted or the cored specimen is placed. The tubing comprises detachable halves which remain connected during sample preparation. Upon increased inclination, one half of the tubing is fixed to the inclined plate and a longitudinal pulling force is generated at the centre of the sample until failure (Figure 2.47b). Tensile strength is then given by the following equation:

$$\sigma_t = \frac{W \sin \beta}{A} \qquad \textbf{2.31}$$

where, W is the weight of the free half of the apparatus including sample fragment, A is the cross-sectional area and β is the angle of inclination.

a)

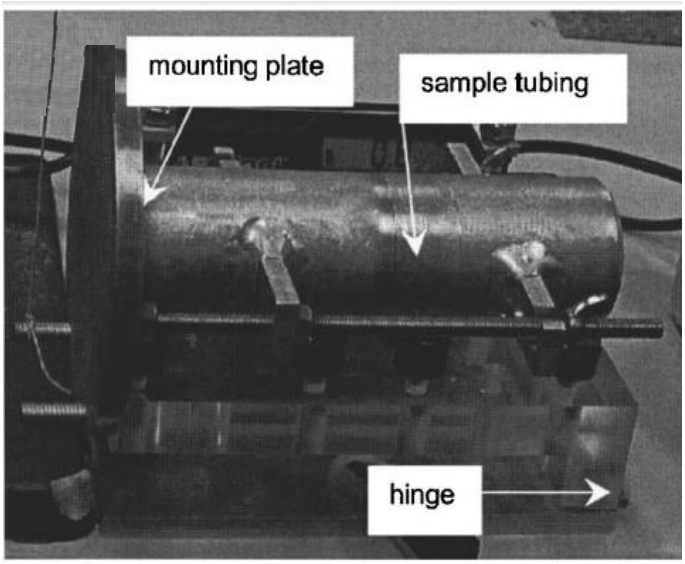

b)

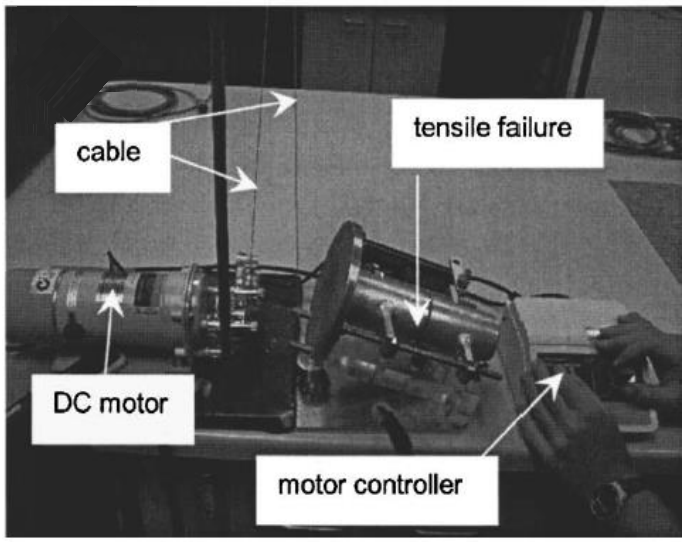

Figure 2.47 Direct tensile strength apparatus (after Lu et al. 2007).

To form samples, oven-dried sand was mixed by hand with the required amount of water before being left overnight beneath a plastic film to allow the mixture water content to homogenise. The required mass of sand was then statically compacted into the tubing before vibration compaction was applied to achieve the desired sample porosity.

The tensile properties of sands are inherently different from those of clays considered in the preceding studies and are largely governed by the combined behaviour of water bridging and negative pore pressure. As a result, tensile strength is up to two orders of magnitude lower than that observed for clay soils. Given the magnitude of sand strengths measured using the tilting apparatus (<2kPa), it is considered unlikely that this method would be practical in the testing of cohesive materials where the sample would likely sustain the force generated by the weight of the clamp half since tensile strengths are commonly in excess of tens of kPa.

Tensile strength as a function of saturation for tests conducted on silty sand is presented in Figure 2.48. The tensile strength trend may be easily described in the context of saturation states with strengths ranging from 0Pa at oven dry to its maximum, 1448Pa at the limit of the pendular state ($Sr = 20\%$). The funicular state sees a broadly linear decrease in tensile strength from $Sr = 20\%$ to 90%. Due to the sand exhibiting high liquidity above $Sr = 90\%$, the apparatus made testing this material impossible.

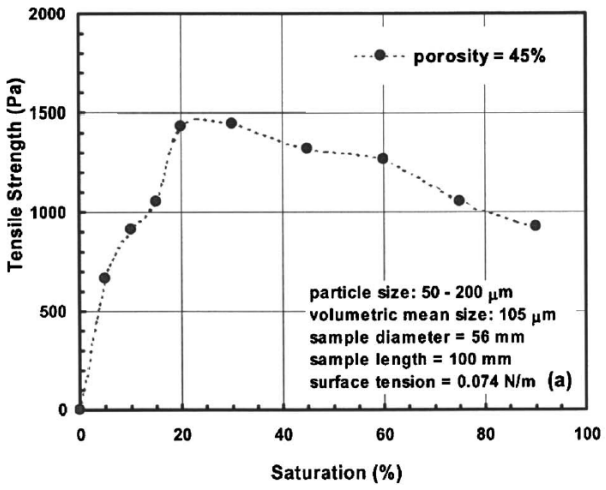

Figure 2.48 Tensile strength characteristic curve for silty sand (after Lu et al. 2007).

2.6 Crack hydrology

Increased macro-permeability is one of the most commonly cited motivations for research into desiccation cracking. Despite this, or perhaps because of it, there is no widely accepted approach to capture this transient property. Traditionally, much of this work has been conducted regarding irrigation in an agricultural context (Stirk, 1954; Chan & Hodgson, 1981; Kosmas et al., 1991; Michell & van Genuchten, 1993; Romkens & Prasad, 2006); however, from an engineering perspective, barrier and cover application competency is commonly cited in the crack infiltration literature (Daniel & Wu, 1993; Albrecht & Benson, 2001; Philip et al., 2002). That said, the dynamic influence cracking is understood to have on the soil-atmosphere interaction has led to crack hydrology becoming important in all applications of shrink-swelling soils. This section describes the principle process behind increased infiltration and bypass flow and how this has been incorporated into the hydraulic modelling of soils subject to cracking.

2.6.1 Crack infiltration framework

The broad mechanism behind the apparent increase in permeability upon cracking has been established for many decades and is described after Bronswijk (1988) herein.

As illustrated in Figure 2.49, rainfall reaching the soil surface (i.e. not intercepted by vegetative cover) is partitioned into water that infiltrates directly through the soil matrix and water that bypasses the surface. The maximum infiltration into the matrix is a function of the soil permeability; this encompasses both the saturated and unsaturated condition, thus varying temporally and spatially. It is upon rainfall exceeding this maximum matrix infiltration rate that water runoff will enter cracks.

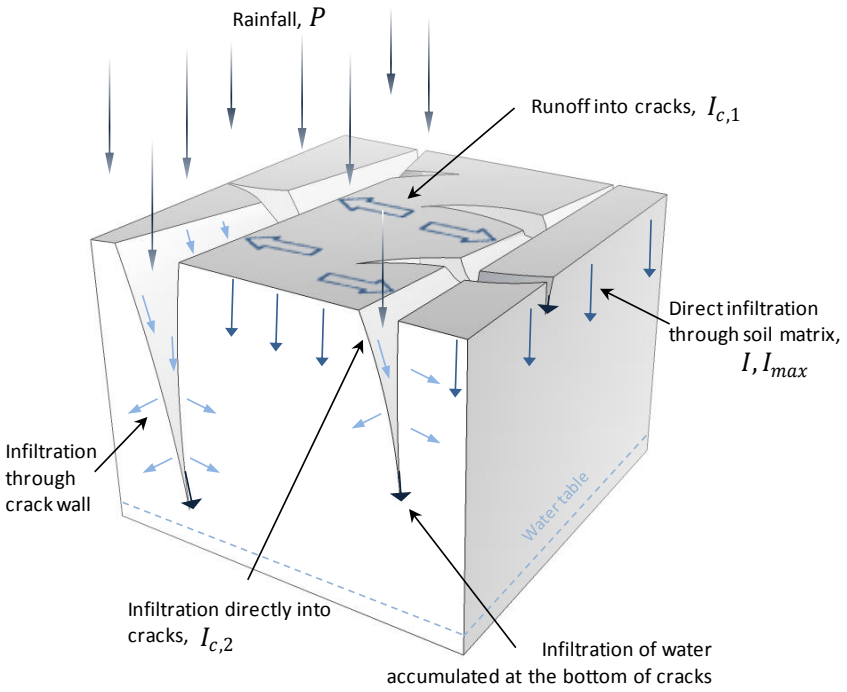

Figure 2.49 Diagram to show aspects of infiltration into cracked soil.

Therefore, crack infiltration is conditional upon the rainfall intensity verses the infiltration capacity of the soil matrix. This was expressed by Bronswijk (1988) in Equation 2.32 and shows that all infiltration rates are based on the relative intact surface and crack area. This framework is recognised not to consider the crack (partial) closing phenomenon commonly observed upon re-wetting.

$$\begin{aligned} P < I_{max}: \quad & I = A_m P \\ & I_c = A_c P \end{aligned}$$

$$\begin{aligned} P > I_{max}: \quad & I = A_m I_{max} \\ & I_{c,1} = A_m (P - I_{max}) \\ & I_{c,2} = A_c P \\ & I_c = I_{c,1} + I_{c,2} \end{aligned} \qquad \textbf{2.32}$$

Where,

$P =$ Rainfall intensity (ms^{-1})

$I_{max} =$ Maximum infiltration rate of soil matrix (ms^{-1})

$I =$ Infiltration rate in soil matrix (ms^{-1})

$I_c =$ Infiltration rate in cracks (bypass flow) (ms^{-1})

$A_m, A_c =$ Relative areas of soil matrix and cracks respectively (-)

$I_{c,1}$ = Part of total crack infiltration caused by rainfall intensity exceeding maximum matrix infiltration rate (runoff) (ms^{-1})

$I_{c,2}$ = Part of total crack infiltration caused by rainfall directly into the cracks (ms^{-1})

All of these parameters vary continuously; rainfall intensity changes with atmospheric conditions, maximum matrix infiltration capacity depends upon porosity and degree of saturation. Shrink-swell behaviour constantly alters the porosity of the soil surface while cracks may widen and narrow changing the relative cracked area.

Water entering cracks is assumed to collect at the bottom and is stored subject to the infiltration capacity of the soil matrix at that depth. Horizontal infiltration of water through the crack walls as the water flows against them was not included in the Bronswijk (1988) model but was shown to be negligible by Hoogmoed and Bouma (1980). As mention earlier, the effects of vegetation have also been excluded in this framework although beyond canopy interception and storage, root networks are also understood to behave as preferential macropore systems enhancing bypass flow as well as macropore features created by soil fauna (Beven & Germann, 1982).

2.6.2 Crack permeability measurement

Measurement of permeability (hydraulic conductivity) is commonly conducted by either the constant head or falling head method depending on the expected nature of the soil in the field or laboratory. There are many issues associated with this practice; however, the scope of this section is focused on measurement in the context of desiccated soils. As such, in the study of cracked soils, it is typically the unsaturated hydraulic conductivity in addition to crack flow that is of concern. Techniques for the quantification of preferential flow were reviewed by Allaire et al. (2009) and include optical and chemical tracing methods. However, all of these techniques require specialist apparatus, knowledge and are subject to their individual benefits and pitfalls. However, the ‘go to’ methods for determining field and laboratory permeability work under the premise of steady state conditions thereby assuming all pore space to be fully saturated including the crack volume which is not necessarily representative.

More commonly, in the study of clay liners, soil cores have been produced to assess their hydraulic conductivity behaviour under desiccated conditions. The influence of drying cycles on four naturally occurring soils was investigated by Albrecht and Benson (2001). Various compactive efforts were applied to specimens that were then saturated according to ASTM D 5084 (ASTM, 2000) using flexible-wall permeameters. Hydraulic conductivity tests were repeatedly performed after each drying stage to assess the influence of cracking. The results presented in Figure 2.50a were obtained and indicated a hydraulic conductivity increase of up to three orders occurred in some cases. Notably, the increase in hydraulic conductivity was found to be most significant after the initial drying stage and is in agreement with contemporary measurement of volumetric shrinkage strain shown in Figure 2.50b.

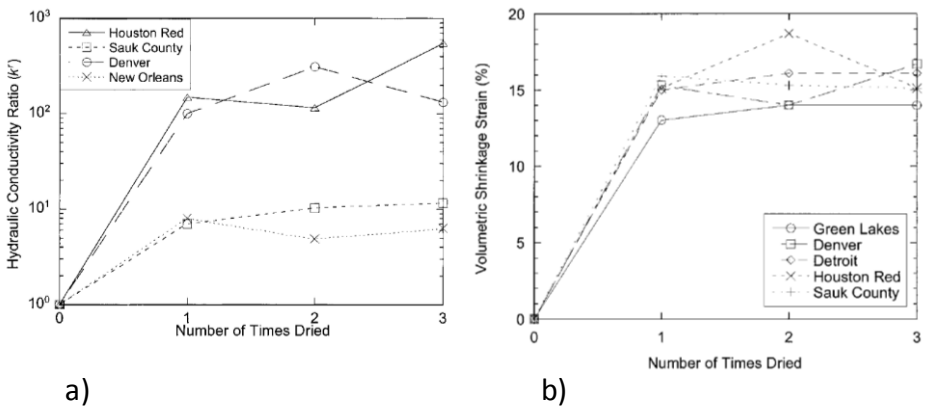

Figure 2.50 Measured changes with repeated drying cycles (a) hydraulic conductivity and (b) volumetric shrinkage strain (after Albrecht & Benson, 2001).

In agreement with the findings of the laboratory work of Albrecht and Benson (2001), researchers have also reported an increase of 2-3 orders in the infiltration rate recorded at known crack sites in the field compared to un-cracked conditions (Anderson et al., 1982; Zhan et al., 2006).

Although these works illustrate the increased bulk hydraulic conductivity of soils experiencing desiccation and cracking, the issue of measurement under fully saturated conditions remains. An accepted, accurate method for directly measuring the bulk hydraulic conductivity of a cracked medium under unsaturated conditions has not yet been developed.

2.6.3 Crack permeability modelling

There have been many attempts to numerically capture the influence of preferential flow due to cracking in the bulk soil mass. One such approach is the dual-permeability concept where for a given unit of soil there exist two permeable systems, the matrix and the crack network. Gerke and van Genuchten (1993) described unsaturated flow using the Richards' equation (Richards, 1931) for both pore regimes. Ahuja and Hebson (1992) cited in Simunek et al. (2003) treated the matrix infiltration and water redistribution using the simple Green-Ampt model (Green & Ampt, 1911) and Richards' equation respectively, and cracks using Poiseuille's law for gravitational flow through idealised tubes.

Numerical adoption of the aforementioned crack infiltration framework may be considered a sub-group of the dual-permeability approach whereby preferential infiltration occurs through statistically described cracks (e.g. spacing and width). The partitioning of infiltration is also temporal according to the dynamic cracked portion of the soil surface and rainfall intensity exceeding matrix infiltration capacity. Novak et al. (2000) presented one such model with unsaturated flow in the matrix described using the standard 1D Richards' equation in addition to an extension according to Feddes et al. (1988). This extension included a source term corresponding to the horizontal infiltration of water accumulated at the crack bottom. From there, a wetting (saturation) front is assumed to advance into the unsaturated matrix as described by the Green-Ampt model. The model presented by Novak et al. (2000) was able to demonstrate the importance of including crack bypass flow to depth. Soil water content profiles after simulated irrigation events showed the infiltration capacity of the soil to more than double with the inclusion of cracking.

Multi-scale approaches such as dual-permeability allow the different features of the desiccated soil to be treated using different concepts and flow rules. However, a relatively simple means to include textural (matrix) and structural (fractures, root channels, piping) effects by combining regions with differing hydraulic properties together was proposed by Durner (1994). The van Genuchten – Mualem model is capable of representing the soil-water retention and unsaturated hydraulic conductivity for a unimodal pore-size distribution

(Section 2.2.5) (van Genuchten, 1980). However, Durner (1994) proposed that structured soils might better be described as multi-modal where macro- and micro-sized pores represent the cracked and matrix portions of the soil respectively. Consider this as a bimodal system; Figure 2.51 depicts the relative SWRC components. It may be seen that a combined SWRC may be formed showing a continuous transition between the two pore-regimes, the coarse fraction typically showing a lower AEV followed by a higher AEV for the finer fraction later on the desorption path.

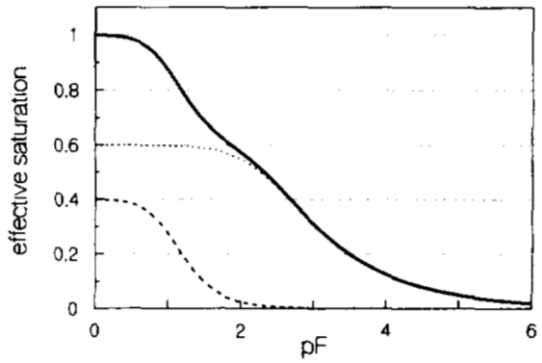

Figure 2.51 Construction of a multimodal retention function: Bimodal retention curve (solid), unimodal sub-curve for the fine pore system (dotted) and unimodal sub-curve for the coarse pore system (dashed) (after Derner 1994).

The linear superposition of the van Genuchten - Mualem expressions of each region produces hydraulic functions for the whole multi-modal pore distribution:

$$S_e(\varphi) = \frac{\theta(\varphi) - \theta_r}{\theta_s - \theta_r} = \sum_{i=1}^{k} w_i \frac{1}{(1 + |\alpha_i \varphi|^{n_i})^{m_i}} \qquad \textbf{2.33}$$

$$K(\theta) = K_s \left(\sum_{i=1}^{k} w_1 S_{e_i} \right)^{l} \frac{\left(\sum_{i=1}^{k} w_i \alpha_i \left[1 - \left(1 - {S_{e_i}}^{1/m_i} \right)^{m_i} \right] \right)^2}{\left(\sum_{i=1}^{k} w_i \alpha_i \right)^2} \qquad \textbf{2.34}$$

Where,

$k =$	Number of overlapping sub-regions
$w_i =$	Weighting factors for the sub-regions
$\alpha_i, n_i, m_i(1 - 1/n_i), l$	Empirical shape fitting parameters
θ_r, θ_s, K_s	Physical parameters

From Equation 2.34, the predicted relative hydraulic conductivity may be plotted for a given multi-modal pore system such as that presented in Figure 2.52. It is important to remember that this approach suffers from a reliance upon the desorption bias in SWRC exploitation. However, this dual-porosity model does allow the influence of macro-pore features to be captured in a continuous manner which is considered extremely useful in the modelling of permeability changes upon drying cycles in a swelling medium.

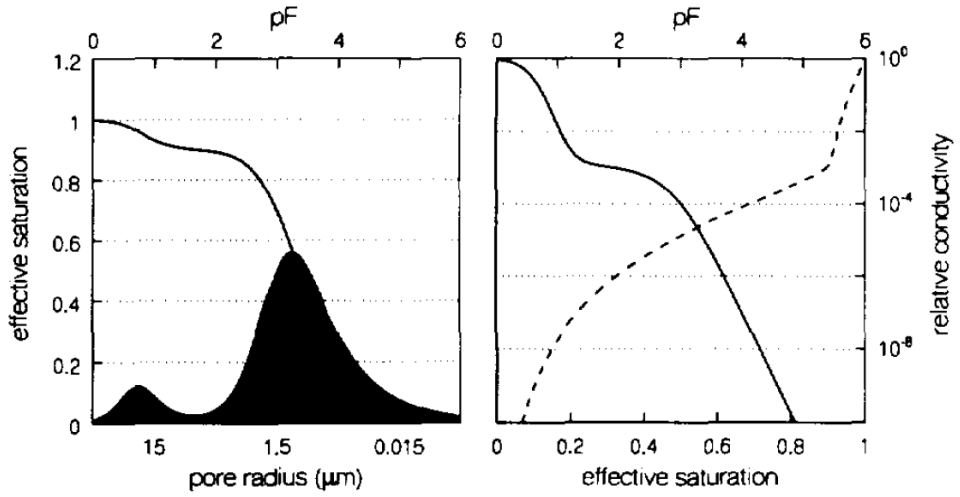

Figure 2.52 Hydraulic properties for a bimodal pore system: (left) Bimodal retention curve (solid) and associated pore-size distribution (shaded); (right) Predicted relative hydraulic conductivity as a function of negative head (solid) and effective saturation (dashed) (after Durner, 1994).

Bimodal air entry features due to cracking are increasingly identified in experimentally derived SWRCs (e.g. Azam et al., 2013), although this appears to be limited to the inclusion of hairline discontinuities present within natural deposits. As such, the above method is suitable to better describe the shrink-swelling matrix and associated micro-fracturing, as the inclusion of discrete macro-scale cracking, like that described in 2.1 is not applicable in such a model. In this scenario, a dual-permeability approach where preferential flow through these large features is better captured.

2.7 Mathematical description and numerical modelling of cracking

The following section provides an outline of the established theoretical mechanics and the mathematical methods that have been used to describe cracking phenomenon.

2.7.1 Fracture Mechanics

Linear Elastic Fracture Mechanics (LEFM) is a commonly used approach to assess the damage tolerant design of materials in many fields of engineering e.g. aerospace, nuclear, shipping industries etc. A brief outline of the fundamentals of LEFM is presented and is followed by an illustration of how the method has historically been applied to the study of desiccation cracking and how this method has developed.

2.7.1.1 Fracture mechanics theory

Firstly, for LEFM to be employed, a series of assumptions must be made:

1. A crack has been initiated and has begun to propagate. In the context of materials testing, this may be a flaw on the microscopic scale.
2. The material is isotropic.
3. The material is predominantly linear elastic during the fatigue process.
4. The plastic zone at the crack tip is small in relation to local geometry.
5. Any given point of analysis is near the crack tip (<10% of the crack length).

There are three modes in which a crack may be loaded/extend; these are presented in Figure 2.53. The crack extension modes are characteristic to certain loading scenarios; however, they may also be combined. Mode I failure is the opening mode and is most commonly studied since cracks tend to propagate on the plane of maximum tensile stress. Therefore, mode I will form the focus of the following description.

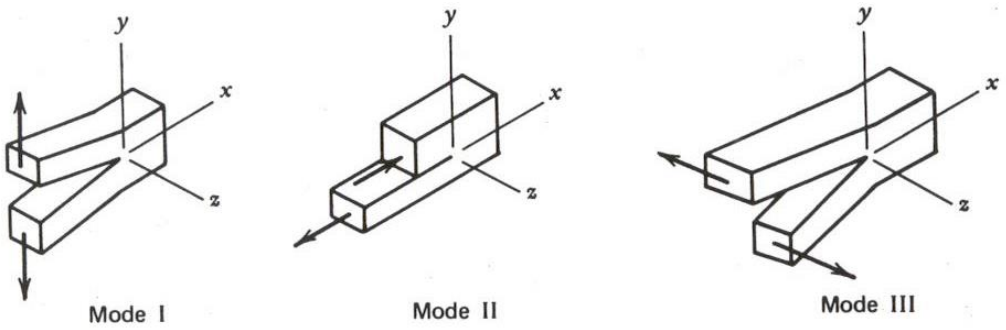

Figure 2.53 Crack opening modes

The stress at any given point in the vicinity of the crack (r/a <<1 where r is the radius to the given point and a is the crack length) is a function of location, loading and geometry. For mode I opening, consider the stress field geometry presented in Figure 2.54 where stresses are given by Equations 2.35 - 2.40. Stresses are dependent on r, θ and K, where r and θlocate the point of interest. The magnitudes of these stresses are entirely dependent on K, the stress intensity factor (MPa.m^{½}). The stress intensity factor is a theoretical construct and a fundamental parameter in LEFM.

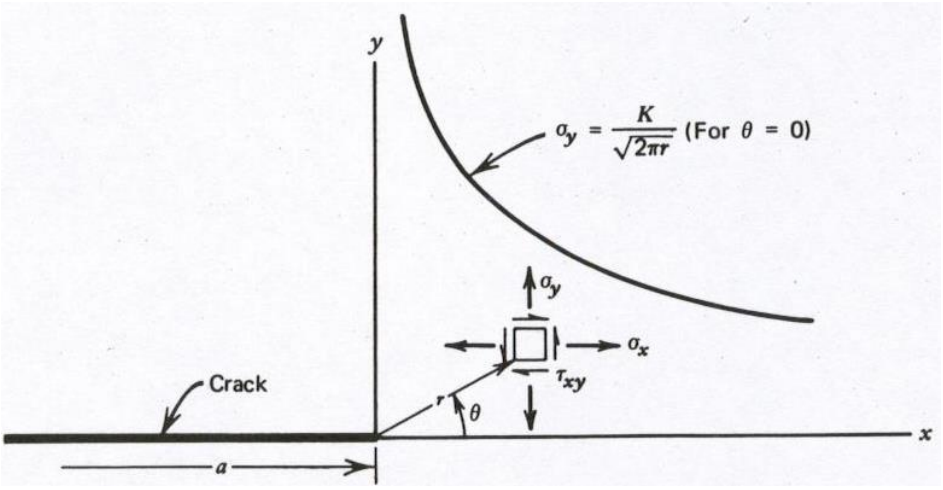

Figure 2.54 Stress field geometry in vicinity of crack

$$\sigma_y = \frac{K}{\sqrt{2\pi r}}\cos\frac{\theta}{2}\left[1+\sin\frac{\theta}{2}\sin 3\frac{\theta}{2}\right] \qquad \textbf{2.35}$$

$$\sigma_x = \frac{K}{\sqrt{2\pi r}}\cos\frac{\theta}{2}\left[1-\sin\frac{\theta}{2}\sin 3\frac{\theta}{2}\right] \qquad \textbf{2.36}$$

$$\tau_{xy} = \frac{K}{\sqrt{2\pi r}} \cos\frac{\theta}{2} \sin\frac{\theta}{2} \cos 3\frac{\theta}{2} \quad \textbf{2.37}$$

$$\sigma_z = \tau_{xz} = \tau_{yz} = 0 \qquad \text{for plane stress} \quad \textbf{2.38}$$

$$\left.\begin{aligned} \sigma_z &= v[\sigma_z + \sigma_y] \quad \textbf{2.39} \\ \tau_{xz} &= \tau_{yz} = 0 \quad \textbf{2.40} \end{aligned}\right\} \text{for plane strain}$$

where, $v = Poisson's\ ratio.$

The stress intensity factor depends on the loading mode, crack shape and the material geometry. There are many analytical stress intensity factor expressions for common configurations in all three modes; these are available in stress intensity factor handbooks such as Tada et al. (2000) and Rooke and Cartwright (1976). Computational methods may also be used (i.e. Finite Element Analysis) in addition to empirical methods (e.g. photo-elasticity, although this is limited to birefringent materials). Two examples of commonly used analytical expressions are presented in Equation 2.41 and 2.42 for the scenarios illustrated in Figure 2.55 and Figure 2.56 respectively.

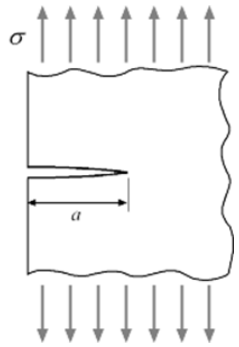

Figure 2.55 Semi-infinite plate with edge crack under tension

$$K = 1.1215\sigma\sqrt{\pi a} \quad \textbf{2.41}$$

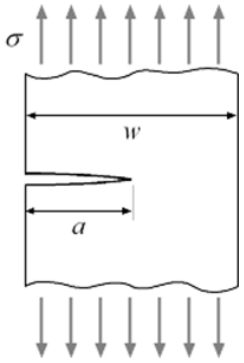

Figure 2.56 Infinite strip with edge crack under tension

$$K = \sigma\sqrt{\pi a}\left(\sqrt{\frac{2w}{\pi a}\tan\left(\frac{\pi a}{2w}\right)}\;\frac{0.752+2.02\left(\frac{a}{w}\right)+0.37\left(1-\sin\frac{\pi a}{2w}\right)^3}{\cos\frac{\pi a}{2w}}\right) \quad \textbf{2.42}$$

A crack will grow when the stress at the crack tip exceeds a critical value. Since the stress intensity factor determines the amplitude of the crack tip stress for a given geometry and loading, unstable crack propagation may be considered to occur when $K \geq K_c$, where K_c denotes the fracture toughness. The stress intensity factor may be calculated; however, the fracture toughness is determined experimentally. Fracture toughness is dependent on the material, temperature, strain rate, environment and material thickness. In plane strain conditions, fracture toughness is considered a true material property (independent of thickness). Several experimental methods to determine the fracture toughness of geomaterials exist including ISRM (1988) and Wang et al. (2007).

It is depicted in Figure 2.54 that as r approaches zero, the elastic stress in the y-direction approaches infinity. This is not physically possible and so in reality there will be a finite plastic zone ahead of the crack tip. No modification to the elastic solution is required if the plastic zone radius, r_y, is small relative to the local geometry, known as 'small-scale yielding' ($r_y \leq (1/8)a$). This represents an important limitation to the use of LEFM for less brittle materials.

In order to evaluate the size and shape of the plastic zone, a failure criterion based on material yielding is needed. Irwin (1958) presented a simplified model

stating that plasticity at the crack tip occurs when mode I tensile stress reaches the material yield value. The plastic zone is assumed to be circular and thus no dependency on the angle θ is included. The radius of the zone can be calculated using the stress field expression for σ_y when $\theta = 0$ by substituting for the yield value, σ_{yield}:

$$r_y = \frac{1}{2}\pi\left(K/\sigma_{yield}\right)^2 \quad \textbf{2.43}$$

To account for all values of θ, a more appropriate yield criterion such as Tresca (1864) or Von Mises' (1913) is commonly used. In terms of principle stresses, the Von Mises' criterion may be expressed as:

$$(\sigma_1 - \sigma_2)^2 + (\sigma_2 - \sigma_3)^2 + (\sigma_1 - \sigma_3)^2 = 2\sigma^2{}_{yield} \quad \textbf{2.44}$$

In terms of stress intensity factor:

$$\sigma_1 = \left(\frac{K}{\sqrt{2\pi r}}\right)\cos\frac{\theta}{2}\left[1 + \sin\frac{\theta}{2}\right] \quad \textbf{2.45}$$

$$\sigma_2 = \left(\frac{K}{\sqrt{2\pi r}}\right)\cos\frac{\theta}{2}\left[1 - \sin\frac{\theta}{2}\right] \quad \textbf{2.46}$$

By substituting Equations 2.45 and 2.46 into the Von Mises' criterion an expression for the plastic zone radius as a function of θ may be obtained. For plane stress conditions where $\sigma_3 = 0$:

$$r_y(\theta) = \left(\frac{K}{\sigma_{yield}}\right)^2\left[(1 + \cos\theta) + \left(\frac{3}{2}\sin^2\theta\right)\right]/4\pi \quad \textbf{2.47}$$

And for plane strain where $\sigma_3 = v(\sigma_1 + \sigma_2)$:

$$r_y(\theta) = \left(\frac{K}{\sigma_{yield}}\right)^2\left[(1 - 2v)^2(1 + \cos\theta) + \left(\frac{3}{2}\sin^2\theta\right)\right]/4\pi \quad \textbf{2.48}$$

The resulting elastic-plastic boundary can then be plotted with the crack tip in the origin and the crack along the line $-\infty < x < 0$ and $y = 0$ in Figure 2.57. The plane stress plastic zone is larger than that of the plane strain due to no accommodation of out-of-plane stress.

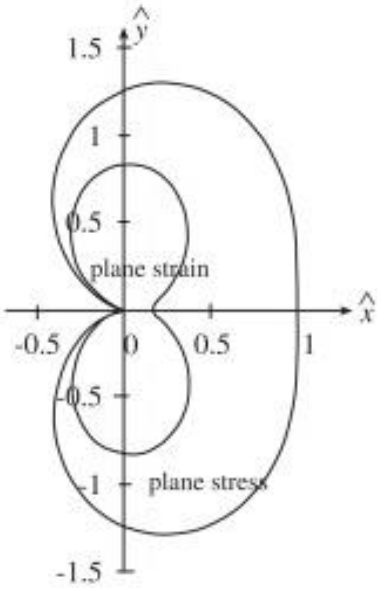

Figure 2.57 Shape of the plastic zone according to Von Mises criterion (after Freed and Banks-Sills (2007))

In plane strain conditions, once the critical stress intensity facture (fracture toughness) is reached, unstable crack propagation occurs. However, under plane stress conditions, the larger plastic zone enables the crack to propagate slowly by stable crack growth prior to unstable fracturing.

To account for limited crack tip plasticity a correction may be included. An effective crack length is calculated to include the region of crack tip plasticity ($\theta = 0$). The resulting effective stress intensity factor may then be considered to account for the plastic crack tip behaviour. Given that K and a' are related by Equation 2.49, the determination of K' is an iterative procedure. The correction is small when $\sigma << \sigma_y$, yet will increase considerably as σ exceeds 0.8σ.

$$a' = a + r_y = a + \frac{1}{2\pi}\left(\frac{K}{\sigma_{yield}}\right)^2 \qquad \textbf{2.49}$$

When a plastic correction of approximately 20% is calculated, small-scale yielding cannot be assumed and LEFM concepts are inappropriate. In this situation Non-Linear Fracture Mechanics (NLFM) or Elasto-Plastic Fracture Mechanics (EPFM) provide alternative concepts.

The crack tip opening displacement (CTOD) approach takes into account the crack tip plastic zone using the effective crack length, a', and is given by Irwin (1958) as:

$$\delta_t = \frac{4}{\pi}\frac{K^2}{E\sigma_{yield}} \quad for\ plane\ stress \tag{2.50}$$

$$\delta_t = \left[\frac{1}{\sqrt{3}}\right]\frac{4(1-v^2)}{\pi}\frac{K^2}{E\sigma_{yield}} \quad for\ plane\ strain \tag{2.51}$$

In LEFM, the CTOD is related to the stress intensity factor; however, in NLFM, the CTOD is a measure of deformation at the crack tip and may be compared to a critical CTOD for use in the crack propagation criterion $\delta_t = \delta_{tc}(\dot{\varepsilon}, T)$. The critical value, δ_{tc}, may be measured and is dependent upon several variables including temperature, T and strain rate, $\dot{\varepsilon}$.

A later development in NLFM was the J-integral. Rice (1968) showed that the J-integral is a path-independent line integral that represents the strain energy release rate of non-linear elastic materials. Given the stress, strain and displacement field, the J-integral may be calculated for an arbitrary contour around the tip of the crack; this makes the method particularly applicable to Finite Element analyses.

For linear elastic materials, the J-integral may be directly related to the strain energy release rate, G and hence relatable to the stress intensity factor and CTOD by the following:

$$J = G = \frac{K^2}{E} \quad for\ plane\ stress \tag{2.52}$$

$$J = G = \frac{K^2}{E}(1-v^2) \quad for\ plane\ stress \tag{2.53}$$

$$J = m\sigma_{yield}\delta_t \tag{2.54}$$

where, $m = dimensionless\ material\ specific\ constant$

The J-integral characterises the crack tip stress and thus may form the basis for a crack propagation criterion i.e. $J = J_c$. Determination of the J-integral value is

recognised to be convenient due to the arbitrary choice of integration path. Additionally, the critical value may be measured using normalised experiments.

2.7.1.2 Early application of LEFM

The principles of LEFM have historically been applied to the study of cracking depth and spacing. This section sets out to provide an overview of the development of such studies culminating in a description of the more recent LEFM framework, that proposed by Konrad and Ayad (1997).

Following the pioneering work into fracture mechanics by Irwin (1958), a thorough application of LEFM theory to geologic settings was undertaken by Lachenbruch (1961). This work primarily considers the quantitative development of tension cracks in basalt and permafrost as a product of thermal contraction. However, a broad account of the mechanism is taken that has allowed the inference of principles on the problem of desiccation cracking.

Lachenbruch (1961) rationalises the use of LEFM in geomaterials by stating that although such materials behave in an elastic manner only when rapidly deformed and the processes that produce tension cracks are generally treated as non-linear, the cracks that result can occur quite spontaneously. Hence, an elastic model is proposed to provide a very good approximation of the stress conditions during and immediately following crack formation.

Arbitrary functions for the initial distribution of stress with depth about a series of problem geometries are proposed. This develops towards the case of a tension crack at the free surface (ground surface) of a semi-infinite medium which is recognised to most closely represent cracks in extrusive rocks, permafrost and clay soils (see Figure 2.55)

The principles of LEFM are applied to the determination of crack depth with special regards to the problem of crack initiation, propagation and arresting. Lachenbruch (1961) asserts that crack initiation is the product of complex and poorly understood processes governed by stress and strength heterogeneities on the micro-scale. The term ‘tensile strength’ is introduced to describe the averaged, macroscopic tension at which flaws grow and coalesce. However, Lachenbruch (1961) states that when a crack develops to the macro-scale (i.e.

crack length is large relative to the radius of the plastic zone), it is not necessary to work in terms of the average stress field but to describe propagation using the crack tip intensity factor alone i.e. LEFM. This approach may be appropriate for the unstable stage where propagation is spontaneous. However, propagation of a macroscopic crack may still occur at subcritical values of K and is termed 'stable' (ASTM Committee on Fracture Testing, 1961). Stable propagation is subject to a negative feedback-loop where the rate of plastic energy dissipation increases faster than the crack extension force. Hence, stable crack propagation is only possible under an increasing tensile stress field. It must be noted that the more brittle a material, the smaller the range of K within which stable propagation can take place in addition to the more precise a definition of K_c. Hence, stable propagation may be considered more prevalent in materials of high plasticity, such as clays.

The depth of unstable crack propagation is assumed to be given by the LEFM criterion $K = K_c$ where K consists of a uniform tension component, K_U and a gravity induced component, K_G, The resulting stress intensity factor trend is depicted in Figure 2.58 where the LEFM criterion for crack propagation is shown to be satisfied twice. The final depth of the crack is shown by "A" with the smaller value, "A_m" representing the initial crack necessary for unstable crack propagation under a given tensile stress.

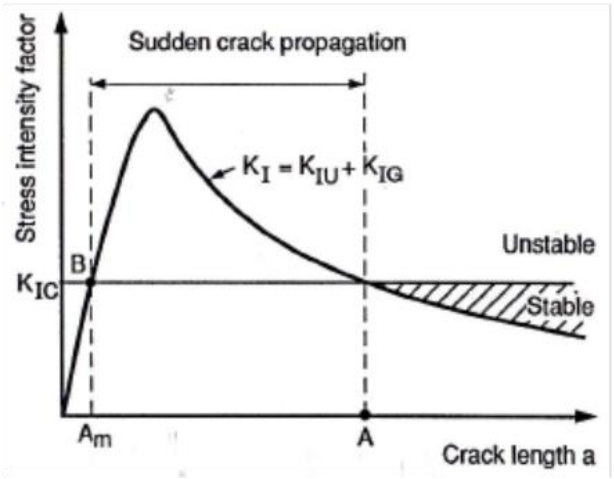

Figure 2.58 Stress intensity factor and crack propagation according to LEFM (after Konrad and Ayad 1997).

For the case of a semi-infinite solid penetrated by a crack (crack length, a) under constant homogeneous stress (depth, b) where $b/a = 1$:

$$K = \sigma\sqrt{a} \qquad \textbf{2.55}$$

This means that should the tensile stress decrease faster than $a^{-\frac{1}{2}}$ then K decreases as the crack extends. Thus, if $K \neq K_c$ by the point at which $a = A_m$ then K will never equal K_c and propagation will only be stable and restricted to a surficial layer less than b deep (Lachenbruch, 1961).

Where unstable crack propagation is induced due to a uniform tensile stress over considerable depth that exceeds the tensile strength at the surface of an initially un-fractured solid, the crack depth, A, may be approximated by (Lachenbruch, 1961):

$$A = \frac{1.1\sigma}{0.68\rho g} \qquad \textbf{2.56}$$

Such a scenario is typical of a tectonic setting but less applicable to the surface desiccation induced stress field. Where unstable cracking is induced by surficial tension the following case is suggested. An initial flaw of length less than the depth of the surficial tensile zone, b, must reach the critical depth at which unstable crack growth occurs, A_m, as illustrated in Figure 2.58. Unstable crack propagation is suggested to occur to a depth $A > b$. An expression for final unstable crack depth in response to surficial tension is given by (Lachenbruch, 1961):

$$A_m{}^2 + \frac{1}{0.68\rho g}\left[\frac{\gamma G_0}{\pi(1-v^2)}\right]^{1/2}\sqrt{A_m} = \frac{0.8\sigma b}{0.68\rho g} \qquad \textbf{2.57}$$

when $b > \sim 2A_m, \gamma \approx 0.8b/A_m$

and $G_0 = crack\ arresting\ energy$

$\gamma = normalised\ intensity\ factor\ (a/b)$

It should be noted at this point that the 'crack arresting energy' concerns the condition of the material through which the crack is propagating. Assuming unstable propagation through a homogeneous medium, control of the ultimate crack depth gradually passes from G_0 to the effect of compressive stress.

Therefore, the case $G_0 = 0$ represents the upper limit of propagation through an ideal medium (i.e. no energy is consumed by crack extension).

Cracks are often observed to occur beyond the depth of the surficial tension that produced them. The above scenario suggests that ultimate crack depth may exceed the depth of the surficial tensile zone, b, by more than a factor of 10 (Lachenbruch, 1961). Therefore, the depth at which the ambient stress passes from tensile to compression does not govern the depth to which unstable cracking extends.

Lachenbruch (1961) describes a simplified illustration of the estimation of crack spacing on the basis of local stress relief. Tensile stress is proposed to rise rapidly, exceeding the tensile strength and resulting in crack initiation. The crack formation to calculable depth represents a relief in tensile stress at the ground surface. A neighbouring crack could not form in the vicinity of this crack in which the stress relief represents a certain proportion of the tensile strength. The subsequent neighbouring crack could also not form beyond the zone of stress relief where the magnitude of relief is equal to the initial tensile stress minus tensile strength, else a third crack would initiate between them. This behaviour has subsequently been termed “sequential infilling” (Peron et al., 2013). However, Lachenbruch (1961) goes on to acknowledge that tensile strength must be treated as a function of position and therefore, account for the statistical distribution of flaws across the medium.

Crack depths computed on the basis of LEFM principles are done so in the presence of a nominal applied tensile stress at the time of initial fracturing. Subsequent increase of the tensile stress above the tensile strength could extend deeper resulting in deepening crack extension. Lachenbruch (1961) asserts that the ultimate crack depth may still be calculated using the above approach so long as the interaction of neighbouring cracks is negligible. In the context of cooling joints in basalt, Lachenbruch (1961) notes that final crack depth far exceeds the crack spacing and attributes this to stable or unstable extension during progressive cooling following the initial crack morphology developing within the relatively thin surficial tension layer where depth is approximately equal to spacing.

On the other hand, in the context of embankment desiccation cracking, the selective deepening of widely spaced cracks is a commonly observed behaviour and the development of numerous orders of cracking is frequently noted both in the field and in laboratory evidence. Greater spacing of deeper cracks relates to the greater area over which stress relief is experienced.

Lastly, Lachenbruch (1961) is among the first contributors to highlight a time effect in the generation of clay cracking, commenting on the occurrence of shallowly, closely spaced cracking formed by the relief of surficial tension in rapidly desiccated clay. Deeper and more widely spaced cracks in clays are attributed to seasonal desiccation while cracks on the order of 100 feet are suggested to form as a result of large scale draining of land or a secular trend towards aridity (Willden & Mabey, 1961).

2.7.1.3 Proposed LEFM framework

The LEFM instantaneous, unstable crack propagation based on stress intensity at the crack tip approach proposed by Lachenbruch (1961) was later adopted by other investigators such as Morris et al. (1992) and was included, alongside a systems approach, by Konrad and Ayad (1997) in their idealised framework to describe the spacing of desiccation cracks in terms of effective stress.

The framework proposed by Konrad and Ayad (1997) is illustrated in Figure 2.59 and shows the three models that are employed;

1. A one-dimensional mass transport model to determine an effective stress profile that satisfies the crack initiation criterion.
2. LEFM to determine ultimate crack depth under the previously calculated stress field.
3. A finite element model to determine average crack spacing from stress relief following crack propagation.

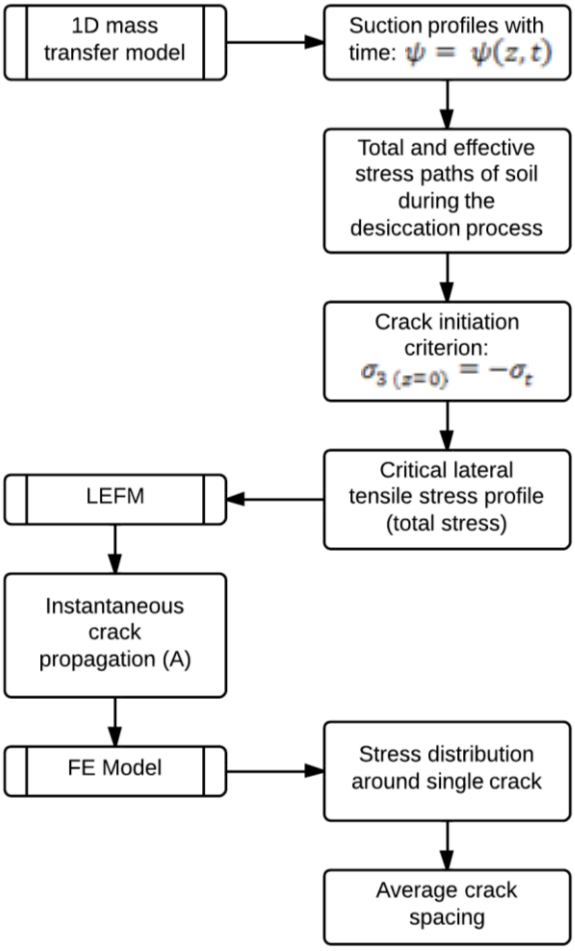

Figure 2.59 Summary of model proposed by Konrad and Ayad (1997)

The suction profile is determined on the basis of a given rate of water removal using the differential equation for water flow in transient conditions (Equation 2.58) in terms of the specific storage coefficient, C, with knowledge of the SWRC and unsaturated hydraulic conductivity.

$$C(\psi)\frac{\partial \psi}{\partial t} = \frac{\partial}{\partial z}\left[k(\psi)\frac{\partial \psi}{\partial z}\right] - \frac{\partial k}{\partial z} \qquad \textbf{2.58}$$

A critical suction approach is developed from the consolidation and desiccation shrinkage theory proposed by Abu-Hejleh and Znidarčić (1995). The original theory is described for a normally consolidated clay slurry and assumes shrinkage due to drying to occur purely during the normal or ‘primary’ shrinkage phase (Haines, 1923). Additional assumptions include; that the soil is homogeneous, the soil skeleton exhibits no intrinsic time effects (i.e. water and solid phases are incompressible) and lastly, that in the following account, the

lateral and vertical planes through which the soil is said to crack represent the principle planes, $\sigma_1 > \sigma_2 > \sigma_3$.

The theoretical model of Abu-Hejleh and Znidarčić (1995) may be described by four chronological stages: one-dimensional normal consolidation; one-dimensional shrinkage; propagation of vertical crack with tensile stress relief and three-dimensional shrinkage. These stages are illustrated in Figure 2.60.

At the start of the consolidation stage, effective and total stress acting on a soil element are represented by O and W respectively in Figure 2.60. The distance between O and W is equal to the initial positive pore-water pressure (and the initial total vertical stress). As consolidation and desiccation progress, the pore-water pressure decreases.

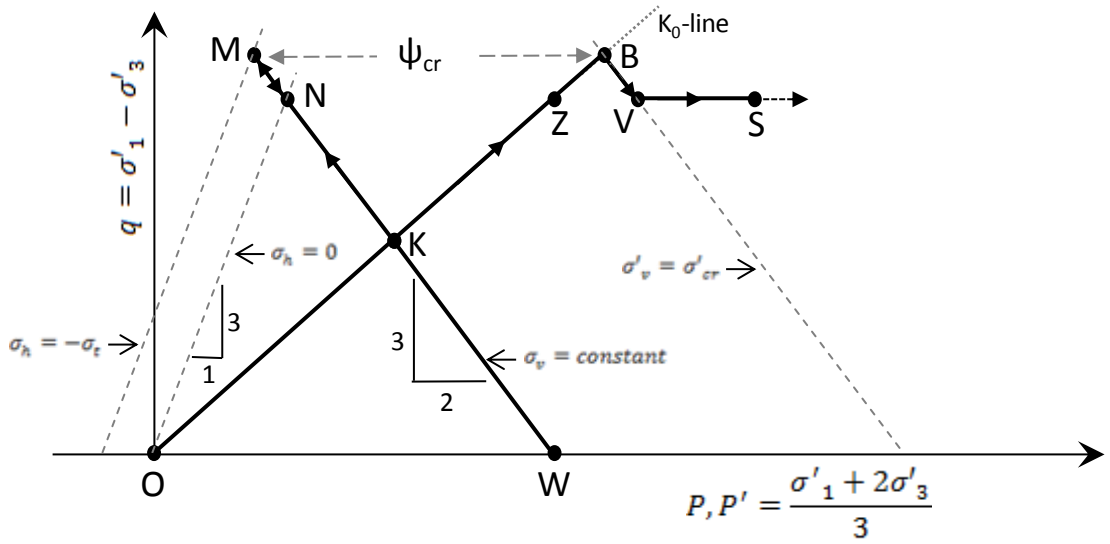

Figure 2.60 Total and effective stress paths during consolidation and desiccation process (after Abu-Hejleh & Znidarcic 1995).

Abu-Hejleh and Znidarčić (1995) consider the soil deformation to therefore comprise of two components; free strain brought about by the change in pore-water pressure and mechanical strain resulting from the change in total stresses. Hence, net strain is associated with a change in effective stress. Prior to crack initiation, net lateral strain is zero, thus the effective stress path during normal consolidation and desiccation follows the K_0-line (coefficient of lateral earth pressure at rest). The lateral total stress decreases due to the reduction in pore-water pressure with continued desiccation. A constant total vertical stress

is assumed for illustrative purposes, this allows the total stress path to follow a slope of $-3/2$ in Figure 2.60.

One-dimensional normal consolidation is depicted by the total and effective stress paths WK and OK respectively while pore-water pressures remain positive. Therefore, point K represents the stress state where pore-water pressure equals zero. One-dimensional shrinkage, where pore-water pressure is increasingly negative is given by the continuation of these paths along KM (total stress) and KB (effective stress). Since zero lateral net strain is maintained in one-dimensional shrinkage, the lateral mechanical tensile strain and corresponding total lateral tensile stress is developed (Abu-Hejleh & Znidarcic, 1995).

The crack initiation criterion is given by:

$$-\sigma_h = \sigma_t \qquad \textbf{2.59}$$

For a soil that is assumed to have no tensile strength, Abu-Hejleh and Znidarčić (1995) state that cracks open when total lateral stress reduces to zero. This state is achieved at N on the $\sigma_h = 0$-line. Here, only atmospheric pressure is said to act on the opening crack wall. The equivalent lateral effective stress is represented at Z where the lateral component is compressive due to suction. However, most soils are assumed to have some component of tensile strength and so a larger suction is required to meet the crack initiation criterion given in Equation 2.59. For this case, the stress paths extend to NM and ZB depending upon the magnitude of tensile strength. The tensile strength of soil is a notoriously difficult property to constrain, as was discussed in Section 2.5.1.

At cracking, the lateral effective stress is given by Equation 2.60 and suction by Equation 2.61.

$$\sigma'_h = K_0 \sigma'_v \qquad \textbf{2.60}$$

$$\psi_{cr} = \sigma'_{v_{cr}} - \sigma_{v_{cr}} \qquad \textbf{2.61}$$

At the onset of cracking, the soil is unloaded elastically. The total lateral stress decreases to zero (point N in Figure 2.60) and the crack is open completely. Abu-Hejleh and Znidarčić (1995) note that if no suction change is assumed

during crack propagation then the effective stress path associated with this stress relief may be represented by BV (parallel to the total stress path MN). The volumetric strain associated with this unloading stage is neglected given the magnitude of observed three-dimensional shrinkage that occurs along the effective stress path VS (Abu-Hejleh & Znidarcic, 1995).

The above method has been employed by Konrad and Ayad (1997) to define the suction at which cracking is initiated (ψ_{cr} in Figure 2.60) as per Equation 2.61.

The relationship between the total stress and suction is dependent on the effective stress path during desiccation which is heavily governed by the stress history of the soil. Although the aforegiven description relates to normally consolidated deposits where the initial stresses at the surface are equal to zero, the principle is proposed to be applicable to any case where the effective stress path may be computed e.g. consolidated, compacted clay (Konrad & Ayad, 1997).

The next stage in the framework proposed by Konrad and Ayad (1997) is to predict the depth to which instantaneous crack propagation will extend. This stage is based on the LEFM approach described above and assumes the required initial length of crack is achieved for unstable propagation (A_m). According to LEFM theory, the final crack depth may be calculated in the knowledge of the tensile stress experienced by the crack walls and the stress intensity factor.

The tensile stress distribution may be computed if the suction profile at crack initiation and effective stress path during desiccation are known (first model of the idealised framework). Konrad and Ayad (1997) present the following approach, again for a normally consolidated soil where the effective stress path follows the normally consolidated K_0-line. Consider a suction profile at crack initiation ($\sigma_3 = -\sigma_t$) as illustrated in Figure 2.61. This profile is the product of the water mass balance model previously described. At depth h_1, total vertical stress is given by $\gamma h_1$and the total stress state is point H on the line $\sigma_1 = \gamma h_1$ (parallel to the $\sigma_v = 0$ line) in Figure 2.62. The value of $\sigma_3$for depth $h_1$is equal to

the distance OM. This procedure enables the lateral tensile total stress profile to be established where lateral tensile stress is shown to extend to a depth b in Figure 2.63. It is important to note that the depth to which tensile total stress extends is different to the depth at which suction equals zero.

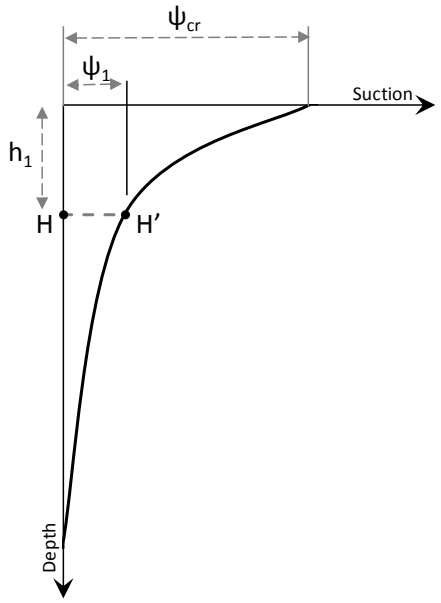

Figure 2.61 Representative suction profile (after Konrad & Ayad 1997).

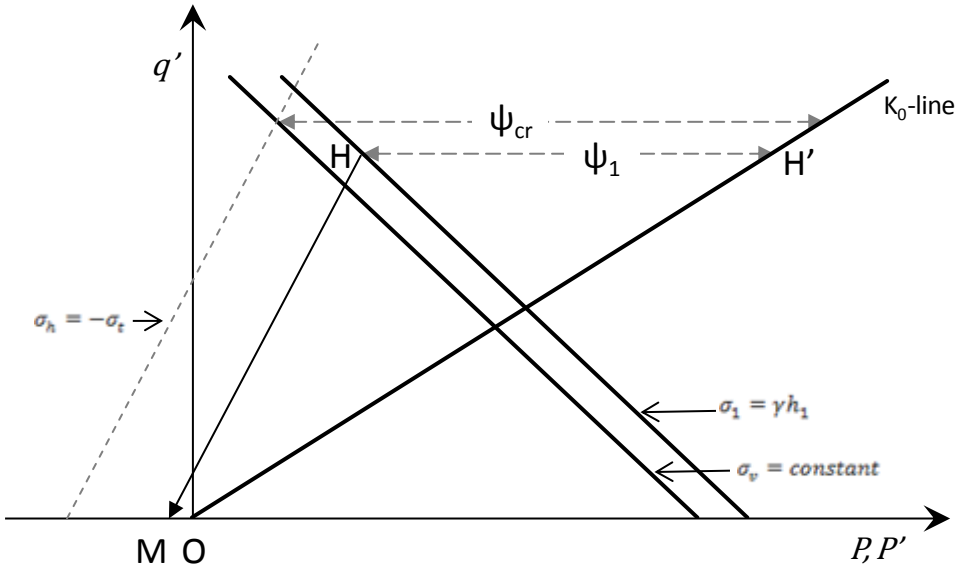

Figure 2.62 Determination of tensile stress from a given suction with depth at the time of crack initiation (adapted from Konrad & Ayad 1997).

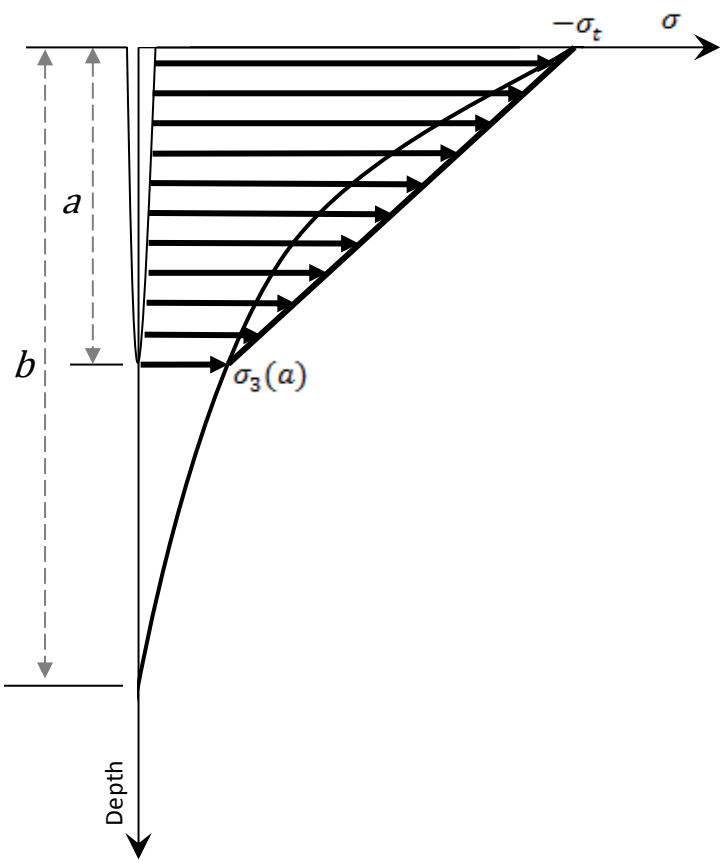

Figure 2.63 Lateral tensile stress profile and approximated stress distribution

In order to calculate the depth of instantaneous crack propagation according to LEFM, the stress intensity factor, K is then calculated as a function of crack length, as per Figure 2.58 where crack length A is defined by $K = K_c$. The approximately trapezoidal distribution of lateral tensile stress on a crack of length a ($a < b$) is assumed as illustrated in Figure 2.63. The simplified expression for K, based on Equation 2.55, may be given as:

$$K = \alpha\sigma\sqrt{a} \qquad \textbf{2.62}$$

where α is a coefficient used to describe the distribution based on the ratio b/a. Konrad and Ayad (1997) use the analytical solutions provided by Lachenbruch (1961) for the case $a < b$. During this stage the depth of stress acting on the crack wall is described as $b = a$ and so α values of 1.1 and 0.68 were used for the rectangular and triangular component of the trapezoidal distribution respectively (Lachenbruch, 1961). For crack lengths $a > b$, the appropriate α value for varying values of b/a were used according to Sih (1973) (cited in Konrad & Ayad 1997). Hence,

$$K = \alpha_1 \left(\frac{b}{a}\right) \sigma_t \sqrt{a} - \alpha_2 \left(\frac{b}{a}\right) [\sigma_t - \sigma_3(b)] \sqrt{a} \quad \textbf{2.63}$$

where α_1 and α_2 refer to the rectangular and triangular component of the trapezoidal distribution respectively for given values of a and b.

The critical stress intensity factor or fracture toughness K_c, is inferred from material constants which may be determined experimentally. A practical application of the proposed framework was undertaken by Ayad et al. (1997) with fracture toughness for plane strain conditions given by:

$$K_c = \left(\frac{E G_c}{1 - v^2}\right)^{0.5} \quad \textbf{2.64}$$

where G_c is the critical energy release rate determined experimentally using an adaptation of fracture testing apparatus for metallic materials i.e. ASTM E399-78 (ASTM, 1983).

Finally, Konrad and Ayad (1997) go on to implement the assumed lateral stress distribution in a Finite Element code to simulate the stress relief zone in the vicinity of the considered crack based on the theory outlined by Lachenbruch (1961). On propagation of the considered crack, the lateral stress disappears at the crack wall. The relief of stress results in a perturbation in lateral stress centred on the position of the crack and extends for a distance, D. Within this zone, $\sigma_3 < \sigma_t$ and no additional cracks will initiate. The crack wall boundary condition is simulated by the application of a fictitious negative normal stress equal in magnitude to the previously deduced lateral stress distribution due to desiccation. It was shown by Lachenbruch (1961) that the size of the stress relief zone is governed by the crack depth and the distributions of the tensile loading i.e. crack depth – surficial tensile stress geometry (if $A < b, b/a = 1$; if $A > b, b/a = b/a$).

At distance D, the lateral stress may approach the tensile strength once more and additional cracking may take place. However, for the modelled linear elastic material in plane strain conditions, the computed lateral stress will only reach the tensile strength when $D = \infty$. Yet, crack spacing is finite. Once more, Konrad and Ayad (1997) adopt the approach suggested by Lachenbruch (1961)

where a crack may initiate at a distance where $\sigma_3 \cong 0.95\sigma_t$. The 95% estimation is acknowledged to appear arbitrary but may be calibrated against field observations and provides a reasonable approximation. Cracking is assumed to occur sequentially, yet essentially instantaneously, under the influence of previously formed cracks which may be a fair approximation of primary cracking. However, in the light of field evidence of orthogonal polygonal cracks, the three dimensional nature of the crack system limits the applicability of the plane strain condition (Kodikara et al., 1998).

The framework proposed by Konrad and Ayad (1997) has allowed the prediction of primary crack depth and spacing to be estimated using fundamental soil mechanics principles, LEFM and a fictitious stress superposition. In order to conduct this approach, the stress history of the soil must be known in addition to the soil tensile strength and fracture toughness. However, knowledge of the initial stress state of overly consolidated soils is often only based on very broad assumptions and the soil strength parameters are difficult to experimentally determine.

This approach brings together proposed models that in isolation represent advances in the understanding of the mechanisms behind crack depth and spacing. The framework presents a simplified approach for the prediction of crack depth and spacing given well defined boundary conditions and soil properties for homogeneous soil. However, it is important to note that only primary crack initiation conditions are identified, followed by instantaneous crack propagation. The period of stable crack growth prior to unstable propagation and any subsequent stable crack growth with progressive desiccation remains largely un-defined.

Following the idealised framework proposed by Konrad and Ayad (1997), the validity of the approach with regards to saturation at cracking was later discussed by Kodikara et al. (1998). The shrinkage of lightly consolidated clay soils is assumed to be dominated by normal shrinkage, where shrinkage is proportional to the removal of water while the soil remains saturated and cracking coincides with the AEV. The stress path approach of Abu-Hejleh and Znidarčić (1995) is thus appropriate for clays where de-saturation occurs

subject to very high suctions (high AEV). The assumption that cracking occurs during saturated, normal shrinkage in the previous framework is offered to apply to heavily over consolidated and compacted clays; however, these soils exhibit unsaturated behaviour during desiccation (Kodikara et al., 1998). Therefore, it is suggested that an unsaturated framework be adopted (e.g. Lau (1987) cited in Kodikara et al. (1998); Morris et al., (1992)).

The net horizontal stress during unsaturated conditions may be expressed by Equation 2.65 where H is an elastic modulus for changes in matric suction, $\Delta\psi$, and for saturated conditions by Equation 2.66.

$$\Delta\sigma_x = \frac{v}{1-v}\sigma_y - \frac{E}{H}\frac{1}{1-v}\Delta\psi \quad \textbf{2.65}$$

$$\sigma'_x = \frac{v}{1-v}\sigma'_y \quad \textbf{2.66}$$

Equation 2.66 is synonymous with the effective stress path for K_0loading employed by Abu-Hejleh and Znidarčić (1995) and Konrad and Ayad (1997) with the exception that $K_0 = v/(1-v)$ in place of $(1-\sin\phi)$ for normally consolidated soils. Upon desaturation, tensile stress is controlled by the E/H ratio and isotropic shrinkage strain may be given by (Kodikara et al., 2004):

$$\Delta\varepsilon_{sh} = \frac{(1-2v)}{E}\Delta\sigma_{sh} + \frac{\Delta\psi}{H} \quad \textbf{2.67}$$

This principle of unsaturated shrinkage is adopted in more recently developed analytical models for desiccation cracking and is discussed in the following section.

2.7.2 Tensile stress failure approach

The accepted mechanics by which cracks initiate in clay soil was established as far back as 1960 and centres on the generation of tensile stresses as a product of restrained shrinkage up to a critical magnitude, designated as the tensile strength (Corte & Higashi, 1960).

Much work has been conducted into the generation of tensile stresses due to restrained shrinkage relatively recently including the following principle contributors, Kodikara et al. (2004), Hu et al. (2006) and Peron et al. (2009). Shrinkage restraints may be considered as internal, external or a combination of the two.

External restraint often takes the form of displacement boundary conditions and frictional interfaces such as those associated with structures in the field (e.g. instrumentation, vegetation or buried infrastructure) or moulds used in laboratory investigations. Peron et al. (2009) described the difference in behaviour between clay desiccated in free shrinkage conditions where a hydrophobic treated Teflon mould was employed to remove as much external cohesive-frictional effect as possible and constrained conditions using a transversally notched metal mould. This study clearly demonstrates the sensitivity of cracking to the presence of an external restraining boundary condition, yet it must be recognised that this effect is amplified given the scale of the mechanical interface in relation to the soil element investigated. However, internal restraint is also an important factor and may be generated by a greater number of sources. Internal restraints may be intrinsic to the soil such as soil texture and structure (e.g. the inclusion of large particles and changes in bedding fabric) or eigen-stress concentrations that develop due to water content heterogeneity brought about by the drying process (Kodikara et al., 2004; Hu et al., 2006). It is believed that in the field, soils predominantly undergo an internally derived, restrained desiccation process brought about by zero net lateral strain prior to crack initiation. Nevertheless, the majority of proposed analytical solutions to the crack initiation problem are centred around a given, isolated soil element for which boundary conditions may be well defined.

An example of the purely tensile stress failure approach was presented by Kodikara and Choi (2006) and was based on laboratory tests conducted by Nahlawi and Kodikara (2006). The experimental work briefly consisted of the controlled drying of a series of slurried and compacted clays in rectangular moulds of considerable length to enable the study of transverse, parallel cracking. The water content at cracking trend in relation to soil thickness was investigated as well as a statistical study into the spacing of the sequential subdivision of the clay cells. Cracks were noted to propagate (sub) perpendicularly the entire depth of the clay layer and continued to initiate with progressive drying until an equilibrium was reached between the moisture content of the clay and the ambient conditions (Nahlawi & Kodikara, 2006). This work informed the following idealised analytical model.

A clay layer is represented as an elastic, homogeneous material positioned upon a rigid, static base as illustrated in Figure 2.64. The base-clay interface is subject to some constitutive relation that governs the shear stress-strain behaviour on the interface e.g. fully elastic, elastic-plastic or zero displacement boundary (Kodikara & Choi, 2006; Hu et al., 2006; Peron et al., 2007). Drying from the upper surface induces shrinkage strains within the clay which, in the presence of the basal restraint, lead to the generation of tensile stresses. As described earlier, additional internal restraint is thought to be brought about by the non-uniform drying throughout the depth of the clay layer though this is often considered negligible in the simplified, laboratory scale analytical models proposed.

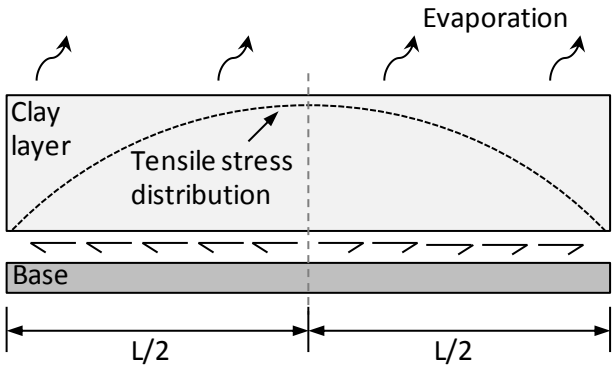

Figure 2.64 Schematic of idealised tensile failure approach (after Kodikara & Choi 2006).

A uniform longitudinal tensile stress across the depth of the layer is assumed based on an average shrinkage strain (i.e. there is no difference in applied shrinkage strain between the upper and lower surfaces). Shrinkage strain is taken as a linear function of the reduction in moisture content. Strains are considered to be a combination of a shrinkage induced (volumetric) component, ε_{sh}, and a mechanical part, $\varepsilon_{\mathrm{ij}}{}^{mech}$ which is related linearly to the total stress by an elastic stiffness tensor, $E_{\mathrm{ij}kl}$. This gives rise to the following expression (Kodikara & Choi, 2006; Peron et al., 2007);

$$d\sigma_{\mathrm{ij}} = E_{\mathrm{ij}kl}(d\varepsilon_{kl} - \delta_{kl} d\varepsilon_{sh}) \qquad \textbf{2.68}$$

where δ_{kl} is Kronecker delta and ε_{sh} is proportional to the reduction in water content, dw, by a shrinkage strain coefficient, α. The shrinkage strain coefficient is defined as the gradient of the free shrinkage strain and moisture loss trend. This allows Equation 2.68 to be expressed more precisely as:

$$d\sigma_{\mathrm{ij}} = E_{\mathrm{ij}kl}(d\varepsilon_{kl} - \delta_{kl} \alpha d\omega) \qquad \textbf{2.69}$$

Peron (2013) notes that this approach holds for strain induced by the first drying cycle (initial shrinkage strain) and is dominantly inelastic and hence, irreversible. This limits the applicability of the modelled shrinkage to simulation of a conceptual singular desiccation path.

Given that the ends of the layer are free, theoretical tensile stress is at a maximum at the middle of the layer length and is symmetrical about this position. Should this stress exceed the tensile strength of the clay, this location is widely assumed to host the initiation of the first crack (Kodikara & Costa, 2013). Subsequent cracking is expected to develop sequentially upon further drying. Laboratory validation of this sequential behaviour is well documented (Nahlawi & Kodikara, 2006; Peron et al., 2013). In such experiments, the number of cracks is observed to increase rapidly once cracking is initiated; the maximum number commonly corresponding to the equilibrium between the clay and ambient environmental conditions.

The cracking process is taken as purely a tensile strength failure problem and cracks are considered to penetrate the entire depth of the clay layer. Hence, no

partially penetrating cracks are accounted for, nor is any subsequent crack propagation (Kodikara & Choi, 2006). The stress distribution is considered dependent upon the length and depth of the layer over which the basal restraint condition is applied. Therefore, for a longer and shallower layer, the tensile stress maximum will occupy a broader and flatter region of the layer making the precise determination of crack initiation location difficult.

The inherent non-linear processes involved in progressive drying are also incorporated. Nahlawi (2004) (cited in Kodikara and Choi (2006)) described the inclusion of an elastic modulus (Equation 2.65) that describes the shrinkage strain relationship with matric suction so as to capture the stiffening of the clay with increased suction. Other drying dependent parameters of the analytical model include the variation in tensile strength and basal friction with respect to a reduction in water content.

2.7.2.1 Numerical implementation

The distinct element method (DEM) is commonly used to model aggregated media due to its ability to efficiently simulate contact breakage and formation conditions. Such programmes are traditionally employed in the modelling of rock materials where the influence of weaker planes or aggregate contacts governs the behaviour of the bulk material. Several studies described in this section have employed a DEM approach to capture the cracking mechanism.

The simplified analytical model presented by Kodikara and Choi (2006) for laboratory cracking has been implemented by Amarasiri et al. (2011) into the distinct element code, UDEC (ITASCA, 2004). Amarasiri et al. (2011) used this ability to model the influence of weak planes to simulate the opening of cracks in slurried clays under given laboratory boundary conditions.

Experiments conducted by Nahlawi and Kodikara (2006) were used to inform the model geometry, the distinct element mesh consisted of a clay block positioned upon a fixed mould similar to that illustrated previously in Figure 2.64. Joints were included via the interface element facility in UDEC and were positioned vertically throughout the mesh as to provide potential crack loci as well as being included at the soil-mould contact to capture basal restraint behaviour. The clay material was simulated using a nonlinear elastic constitutive model where the stiffness of the mesh was considered a function of moisture content. To achieve this, the inbuilt ITASCA programming language was employed. Similarly, shear and normal behaviour at interfaces were programmed to be functions of moisture content according to the results of tests by Nahlawi (2004) and reported by Nahlawi and Kodikara (2006) (e.g. basal shear strength and stiffness, tensile strength)

The modelling approach enabled the interaction of simultaneously evolving, moisture dependent material properties to be captured during the desiccation process. However, critical in the inclusion of such functions is the method in which the model is made to ‘dry’. The principle limitation in the use of UDEC is the lack of capability to simulate fluid flow through the media itself. The programme is considered well suited to applications where fluid flow predominantly occurs along joints in the mesh and so may be best employed in

the modelling of post-desiccation infiltration through an existing crack network. Since the desiccation process is fundamentally governed by the removal of water from the soil matrix, Amarasiri et al. (2011) were forced to adopt a prescriptive approach to moisture content throughout the mesh. An upper and lower desiccation coefficient was devised to translate empirical water loss trends to mechanical negative stresses via an exponential description of the SWRC. Hence, a linear vertical distribution in moisture content as a function of time was incorporated rather than a more gradually developing and realistic nonlinear distribution.

The results of the DEM version of the simplified analytical model compared well with the experimental data in terms of the water content at initiation of cracking (Figure 2.65a) and the final number of cracks (Figure 2.65b) although it may be noted that there is a relatively poor correlation between the observed and modelled sequential crack number development.

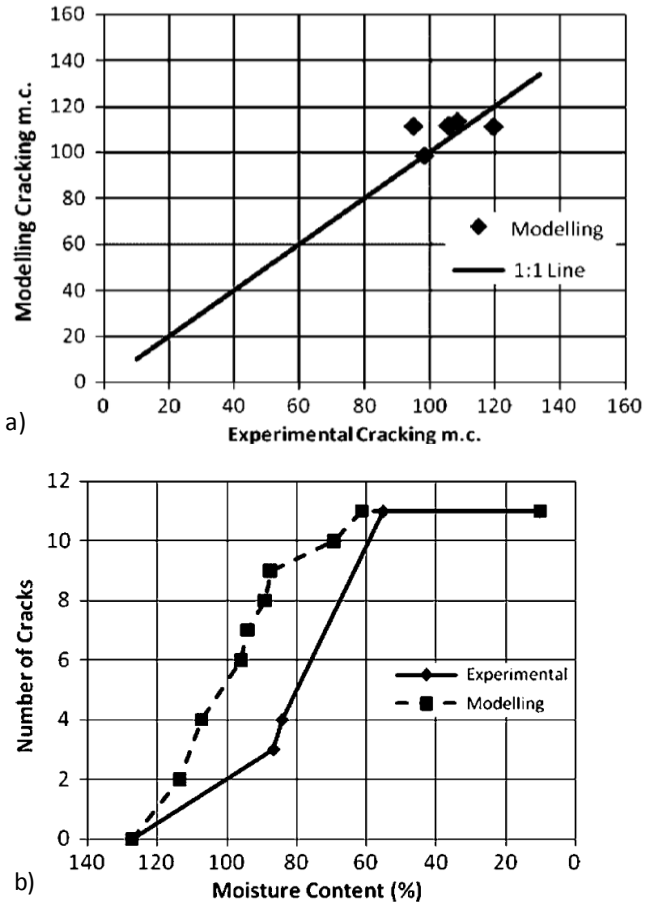

Figure 2.65 Validation of model (a) moisture content at initiation of cracking and (b) crack evolution (after Amarasiri et al. 2011).

The development of the crack pattern for a typical simulation is illustrated in Figure 2.66. It may be seen that the sequential initiation of cracking from first to third order is captured. Amarasiri et al. (2011) highlight the asymmetry in tertiary cracking and relate this to observed behaviour in long mould experiments. Preferential slippage where the shear strength of the soil-mould contact is met in one region allows differential shrinkage with the restrained portion yielding further cracking. The model is therefore thought to capture the physics of the complex real behaviour (Amarasiri et al., 2011). However, the modelled distribution of cracking is extremely regular compared to experiment observations despite conforming to the general analytical model. Cracks are noted to occur at near perfectly regular spacing, a product of the numerical nature of the cracking condition. Given the essentially one-dimensional stress generation throughout the majority of the mesh, any apparent asymmetry within the model is possibly the manifestation of the explicit time marching method in which the programme reaches mechanical equilibrium. This is considered in the light of there being no means of soil strength heterogeneity in the modelled material.

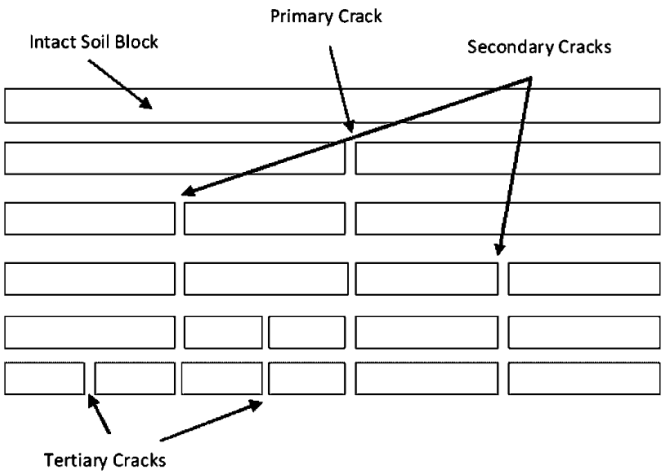

Figure 2.66 Modelled crack progression (after Amarasiri et al. 2011).

The heterogeneity concept was then applied by (Amarasiri & Kodikara, 2011) into the UDEC approach and was shown to produce a better fit with the progression of crack number with progressing desiccation. Cracks were initiated more uniformly with time compared to the step-wise initiation when joint tensile strengths were uniform across the mesh. Additionally, at high levels of variability, cracks were found to have initiated earlier in the desiccation process

due to the increased likelihood that weaker joints would fail under lower tensile stress. Lastly, beyond a critical degree of variability, model output did plateau; in fact the total number of cracks was found to decrease to a residual number and was explained by the dominant release of stored strain energy at the significantly earlier onset of tertiary cracking.

A similar approach was adopted by Musielak and Sliwa (2012) who proposed a coupled distinct element model. The drying process is divided into two stages, firstly when drying rate is approximately constant and the second when drying rate is falling (Musielak & Banaszak, 2007). Only the constant drying stage was captured in the model by a convective mass exchange boundary condition and the internal moisture distribution was simulated using a two-dimensional moisture diffusion equation. Two cases were considered and are illustrated in Figure 2.67.

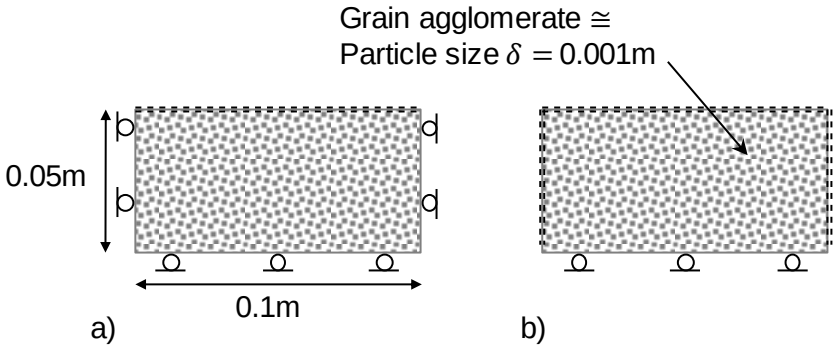

Figure 2.67 Modelled cases (a) case 1 - drying plate, upper surface only and (b) case 2 - drying brick, drying boundary at free ends and upper surface.

Both cases are not uncommon throughout the literature and require some moisture removal rate term. This was prescribed by a moisture exchange coefficient, in this case assumed to be constant at $1 \times 10^{-5}\ m\ s^{-1}$.

The important difference between the DEM models of Musielak and Sliwa (2012) and Amarasiri et al. (2011) is the manner in which the propagation mechanism was captured. Where Amarasiri et al. (2011) prescribed the position and orientation of planes along which separation may be facilitated; Musielak and Sliwa (2012) allowed the initiation and propagation of cracking to be captured not restricted to artificial joints. The material is considered brittle-elastic and modelled quasi-statically i.e. inertia forces are neglected. Using a

network model, the material is divided up into particles linked via cohesive forces that give rise to local strength. The length of this link is determined from the moisture content leading to the simulation of expansion and/or shrinkage. As desiccation cracking is understood to result from the generation of tensile stresses, the inter-particle link is governed by two moisture dependent parameters: a spring constant (stiffness) and a critical force. These parameters are calculated from the Young's modulus and material tensile strength with both being a function of moisture content. Musielak and Sliwa (2012) also recognised that local strength and stiffness in reality have a randomised nature. In order to capture this, a random number between 0.9-1.1 with a Gaussian distribution of 5% standard deviation was multiplied by the particle link stiffness and critical force. To avoid propagation of cracking at the artificial vertical boundaries due to horizontally uniform moisture content in case 1 drying, a flaw was introduced by a reduced set factor (0.8) to parameters at a central particle link.

During drying, the forces in the inter-particle links change and vary from one to the other given their randomised stiffness. If the tensional force in a given particle link exceeds the critical force then the link is broken and a micro-crack is generated. This micro-crack changes the network and stress concentrates on surrounding particle links leading to further micro cracking and coalescence.

The upper surface of the plate in case 1 is in tension due to drying shrinkage and the fixed vertical boundaries. This developing tension increases the force within the particle links in this region until the weakest link breaks leading to an instantaneous increase in tensile force in the immediately surrounding links. Following initial fracturing via coalescence of micro-cracks/link breakage, the tensile force in the upper section is decreased and the moisture content at the crack tip is approximately equal to the initial. Hence, crack propagation is temporarily halted (Figure 2.68a). Meanwhile drying continues at the upper surface and tensile force continues to rise in particle links. As this tensile force grows, stress concentrates at the crack tip and the crack propagates slowly. In Figure 2.68b–c, the direction of fracture is found to change as delamination of the dried crust is captured. Tensile forces concentrate on this plane due to the contrast between the higher strength, dry material close to the surface and the

weaker, wet material below. Such behaviour is common in rapidly desiccated silt-clay soils as depicted in Figure 2.68d.

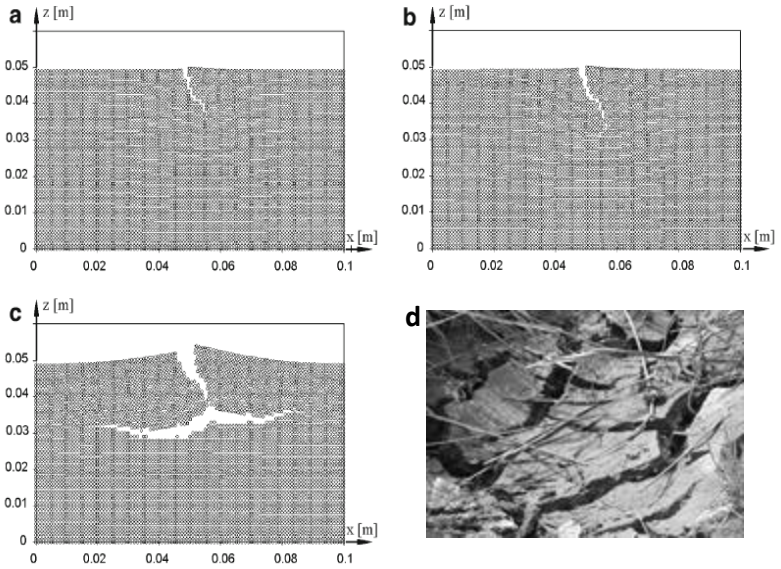

Figure 2.68 Particle locations in case 1 at (a) 69s, (b) 92s and (c) 389s and (d) example of naturally desiccated surface (after Musielak & Silwa 2012).

Musielak and Sliwa (2012) report that the moisture content close to the drying boundaries in case 2 decreases significantly while little change is seen to the interior of the brick section. Here, the moisture content is found to remain greater than the shrinkage limit, this fact is used to justify the use of a constant moisture removal rate. However, the moisture content reduction at the boundary had surpassed this critical water content.

The boundary conditions prescribed in case 2 caused tensile stress close to the top of the material to be generated slower than in the drying plate (case 1) leading to later crack initiation. The first crack is observed to be larger than that in case 1 with relatively rapid progression to the bifurcated fracture pattern. To confirm the random character simulated by the normal dispersion of model parameter values, four different simulations are presented in Figure 2.69, each displaying different geometries at 150s.

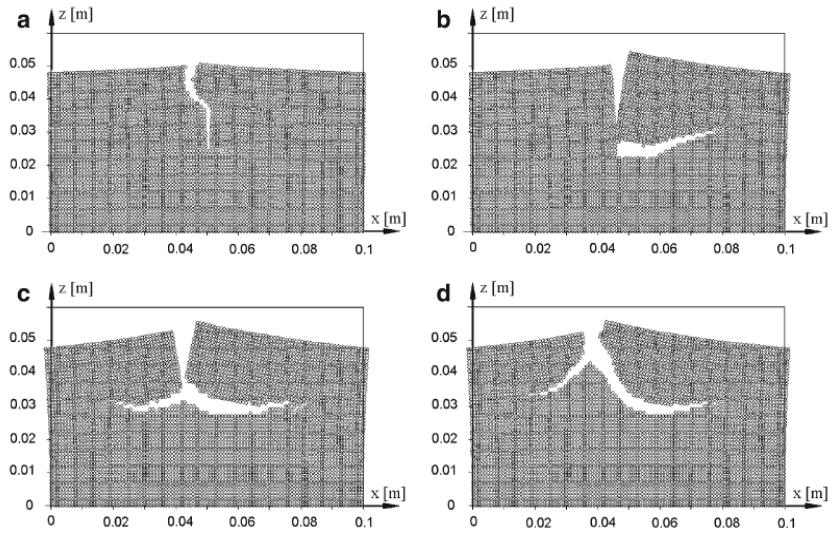

Figure 2.69 Particle locations in different case 2 simulations at 150s (after Musielak & Silwa 2012).

However, their common feature is the starting point—close to the centre of the top side of the bar because the maximum drying-induced tensile stress is generated at this point due to the analytical tensile failure model. A second common feature is that all fracture patterns obtained in the dried bar are broadly similar—vertical cracks starting from the surface branch into two horizontal cracks. The ability to simulate delamination behaviour testifies to the benefits of DEM in capturing irregular cracking geometries albeit in this case, behaviour specific to very high drying rates. However, this method is limited to small model geometries where discrete elements have been used to represent the soil at either grain or microscopic-aggregate scale.

An attempt to model the behaviour of larger scale sample cases was undertaken by Peron et al. (2009). Drying induced shrinkage is simulated at the grain level by an exponential reduction of grain radii with time, although real fine grained soils are recognised not to comprise shrinkable spherical grains as modelled. Therefore, the mechanics of simulated shrinkage differs to the reduction in element linkage length with change in water content approach employed by Musielak and Sliwa (2012).

In the work presented by Peron et al. (2009) grain shrinkage is related to time by a material parameter, α and volumetric shrinkage on the macroscopic level is directly related to the grain scale deformation. The authors describe how many bulk physical properties and processes are incorporated into the parameter α

including hydraulic conductivity and the influence of physical boundary conditions. Further than providing a single α value which would inherently describe homogeneous response (e.g. homogeneous water content at a given time), a location-specific α value was later adopted to describe differential shrinkage due to heterogeneous water content and leads to some grains shrinking faster than others. Grain contact/interaction is based upon a brittle elastic law where failure is defined by exceeding prescribed values of critical normal (tensile) force, tangential (shear) force and/or the contact torque. As in the DEM model of Musielak and Sliwa (2012), bond breakage represents irreversible separation i.e. micro-cracking. The modelled geometry consisted of a 2D longitudinal cross-section intended to represent previously conducted laboratory experiments. The grid comprised a total of 9943 grain elements within a 300 x 12mm rectangle. Grain element configuration was achieved through simulated sedimentation under gravity to generate a compact and stable sample. Given the above specification, the average diameter of each grain corresponds to that of a coarse sand (>0.6mm), larger than that of the Bioley clayey silt used in the laboratory to which the modelling results are compared. However, grain radii were randomly distributed according to a Gaussian distribution although the specifics of this procedure are not provided.

The first simulations conducted were under free shrinkage conditions where all boundaries remained mechanically free. Experimental evidence of small water content gradients in the 12mm thick laboratory sample justifies the use of a homogeneous drying kinetic (single α value) in the preliminary simulations. This value was back-calculated to achieve an acceptable match to water loss with time and volumetric strain records. Results showed that at the limit of drying (22%) i.e. beyond which no further shrinkage was anticipated, the grid shrank homogenously and all grains remained in contact; no cracking was produced and corroborates experimental observations in free shrinkage tests. Next, constrained shrinkage was simulated by applying a fixed zero displacement boundary condition to the bottom of the grid while the top of the sample remained free. Homogenous drying from 32% to 22% water content over a period of 7.2×10^4s was again considered using the back-calculated α value

from the free shrinkage test. The strain evolution of the grid showed a good comparison to the experimental data, as shown in Figure 2.70.

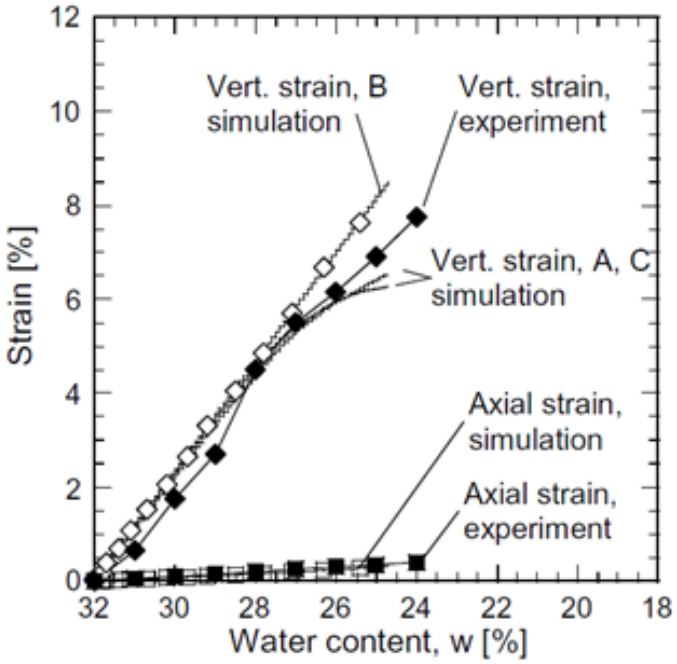

Figure 2.70 Evolution of strains with respect to water content for constrained drying shrinkage where A, B & C refer to left, centre and right of the grid respectively (after Peron et al, 2009).

Given the constrained lower boundary and the rigidity of the grain contacts, a network of forces, dominantly orientated in the axial direction, were generated. Throughout the body of the grid, these forces are homogenous although the extremities of the bar are found to show some difference. The free upper corners of the grid show a reduction in the tensile force to null values while at the lower corners, adjacent to the fixed boundary, tensile forces are larger than average and are orientated sub-vertically. This highlights the influence of basal restraint on the generation of tensile stress in shrinking media. Importantly, these lower corners were the sites of initial cracking although due to the partitioning of forces in these regions, the cracks did not propagate to a great extent. Elsewhere, upon further drying, cracking was seen to occur through the vertical section of the grid. Given the homogeneous mode of simulated drying, cracking was observed to initiate anywhere between the top and bottom boundary before propagating further with cracking not possible at the very bottom boundary due to the fixed displacement condition. The randomness of the grain assembly led to tensile force heterogeneity and cracking initiation anywhere along a vertical axis. Importantly, crack propagation was observed to

occur both gradually and instantaneously within the same simulation. Lastly, a heterogeneous water content method was attempted via the use of α as a function of vertical position. This was aimed at capturing the drying at the upper surface by applying a more rapid shrinkage kinetic towards the top of the sample. This resulted in cracking consistently initiating at the upper surface where the highest tensile forces concentrated.

For a given time during drying, many discontinuities were not completely developed and micro-cracking was observed as localised grain contact breakage. Figure 2.71 presents the occurrences of these bond breakages as a function of time for given distances across the principle axis of the grid. Here, continuous bond breakages at a consistent distance from the sample extremity represent the formation of vertical cracking. However, due to the discrete nature of the medium, cracks are never perfectly straight and the total number of macro-cracks (coalesced bond breakages) was determined by applying a transformation based upon a Gaussian distribution with a standard deviation broadly equivalent to a distance of 10 grains.

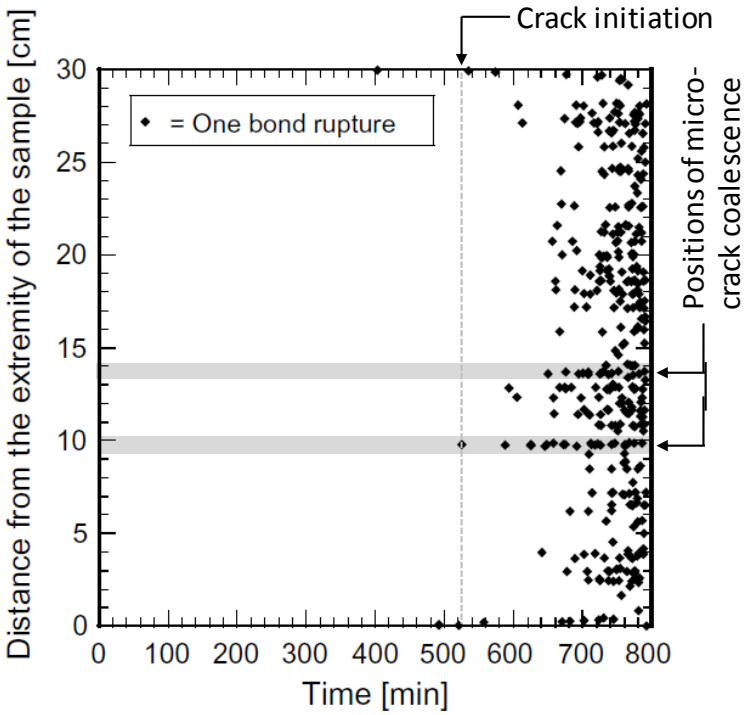

Figure 2.71 Bond breakage with respect to time and abscissa (after Peron et al. 2009).

Peron et al. (2009) concluded that this approach generated an acceptable reproduction of final crack patterns and the final crack number and spacing is directly controlled by the drying kinetics and limit of shrinkage. Possible enhancements of the model are noted by the authors to include the increase in stiffness and strength brought about by the drying process, as was later adopted by Amarasiri et al. (2011) and Musielak and Sliwa (2012).

Finally, the DEM model of Peron et al. (2009) was compared to a simulation conducted in a continuum code, specifically the 2D finite element code Gefdyn (Aubry et al., 1986). A hydro-mechanical formulation was used with the total strain increment divided into drying and mechanical components. Water mass transport was assumed to be governed by a diffusion law. Cracking was not incorporated in the FE model; simulations were therefore only conducted up to the point of grain contact breakage in the equivalent DEM model i.e. the continuous stage of drying shrinkage. The mesh comprised a half bar simulation (using axial symmetry) with a fixed zero displacement lower boundary and a fixed condition in the horizontal direction at the right-hand boundary (bar centre). To simulate drying, the water content on the external boundaries (upper and left-hand) was linearly reduced from 32% - 22% and using an unspecified diffusivity coefficient, a water gradient was achieved throughout the mesh.

By comparing the FE and DEM models, Peron et al. (2009) was able to demonstrate very similar trends in the generated tensile forces/stresses. Particularly of note is the behaviour toward the free end of the bar section. In the FE model, maximum tensile stress is found at the lower, constrained corner in addition to a degree of shear stress. This combined effect was found to result in the first onset of cracking in this region in the DEM model. The minimum tensile stress was found to be generated in the upper corner where boundaries remained free and were therefore able to deform freely without the development of tension. The remainder of the mesh possessed a broadly homogeneous tensile stress field with the maximum at the centre of the bar. This directly conforms to the generalised analytical model, described previously, up to the initiation of cracking (Kodikara & Choi, 2006; Hu et al., 2006; Peron et al., 2009). However, the inferred regularity of the resulting symmetrical crack pattern is recognised to be unrealistic.

The DEM has been shown to be an appropriate tool in the modelling of tensile stress generation and simulated critical tensile failure at a grain-grain contact scale. The mechanics used to simulate the drying process is varied and remains physically simplistic. However, there is a consistency in approach with regard to the underlying understanding of crack initiation and propagation. Material heterogeneity is the key factor in stress heterogeneity that leads to strain localisation and thus crack initiation. This concept was formulated as far back as 1921 in the seminal work of Griffith (1921; Griffith, 1924) where it was stated that any material has within it a pervasive system of random flaws that determine the overall strength of the material. The various discrete approaches have attempted to include this key factor although little statistical work has been conducted on this basis. The material heterogeneity has not been facilitated in continuum modelling. In conclusion, each DEM approach tackles the desiccation and cracking problem in a slightly different way with each model capturing various aspects of the typical behaviour. However, in common engineering scenarios such as slope stability analysis or clay liner design, it is routinely required that the ground be treated as a continuum. In setting up large scale DEM geometries there exists the inherent limitation on modelling efficiency verses element size and number. The modelling schemes commonly selected are typically either FE or FD. Therefore, there is a clear benefit in being able to incorporate the identified drying and cracking mechanics into a continuum code.

2.8 Concluding remarks

A review of the current understanding of desiccation cracking and the approaches used to capture the mechanism has been presented. It is clear that a vast amount of research effort has been conducted on the subject. This is in no small part due to the breadth of applicability of the theoretical basis upon which contemporary understanding is founded.

In presenting the above review, a research gap has been identified. Although existing models reliably capture the initiation of cracking, simulated drying and shrinkage is often prescriptive and lack the unsaturated physics accepted to dominate the soil behaviour under these conditions. The practicability of up-scaling existing models is also considered limited in the study of climatic implications on the behaviour of large scale structures such as infrastructure corridor slopes. In light of this, the following Chapters present the development of a numerical modelling and laboratory test framework to investigate the characterisation of desiccation behaviour as reviewed above.

Chapter 3 Modelling Strategy

3.1 Introduction

As discussed in Chapter 2, in order to investigate the mechanisms believed to control the extent of desiccation cracking, the ability to model hydrological and mechanical behaviour is required. The instigation of critical tensile stress at the ground surface is believed to be brought about by the generation of highly negative pore pressures in the presence of restraint, be this external or internal in origin. Therefore, the modelling tool is needed to be capable of simulating the flow of water through the porous media during drying up to the point of complete desiccation. It must also be able to capture the soil deformation that this process brings about.

Several commercially available packages are commonly used to model soil structures including PLAXIS, FLAC and SAFE. These codes commonly employ a continuum approach and either a finite element or finite difference procedure. Discrete element codes have also been used given the inherent discontinuous nature of the soil fracturing problem. However, DEM programs typically allow fluid flow to be modelled through the bulk media via the networks between the discrete mesh elements and not through the soil element components themselves. They are therefore potentially effective in the modelling of crack bound flow but restrictive in the modelling of macro-scale unsaturated soil behaviour, a prerequisite for the crack formation due to drying. Additionally, DEM methods are not compatible with traditional slope stability investigations that use continuum modelling.

Most mechanical packages include some form of fluid flow calculation, although these often assume saturated soil behaviour. However, PLAXIS flow and FLAC tp-(two phase) flow allow modelling of unsaturated flow. Unsaturated constitutive models are not included as standard in either of these programs. Therefore, increased strength due to suction is normally only included in the form of increased effective stress.

The package selected for the work herein was FLAC 2D with the two-phase flow add-on. There exists a 3D version of this program; however, two-phase flow is only available with the 2D version. The main advantage in using this package is an in-built programming language that enables the user to write

functions within the code. In this way, variables may be updated during the calculation. For example, this enables material properties to be controlled as a function of the drying process.

This Chapter will first describe FLAC starting with an outline of the solution procedure and moving on to the available features that make the program suitable for the intended application. Secondly, the application of each feature is presented, describing the development of the model. Finally, an illustrated summary of the fully compiled model is provided.

3.2 FLAC 2D

FLAC (Fast Lagrangian Analysis of Continua) is an explicit finite difference code developed by Peter Cundall in 1986 for the Itasca Consulting group (ITASCA, 2002). The version used in this thesis is FLAC 2D v.4.00. In this program the soil continuum is descretised into a series of elements which deform (in large-strain mode) according to linear or non-linear stress/strain laws in response to applied forces or restraints specific to the problem.

FLAC was developed for geotechnical engineering analyses and provides a variety of mechanical modelling capabilities. The principle facilities used in this work include the following:

- Interface elements – these are distinct planes along which slip or separation is facilitated and allow soil cracking to be simulated in the form of opening discontinuities within the otherwise continuum mesh.
- Two-phase flow – this add-on allows the modelling of two immiscible fluids within a porous medium and as such enables unsaturated soil behaviour to be captured.
- FISH –a built-in programming language (FLAC-ISH) that allows the user to write custom functions to tailor the model e.g. grid generation, property variation spatially and temporally.

The numerical principle underlying FLAC is explained here followed by an overview of the model construction process with specific reference to the use of interfaces.

3.2.1 Solution scheme

As previously mentioned, FLAC uses an explicit, time marching scheme to find a static, stable solution to potentially unstable, physical problems. Figure 3.1 depicts the general calculation sequence employed.

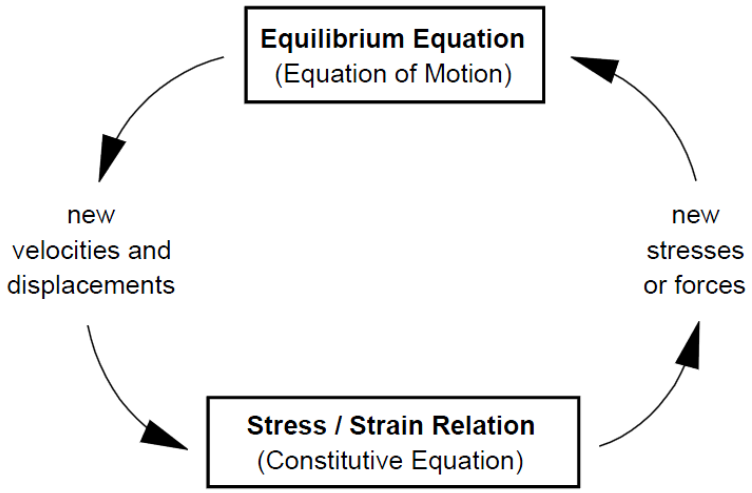

Figure 3.1 Explicit calculation cycle (after ITASCA, 2002)

The dynamic equations of motion are used to estimate velocities and displacements from forces and stresses. Velocities are then used to derive strain rates from which new stresses are generated. Crucially, the grid variables are derived from values that are fixed during the operation of each box (Figure 3.1). For instance, new stresses are calculated for each element while control is within the lower box from frozen velocities i.e. the resulting new stress does not affect the velocities. When new stresses are defined, one would expect these to instantly alter the velocities of surrounding elements making the assumption of 'frozen' velocities inappropriate. However, the calculation cycle is only valid when the time-step for one loop of the cycle is smaller than the time taken to physically transmit information between neighbouring elements. A complete loop through the calculation cycle constitutes one time-step meaning neighbouring elements cannot influence each other during a single calculation cycle. Repetition of this cycle allows the propagation of stresses and velocities across the grid, much as in a physical system.

3.2.1.1 Time-step

As previously described, the time-step in FLAC must be smaller than the physical time taken for information to propagate. Therefore, a time-step, Δt, is chosen that is less than the critical time-step. For an elastic grid comprising elements of size Δx:

$$\Delta t < \frac{\Delta x}{C} \quad \textbf{3.1}$$

Where C is the maximum speed at which information can propagate through the material. This is typically considered as the p-wave velocity and is dependent upon the bulk and shear moduli (K and G respectively) and the density,ρ of the medium given by:

$$C_p = \sqrt{\frac{K + 4G/3}{\rho}} \quad \textbf{3.2}$$

It may therefore be seen that the time-step size is controlled by the stiffness of the modelled material and the spacing of the grid used to represent the problem. Consequently, densely meshed, stiff materials are modelled using extremely small time-steps which may lead to impractically long run times.

3.2.1.2 Field equations

FLAC invokes the equations of motion and constitutive relations to describe the deformation of a problem. In the simplest form, the equation of motion describes the acceleration of a mass, m, due to an applied force, F, over time. In Figure 3.2, such motion is illustrated in terms of acceleration, velocity and displacement. Newton's law of motion for the mass-spring system is given by Equation 3.3 where the notation, $\dot{}$, signifies the derivative.

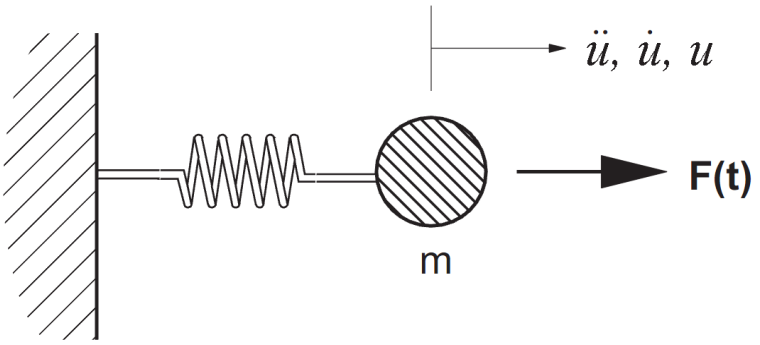

Figure 3.2 Time-varying force applied to a mass resulting in acceleration, $\ddot{u}$, velocity, $\dot{u}$ and displacement, u (after ITASCA, 2002).

$$m\frac{d\dot{u}}{dt} = F \qquad \textbf{3.3}$$

When the sum of all forces acting on the mass equals zero, acceleration will also equal zero. This principle is used by FLAC to represent the static equilibrium condition. For a continuous solid-body, Equation 3.3 may be considered in the form of Equation 3.4 where the indices i and j are components in a Cartesian coordinate frame.

$$\rho\frac{\partial\dot{u}_i}{\partial t} = \frac{\partial\sigma_{ij}}{\partial x_j} + \rho g_i \qquad \textbf{3.4}$$

where, $\rho = \text{mass density};$

$x_i = \text{components of coordinate vector};$

$g_i = \text{components of gravitational acceleration (body forces); and}$

$\sigma_{ij} = \text{components of stress tensor.}$

In addition to the law of motion, a constitutive relation (stress/strain law) is required where firstly strain rate is derived from the velocity gradient using the following equation:

$$\dot{\varepsilon}_{ij} = \frac{1}{2}\left[\frac{\partial\dot{u}_i}{\partial x_j} + \frac{\partial\dot{u}_j}{\partial x_i}\right] \qquad \textbf{3.5}$$

where, $\dot{\varepsilon}_{ij} = \text{strain-rate components; and}$

$\dot{u}_i$ = velocity components.

The mechanical constitutive law is in the form:

$$\sigma_{ij} := M\left(\sigma_{ij}, \dot{\varepsilon}_{ij}, \text{Ƙ}\right) \quad \textbf{3.6}$$

where, $M(\quad)$ = functional form of the constitutive law;

Ƙ = history parameter (depending on particular law); and

$:=$ means "replaced by"

Equation 3.6 estimates the new stress tensor from an old stress tensor and strain rate/increment. An example of a simple constitutive law is isotropic linear elasticity where the new stress tensor is calculated by the following:

$$\sigma_{ij} := \sigma_{ij} + \left\{\delta_{ij}\left(K - \frac{2}{3}G\right)\dot{\varepsilon}_{\text{ƘƘ}} + 2G\dot{\varepsilon}_{ij}\right\}\Delta t \quad \textbf{3.7}$$

where, δ_{ij} is the Kronecker delta;

Δt = timestep; and

G, K = shear and bulk modulus, respectively.

In FLAC, the option to conduct analysis in 'Large strain' mode is available whereby the grid can deform according to the calculated stress tensor. In order to accommodate this, the stress components are modified in one time-step according to the rotated frame of reference. Hence, the new stress tensor is calculated using the following equation:

$$\sigma_{ij} := \sigma_{ij} + \left(\omega_{ik}\sigma_{kj} - \sigma_{ik}\omega_{kj}\right)\Delta t \quad \textbf{3.8}$$

where,

$$\omega_{ij} = \frac{1}{2}\left\{\frac{\partial \dot{u}_i}{\partial x_j} - \frac{\partial \dot{u}_j}{\partial x_i}\right\} \quad \textbf{3.9}$$

3.2.1.3 The grid

The geometry of the problem is defined by a finite difference grid consisting of quadrilateral elements (Figure 3.3a). This grid is then internally sub-divided into overlaid constant-strain triangular elements, as illustrated in Figure 3.3b and c.

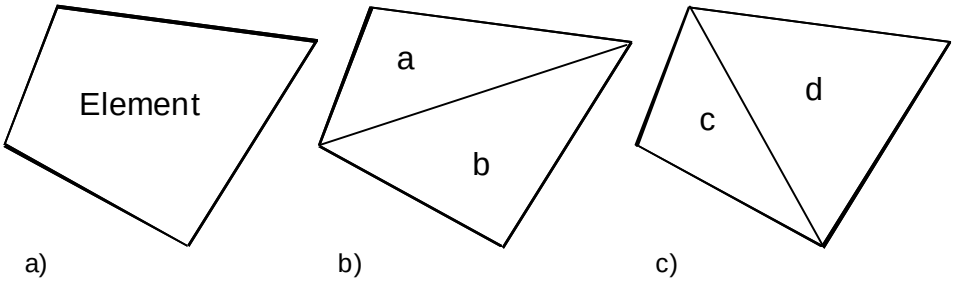

Figure 3.3 (a) quadrilateral element (b) triangular sub-elements a & b (c) triangular sub-elements c & d (after ITASCA, 2002).

The force vector acting at each node is taken as the mean of the two vectors exerted by the two overlaid quadrilaterals. Should a pair of triangles excessively distort, for example the area of a single triangle becomes disproportionate to that of its companion, the corresponding quadrilateral is not used and the force vectors from the reasonably-shaped quadrilateral are substituted. When both sets of triangles are too heavily distorted, an error is reported and the calculation is halted.

Triangular elements eliminate the occurrence of hourglass deformations. This issue originates with the use of constant-strain finite difference quadrilaterals where combinations of nodal displacements for polygons of four nodes may result in no opposing forces and therefore unopposed deformations in opposing directions.

3.2.2 Fluid flow

FLAC allows modelling of fluid flow in addition to or in the absence of the mechanical calculation. A simulation involving both mechanical and fluid flow calculations is referred to as a coupled calculation. The single-phase fluid flow model simulates fully saturated flow and, where a phreatic surface develops, pore pressures above this surface are assumed to be zero i.e. the non-wetting fluid (e.g. air) is passive. This situation may be applicable to the modelling of coarse, granular materials where capillary effects are neglected. However, the significant capillary effects observed in fine grained materials may be included through the use of the two-phase flow add-on.

At this stage it is important to clarify that the “permeability” used in FLAC is referred to as the mobility coefficient, k (m^2/(Pa.s)). The mobility coefficient is defined by Equation 3.10 where k_H is the saturated hydraulic conductivity (m/s), ρ_w is the density of water (kg/m^3), κ is the intrinsic permeability (m^2) and μ is the dynamic viscosity (Pa.s).

$$k = \frac{k_H}{g\rho_w} = \frac{\kappa}{\mu} \qquad \textbf{3.10}$$

3.2.2.1 Single-phase flow

The governing differential equations corresponding to *FLAC*’s numerical implementation of coupled deformation-diffusion processes are provided. The fluid transport is expressed using Darcy’s law:

$$q_i = -k_{\mathrm{ij}}^{a} \frac{\partial}{\partial x_j}(P - \rho_w g_k x_k) \qquad \textbf{3.11}$$

Where, q_i is the specific discharge vector and k^a_{ij} is the apparent mobility coefficient which is a function of the saturation, s, and fluid pressure, P. The fluid mass balance is presented in Equation 3.12 and relates the variation of fluid content, ζ, and the volumetric fluid source intensity, q_v. The balance of momentum is described by Equation 3.13.

$$\frac{\partial \zeta}{\partial t} = -\frac{\partial q_i}{\partial x_i} + q_v \quad \textbf{3.12}$$

$$\frac{\partial \sigma_{ij}}{\partial x_j} + \rho g_i = \rho \frac{d\dot{u}_i}{dt} \quad \textbf{3.13}$$

where, ρ is the bulk density given by Equation 3.14. Here, the porosity of the medium, n, the density of the fluid, ρ_w, and the dry density, ρ_d, is used where the dry density is calculated using the density of the solids in Equation 3.15.

$$\rho = \rho_d + n\rho_w \quad \textbf{3.14}$$

$$\rho_d = (1-n)\rho_s \quad \textbf{3.15}$$

The constitutive response for pore fluid is related to the saturation of the medium. When fully saturated, S=1, the apparent mobility coefficient equals the saturated mobility coefficient. Under these conditions, the pore fluid can sustain a tension up to a user defined limit T_f and the response is described by:

$$\frac{\partial P}{\partial t} = M\left(\frac{\partial \zeta}{\partial t} - \alpha \frac{\partial \epsilon}{\partial t}\right) \quad \textbf{3.16}$$

where,

$$M = \frac{K_w}{n} \quad \textbf{3.17}$$

Where ϵ is the volumetric strain, α is the Biot coefficient (equal to 1 assuming the grains to be incompressible in comparison to the drained bulk medium) and M is the Biot modulus calculated using the bulk modulus of water, K_w.

When unsaturated, S<1, the constitutive response is calculated by:

$$\frac{\partial s}{\partial t} = \frac{1}{n}\left(\frac{\partial \zeta}{\partial t} - \alpha \frac{\partial \epsilon}{\partial t}\right) \quad \textbf{3.18}$$

As mentioned earlier, pore pressure in the unsaturated zone is zero. The resulting soil water retention curve is illustrated in Figure 3.4a. Unsaturated flow is governed by gravity with the relation between saturation and relative permeability given by Equation 3.19 and illustrated in Figure 3.4b.

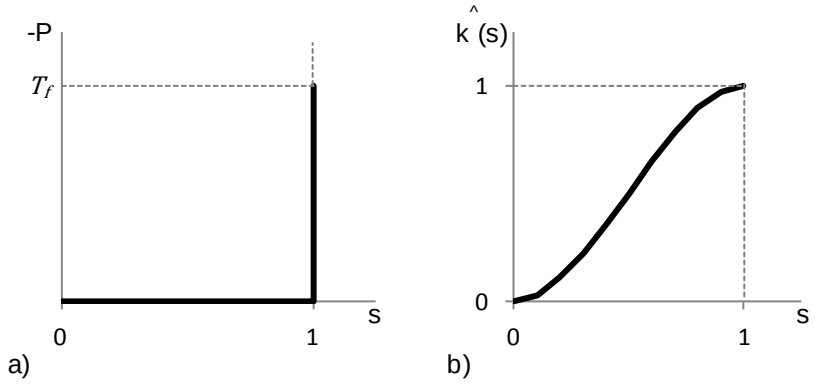

Figure 3.4 Single-phase unsaturated behaviour (a) retention curve and (b) relative permeability as a function of saturation (after ITASCA, 2002).

$$\hat{k}_{(s)} = s^2(3 - 2s) \quad \textbf{3.19}$$

where,

$$\hat{k}_{(s)} = \frac{k_{\mathrm{ij}}^{a}}{k_{\mathrm{ij}}} \quad \textbf{3.20}$$

The small strain constitutive response of the porous media is given by Equation 3.21, where H is the functional form of the constitutive law, K is a history parameter and α=1.

$$\frac{d}{dt}\left(\sigma_{\mathrm{ij}} + \alpha P \delta_{\mathrm{ij}}\right) = H\left(\sigma_{\mathrm{ij}}, \dot{\epsilon}_{\mathrm{ij}}, \mathbb{K}\right) \quad \textbf{3.21}$$

The elastic constitutive response which relates effective stresses to strains, takes the following form; where the superscript ^{o} refers to the initial state:

$$\sigma_{\mathrm{ij}} - \sigma_{\mathrm{ij}}^{o} + (P - P^{o})\delta_{\mathrm{ij}} = 2G\epsilon_{\mathrm{ij}} + \left(K - \frac{2}{3}G\right)\epsilon_{kk}\delta_{\mathrm{ij}} \quad \textbf{3.22}$$

where,

$$\epsilon_{kk} = \epsilon_{11} + \epsilon_{22} + \epsilon_{33} \quad \textbf{3.23}$$

3.2.2.2 Fluid flow time-step

As described in Section 3.2.1.1, explicit time-steps correspond to the time taken for information to propagate through the medium. As such, the explicit fluid flow time-step is based upon the diffusivity of the fluid. The characteristic time for the diffusion process is calculated using the following equation:

$$t_c = \frac{{L_c}^2}{c} \tag{3.24}$$

where,

$$c = k\frac{K_w}{n} \tag{3.25}$$

where, $L_c = \text{characteristic length};$

$c = \text{fluid diffusivity};$

$K_w = \text{fluid bulk modulus};$

$k = \text{mobility coefficient; and}$

$n = \text{porosity}.$

The characteristic length refers to the average length of the fluid flow path. When defining the minimum characteristic time, this length represents the smallest grid-point spacing. Therefore, by substituting Equation 3.25 into Equation 3.24, the fluid flow time-step may be defined by the following expression:

$$\Delta t = min\left(\frac{{L_z}^2 n}{kK_w}\right) \tag{3.26}$$

It may be seen that the time-step is inversely proportional to the bulk modulus of the fluid. A realistic K_w of approximately 2.15x10^9 Pa will result in small time-steps meaning a large number of steps are required to conduct the fluid flow calculation. This situation is necessary for problems where the required flow time is much less than the characteristic time (undrained analysis). However, for steady state analyses where the required flow time is by far in excess of the characteristic time, the solution may lead to excessive run times. Therefore, by artificially decreasing K_w, the solution run time may be reduced with little

discernible impact on the final solution. Numerical instability will result from a K_w that is too low, yet care must be taken to maintain a high enough K_w such that water remains incompressible relative to the solid medium, i.e. (ITASCA, 2002):

$$maxK_w \approx 20 \times n\left(K + 4\frac{G}{3}\right) \quad \textbf{3.27}$$

3.2.2.3 Two-phase flow

The standard version of FLAC allows modelling of a single fluid phase where the medium is considered saturated or completely unsaturated. However, with the addition of the two-phase flow option (henceforth referred to as 'tp-flow'), modelling of two fluid phases may be conducted. If it is assumed that fluids represent air and water, the behaviour of unsaturated soil may be investigated. The tp-flow logic may be used to solve a fluid or mechanical only calculation or a fully coupled fluid-mechanical calculation. An overview of the tp-flow approach is presented here.

The fluid-mechanical coupling incorporates the influence of volumetric deformation on porosity and the associated change in permeability and capillary pressure characteristics.

In implementing the tp-flow logic, the following features are available:

1. Fluid transport laws corresponding to isotropic and anisotropic permeability
2. Fluid-flow properties may be varied across the grid
3. Fluid specific boundary conditions may be applied
4. Fluid sources (inflow/outflow) may be inserted anywhere within the grid

The tp-flow module allows flow of two immiscible fluids through a porous media to be modelled where no mixing is permitted and void space is assumed to be saturated:

$$S_w + S_{nw} = 1 \quad \textbf{3.28}$$

Of these two fluids, one is said to be wetting, S_w, while the other non-wetting, S_{nw}. In partially saturated media the non-wetting fluid pressure, P_{nw}, (e.g. air) will be larger than the pressure of the wetting fluid, P_w, (e.g. water).

Fluid pressure increments, based on the weighted presence of each fluid, are used in place of pore pressure increments in the calculation of Terzaghi's effective stress increment. Pore (Capillary) pressure, P_c, is identified as the difference between the two fluid pressures [Equation 3.29] and is fundamentally linked to the effective saturation by the van Genuchten approximation (van Genuchten, 1980). The form used by FLAC is given by Equation 3.30.

$$P_c = P_{nw} - P_w \tag{3.29}$$

$$S_e = \left[\left(\frac{P_c}{P_0}\right)^{\frac{1}{1-a}} + 1\right]^{-a} \tag{3.30}$$

Where parameter a is equivalent to the van Genuchten constant, m and S_e is the effective saturation which is related to the actual, S_w and residual saturation, S_r, by:

$$S_e = \frac{S_w - S_r}{1 + S_r} \tag{3.31}$$

P_0 is also a van Genuchten constant related to the coefficient, α, the density of the wetting fluid, ρ_w and the force due to gravity, g, by the following definition:

$$P_0 = \frac{\rho_w g}{\alpha} \tag{3.32}$$

The tp-flow add-on allows the water retention path to be described using a single set of van Genuchten parameter values. Typically desorption and therefore hydraulic hysteresis is not automatically included.

Fluid flow is described by Darcy's law for each fluid:

$$q_i{}^w = -k_{ij}{}^w k_r{}^w \frac{\partial}{\partial x_j}\left(P_w - \rho_w g_k x_k\right) \tag{3.33}$$

$$q_i{}^{nw} = -k_{ij}{}^{nw} \frac{\mu_w}{\mu_{nw}} k_r{}^{nw} \frac{\partial}{\partial x_j} (P_{nw} - \rho_{nw} g_k x_k) \quad \textbf{3.34}$$

where k_{ij} is the saturated mobility coefficient, k_r is the relative mobility coefficient, μ is dynamic viscosity, P is pore pressure and ρ is the density of the fluid. The relative permeability is related to the effective saturation of that fluid by the van Genuchten empirical expressions:

$$k_r{}^{w} = S_e{}^{b} \left[1 - \left(1 - S_e{}^{1/a}\right)^{a}\right]^2 \quad \textbf{3.35}$$

$$k_r{}^{nw} = (1 - S_e)^{c} \left[1 - S_e{}^{1/a}\right]^{2a} \quad \textbf{3.36}$$

When the porous medium is considered as to be an unsaturated soil, the above equations correlate to those for the relative permeability of water proposed by van Genuchten (1980) and air by Parker et al. (1987). In these equations, b and c are constants equal to 0.5 for both water and air.

The fluid balance relation takes the form of the single-phase formulation for each fluid:

$$\frac{\partial \zeta_w}{\partial t} = -\frac{\partial q_i{}^{w}}{\partial x_i} + q_v{}^{w} \quad \textbf{3.37}$$

$$\frac{\partial \zeta_{nw}}{\partial t} = -\frac{\partial q_i{}^{nw}}{\partial x_i} + q_v{}^{nw} \quad \textbf{3.38}$$

The balance of momentum is again in the same form as that used for the single-phase calculation (Equation 3.39). However, bulk density, ρ, is calculated using Equation 3.40 where the fluid density term is weighted according to saturation (although when modelling unsaturated flow, the density of air is assumed to be zero).

$$\frac{\partial \sigma_{ij}}{\partial x_j} + \rho g_i = \rho \frac{d\dot{u}_i}{dt} \quad \textbf{3.39}$$

$$\rho = \rho_d + n(S_w \rho_w + S_{nw} \rho_{nw}) \quad \textbf{3.40}$$

The fluid constitutive laws are:

$$S_w \frac{\partial P_w}{\partial t} = \frac{K_w}{n}\left[\frac{\partial \zeta}{\partial t} - n\frac{\partial S_w}{\partial t} - S_w \frac{\partial \epsilon}{\partial t}\right] \quad \textbf{3.41}$$

$$S_{nw} \frac{\partial P_{nw}}{\partial t} = \frac{K_{nw}}{n}\left[\frac{\partial \zeta}{\partial t} - n\frac{\partial S_{nw}}{\partial t} - S_{nw} \frac{\partial \epsilon}{\partial t}\right] \quad \textbf{3.42}$$

where, $K_w, K_{nw} = \text{fluid bulk moduli; and}$

$\epsilon = \text{volumetric strain.}$

After substituting the fluid balance laws for each fluid into Equations 3.41 and 3.42, we obtain:

$$n\left[\frac{S_w}{K_w}\frac{\partial P_w}{\partial t} + \frac{\partial S_w}{\partial t}\right] = -\left[\frac{\partial q_i{}^w}{\partial x_i} + S_w \frac{\partial \epsilon}{\partial t}\right] \quad \textbf{3.43}$$

$$n\left[\frac{S_{nw}}{K_{nw}}\frac{\partial P_{nw}}{\partial t} + \frac{\partial S_{nw}}{\partial t}\right] = -\left[\frac{\partial q_i{}^{nw}}{\partial x_i} + S_{nw} \frac{\partial \epsilon}{\partial t}\right] \quad \textbf{3.44}$$

For a fluid-only calculation where volumetric deformation is not considered, the volumetric strain term, $\frac{\partial \epsilon}{\partial t}$, is omitted. The four unknowns, P_w, P_{nw}, S_w and S_{nw}, may then be calculated using Equations 3.28, 3.29, 3.43 and 3.44.

The incremental mechanical constitutive response to change in effective stress takes the form:

$$\Delta\sigma'_{\text{ij}} = H\left(\sigma_{\text{ij}}, \Delta\epsilon_{\text{ij}}, \mathbb{K}\right) \quad \textbf{3.45}$$

where $\Delta\sigma'_{\text{ij}}$ takes the form:

$$\Delta\sigma'_{\text{ij}} = \Delta\sigma_{\text{ij}} + (S_w \Delta P_w + S_{nw}\Delta P_{nw}) \quad \textbf{3.46}$$

3.2.3 Problem solving using FLAC

The general methodology for problem solving is outlined in the following section. There are three main considerations in the construction and solution of a problem in FLAC:

- Grid generation
- The choice of constitutive model and material properties
- Boundary and initial conditions

3.2.3.1 Grid generation

The finite difference grid defines the geometry of the problem under investigation. There are many components to consider in the construction of the grid including the incorporation of any existing structures, specific grid boundaries, grid density and any discontinuities that may divide the grid. Within FLAC, a number of commands allow the creation of commonly used internal and external boundary shapes. The facility to connect sub-grids is also available to allow sequential changes in problem geometry.

There are recommendations to consider when generating the grid. Firstly, boundary effects on the region of interest should be evaluated through a series of runs conducted using varying levels of grid refinement. The grid density must then be considered. For greatest accuracy the aspect ratio of element dimensions should be as close to unity as possible. Ratios above 5:1 are potentially inaccurate although higher ratios may be acceptable in regions of the grid where low strain gradients are anticipated i.e. towards grid boundaries. The highest grid density should be reserved for regions of highest stress/strain gradients e.g. where loading/unloading is applied. Adjacent element area ratios are recommended to be kept below 4:1 to enable accurate propagation. A command is hence provided to allow the user to gradually grade the grid between regions of interest and the model boundaries.

3.2.3.2 Constitutive models and material properties

A selection of constitutive models is available in FLAC and these are arranged into three model groups: null, elastic and plastic.

- The null material model represents space where all stresses are zero. This model is commonly used in the simulation of material removal e.g. excavation. In this work, a null material is merely employed in the generation of the required geometry, namely in the installation of interfaces (Section 3.2.4).
- Two elastic models are available, isotropic and transversely isotropic where the stress-strain relationship is linear and all strains are recoverable.
- A total of seven plastic models are available including the Mohr-Coulomb, ubiquitous-joint, strain-hardening/softening and modified Cam-clay models. These all entail a degree of non-recoverable deformation and require the input of model-specific material properties that enable the yield conditions to be constrained.

The choice of constitutive model is fundamental to the type of analysis to be undertaken. For the purposes of this work, a modified elastic model has been implemented as is presented in Section 3.3.3.

3.2.3.3 Boundary conditions

Boundary conditions are used to prescribe the behaviour at the grid boundary. These are conventionally set prior to the application of loading/unloading though the condition may be made to vary during a run via FISH. Boundaries may be split into two categories: real boundaries that exist in the physical problem (e.g. tunnel surface, ground surface); and artificial boundaries that are used to enclose a grid representing a region of infinite extent.

Mechanical boundaries are free by default and may be defined as two main types: prescribed-displacement (e.g. velocity, fixed) or prescribed-stress (e.g. force, free). Prescribed boundary variables may be made to vary linearly over a specified range, commonly depth. It may also be desirable to vary the magnitude of prescribed stresses gradually using FISH in order to minimize the shock to a sensitive system.

Fluid flow boundaries are impermeable by default, meaning all grid-point pore pressures and zone saturations are free to vary according to net in or outflow from surrounding zones. No exchange between the grid and outside world is allowed under this condition. However, pore pressure and saturation may be

prescribed independently at the grid boundary. This allows fluid exchange between the grid and outside world to be modelled. A discharge command is available to allow prescribed inflow or outflow of fluid to/from the grid in place of prescribed pressures.

3.2.3.4 Initial conditions

In any ground engineering problem, there exist in situ stresses in the ground that will influence the behaviour of the model. Usually for a given uniform material, vertical stresses are equal to ρgz where ρ is mass density, g is acceleration due to gravity and z is depth from the free surface. In situ horizontal stresses are often calculated using an assumed ratio between the horizontal and vertical stresses according to $v/(1-v)$ where v is Poisson's ratio. However, this assumes that gravity is suddenly applied to an elastic mass where lateral movement is prevented which rarely applies in practice. Ideally, field measurements would provide information about the in situ condition yet these are not always available.

A compromise is often made whereby stresses are installed through a combination of boundary conditions and the application of gravity throughout the grid before the model is then stepped until an equilibrium state is achieved. The model may be stepped for a range of possible mechanical conditions so long as the system is finally in equilibrium and any chosen yield criteria is not met anywhere in the grid. It is important to consider that during the stepping process, fluid flow will occur (if fluid calculation is included) in the establishing of mechanical equilibrium. Once the equilibrium state is achieved, investigative changes in the model may be undertaken.

3.2.4 Interfaces

Interfaces divide the continuum grid into regions between which slip and separation can occur subject to Coulomb sliding and/or tensile separation criteria. This facility is commonly used by finite element and finite difference programs to simulate jointing, faulting, bedding or any discontinuous feature of a material, typically a rock mass. The specific application of this facility is later discussed in Section 3.3.4.

The introduction of discontinuities in a continuum mechanics formulation includes several limitations. There is commonly a restriction placed on the complexity of interface geometries where the use of a continuum may be considered inappropriate. These include the intersection of many interfaces, an inability of the scheme to automatically recognise the contact of interface surfaces following separation or that the formulation is restricted to small interface displacements and/or rotation (ITASCA, 2002).

A discrete element code such as UDEC would traditionally be employed to model a discontinuum where the medium is represented as an assemblage of discrete blocks sub-divided into individual finite-difference elements (ITASCA, 2011). However, fluid flow is treated very differently at the discontinuities in such programs where flow is modelled through the space between impermeable blocks. The hydraulic influence on material deformation therefore originates between the blocks and cannot be modelled through the solid medium i.e. discontinuities must exist prior to flow. This issue was discussed in Section 2.7.2.1.

3.2.4.1 Formulation

The general concept used to define the plane between two mesh regions is depicted in Figure 3.5.

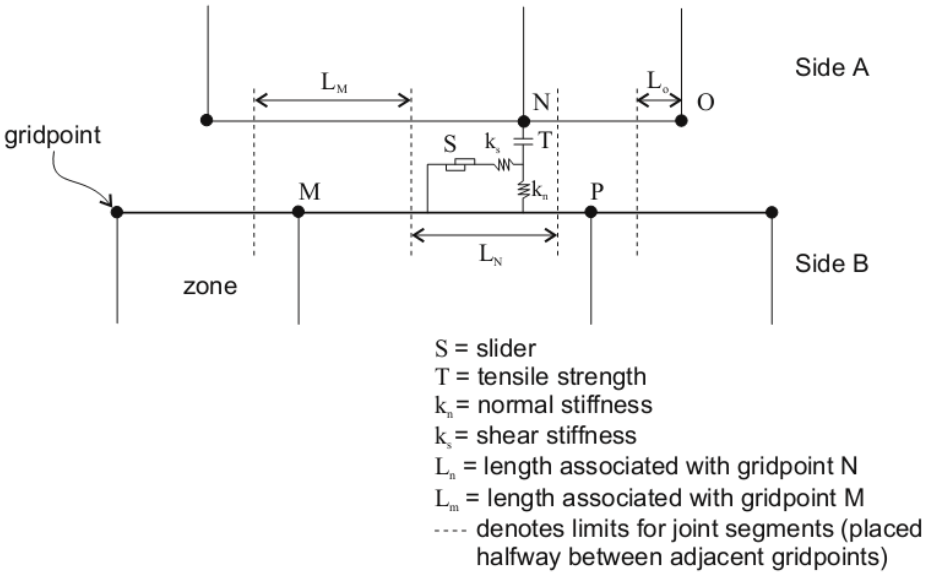

Figure 3.5 Interface between sides A and B (after ITASCA, 2002)

Grid-points positioned on both sides of the interface are recorded and checked for contact with their opposing neighbour. If for example, point N in Figure 3.5 is found to lie on the segment between points M and P, then the vector normal to the interface is calculated. In addition to this, the length, L, is defined as half the distance to the nearest grid-point to the left (regardless of whether this grid-point is on the opposite or same side) plus half that to the right. It is by this method that the interface is divided into connected segments.

For each segment of the plane, the velocity of the associated grid-point is computed per time-step. Using the relation between velocity and displacement per time-step, the incremental displacement, and therefore force, is calculated and resolved into the normal and shear directions. For further details regarding the interface formulation, see (ITASCA, 2002).

3.2.4.2 Slip/Separation modes

There are three modes of operation available for a given interface:

1. **Glued** – The interfaces are declared glued and so neither slip nor separation is allowed. Elastic displacements are still accommodated subject to the stiffness of the interface.

2. **Coulomb Shear-Strength** – The interface is able to accommodate slip according to the Coulomb shear-strength criterion:

$$F_{smax} = cL + \tan\phi\, F_n \qquad \textbf{3.47}$$

Where c = cohesion (Pa), L = effective contact length (Figure 3.5), ϕ = friction angle and F_{n} = effective normal force on the interface. The criterion for interface slip is satisfied if the shear force F_s = F_{smax} (with sign of shear preserved). Dilation may be accommodated by specifying a dilation angle, ψ. Dilation will increase if the displacement increment direction is the same as the total shear displacement and vice versa if the directions are opposite.

3. **Tension Bond** – The interface may be declared bonded subject to a tensile strength criterion:

$$\sigma_n{}' \leq \sigma_{tbond} \qquad (bonded) \qquad \textbf{3.48}$$

$$\sigma_n{}' > \sigma_{tbond} \qquad (un\text{-}bonded) \qquad \textbf{3.49}$$

   For so long as the magnitude of tensile normal stress is below or equal to the specified tensile bond strength, the interface behaves bonded and responds elastically subject to the interface stiffness (Equation 3.48). However, should the magnitude of the tensile normal stress exceed the bond strength, then the bond will break allowing the interface segment (Figure 3.5) to behave un-bonded (separation and slip allowed).

Slip may be included to occur prior to segment separation with shear yield controlled by friction, cohesion and the effective normal force. Alternatively, shear bond strength may be specified and works much as Equations 3.48 and 3.49 for tensile bonds, both criteria may be applied to the same interface. By default, shear bond strength is set to x100 that of the tensile bond strength.

Interface properties are used to moderate the above modes of operation and control the behaviour of interfaces. Properties comprise: the friction angle, cohesion (shear bond strength), tensile (bond) strength and stiffness in both the normal and shear orientations as depicted in Figure 3.5. It is important to note that in using the effective normal and shear stresses in the yield criteria for the aforementioned interface behaviour modes, the effect of pore pressure in the generation of stress either side of the interface is included.

3.2.4.3 Creation of interface geometry

When placing interfaces, a methodical approach to the construction of the final geometry must be taken. For example, the following steps have to be taken to place a single horizontal interface within a rectangular mesh as depicted in Figure 3.6:

1. When generating the initial mesh, additional element rows/columns are included in the location and orientation of the desired final position of the

interface (Figure 3.6a). It must be remembered that the final geometry will be an element width smaller normal to the interface.

2. The mesh is then divided into two regions, distinct from one another by the element thick region. The row/column designated as the interface is then defined using the null constitutive model, effectively deleting the elements (Figure 3.6b).
3. The remaining mesh regions are then juxtaposed in (i,j) space. However, these regions are still considered materially discrete. Finally, the two sides are joined by defining an interface relating to the adjacent grid-point ranges (Figure 3.6c).

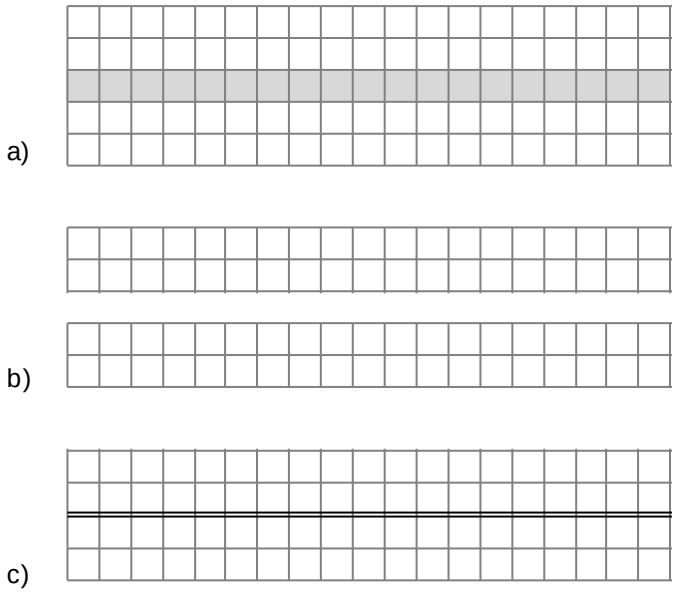

Figure 3.6 Interface geometry assembly: (a) additional element row, (b) separation of mesh by null region and (c) final geometry including interface.

Interface geometries are restricted to straight lines by the boundaries created between elements. It is possible to create the effect of intersecting interfaces, though interfaces either side are defined separately. It is recommended by the FLAC manual (ITASCA, 2002) that the program UDEC be used where complex interface geometries are to be prescribed. However, in FLAC simple repetitive geometries are easily created using a bespoke FISH function.

3.2.4.4 Interface properties

Material properties are given to the entire length of an interface according to the modus operandi. For example, properties may be assigned on the basis that the

interface is glued, thus allowing no slip or separation to occur. Where slip is to be modelled, shear properties are provided representative of the physical case though properties normal to the interface may be prescribed artificially high to negate separation. Slip is accommodated despite the interface remaining bonded where yield is controlled by the input friction angle and cohesion values. Alternatively, physically representative values of tensile strength and normal stiffness may be required in the case of separation. Such physically based values have been determined in Section 3.3.4.

Property values for cohesion, friction angle and tensile strength may be constrained experimentally using laboratory tests. Interface shear and normal stiffness may also be determined experimentally; however, their magnitude is important in relation to mass scaling and this therefore influences solution convergence. Consequently, recommended maximum stiffness may be calculated by:

$$k_n \; and \; k_s = \left[\frac{\left(K + \frac{4}{3} G \right)}{\Delta z_{min}} \right] 10 \qquad \textbf{3.50}$$

where, K and G are continuum elastic moduli bulk and shear respectively and Δz_{min} is the smallest adjoining zone width (ITASCA, 2002).

3.3 Model development

The facilities available in using FLAC and their associated operating procedure have been examined in Section 3.2. The following section will outline the features included in the development of the cracking model. Firstly, laboratory experiments are presented; these were aimed at informing the development of the numerical model in terms of boundary conditions, material properties, drying conditions and typical cracking behaviour. Next, the systematic building of the model is considered including the generation and processing of data used to capture the various aspects of the clay behaviour undergoing drying. Finally, initial conditions are presented prior to the onset of the applied drying condition.

3.3.1 Indicative laboratory experiment

The model developed in this work was based on the desiccation of compacted fill in the laboratory. This approach was selected due to the scale of the processes under investigation and to better constrain the physical boundary conditions of the problem. Indicative laboratory experiments were conducted collaboratively with Dr Zhang Dingwen, a Visiting Fellow from Southeast University, School of Transportation, China during 2011. These were designed to inform various aspects of the numerical model; for example, water loss was determined on the basis of mass loss and enabled discharge rates to be calculated (Section 3.3.6.2). An overview of the experiments is provided here.

The clay was compacted into steel moulds of semi-circular cross-section approximately 10 times larger than moulds used for linear shrinkage testing according to BS 1377-2 (British Standards, 1990) while retaining the same length-width ratio, as illustrated in Figure 3.7. It was observed during preliminary testing that the dominant mode of shrinkage upon drying was that of free, linear shrinkage with no substantial cracking despite no lubrication of the mould being used. The requirement of a frictional boundary condition for the formation of cracking is consistent with a number of previous studies (Peron et al., 2009; Kodikara et al., 2004). For this reason, the suite of experiments was conducted using an interior mould surface coated with coarse sand that was fixed with contact adhesive as shown in Figure 3.7.

A total of 5 experiments were conducted subject to a range of environmental conditions designed to establish an appropriate drying flux (Table 3.1). Engineered fill sourced from the trial embankment at Nafferton Farm, near Newcastle (Hughes et al., 2007) was hand sieved to <20mm in order to remove coarse gravel and any substantial organic matter i.e. large roots. This was then air dried on a bench top before being wetted up to an initial water content of between 20-25% and allowed to equilibrate for a period of 48hrs. The soil was then compacted in three layers using a 2.5kg hammer to achieve a desired dry density (i.e. M_{dry}/V). This was based upon core cut samples of the in situ embankment fill which were found to have an average dry density of 1.65 Mg/m^3, wet of optimum (15% OMC) at a depth <1m from the surface.

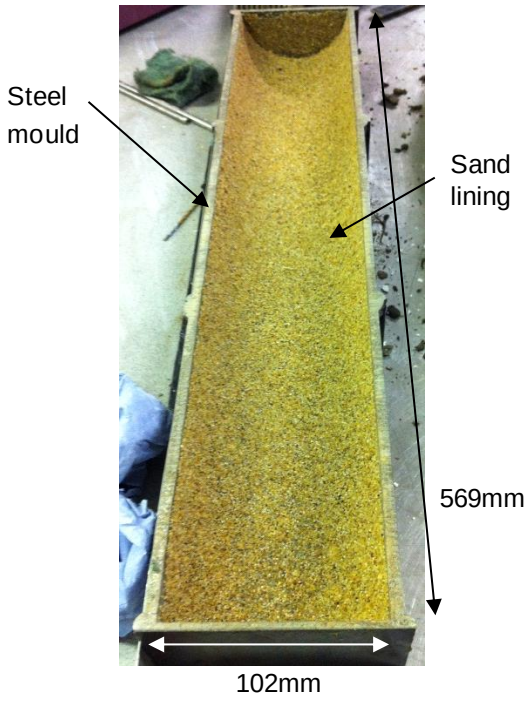

Figure 3.7 Steel mould with sand lining.

Table 3.1 Indicative laboratory test conditions.

Test number	Initial gravitational water content	Dry density (Mg/m^3)	Mean temperature (°C) [Std. deviation]	Test duration (hours)
1	25	1.61	49.4 [0.9]	161
2	20	1.68	50.9 [0.6]	168
3	23	1.66	51.5 [1.2]	144
4	21	1.62	71.3 [2.6]	144
5	23	1.61	103.4 [3.2]	144

A pair of experiments is presented in Figure 3.8 after drying for 6 days. Cracking was observed normal to the longitudinal axis and predominantly initiated at the mould edges, propagating across the centre before extending vertically. Crack initiation is thought to take place at the edges due to the greater influence of the frictional constraint offered by the mould contact at relatively shallow depth due to the semi-circular cross-section. One-to-two dominant cracks were found to extend to the mould base (considered as the vertical radius of the mould) with secondary cracking dividing the clay over the remaining segments. The term ‘sequential filling’ has been used to describe such behaviour (Peron et al., 2013). The series of photographs presented in Figure 3.9 shows the typical shrinkage and crack development. After one hour crack initiation may be seen to have started at the contact between the clay and the coarse mould interior. However, at 17 hours cracks are seen to extend the full width of the clay in addition to shrinkage away from both the ends and longitudinal edges of the mould. Little change is found to have taken place between 17 and 24 hours indicating that the maximum shrinkage potential of the clay due to drying has been reached and the final extent of cracking has formed.

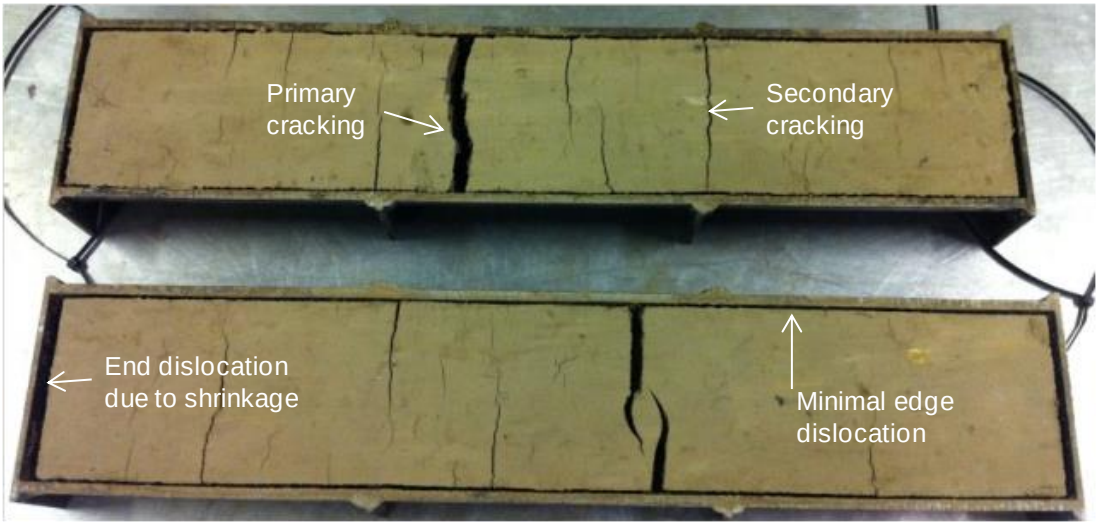

Figure 3.8 Photograph of final cracking in tests 3 (top) and 4 (bottom).

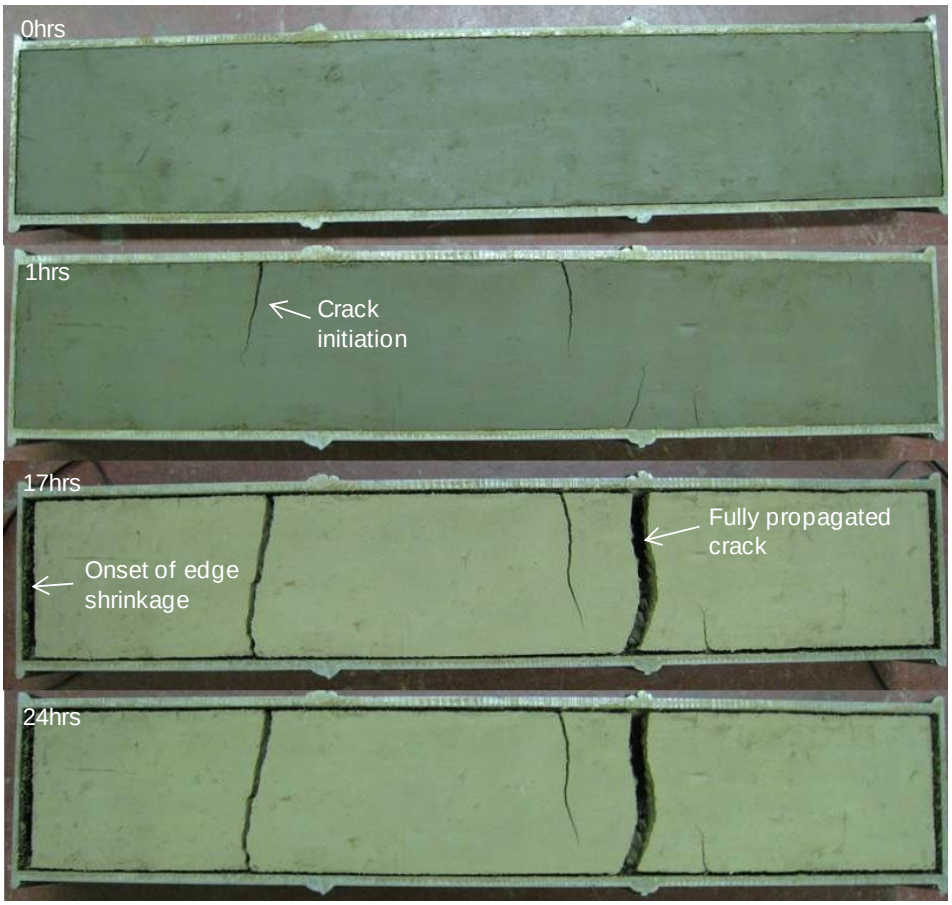

Figure 3.9 Typical shrinkage and crack pattern development (test 5).

3.3.2 Grid geometry

The grid designed to represent the modelled problem is based on the geometry of the mould used in the laboratory experiments. A simple schematic is presented in Figure 3.10.

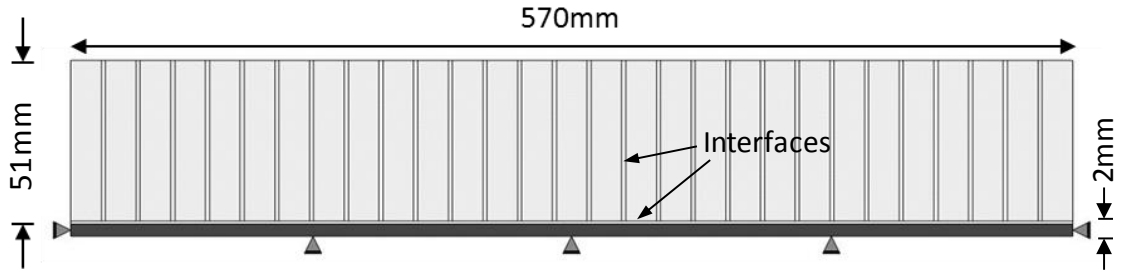

Figure 3.10 Geometry of the model mesh

The grid comprises two regions; the clay medium and the steel mould. The mould was included to enable the inclusion of basal restraint, an identified principle factor in the generation of tensile stresses within a shrinking soil mass (Hu et al., 2006; Peron et al., 2009). In order to be able to model shear behaviour at the clay-mould contact, 95 horizontal interface elements form a continuous plane between the mould and clay regions. The method of interface element installation, described in Section 3.2.4.3, required there to be grid-points positioned either side of the interface. Hence, it was necessary to include the mould in the problem. The modelled mould consists of a 190(L) x 2(D) element region located at the bottom of the grid.

The majority of the grid represents the clay fill component and comprises 190(L) x 17(D) quadrilateral elements. The dimensions in Figure 3.10 correspond to the central cross-section through the filled mould. Hence, a single element constitutes 3mm^2.

In addition to the horizontal interfaces, 94 vertically orientated interfaces pervade the clay grid. These discontinuities have been included to allow the grid to divide according to the development and distribution of normal effective stress. In this way, the interfaces have been used to simulate potential cracking loci. It is recognised that this method prescribes possible crack locations and is therefore limiting in terms of crack spacing and orientation. In using a continuum code, it is not possible to allow the grid to divide at any location not subject to

an interface facility. Initial geometry trials placed interfaces at single element intervals, this did not allow zone variables to be correctly plotted and so the interval spacing was corrected to two elements. In the course of conducting indicative laboratory tests, the observed crack trend was for sub-vertical cracks to form with a minimum spacing of approximately 15mm. It is accepted that the size of the mould and hence the relative scale of the clay block to frictional boundaries will heavily influence the extent of the generated crack trend e.g. small/shallow desiccation tests produce more closely spaced crack patterns. In this case, the interface spacing of 6mm is therefore considered suitable to capture the spacing of cracks to an acceptable degree of accuracy.

The internal programming language, FISH allowed a grid generation function to be developed that specified the generation of the required grid components and subsequent interface installation.

3.3.3 Constitutive parameters

The continuum properties are dependent upon the constitutive model used to govern the stress-strain response of the material.

The clay was assumed to behave elastically during the drying process, this is essentially a single loading direction where upon unloading, all deformation is recoverable. Within FLAC, the linear elastic model was used to form the basis of the final model employed. The in-built isotropic elastic model is expressed by Hooke's law and an incremental form is provided:

$$\Delta\sigma_{11} = \alpha_1 \Delta\varepsilon_{11} + \alpha_2 \Delta\varepsilon_{22}$$

$$\Delta\sigma_{22} = \alpha_2 \Delta\varepsilon_{11} + \alpha_1 \Delta\varepsilon_{22}$$

$$\Delta\sigma_{12} = 2G\Delta\varepsilon_{12} \qquad (\Delta\sigma_{21} = \Delta\sigma_{12}) \tag{3.51}$$

$$\Delta\sigma_{33} = \alpha_2(\Delta\varepsilon_{11} + \Delta\varepsilon_{22})$$

where, $\alpha_1 = K + (4/3)G;$

$\alpha_2 = K - (2/3)G;$

$$\Delta\varepsilon_{ij} = \frac{1}{2}\left[\frac{\delta\dot{u}_i}{\delta x_j} + \frac{\delta\dot{u}_j}{\delta x_i}\right]\Delta t \quad \textbf{3.52}$$

where, $\Delta\varepsilon_{ij} = \text{incremental strain tensor};$

$\dot{u}_i = \text{displacement rate.}$

$\Delta t = timestep$

Due to the finite out-of-plane dimension of the clay confined within the mould, plane-stress conditions are assumed. The incremental form of the elastic model is provided for plane-stress conditions:

$$\begin{aligned} \Delta\sigma_{11} &= \beta_1\Delta\varepsilon_{11} + \beta_2\Delta\varepsilon_{22} \\ \Delta\sigma_{22} &= \beta_2\Delta\varepsilon_{11} + \beta_1\Delta\varepsilon_{22} \\ \Delta\sigma_{12} &= 2G\Delta\varepsilon_{12} \qquad (\Delta\sigma_{21} = \Delta\sigma_{12}) \\ \Delta\sigma_{33} &= 0 \end{aligned} \quad \textbf{3.53}$$

where, $\beta_1 = \alpha_1 - (\alpha_2^2/\alpha_1)$; and

$\beta_2 = \alpha_2 - (\alpha_2^2/\alpha_1).$

As indicated in the above equations, bulk, K and shear, G, moduli are required and control the elastic deformation of the modelled material. These parameters are derived from the Young's modulus, E, and the Poisson's ratio, v (ITASCA, 2002):

$$K = \frac{E}{3(1-2v)} \quad \textbf{3.54}$$

$$G = \frac{E}{2(1+v)} \quad \textbf{3.55}$$

where,

$$E = \frac{\sigma_a}{\varepsilon_a} \quad \textbf{3.56}$$

and,

$$v = \frac{\varepsilon_r}{\varepsilon_a} \quad \textbf{3.57}$$

where, $\sigma_a = \text{axial stress};$

$\varepsilon_a = \text{axial strain (i.e. parallel to axial stress); and}$

$\varepsilon_r = \text{radial strain (i.e. normal to axial stress).}$

However, it is accepted that as the clay undergoes drying, the material stiffness increases. For this reason, the built-in elastic model was modified using FISH to account for non-linearity by controlling the Young's modulus of the material as a function of soil-water content, ω. This relationship for the Nafferton clay was constrained using experimental results from constant water content triaxial testing as described by Fredlund et al. (1993) and conducted by Mendes (2011). The secant moduli were calculated at the 50% maximum deviatoric stress and corresponding axial strain and are presented in Figure 3.11.

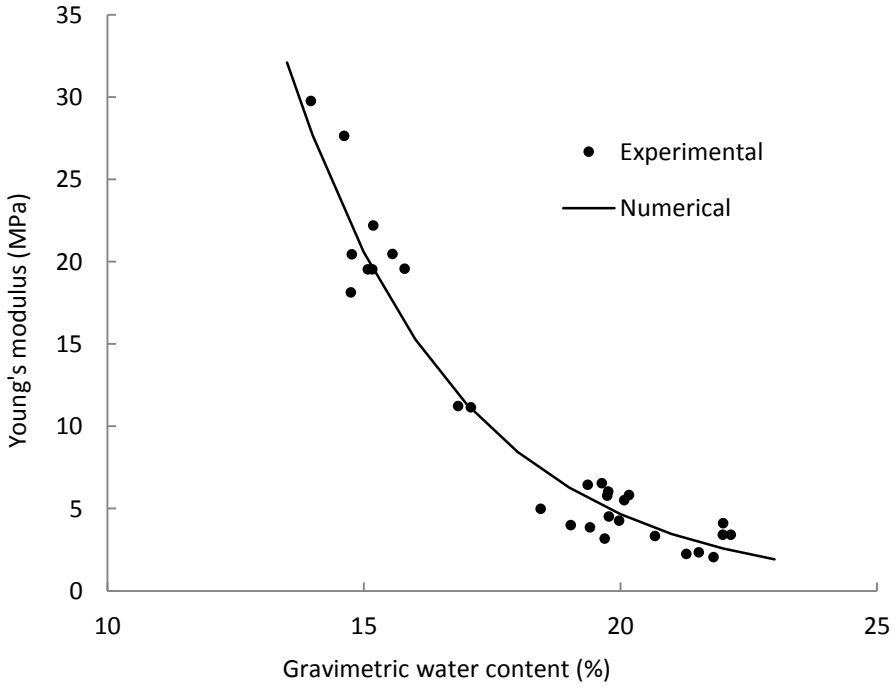

Figure 3.11 Young's modulus relationship to soil water content.

An exponential trend has been fitted to the above data and gives the following expression:

$$E = 1770\, e^{-0.297\,\omega} \quad \textbf{3.58}$$

where, $\omega = \text{gravimetric water content.}$

Through Equations 3.54 and 3.55, $E(\omega)$ is substituted and updated each time-step for all elements of the mesh using a constant, typical stiff clay Poisson's ratio of 0.3.

The non-linear elastic model implemented accounts for the empirical increase in soil stiffness upon progressive drying. However, this is only considered appropriate to the single drying path. Upon re-wetting and any subsequent cycles of drying and wetting, irrecoverable strains will not be captured. This is a considerable limitation to the application of the employed function, although subsequent prescription of hysteretic or cycle number dependent stiffness functions may be incorporated using a similar procedure.

In addition to the elastic moduli, the mass density is required to be specified. As the modelling conducted in this work includes the fluid calculation, a dry density is used where FLAC internally computes the saturated density of each element according to the porosity, saturation and density of water, described in Section 3.2.2. The initial dry density of the soil was 1.65Mg/m^3; this was based upon data from samples taken from the trial embankment (Hughes et al., 2007).

3.3.4 Interface parameters

Interface properties are assigned based on the required function of the interface. The interfaces that are included in the crack model geometry perform two distinct, real functions and therefore require very different property types and magnitudes to be specified. These are described individually in the following sub-sections.

3.3.4.1 Crack interfaces

Interfaces were placed vertically throughout the grid at 2mm spacing as illustrated in Figure 3.10. The purpose of these interfaces was to enable the simulation of crack initiation and propagation. The criterion considered here was

that of a ‘tension bond’ (Section 3.2.4.2) where the interface behaves bonded and deforms elastically while the tensile normal effective stress is below or equal to the tensile strength. Therefore, cracking is initiated when the normal tensile stress adjacent to the interface exceeds the tensile strength assigned to that interface.

The failure of the tension bond is therefore highly dependent on the specified tensile strength parameter. The magnitude of tensile strength, σ_t is recognised to vary with soil-water content (Heibrock et al., 2003; Nahlawi et al., 2004; Tamrakar et al., 2005; Trabelsi et al., 2010). However, there currently exists no standard method of determining this relationship and so a method has been proposed as part of this thesis and is presented in detail within Chapter 4. In developing the laboratory apparatus and method, tensile strength testing was conducted on samples of Nafferton clay at a range of water contents. For details of the Nafferton clay testing procedure, please see Section 4.4.2. The collated data is presented in Figure 3.12.

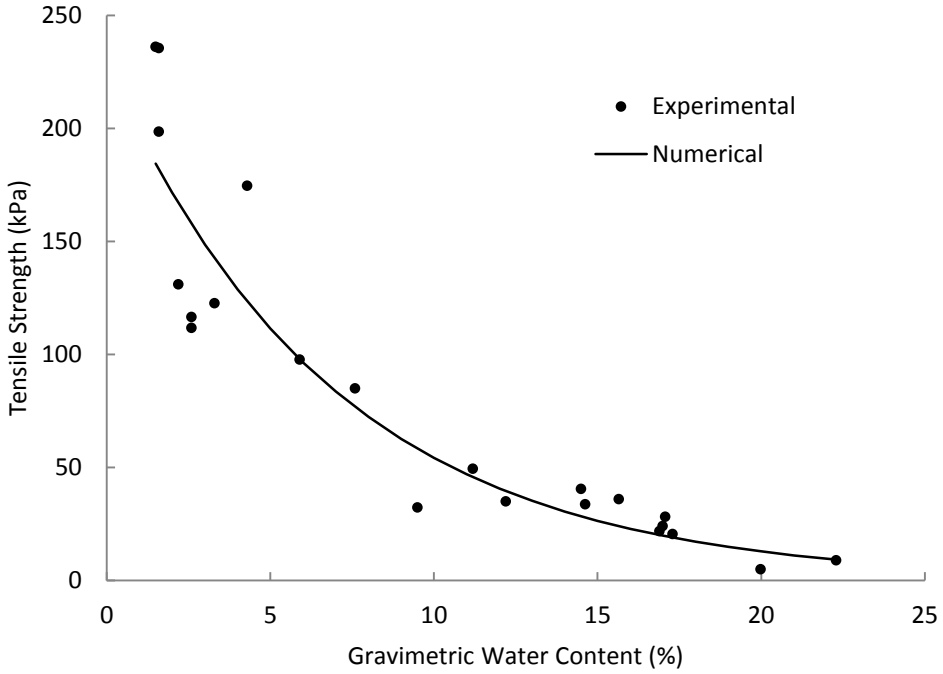

Figure 3.12 Tensile strength change with varied soil-water content

An exponential trend line has been fitted to the above data and provides the following expression:

$$\sigma_t = 228.85e^{-0.14\omega} \quad \textbf{3.59}$$

This expression is seen to fit the data with decreasing accuracy at lower water contents where there is greater variability in the data in drier conditions. Drier samples from a batch compacted at consistent water content undergo a period of drying during which it is believed that the micro-scale structure of the sample changes. The dominant change is shrinkage where micro-cracks are understood to form. The formation of these randomly orientated flaws in the sample is thought to contribute to the greater variability in failure strength during testing. A series of strength vs. water content experiments were performed at different strain rates to investigate the influence upon this error. However, the data presented is the best constrained relationship and was therefore adopted for the purposes of model development.

As with any parameter assigned to an interface, the tensile bond strength is applied to the entire length of the interface. Hence, when updating the bond strength, the point on the interface at which soil-water content is queried is understood to affect the value assigned according to the established empirical expression. As the applied drying flux (further described in Section 3.3.6.2) acts predominantly from the upper surface of the grid, it is reasonable to assume that the greatest normal tensile stress acting on the vertical interface will be experienced at the uppermost grid-point pair along the interface. Consequently, the interface is repeatedly assessed for separation on the basis of an x-displacement threshold for corresponding grid-point pairs at the upper surface.

In addition to the variation of each interface tensile bond strength with water content, variability in soil strength throughout the grid was also included using a normally distributed random number facility about the mean where the mean was set as the experimentally derived value. This degree of variability was included because uniform strength leads to a situation where tensile stress throughout the entire mesh simultaneously exceeds the strength of each interface resulting in regular interface separation of minimal displacement. This behaviour is recognised as being unrealistic and so an effort to capture the

inherent heterogeneity of the compacted clay was considered physically reasonable.

Given the physical behaviour to be captured in the use of the vertical interfaces, the friction angle and, in this case tension bond strength, are important and the elastic stiffness is less significant (ITASCA, 2002). A 26° angle of friction was measured by the standard direct shear test, BS1377-7 (British Standards, 1990). Within the model, this parameter is considered independent of the soil-water content and remained constant. This is in agreement with the interpretation of partially saturated shear strength tests (e.g. Ho & Fredlund (1982), Fredlund & Rahardjo (1985)) by Alonso et al. (1990) noting "…that an increase in suction results in an increase in effective cohesion while maintaining constant the (saturated) friction angle." (pp407-408). However, apparent friction will be modified by changes in effective normal stress brought about by changes in pore pressure. Stiffness has a direct bearing on the solution response and so the magnitude of given values require careful consideration. The FLAC user guide states the general rule-of-thumb that for real interfaces (allowed to slip/separate) the interface stiffness k_n and k_s should be set to ten times the respective stiffness of the stiffest neighbouring element. Since these neighbouring moduli are ultimately dependent on the saturation condition of the element, interface stiffness is also governed by saturation and repeatedly updated during calculation cycling. As the intended behaviour of the interface is separation, the tension bond criterion is applied where the shear bond strength remained at the default value of 100 times the tension bond strength (ITASCA, 2002).

3.3.4.2 Base interface

The shear properties of the soil-mould contact are widely accepted to have a great influence on the shrinkage/cracking behaviour of laboratory drying tests (Peron et al., 2009) and were shown to be the case in the indicative experiments (Section 3.3.1).

Interfaces used to represent the mould-sample contact were considered to behave according to a shear bond criterion (Section 3.2.4.2). Therefore, a friction angle and shear bond strength are required to be defined. These

properties were measured by experimental means using a second modification to the standard direct shear apparatus. As opposed to the standard shearing across a predetermined plane about the vertical centre of the sample, the sample-mould system was sheared about the contact plane. As illustrated in Figure 3.13a, the lower half of the shear-box was replaced by a steel plate with an identical surface to that of the inside of the mould. This results in the laterally restrained sample being sheared along the plane defined by the surface of the mould plate. Vertical load and shear force were applied and recorded according to BS1377-7 (British Standards, 1990). An example of the sample following testing is shown in Figure 3.13b where slickenside features may be seen across the upturned sample surface.

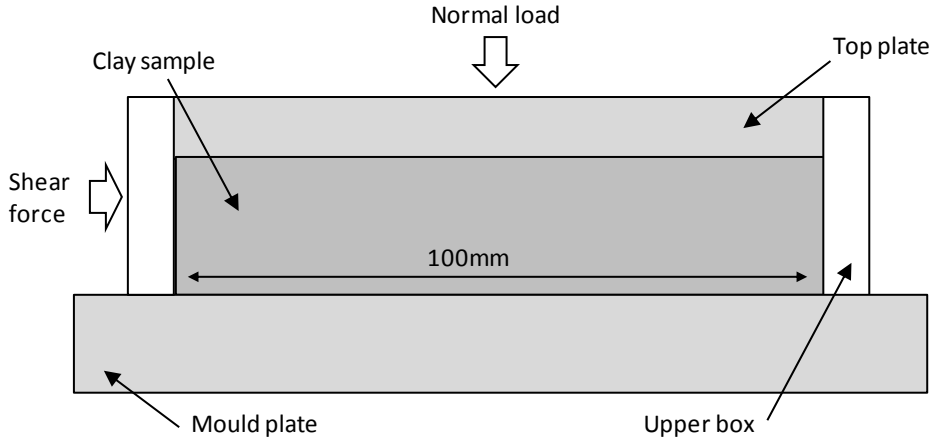

a)

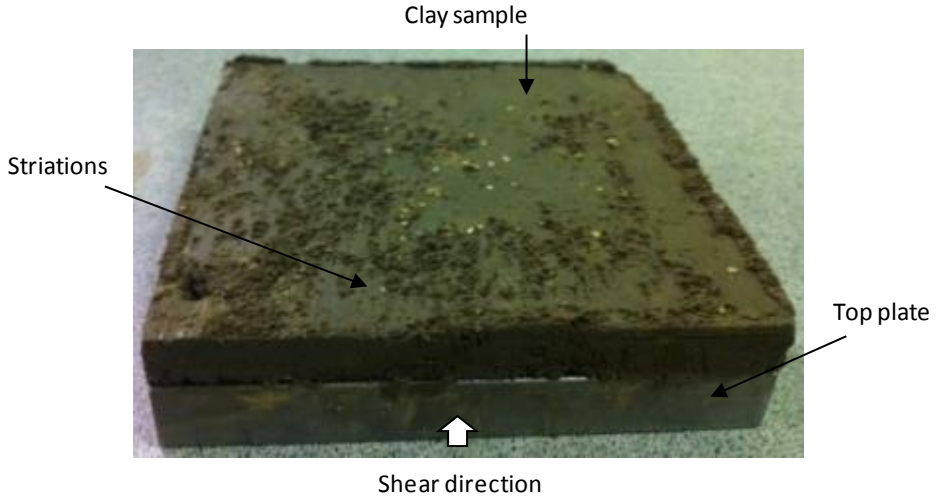

b)

Figure 3.13 Modified shear box (a) schematic of modification and (b) example sample post-test.

A series of typical shear stress-strain results for a Nafferton clay sample at ~17% gravimetric water content is presented in Figure 3.14. As would be expected, for increased applied normal stresses, the recorded maximum shear stresses increase. Final shear stress values are consistent for strain between 3% and 7% where the clay is believed to be under continuous, smooth sliding conditions against the mould plate. Initial strain values at zero stresses is the product of the period preceding carriage contact with the loading pin and hence no shear stress was transmitted across the sample-plate interface during this time.

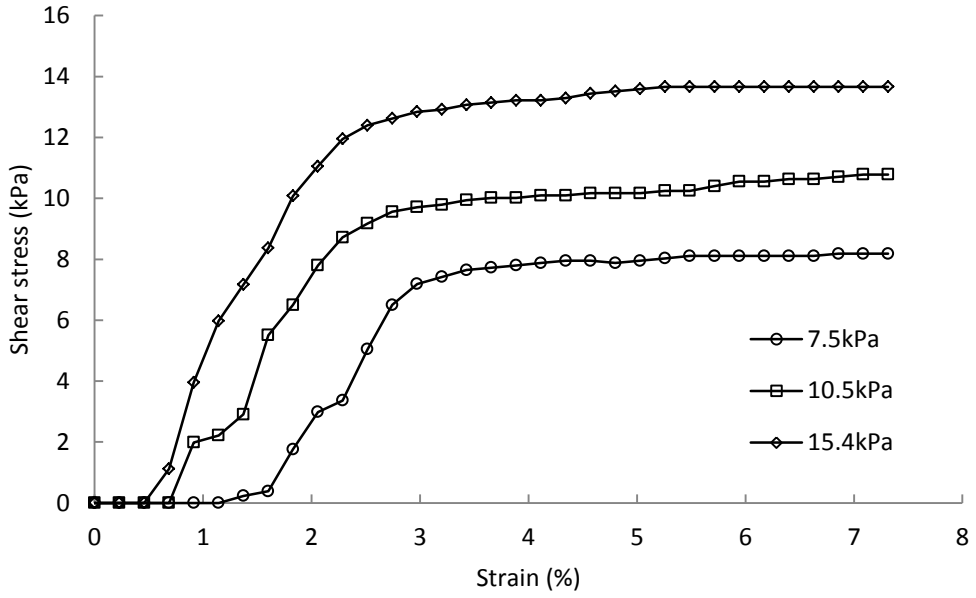

Figure 3.14 Shear stress plotted as a function of shear strain.

For the same series of tests, the maximum shear stresses have been plotted against the corresponding normal stress in Figure 3.15. A reasonable linear correlation may be seen, using this regression a cohesion value of 3.2kPa has been obtained. This procedure was conducted for a total of 8 water contents 10-28%. A friction angle of 35° ±2.3° was measured and applied as a constant to the base interfaces.

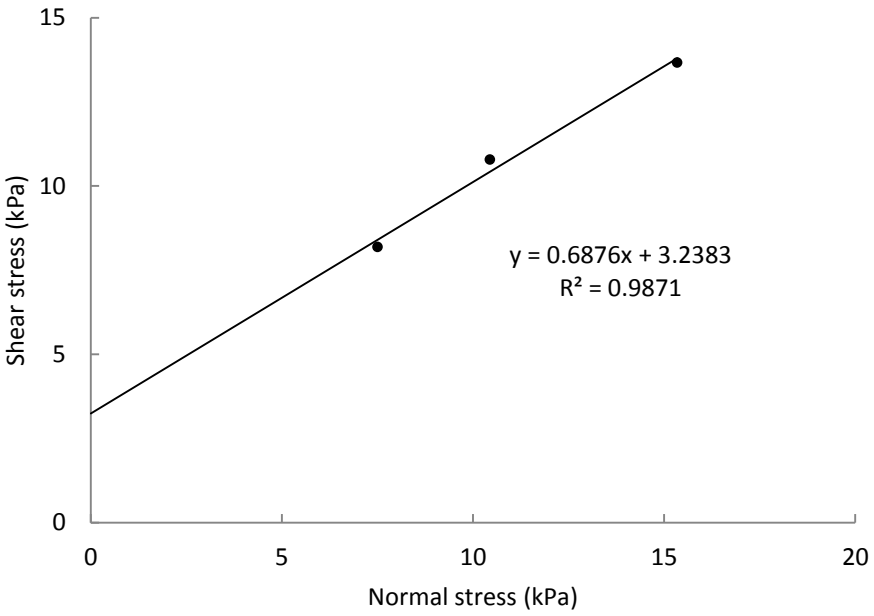

Figure 3.15 Shear stress plotted as a function of normal stress.

Given the relatively shallow depth at which the mould-clay interface is positioned in the bench-top experiments, the shear strengths for various soil-water contents taken at zero confining stress have been collated and are presented in Figure 3.16. The function given in Equation 3.60 has been fitted to the experimental data and was input to the model using FISH, parameter values are provided in Table 3.2. The clay water content of the lower grid elements is used to control the shear bond strength of the neighbouring interface segment. The expression describes a gradual loss of shear strength with drying. At water contents below ~10%, minimum bond strength of 0.3kPa represents the residual bond between the mould and the dislocated, desiccated clay block.

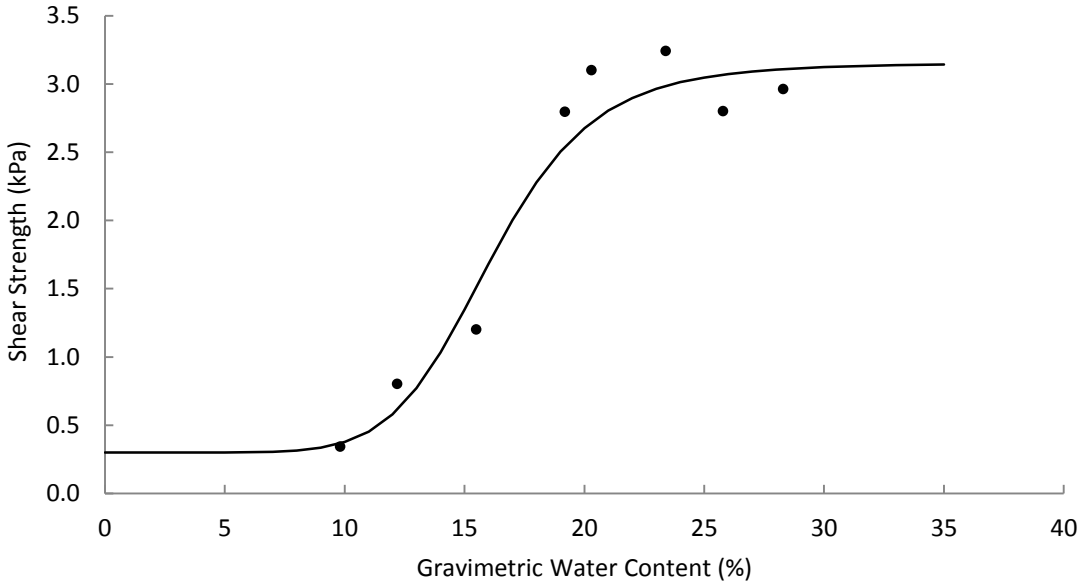

Figure 3.16 Mould-clay contact shear strength with clay water content relationship

$$C = a + \left[\frac{(b-a)}{1 + c\omega^{d}}\right] \qquad \textbf{3.60}$$

where, $C = \text{shear strength (kPa)}$

$\omega = \text{water content (\%)}$

$a, b, c, d = \text{curve fitting coefficient}$

The shear stiffness of the mould-clay interface behaves in a very different manner to the stiffness of the soil continuum. Shear stiffness has been shown to increase with drying, much as would be expected from Figure 3.11. During this time, apparent cohesion increases. However, as presented in Figure 3.17, when the clay is dry of approximately 15%, the stiffness of the mould-clay interface is found to decrease. This is the result of the loss in apparent cohesion brought about by the continued removal of water and the reduced effect of capillary pressure. A residual value again correlates to the dislocation of the desiccated clay from the mould surface. Such behaviour is similar to that observed by Nahlawi (2004) (cited in Amarasiri et al., 2011). The expression provided in Equation 3.61 has been implemented in a FISH function based on the water content at the base of the grid, parameter values are provided in Table 3.2.

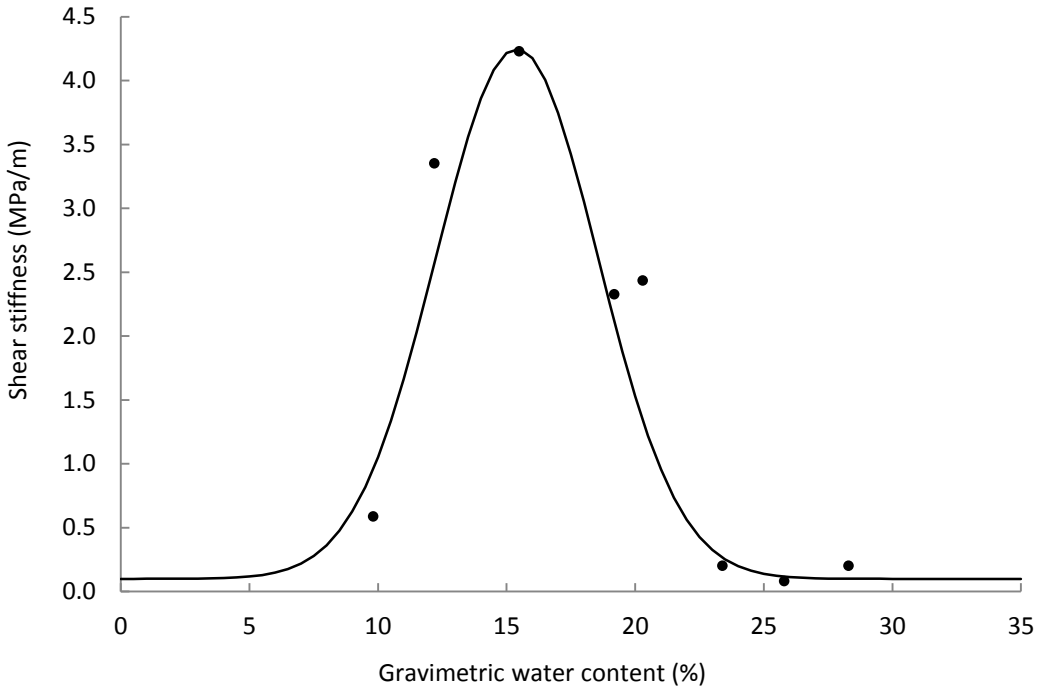

Figure 3.17 Mould-clay contact shear stiffness with clay water content relationship

$$G = me^{-\frac{\left(\frac{\omega}{n}-p\right)^2}{2q^2}} \quad \textbf{3.61}$$

where, $G =$ shear stiffness (kPa/m)

$m, n, p, q =$ curve fitting coefficient

Table 3.2 Basal shear parameter summary

	Parameter	Value
Shear strength	Peak strength, a	3.15 kPa
	Residual strength, b	0.3 kPa
	Fitting coefficient, c	6.2×10^{-2}
	Fitting coefficient, d	7.5
Shear stiffness	Peak stiffness, m	4.15 MPa/m
	Fitting coefficient, n	35
	Fitting coefficient, p	0.44
	Fitting coefficient, q	0.09

3.3.5 Hydrological parameters

In implementing the tp-flow calculation in FLAC, the hydrological properties of the clay are required and were established predominantly by experimental means. The majority of these properties refer to the van Genuchten expression that relates the level of soil saturation to suction and unsaturated permeability (van Genuchten, 1980). The van Genuchten parameters for the clay were obtained from the soil water retention curve that was derived using the Filter Paper Technique according to the methodology described in ASTM D5298-10 (ASTM, 2003). These data are shown in Figure 3.18 alongside the fitted van Genuchten approximation implemented. Porosity is deemed equal to the saturated volumetric water content. The residual saturation is by default 10^{-5} and acts to limit the negative pore pressure that will be generated. Based on the SWRC presented, a larger residual saturation value was included and is given alongside the other van Genuchten parameter values in Table 3.3.

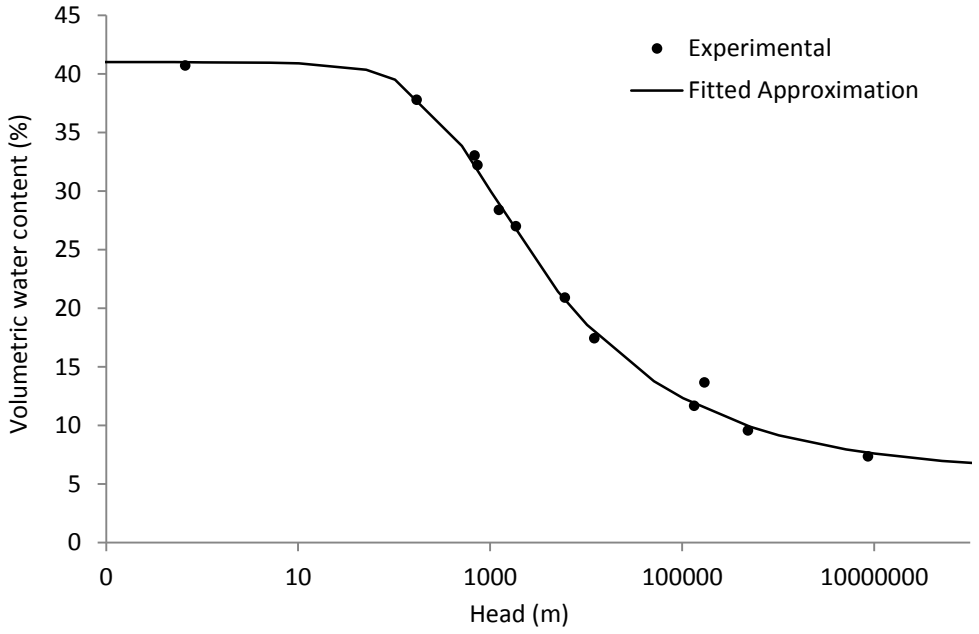

Figure 3.18 Nafferton clay soil-water retention curve.

Table 3.3 FLAC tp-flow parameters

Porosity	0.41
Residual Saturation	0.15
P_o*	3.6×10^5 Pa
a*	0.231
b*	0.5
c*	0.5
Viscosity ratio (wet/non-wet)	100†
Fluid bulk modulus (wetting)	10^6 Pa (or 10^3 Pa)
Fluid bulk modulus (non-wetting)	10^3 Pa (or 1 Pa)

*van Genuchten SWRC fitting parameters [Section 3.2.5.3]

† **(Fredlund & Rahardjo, 1993)**

The saturated mobility coefficient input to FLAC was calculated using the saturated hydraulic conductivity, acceleration due to gravity and density of water according to Equation 3.10. However, the confident selection of an appropriate single saturated hydraulic conductivity value was very difficult. As has been described in Chapter 2, the conductivity of embankment fill is widely recognised to be a highly variable property both spatially (e.g. with respect to slope aspect, depth, height, proximity to known macro-features) and temporally (e.g. seasonally and with respect to antecedent soil-water conditions and embankment consolidation). To illustrate such variability, Figure 3.19 shows hydraulic conductivity values measured during the period 2009-2012 across the trial embankment at Nafferton. Measurements were taken at a number of different depths using a Guelph permeameter (constant head test) at sites presumed to be clear of cracks/fissures and in known proximity to such features. As shown in the plot, the range in values is found to reduce with increased depth from an approximately 5 order range at the very near surface. As would be expected, tests conducted near to known crack locations show high permeability compared to values at below a metre depth. Importantly, tests conducted at sites thought to be absent of cracks show a highly comparable variability suggesting possible hidden crack networks.

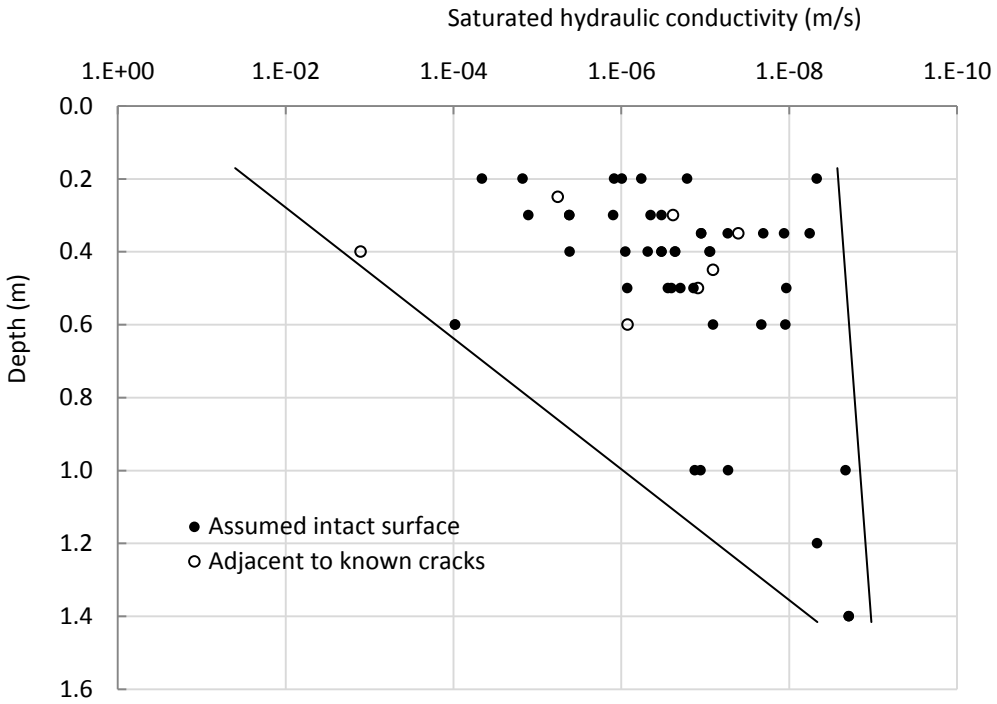

Figure 3.19 Permeability measured at the trial embankment during the period 2009-2012.

The viscosity ratio (μ_w/μ_g), is used within FLAC tp-flow (Equation 3.34) in place of individual fluid viscosities. An increase in this ratio results in increased flow rate for the non-wetting (air) phase relative to the wetting phase. It has been determined experimentally that the viscosity of air is roughly 100 times less than the viscosity of water (Fredlund & Rahardjo, 1993). Therefore, it follows that air within the model will flow much more readily than water and so air pressure will dissipate rapidly.

The modelling approach taken is fully coupled and so consideration of the relative bulk moduli of the fluids with respect to one another as well as to the porous medium must be made. As the non-wetting bulk modulus cannot be zero, the default value is defined as 10^{-3} x wetting bulk modulus. The bulk modulus of pure water at room temperature is 2.2×10^9 Pa. However, soil pore water contains dissolved air which will reduce the apparent bulk modulus. Since the specified bulk modulus of any material in the system influences solution speed, a value of 10^6 Pa has been used. It is important that the bulk modulus of water is significant during coupled calculation so that water remains incompressible in comparison to the porous media. For mechanical coupling, an

undrained coefficient of unity is included to account for the pore pressure increment generated by volumetric straining.

Given the two distinct regions in the model grid geometry, fluid flow properties were divided into two categories based on whether or not flow was to be simulated. Coupled mechanical-fluid flow modelling was desired for the region of the grid representing the clay; however, the mould grid was to take no part in the flow simulation. To achieve this, the mobility coefficient (FLAC ‘permeability’) in the mould grid was set to zero. Additionally, wetting fluid pore pressure at grid-points making up this region of the grid were set and fixed at zero.

3.3.6 Boundary conditions

3.3.6.1 Mechanical boundaries

The grid used to simulate the clay was bounded at its lower edge by the additional grid used to represent the steel mould which was fixed in ij-space. The mould essentially provides a fixed y-displacement boundary condition to the lower side of the clay grid where x-displacement is considered free although subject to shear resistance provided by the inclusion of basal interfaces.

The upper and lateral boundaries of the clay grid remained free and in doing so allowed the grid to deform in any direction at these boundaries.

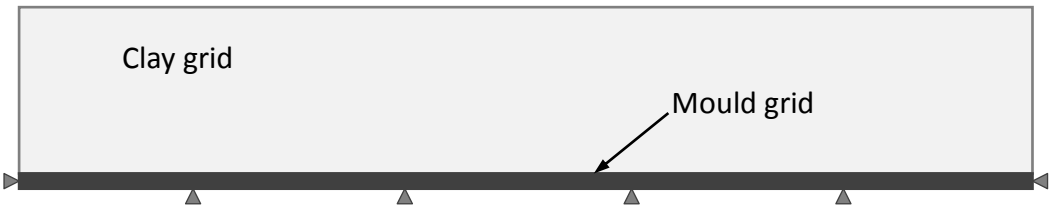

Figure 3.20 Mechanical boundaries.

3.3.6.2 Hydrological boundaries

The physical mould used in the laboratory simulations was semi-circular in cross-section and so drying may only have initially occurred at the exposed, upper surface of the clay. By default, the lateral boundaries of the clay grid were initially impermeable for both fluids. The drying flux was numerically simulated by application of a discharge boundary condition where inflow/outflow is governed by the sign of the discharge rate (m/s).

From the outset, the discharge condition was statically located at the upper surface of the model mesh. However, during the indicative laboratory experiments, shrinkage was observed as both ends of the soil sample moving inward, away from the mould resulting in an increase in the exposed surface area of the sample. Therefore, in addition to simulated discharge from the upper surface of the sample mesh, the transient behaviour of the exposed end surfaces was accommodated in the model. Furthermore, the evaporative surface area increases upon the onset of cracking and this was also included.

At every simulated hour of drying, each interface was assessed for separation (i.e. crack opening) according to the function depicted in Figure 3.21. When separation is identified, the exposed ‘crack wall’ is subjected to a discharge condition. An example evolution of the drying boundary geometry is provided in Figure 3.22.

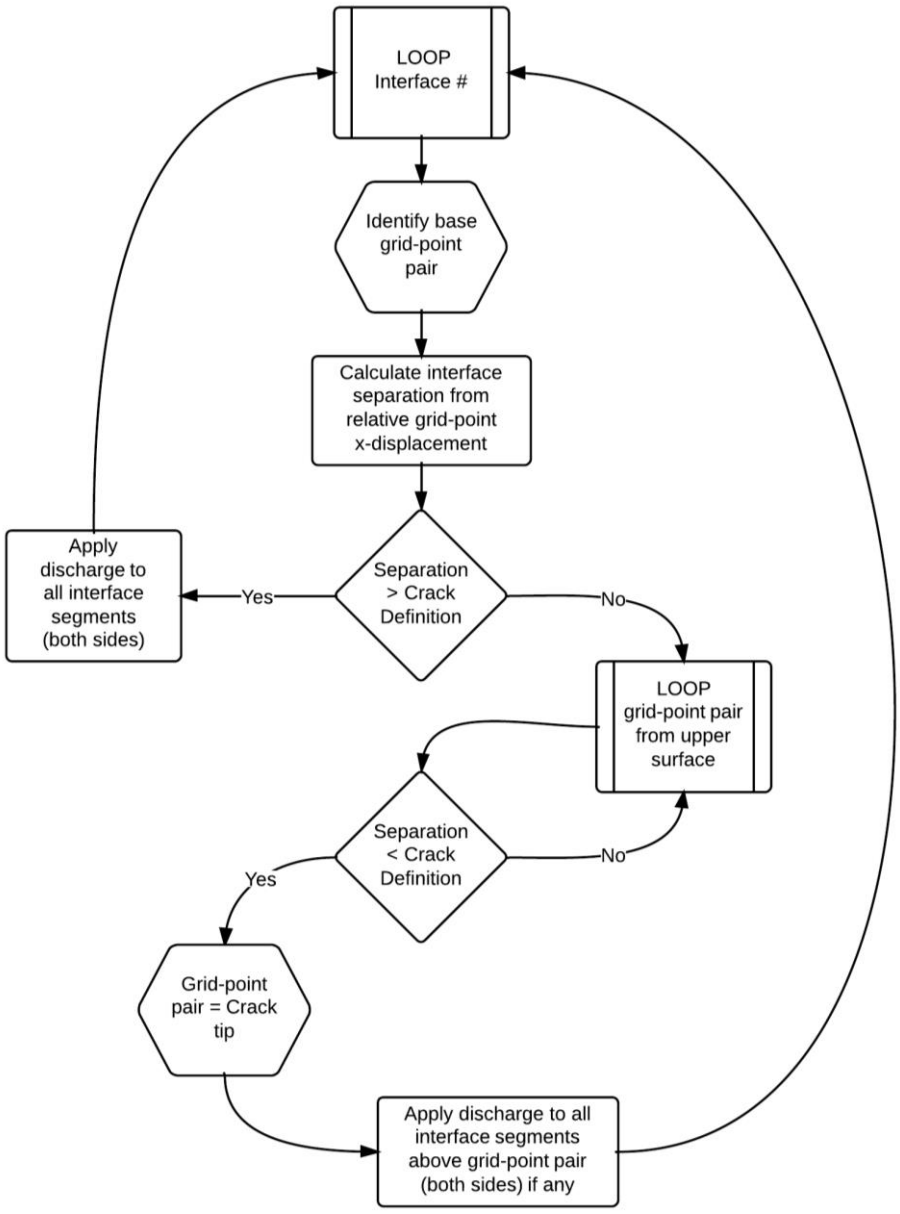

Figure 3.21 Illustration of the crack discharge boundary function.

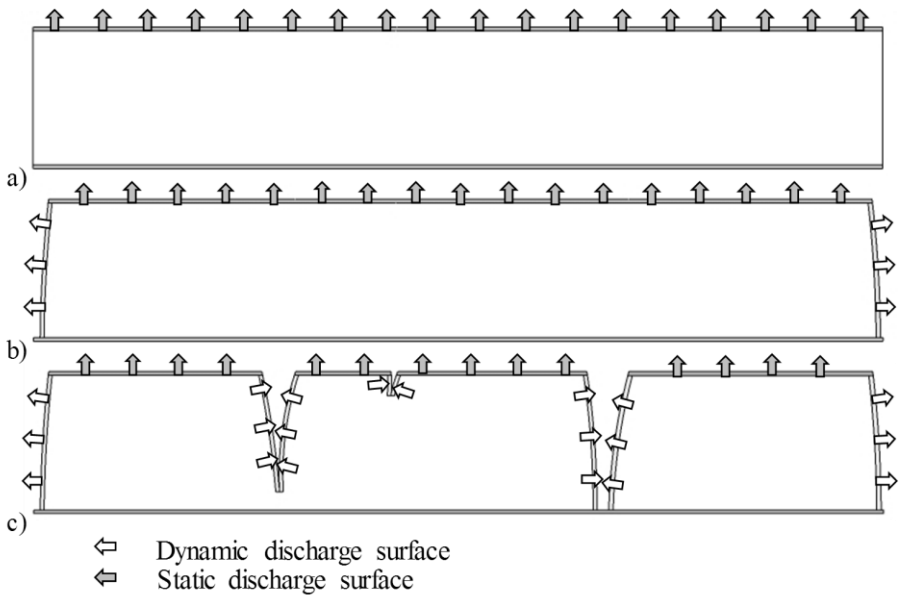

Figure 3.22 Illustration of the drying boundaries (a) initial upper surface (b) upper surface plus exposed sample ends and (c) upper surface, exposed ends plus crack walls.

The discharge rate corresponds to the drying rate and was estimated from the laboratory experiments. Drying curves such as those presented in Figure 3.23 were calculated from mass data recorded during drying. Mass loss is considered to be solely that of water; hence the volume of water lost as a function of time is defined by Equation 3.62. The incremental discharge rate may therefore be calculated using Equation 3.63 where the evaporative surface area, A, is $5.81 \times 10^{-2} m^2$ and assumed constant.

$$\frac{\partial V}{\partial t} = \Delta M / \rho_w \quad \textbf{3.62}$$

$$q = \frac{\partial}{\partial t} . \frac{V}{A} \quad \textbf{3.63}$$

Exponential best fit curves have been applied to the calculated discharge data for the laboratory experiments and are presented in Figure 3.24. An estimation of the initial evaporation rate was made using the intercept of such curves. This process informed the applied discharge rate at the collective discharge surfaces.

Calculation of drying curve data is acknowledged to be more accurately conducted on the basis of temperature and relative humidity in the manner of Aluwihare and Watanabe (2003) and Cui et al. (2013). However, the indicative laboratory experiments (Section 3.3.1) were unable to be isolated and so such

data could not be prescribed solely to each soil mass and hence, this method was not possible.

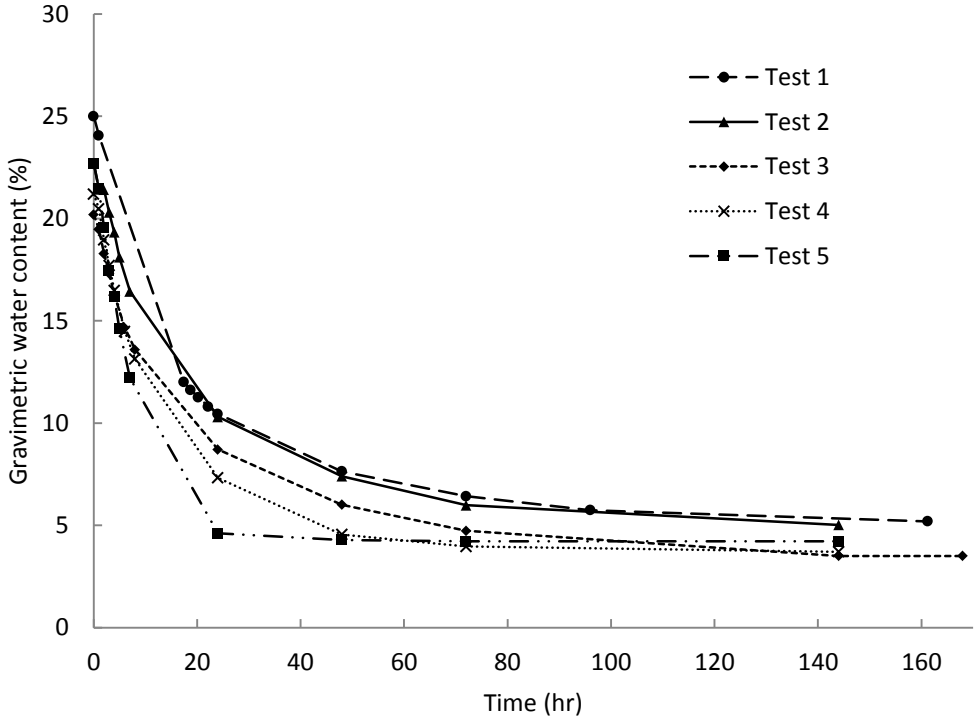

Figure 3.23 Laboratory experiment drying curves

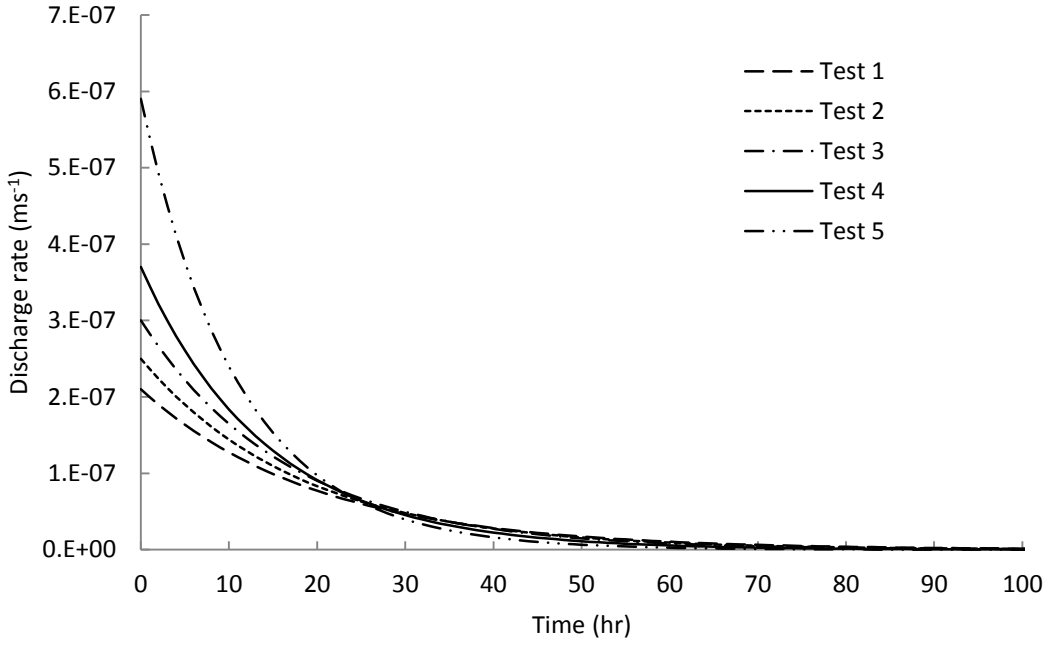

Figure 3.24 Laboratory experiment discharge curves

The magnitude of the additional drying applied to the dynamic discharge boundary was 10% of the calculated static discharge boundary. This value was selected on the basis that evaporation from these relatively enclosed surfaces will be significantly smaller than that of the upper surface. These surfaces were considered sheltered from atmospheric turbulence experienced by the upper surface leading them to be subject to a lower humidity gradient. Additionally, experimental evidence indicates that the crack wall interface experiences a hydraulic conductivity several orders of magnitude smaller than that of the matrix (Gerke & Genuchten, 1993). This is believed to suppress the evaporative loss from these surfaces.

3.3.7 Initial conditions

Prior to the application of the drying boundary condition, in situ stresses in the clay grid are installed through the combination of mechanical boundary conditions and the application of acceleration due to gravity. As previously mentioned, the base of the clay grid is restrained vertically by the position of the mould grid. However, during the generation of the initial stress state a fixed displacement condition was also applied to the lateral boundaries. This captures the confining effect of the mould interior ends, immediately following compaction. Acceleration due to gravity was applied at $9.81 ms^{-2}$ and the model stepped to equilibrium. The application of gravity causes body forces to act on all grid-points where these forces correspond to the weight of the material. The equilibrium state is defined as being when the ratio of the unbalanced mechanical force over the applied mechanical force (body forces) for all grid-points is reduced to a value of 1×10^{-3}. Equilibrium is achieved relatively quickly due to the absence of any yield criteria in using the elastic constitutive model. The initial stress conditions are generated in the absence of the flow calculation. Total stress distributions[1] are presented in Figure 3.25 and Figure 3.26, stress is expressed in units of Pa according to the following sign convention: Positive stresses indicate tension; negative stresses indicate compression.

[1]A FISH function that extrapolates zone-based variables (e.g. stress) to grid-points, hence to the model boundaries, has been employed in the production of contoured plots. Zone-based values are assumed to be constant across an element meaning contours do not automatically extend to the model boundaries. Given the interface geometry used, inbuilt contour-plotting logic results in the segmentation of data confined to the 2-element thick inter-interface region. A simple averaging procedure was used where the value at each grid-point reflects the average of values from all non-null zones that use the grid-point.

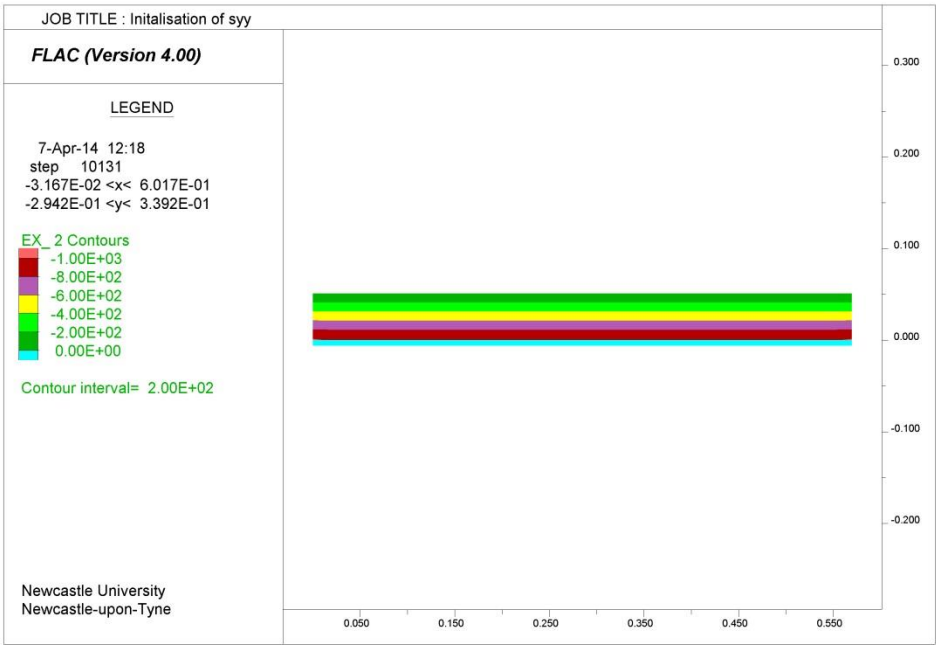

Figure 3.25 Distribution of total vertical stress at equilibrium

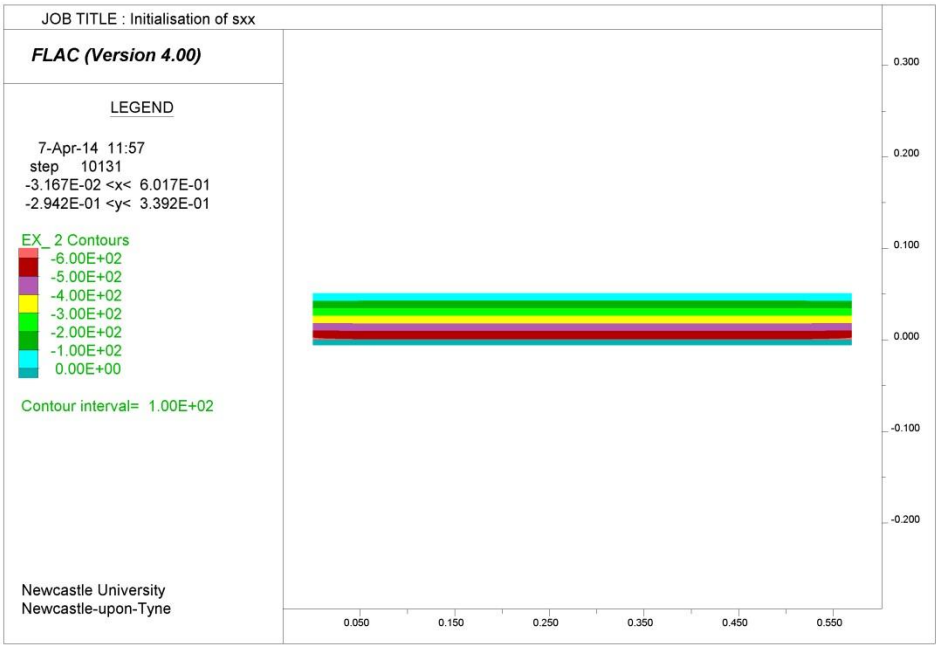

Figure 3.26 Distribution of total horizontal stress at equilibrium

When including the tp-flow option, FLAC requires that the initial saturation, S_0 and wetting pore pressure, P, be specified prior to running the flow calculation. Therefore, the van Genuchten expression presented in Equation 3.64 was employed to calculate the initial wetting pore pressure using the input initial saturation. The initial non-wetting pore pressure was internally derived from the same expression adopting the resultant effective non-wetting fluid saturation. As the clay grid was assumed to be initially of homogeneous saturation, the initial pore pressure was applied to the entire grid.

$$P = -P_0\left({S_0}^{-1/a} - 1\right)^{1-a} \qquad \textbf{3.64}$$

Although the process of generating the initial stress conditions by establishing mechanical equilibrium was conducted in the absence of the flow calculation, a mechanically induced pore pressure gradient is generated. Given that the clay-grid is defined as having a saturation prior to stepping to equilibrium, in this case S=1, the hydrostatic gradient presented in Figure 3.27 is produced.

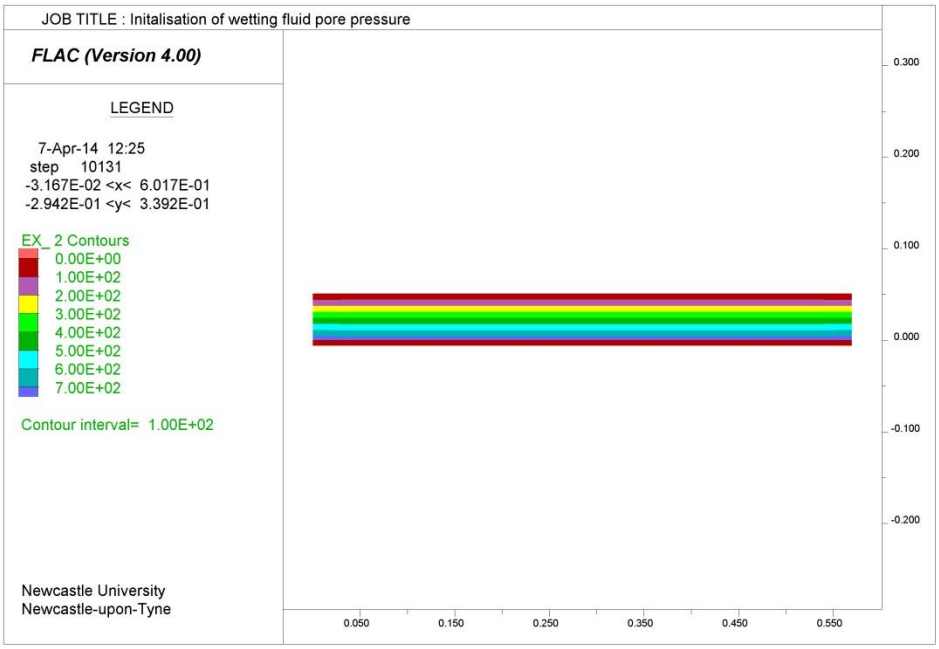

Figure 3.27 Hydrostatic distribution of wetting fluid pore pressure at equilibrium

Following this process and before the drying simulation is conducted, the lateral boundaries were once again freed according to Section 3.3.6.1.

3.4 Model summary

The modelling components described in this chapter were compiled to form the cracking model. The order in which they are included/performed is presented in Figure 3.28 where units are defined as user input, functions, loops and processes.

The model may be divided into four broad sections. Firstly, the model is set up using input continuum, interface and hydrological properties and the dimensions of the required geometry. A geometry generation function developed in FISH combines these components and forms the basic model. Initial stress and hydrological conditions are then generated. At this point, functions are introduced which are invoked repeatedly at each calculation step. These include the modification of soil stiffness as a function of saturation, crack width/depth assessment as well as a selection of bespoke monitoring functions such as the writing of mechanical or hydraulic variable histories or any other parameter measurement. Groundwater flow time is a key monitoring variable as this allows the progress of all variables to be considered against a meaningful time scale other than an abstract step number. The final section invokes the drying condition. The drying phase of the model is conducted on the basis of hourly loops whereby the extent of the flux boundary condition is reassessed and interface properties are updated according to saturation. The resulting model state may then be queried using an array of inbuilt facilities in addition to those put in place in the third section prior to the application of the drying condition.

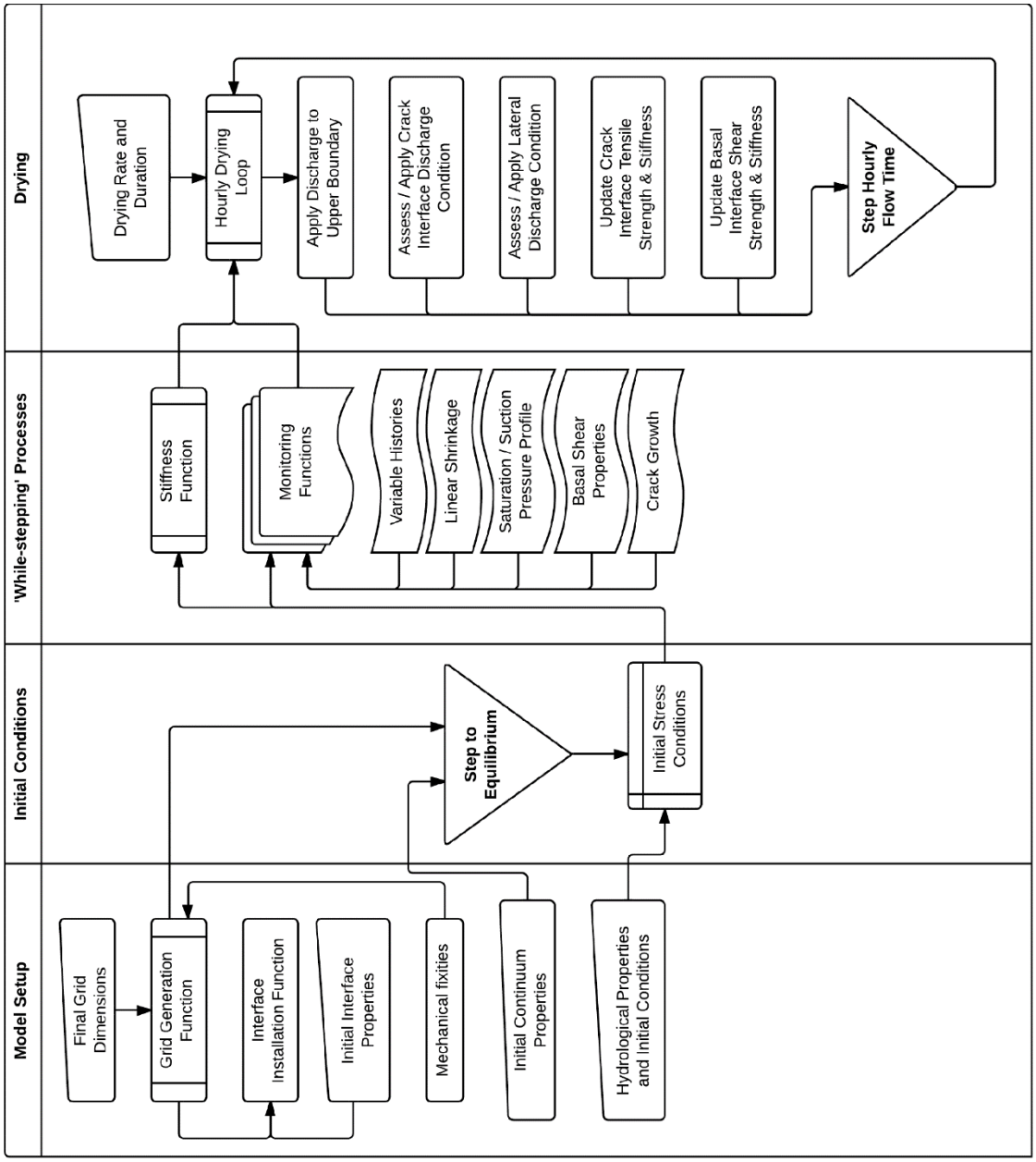

Figure 3.28 Diagram of model assembly

3.5 Concluding remarks

The above described modelling methodology has been designed and executed in production of the work presented in Chapter 5. However, a gap in the range of modelling parameters was identified, namely the specification of interface bond tensile strength as there is no definitive method for its quantification, particularly in drying conditions. Hence, the following chapter details the design, development and testing of laboratory apparatus intended to fulfil the requirements of the above method.

Chapter 4 Tensile Strength

4.1 Introduction

The design of a test capable of establishing the tensile strength of cohesive soils under saturated and partially saturated conditions has been identified as a necessary requirement of this work. Currently, there is no standard method for measuring the tensile strength of soils though several authors have proposed techniques using bespoke equipment. This chapter introduces a test apparatus and procedure that has been specifically designed to establish the tensile strength of clay soils at a range of water contents quickly and reliably. The newly developed method has been employed to test three different soil types as well as being evaluated using Digital Image Correlation for the purposes of assessing sample behaviour and apparatus performance. Finally, the results obtained have been validated against an established method for measuring rock tensile strength. The application of this method of testing has itself been validated to ensure a reliable comparison is achieved.

4.2 Experiment Design

4.2.1 Test principle

The fundamental principle behind the apparatus is that direct tensile stresses are measured via a simple modification of the standard direct shear strength test (commonly known as the shear box) BS1377-7 (British Standards, 1990). In this way, the means of both generating and measuring load are established prior to the addition of loading jaws.

Specially designed jaws that grip the sample (Figure 4.1) are mounted together firmly into the standard shear box carriage shown in Figure 4.2. Crucially, these jaws are made to separate in a uniaxial manner at an adjustable, constant rate. To achieve this, the jaws are placed within the carriage that is propelled by the motor; however one jaw is restrained by a brace (restrained jaw, Figure 4.2). Hence, the carriage jaw is made to move along greased bearings relative to the restrained jaw. As the carriage jaw is propelled, load is transferred evenly through the cross-section of the sample to the restrained jaw. A brace element allows the load to be transmitted to the load gauge positioned at the opposite end of the rig. The sample possesses a mirrored isosceles trapezium horizontal cross-section (commonly referred to as a ‘bowtie’ shape) that aids the constraint of the sample and induces failure at the centre due to the reduced cross-sectional area. Tensile strength is defined as the peak load the sample experiences over the area of fracture.

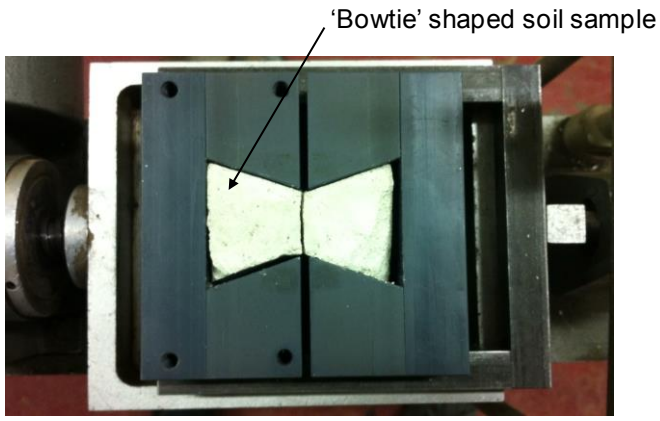

Figure 4.1 Soil sample positioned within loading jaws

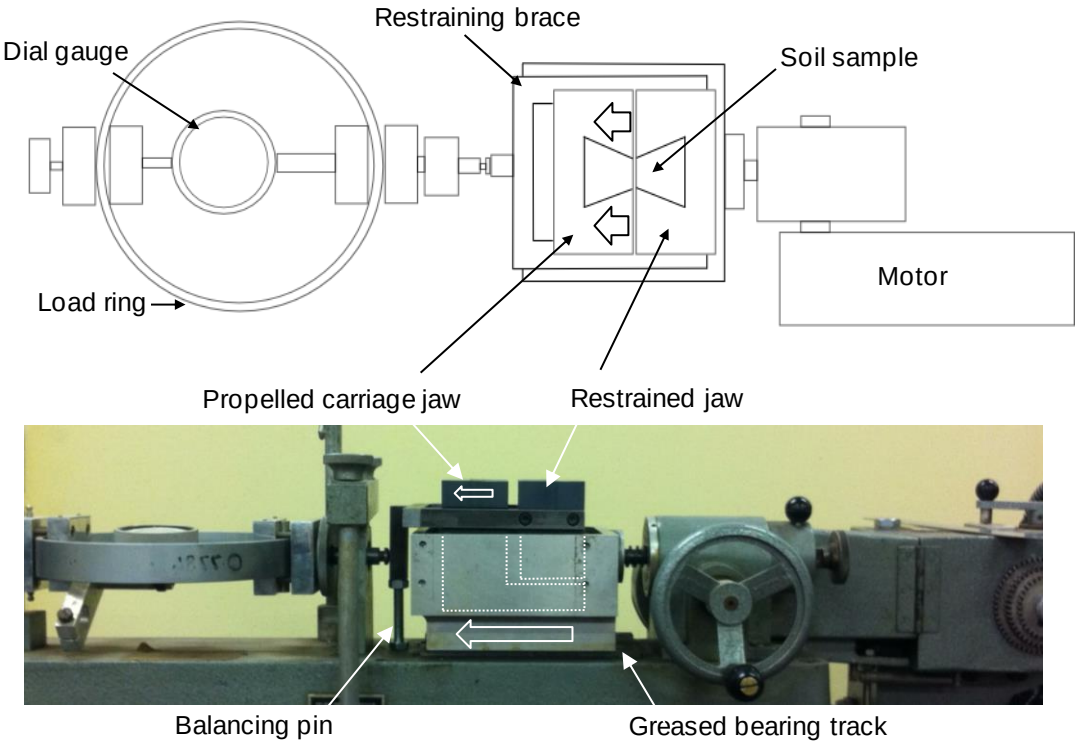

Figure 4.2 General assembly of the direct tension apparatus.

4.2.2 Apparatus design

A standard Wykham Ferrance 60mm square direct shear testing rig was used. This rig consists of a fixed frame upon which an electric motor and means of measuring load (ring gauge/load cell) are mounted at opposing ends.

In order to induce tension, a pair of loading jaws was designed between which the soil sample is mounted. Several designs of jaws/platens have been proposed including internally or externally glued fixings (Heibrock et al., 2003), truncated cylinders (Tamrakar et al., 2005) and truncated triangular prisms (Trabelsi et al., 2010), as discussed in Section 2.5.1.3. No adhesive was used in an effort to avoid the introduction of any additional media as it is thought that this may influence the measurement of tensile stress and complicate the quick and easy production of test samples.

A friction based system was selected and is shown in Figure 4.1. This shape is relatively simple to manufacture and allows for easy alteration of loading angle if required as part of future development by the replacement of removable side portions. The jaws were constructed using rigid PVC and assembled components comprise a 90x90x79mm (LxWxD) block with a centrally located

‘bowtie’ shaped sample space of 38x54x50mm (78.3ml volume). A brace component is fitted to one jaw (left) which passes around the remaining, free jaw (right).

Modification of the brace location was a key element of the apparatus development. Initial trials relied on the transmission of load through a top mounted brace (Figure 4.3a). However, at high loads experienced when testing strong materials (>100 kPa) this resulted in an unstable cantilever where the sample is rotated, causing a preferential tear from the underside (Figure 4.3b). This meant that tensile loading no longer remained one-dimensional. This deviation from 1D tensile loading was considered undesirable in the measurement of direct tensile stress and a solution was sought.

An attempt to solve this issue involved the addition of an adjustable support mounted beneath the end of the brace to guard against vertical movement. Although this reduced the rotational effect, the issue was ultimately resolved by relocating the brace centrally over the height of the loading jaws (Figure 4.3c). The brace remained secured to the restrained jaw, yet was made to pass through channels positioned on the sides of the carriage jaw. The channel provided 2mm clearance so as not to add any additional friction to the system. However, the channel did provide a mechanism to ensure the test acted uniaxially.

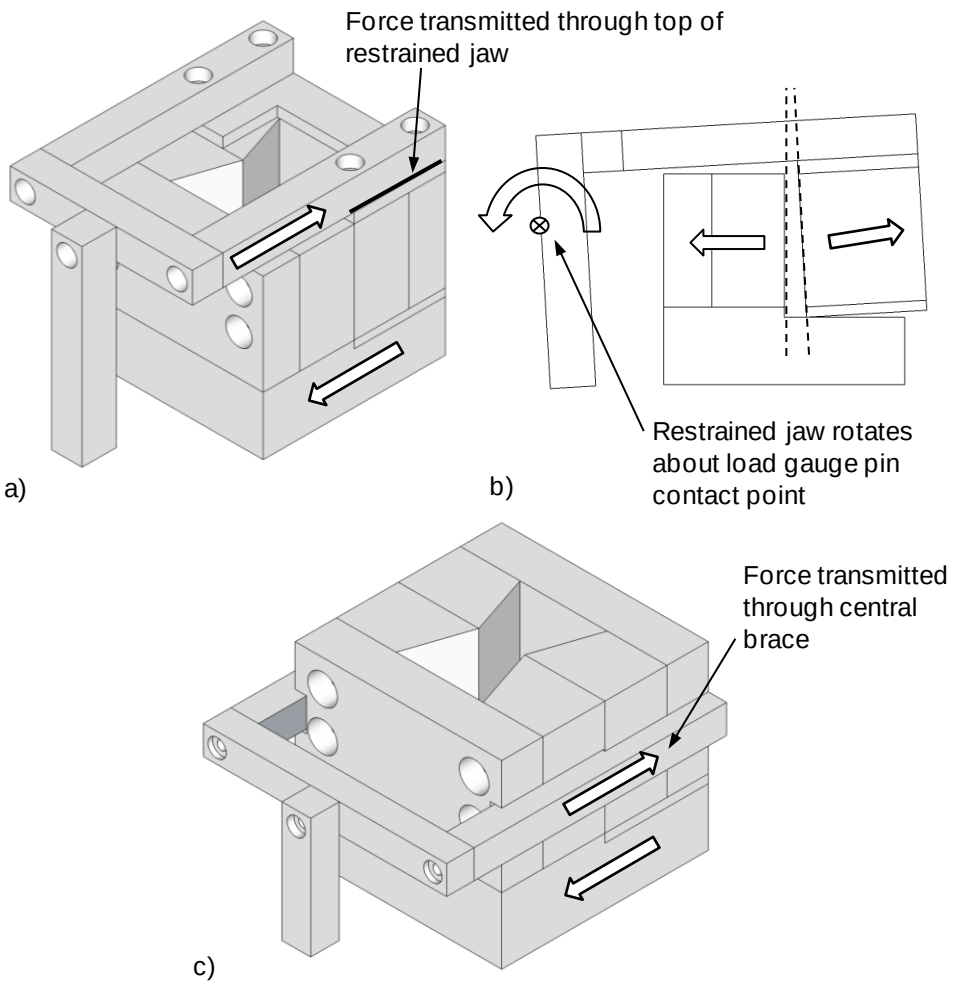

Figure 4.3 Tensile test brace configurations (a) top mounted (b) cantilever effect and (c) middle mounted.

4.3 Validation Methodology

It was necessary to conduct a programme of testing using the newly developed direct tension apparatus in order to gain an understanding of its performance. Soil samples were to be tested under a number of different conditions such as variable water content, dry density and strain rate. Three different soils were selected including artificially produced sandy clay, glacial till and stabilised silty sandy clay. It was aimed that these soils aided the investigation into the applicability of the new apparatus in testing a variety of cohesive materials.

The primary method by which the new direct tension apparatus was evaluated was by comparison with an established indirect method, the Brazilian test ASTM D3967 – 08 (ASTM, 1984). It was recognised that this method is principally used in the testing of brittle materials; however, it is justifiable to apply the technique to soils when samples are of a suitable condition i.e. dry enough to behave in a brittle manner. The direct tension test was aimed at testing soils in a wider range of saturation conditions than that suitable for Brazilian testing. The aforementioned three materials were used in the narrow range of conditions that allow for a fair comparative study to be conducted between the direct and indirect method.

Digital image correlation was employed to investigate the generation of full-field strain during direct and indirect tensile strength testing. Strain generation was assessed in order to establish the distribution of inferred stresses across the ‘bowtie’ samples and therefore allow the performance of the jaw design to be evaluated. This optical technique, along with a Brazilian disc deformation criterion (Frydman, 1964), also allowed the appropriate use of the Brazilian test to be confirmed. Only adequately reliable results can be confidently compared, ultimately ensuring a reliable validation is conducted.

4.4 Direct Tensile Strength Testing

4.4.1 Sample preparation

The three selected soils were prepared according to the following general specification prior to sample formation. Bench dried material was sieved to ensure a particle size <5mm. It was deemed necessary to restrict the largest grains to 5mm as larger grains would act as loci for preferential tensile failure during testing. Although this process is recognised to artificially refine the particle size distribution of the glacial till material from its natural condition, samples whereby individual grains constituted greater than 2% of the total volume of the sample were undesirable. This procedure is in accordance with the preparation of direct shear (shearbox) samples BS1377-7:1990 sub-section 7.7.2 where the maximum particle size is given by $\mathrm{H}/10$ where H is the sample height taken as perpendicular to the shear plane (British Standards, 1990). In production of tensile test samples, the dimension normal to the intended fracture plane is 54mm.

In order to form samples at desired water contents, the required volume of water was added to the dried material in a mixer. The calculated volume of water added was increased by 10% to allow for evaporative loss during the mixing process. The mixture was then sealed in an air tight bag and left to equilibrate for a minimum of 24hours. This ensured that the water content was evenly distributed throughout the bulk material.

Sample formation was conducted on the basis of achieving a prescribed dry density, ρ_d by compaction of a mass, m into a mould of known volume, V according to equation 4.1.

$$m = \rho_d V \left(\frac{100 + \omega}{100}\right) \qquad \textbf{4.1}$$

The mould used was specially designed to produce samples of the required shape and is illustrated in Figure 4.4. The mould was constructed out of 4 individual mild-steel plates that were secured together by 8 bolts which ensured that the plates did not separate during compaction and that the sample formed was of a consistent size and shape that would fit within the testing jaws easily.

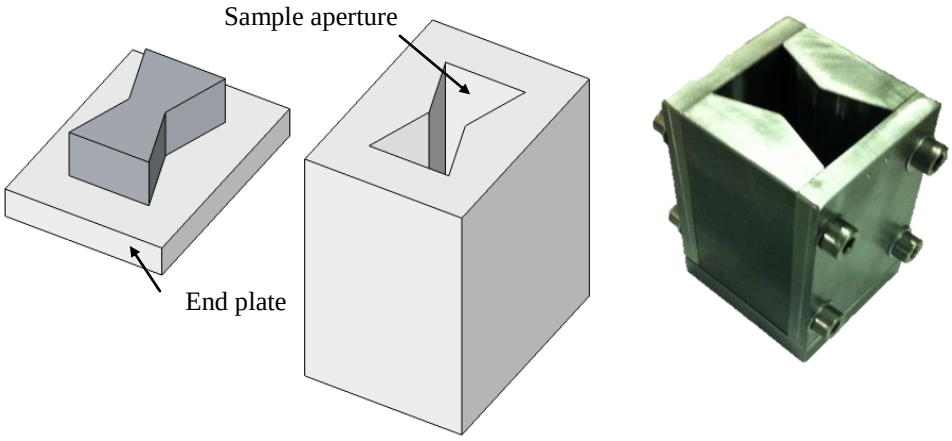

Figure 4.4 Mould used to form samples

4.4.1.1 Sample compaction

Following soil preparation, the following procedure was adopted to form the compacted sample:

1. The mould interior was greased using petroleum jelly prior to filling to aid sample recovery following compaction. It was found that if no grease was applied, samples wet of their plastic limit would exhibit excessive adhesion to the mould walls leading to sample disintegration and poor recovery. Lubrication of the mould end plates further aided the interlocking of the mould components.
2. The required mass, as determined using Equation 4.1, was inserted into the mould in three layers as evenly as possible and tampered down leaving enough recessed space to accommodate the top plate securely.
3. The assembled mould was then placed between platens of a universal testing rig and loaded at approximately 0.5kNmin^{-1}. Loading was halted once the top plate had lowered and the sample was completely encased within the mould.

4. The sample was then extracted. In order to ensure the integrity of the sample edges, this process often required the mould to be dismantled using conveniently located bolts.
5. Once free, the sample was then wrapped using cling film and allowed to equilibrate for a period of at least 24hours.

Immediately following sample compaction, the bowtie shaped samples are at the precise required size and shape of the sample space in between the loading jaws. However, it is important to note that as samples are allowed to bench dry to varying degrees as part of investigations into the influence of water content on tensile strength, shrinkage of the clay was identified. This causes samples that have been allowed to dry for prolonged periods to reduce in size by up to 4mm in the most extreme cases. The nature of the bowtie shape and the angled jaws means that this reduction in size is accommodated by a period of sample bedding at the beginning of the tests. Such behaviour is described further in Section 4.4.5.3.3.

The three soils each required a minor variation from the general description presented above. These are provided along with descriptions of each material.

4.4.1.2 Artificial mix

A sandy clay was produced in the laboratory from commercially available products making it easy to replicate and homogeneous. The following materials and proportions were used: sharp sand 50%; kaolin 47.5%; bentonite 2.5%. Initially, 95% kaolin: 5% bentonite mix was trialled. However, this was found to be unworkable during the sample preparation process as at water contents in excess of the plastic limit, poor sample recovery was experienced when extruding from the sample mould. To combat this, sand was added to reduce the cohesiveness and raise the plastic limit. A relatively small component of bentonite was added to act as a binder. This mixture proved to be a much more compliant material.

A series of classification tests was undertaken. A uniform particle size distribution (PSD) was determined by dry sieving of the sand component according to BS1377-2 (British Standards, 1990) and is provided in Figure 4.5. The low-intermediate plasticity classification and compaction characteristics are

presented in Figure 4.6 and Figure 4.7 respectively. An optimum water content of 16.2% is found to achieve a maximum dry density of 1.76Mg/m^3 by compaction testing using a 2.5kg rammer according to BS1377-4 (British Standards, 1990).

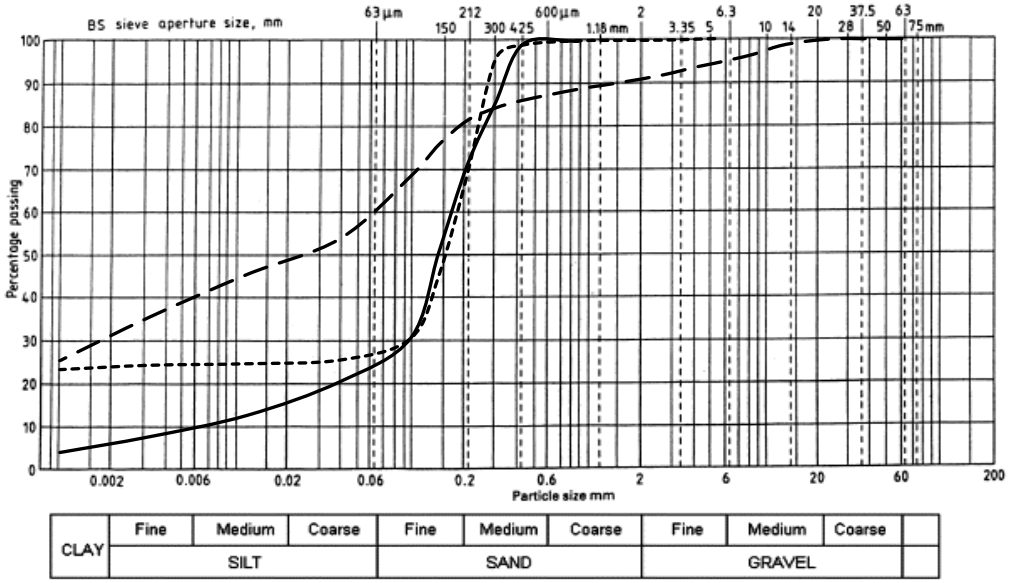

Figure 4.5 Particle size distribution BS1377-2 (British Standards, 1990).

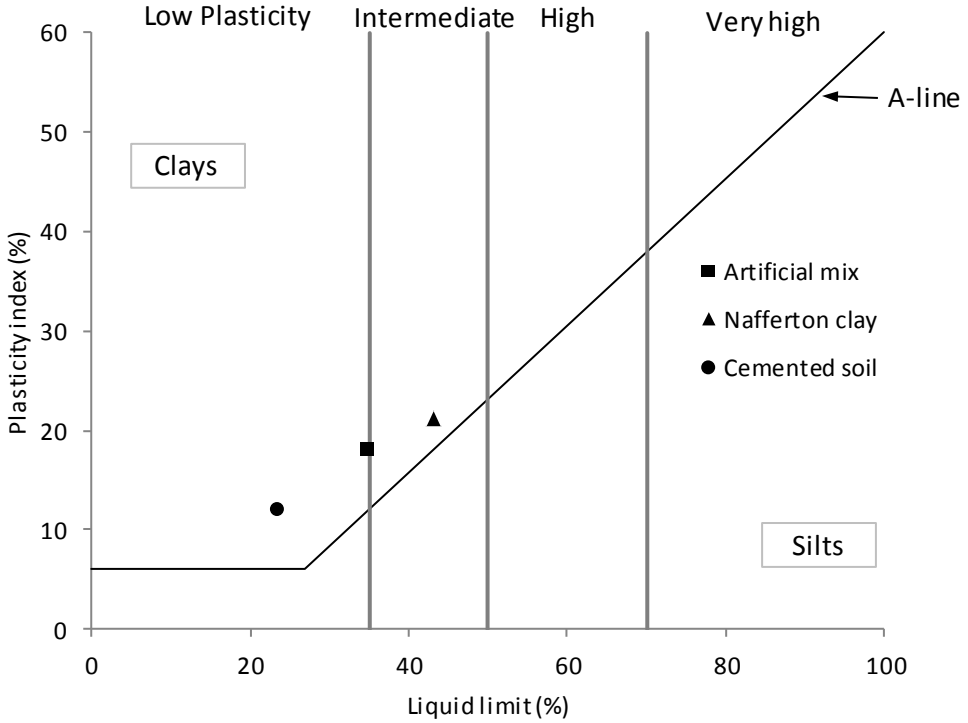

Figure 4.6 Casagrande chart BS1377-2 (British Standards, 1990).

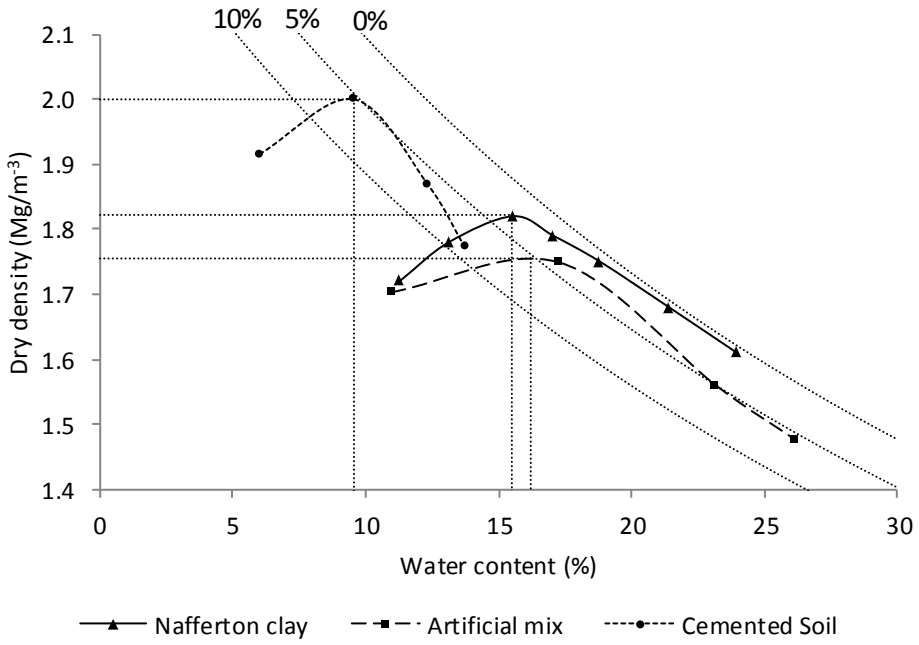

Figure 4.7 Compaction curve BS1377-4 (British Standards, 1990).

4.4.1.3 Nafferton clay

The Nafferton clay constitutes the main material investigated in this work and was sourced near Durham, northeast England. It has been used as the fill material in the construction of the BIONICS full-scale trial embankment at Nafferton Farm, near Newcastle.

As part of the BIONICS trial embankment project, a range of classification tests have been performed. As this work ultimately aims to capture behaviour of the fill in situ; data is presented from the field as well as laboratory tests. The PSD is presented in Figure 4.5 where the soil is shown to be relatively well-graded in the portion >2μm. The liquid and plastic limits were tested and the clay has been classified as being of intermediate plasticity (Figure 4.6). An optimum water content of 15.5% and maximum dry density of 1.82Mg/m^{-3} was also established (Figure 4.7). Core cut samples of the in situ embankment fill were found to have an average dry density of 1.65Mg/m^{-3}, wet of optimum (15% OMC) at a depth <1m from the surface.

The glacial till, being a naturally sourced material required greater preparation before tensile testing. The material was excavated from a stock pile adjacent to the trial embankment, recovered in bulk bags and transported to the laboratory. The bulk material was then pushed through a 20mm sieve by hand to remove

large gravel sized particles and extract organic debris. The <20mm sieved soil was then air dried on and not within a laboratory oven. A ‘crusher’ was then used to break the clods of clay before being sieved to <5mm as per the general preparation procedure described above. As highlighted previously, the artificially skewed particle size distribution and removal of roots is accepted to influence the mechanical data obtained in contrast to the properties in situ. However, this process is deemed necessary due to the scale of the testing equipment employed.

4.4.1.4 Cemented soil

A stabilised soil was produced for the purpose of broadening the range of materials tested using the direct and indirect tensile strength testing methods. The cemented artificial silty sandy clay comprised silica sand 70%, kaolin 30% and CEM-1 binder 5% by dry mass and was mixed at 15% water content. A uniform particle size distribution established by dry sieving is provided (Figure 4.5) as well as the result of plasticity testing (Figure 4.6).

Given the nature of the material, a period of curing was allowed for the binder to take effect. It is recognised that water content will reduce as a function of curing time due to the on-going pozzolanic reaction. Cemented soil samples were wrapped immediately after compaction and allowed to cure for 7 and 21 days prior to air drying.

4.4.2 Testing procedure

Prior to setting up the testing equipment, a record of the test was produced comprising a test reference number, the intended displacement rate, intended sample water content and calibration data required in the processing of output data post-testing.

The displacement rate was set from those available using the Wykham Ferrance direct shear rig. These are provided in Table 4.1 where the rate corresponds to the motor speed setting and gearing configuration.

Table 4.1 Wykham Ferrance WF25000 displacement rates (mm/min).

	Gear configuration		
Speed	45/45	60/30	30/60
A	0.6106	1.2192	3.0480
B	0.1229	0.2448	0.0610
C	0.0244	0.0498	0.0122
D	0.0059	0.0108	0.0024
E	0.0010	0.0020	0.0005

The loading jaws were placed into the carriage and the brace was positioned against the load gauge pin. The sample was then positioned between the jaws. The motor was then started, propelling the carriage forward while load was recorded for the duration of the test. The tests continued until load readings were seen to return to an unchanging residual value. At this point, the motor was stopped.

The jaws were then removed, including the failed sample. In order to calculate tensile stress for the duration of the test, the cross-sectional area of the failure plane was measured and recorded. A sample was taken for the determination of water content by oven drying. This is then assigned as the water content at testing.

4.4.3 Testing results

Tensile stress was calculated using σ_t (kPa) = F/A where F (kN) is recorded load and A (m^2) is the cross-sectional area over which failure occurred. Strain was calculated using directly measured carriage jaw displacements and original sample length. Typical stress-strain results for tests conducted on soils at varying water contents are provided in Figure 4.8 and Figure 4.9 for the artificial soil and Nafferton clay respectively. For illustration purposes, the results presented are for tests conducted at a rate of 1.22mm/min.

For testing of the artificial soil (Figure 4.8), a clear increase in tensile strength and stiffness can be seen with deceasing water content. Samples tested at and below 21% show a broadly linear increase in stress with strain until the ultimate tensile stress. At peak stress, the drier samples (below plastic limit) show brittle failure with a well-defined fracture i.e. complete separation of the two halves. Hence a rapid drop off in sustained stress is seen. However, samples at greater saturation (above plastic limit) are more ductile and typically show a strain softening behaviour post-failure.

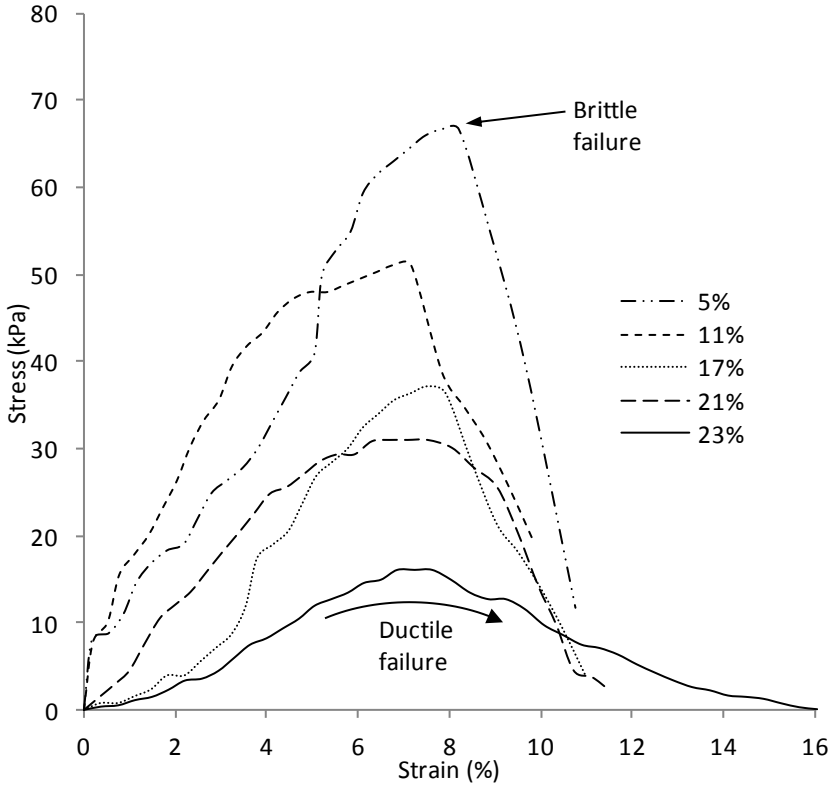

Figure 4.8 Stress-strain relationship for artificial soil samples

Results from the testing of Nafferton clay demonstrate a much greater degree of variability. Where the uniformity of the artificial soil has resulted in consistent strain at failure and a progressive softening behaviour with increasing saturation, the natural variability inherent in the glacial till is shown to greatly influence both the tangential stiffness and strain at failure. Despite this, the broad trend of increasing strength and stiffness with decreasing water content remains apparent with the magnitude of tensile strength being greater for the compacted till material.

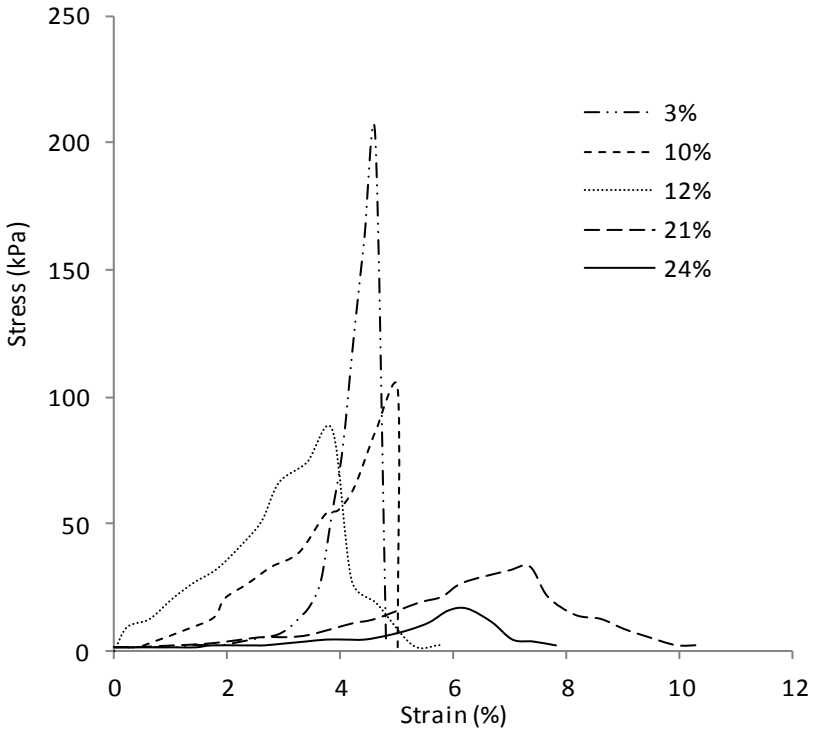

Figure 4.9 Stress-strain relationship for Nafferton clay

4.4.4 Cyclic tensile strength

This section presents a study to establish the cyclic relationship between tensile strength and soil water content for the re-moulded glacial till, Nafferton clay. In this work, the direct tensile strength test has been used to investigate the effect of drying-wetting cycles on the development of the tensile strength – water content relationship. This has been conducted in the context of observed degradation of compacted engineered fill at the near surface of infrastructure embankment structures.

4.4.4.1 Sample preparation and testing

Clay samples were produced according to Section 4.4.1 whereby samples were air dried to successive water contents. On reaching the required water content, samples were then re-sealed for 24 hours to ensure an even re-distribution of water within the specimen prior to testing. However, where samples were required to be tested along the wetting path, samples were first allowed to dry to their residual value (where no mass change was observed). A humidity chamber was then employed in order to gradually increase the water content of these samples.

The insulated chamber measured approximately 450 mm x 300 mm x 300 mm (Figure 4.10) and contained a 30-40mm water bath within which was placed up to 3 ultrasonic water foggers. A fogger will emitted a fine mist when water covers the actuated diaphragm; the water bath level must therefore be monitored regularly and maintained (Figure 4.11). A high relative humidity was maintained enabling the samples to absorb moisture gradually as a more rapid approach would inevitably lead to destruction of the soil fabric and likely sample disintegration. For a typical dried sample to be returned to a water content of 20%, a period of approximately 7 days was required. Upon reaching the required position along the wetting path, samples were removed and sealed for 24 hours to re-equilibrate.

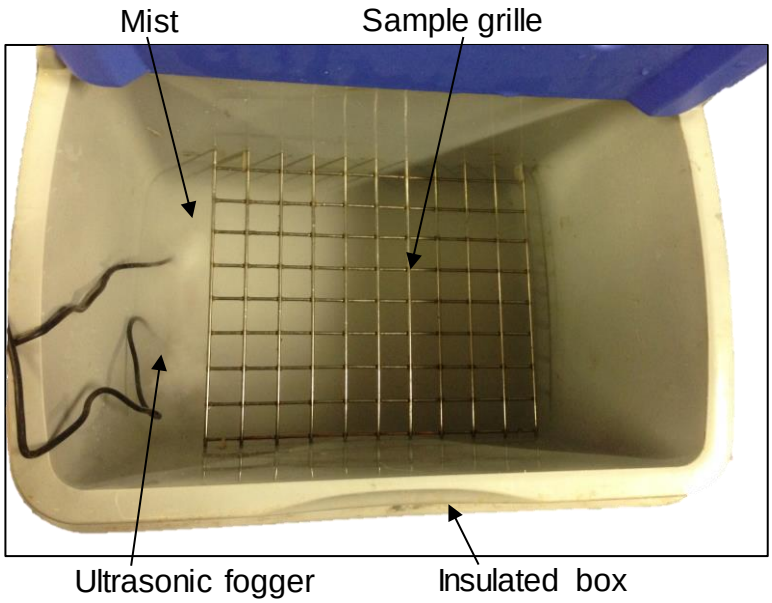

Figure 4.10 Humidifying chamber

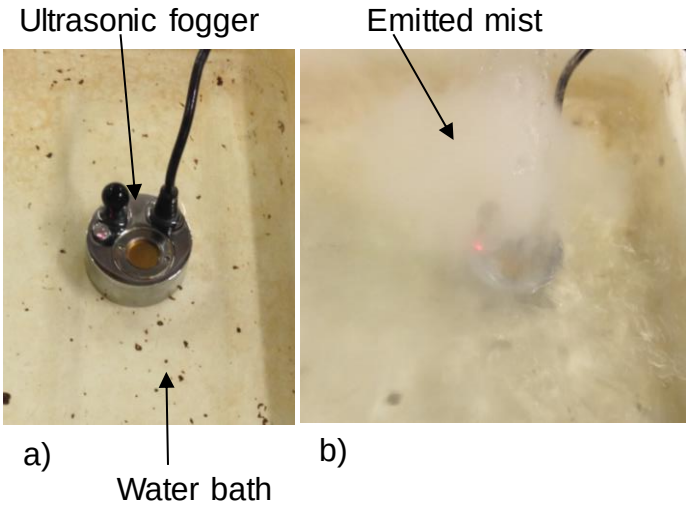

Figure 4.11 Ultrasonic fogger (a) low water bath and (b) raised water level

Samples to be tested along the secondary drying path were subjected to full re-wetting (returning to the at-compacted water content) before being sealed once more and then air dried as required. These supplementary stages produced a sufficient sample set at intervals along the three complete saturation paths. Finally, all samples were tested according to Section 4.4.2 at an applied displacement rate of 0.61 mm/min.

4.4.4.2 Drying-wetting-drying results

The following data is present the results of tensile strength testing along the initial drying, wetting and subsequent re-drying path (Figure 4.12). The initial drying path shows a typical trend of exponentially increasing tensile strength with decreasing water content. This data has been curve fitted with an R^2 value of 0.84, the highest fit of all the strength-water content data. Upon wetting, a similarly exponential trend may be fitted. However, the wetting relationship follows much lower strength values and at water contents >20%, negligible tensile stress is maintained. The second drying path exhibits higher tensile strengths than that of the wetting trend yet is considerably weaker than the initial drying curve.

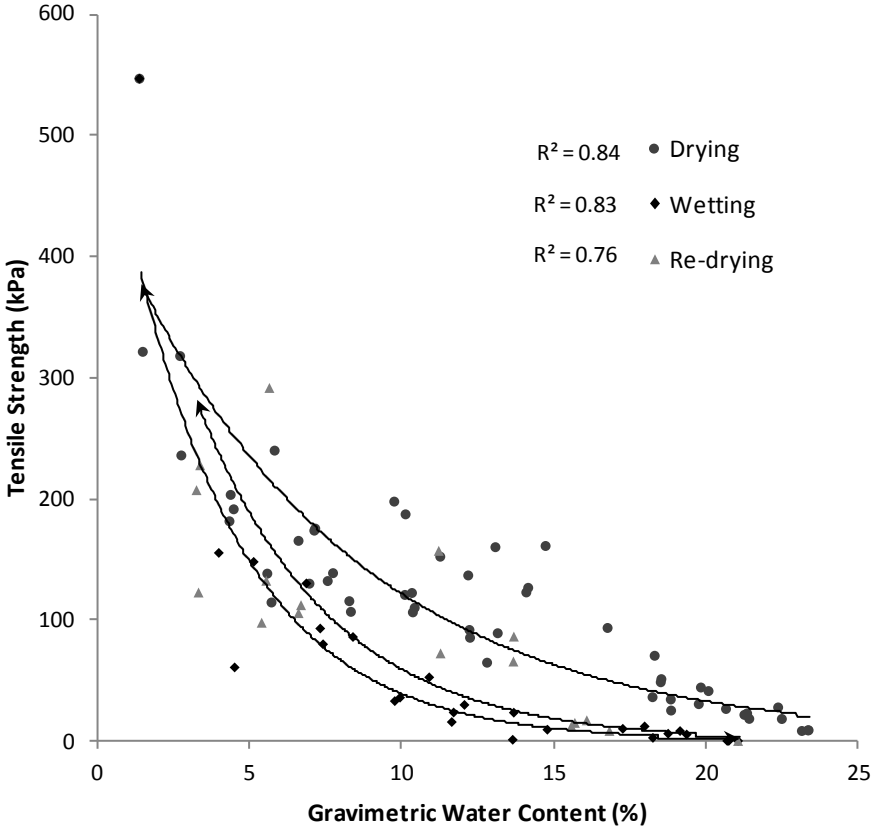

Figure 4.12 Tensile strength relationship upon initial drying, wetting and re-drying

4.4.4.3 Discussion on cyclic tensile strength

Traditionally, the relationship between tensile strength and water content established along an initial drying path has been considered an influence on the temporal distribution of crack initiation during progressive soil drying. However, this relationship has been found to undergo translation toward the origin of both tensile strength and water content axes upon cyclic wetting and drying.

The development of tensile strength in clay soils with changing water content is understood to be related to (but not solely a result of) an inherent change in matric suction. In granular soils, suction is the governing mechanism behind resistance to tensile stresses, although in compacted clay fills soil fabric is considered to play a significant role.

Crack initiation is assumed to occur by induced tensile stress brought about by restrained shrinkage due to surface desiccation exceeding the soil tensile strength under a given condition. A cracking analysis on this basis would indicate that crack initiation would occur at a given tensile strength which exists at specific water content. The following discussion precedes under the supposition that cracking may or may not have occurred in the initial drying of the subject soil. Should the cracking condition have been met under initial drying then sufficient stress ‘relaxation’ behaviour may well take place whereby subsequent generation of tensile stress may not exceed critical tensile strength and no further cracking can proceed. Notwithstanding, the use of a single, initial drying relationship is understood to result in an underestimation in the later development of crack networks.

By measuring the cyclic tensile strength-water content relationship, deterioration in the clay is evident. Hysteretic phenomena are familiar in the study of soil wetting. In the context of soil-water retention, upon wetting, lower suction is developed at a given water content than would be generated upon drying (Section 2.2.5). This effect may well contribute to explaining the reduced strength shown along the wetting path. However, it is believed that deterioration of the soil fabric is the primary means of strength reduction. The development of micro-flaws during the initial desiccation stage is believed to have led to an increment of non-recoverable destruction in the structure of the compacted clay.

The second drying stage illustrates this loss in soil integrity. Tensile strengths are higher on drying than wetting once again though are considerably lower than on the initial drying path. The return of the curve to higher strength values on drying indicates the influence of hysteretic soil-water-air phenomena. However, the large contrast between the two drying paths signifies a more fundamental deterioration. This has been described as aggregation and an increased porosity upon cyclic wetting and drying (Tang et al., 2011).

On establishing lower tensile strengths as a result of cyclic wetting and drying, the criterion by which crack initiation is believed to occur is met by the generation of lower tensile stresses. This would lead to an increased occurrence of cracking (e.g. development of an inter-connected network) with progressive drying-wetting cycles. Such behaviour was reported by Tang et al. (2011) whereby the degree of cracking in slurried clay increased significantly after three cycles before reaching equilibrium. Similar behaviour has also been observed in volumetric shrinkage after 2-3 cycles by Albrecht and Benson (2001). A residual drying/wetting (as soil-water hysteresis is believed to remain) tensile strength – water content relationship is therefore anticipated upon repeated cycling.

4.4.5 Digital Image Correlation

The 3D Digital Image Correlation (DIC) technique detects displacements on a deformed surface by correlating images of the surface before and after deformation. The technique has been employed to identify the distribution and development of strains across the ‘bowtie’ shaped surface of the soil samples in order to assess the performance of the test. Given that this method is completely contactless, the full-field strain development is measured without the complication of introducing any instrumentation into the soft and friable samples. Using high rate digital photography required for DIC, measurement of the loading jaws’ displacement has been possible and has allowed for assessment of the jaws’ performance with respect to different sample conditions.

4.4.5.1 Principles of Digital Image Correlation

The use of computer-based image acquisition and deformation measurement in material testing dates back to the early 1980s (Peters & Ranson, 1982; Sutton et al., 1983) and has seen an exponential growth in its frequency and breadth of applications ever since. However, the principle of identifying 2D motions by correlating digital images remains the same with advances in the sensors and algorithms used continuing to improve resolution and software performance respectively. An outline of the principle behind the technique is presented here.

The surface of an object is viewed using a high-resolution digital camera with which images are captured both before any deformation takes place and following successive deformation increments.

Importantly, the observed surface is textured, either through natural variation in the material or by the application of an artificial speckle pattern. Automated correlation of matched points is then conducted between captured images. Since matching of individual pixels is difficult, a small area anywhere between 2-30 pixels across is defined and used to perform the correlation. The area is commonly referred to as a subset and is characterised by a light intensity distribution or 'grey level' which is assumed not to change during deformation. Subset deformation is illustrated in Figure 4.13, initially in the un-deformed (reference) image (left) followed by successive increments of deformation. The deformed subset is then identified at each successive image using the unique 'grey level' defined in the reference image. The displacement of the subset may then be determined, from which the strain tensor is calculated.

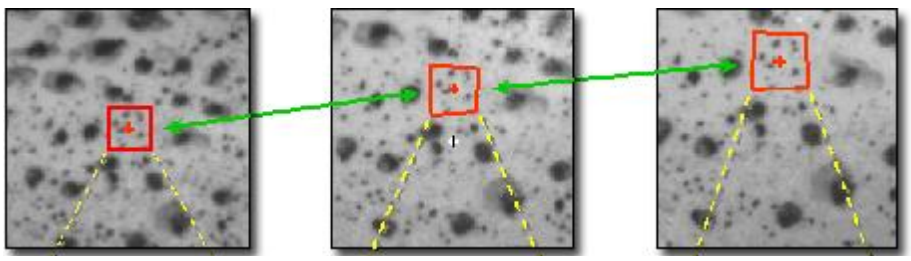

Figure 4.13 Example subset deformation (after Correlated Solutions, 2010).

Several functions exist to match the defined subset based on the general principle described and vary depending on the system employed. The most common of these is cross-correlation, illustrated by

$$C(x, y, x^*, y^*) = \frac{\sum F(x, y) G(x^*, y^*)}{\sqrt{\sum F\,(x, y)^2 \sum G(x^*, y^*)^2}} \quad \textbf{4.2}$$

Where $\mathrm{F(x,y)}$ represents the 'grey level' at the point $\mathrm{(x,y)}$ in the reference image and $\mathrm{G(x^*,y^*)}$, the 'grey level' at point $\mathrm{(x^*,y^*)}$ in the deformed image. The coordinate change from $\mathrm{(x,y)}$ to $\mathrm{(x^*,y^*)}$ represents the deformation that has occurred between the two images.

Correlation is initiated at a user defined coordinate known as the 'seed point'. The results obtained at the seed point are used by the correlation algorithm to form the first iteration of analysis at the second point and so on until the entire area of interest is analysed. Consequently, the optimum position of a seed point is where the least deformation is anticipated.

The size of the subset can have major implications on the resolution of the final interpolation. A greater number of subsets enables a better resolution; however, the practicality of any given subset size is dependent upon the texture or pattern used. For example, a particular subset may encompass an entirely black field (Figure 4.14a). This makes accurately matching the deformed subset difficult as matching will occur too frequently across the entire field producing errors in black areas. To compensate, the subset size can be increased (Figure 4.14b) so that there is a sufficiently distinctive pattern within the area though this is at the expense of spatial resolution. If the speckle pattern is too fine, the specimen may not be accurately represented due to aliasing.

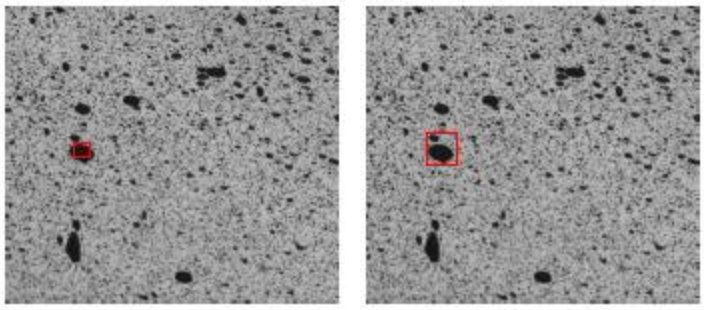

a) b)

Figure 4.14 Subset size limitations (a) small subset and (b) large subset (after Correlated Solutions 2010).

The pattern applied to the object's surface is therefore highly influential on the successful correlation process. There exist three main criteria for an appropriate

speckle pattern. Firstly, high contrast must be maintained during image capture to ensure a consistent, easily distinguishable pattern for subset matching. Secondly, the pattern must be isotropic to allow for correct determination of motion vectors and lastly, non-periodic as repeating patterns may lead to mis-registration of subsets. Examples of poor pattern characteristics are illustrated in Figure 4.15.

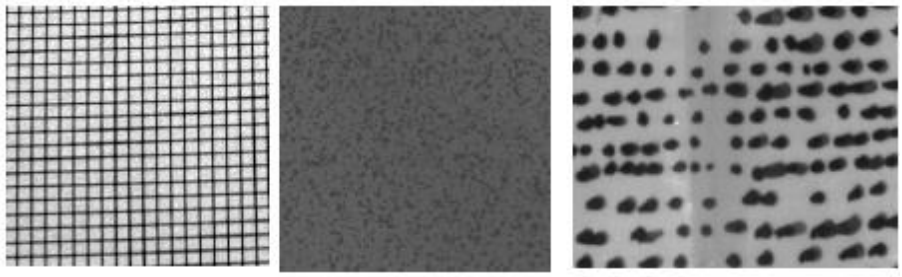

Figure 4.15 Example poor speckle patterns (after Correlated Solutions 2010).

The application of 2D-DIC provides in-plane displacements and strains; however, out-of-plane displacement introduces error into these measurements. Therefore, the stereoscopic sensor setup developed in3D-DIC has improved the accuracy of in-plane strain calculations when analysing both planar and non-planar shapes. In using a stereoscopic setup, each point on the object surface is focused as a specific pixel on the image plane by both cameras. By knowing the geometric position and orientation of each camera, the position of that object point can be calculated in three dimensions. Strains are only defined in the tangential plane of the surface, though out-of-plane displacement may be output.

Calibration is vital to the accuracy of the DIC system. It is this that provides the metric information that describes the physical camera position and orientation which is necessary for the conversion of the image coordinate to a geometric coordinate by the correlation software. Two types of parameters are defined during calibration, intrinsic and extrinsic. Intrinsic parameters relate to the internal geometric and optical aspects of each camera e.g. focal length, aspect ratio and sensor centre. Extrinsic parameters define the relationship between the two cameras. The X, Y, and Z displacements between the cameras and the angles between the cameras (alpha, beta, gamma) are calculated. It is

therefore important that the camera-sample system is not disturbed after calibration. The calibration process involves compiling images of a calibration plate subjected to a series of random orientations and angles at the same approximate distance as the object under analysis i.e. within the focused depth of field (Figure 4.16).

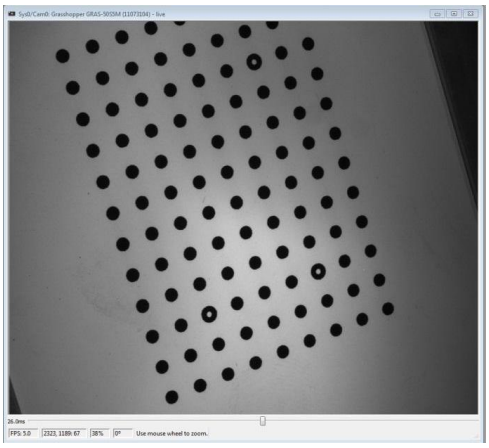

Figure 4.16 Calibration plate.

4.4.5.2 DIC laboratory setup

The direct tension test, having been set up as described in section 4.4.2, was monitored using the Vic-3D Digital Image Correlation equipment (Correlated Solutions Ltd., 2010). Given the time involved in analysis and post-processing of captured images, monitoring was restricted to testing of the artificial soil (Section 4.4.1.2).

The pale kaolin-based soil provided the perfect contrasting colour on which to apply the speckle pattern required. This was done using black aerosol paint applied from an appropriate distance to achieve the specified dispersal and coverage i.e. a fine 50/50 black and white pattern (Figure 4.17). The sample surface was prepared by way of removing any residual lubricant used in the sample formation process as this inhibited the adhesion of the paint.

Figure 4.17 Sample with speckle pattern.

Two high resolution cameras were mounted on a profile bar positioned vertically above the testing rig at a distance of approximately 150mm apart and approximately 300mm above the upper, exposed surface of the sample. They were positioned symmetrically about the sample so as to keep a consistent magnification between the images. The cameras were fitted with telephoto lenses of 28mm focal length; this was considered the appropriate selection given the anticipated depth of field required during the essentially horizontal motion of the sample. Additional cold source lighting was positioned to maintain the optimum speckle pattern contrast. The final setup described may be seen in Figure 4.18.

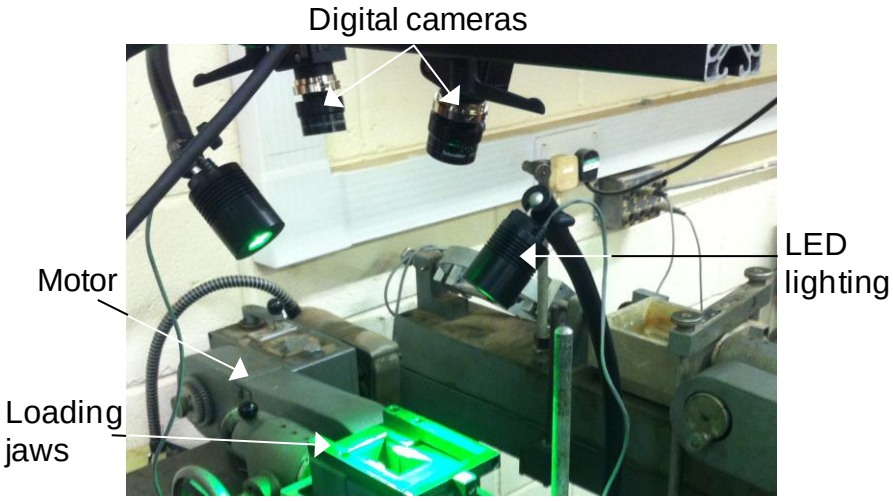

Figure 4.18 Direct tension test DIC setup.

The sample image taken by each camera was then focused manually using a combination of lens aperture, exposure and focus. These three variables interact and the optimum setting requires several adjustment iterations. A clear, sharp image where speckles are easily defined is required. To minimise the

effects of motion blur, exposure is ideally set to a minimum (26ms) with the aperture increased to compensate for the reduced light input. However, an increased aperture can easily result in over-exposure as demonstrated in Figure 4.19. Areas of over-exposure cannot be analysed by the correlation software.

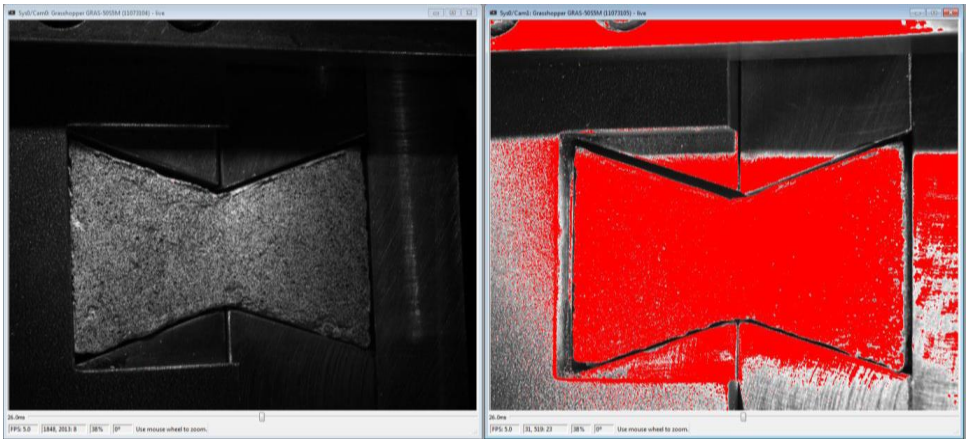

Figure 4.19 Effects of aperture: correct aperture (left) and oversized aperture (right).

An increased aperture size causes a reduction in the depth-of-field. This is the range in distance from the camera within which out of plane movement can be acceptably resolved. This is not of concern given the essentially 2D analysis required of the plane on which the sample is displaced.

Finally, the lenses are focused separately by applying the maximum digital zoom via the image capturing software in order to observe the speckle pattern at the pixel level. The focus is adjusted until the best contrast is seen between the white background and the black speckles. It is at this point that the 2-30pixel sized speckle condition for effective analysis is confirmed. This process is repeated for the remaining camera to achieve the sharpest images possible.

In order for strains to be calculated accurately during post-processing, the set-up was calibrated. A selection of calibration plates is available specific to the field of view size. The plate used consisted of points spaced 6mm apart and is positioned in place of the sample in a series of random orientations during manual image capture as shown in Figure 4.20 . A total of 30 images were obtained and compiled as part of the stereo system calibration function of the VIC-3D software (Figure 4.21).

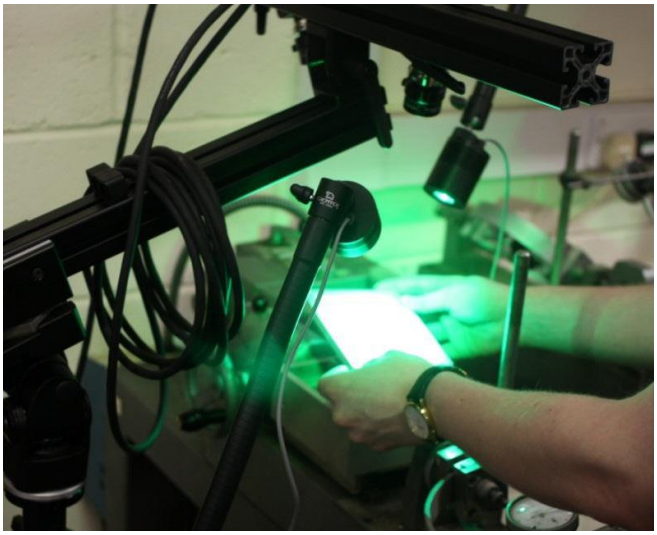

Figure 4.20 Orientating calibration plate.

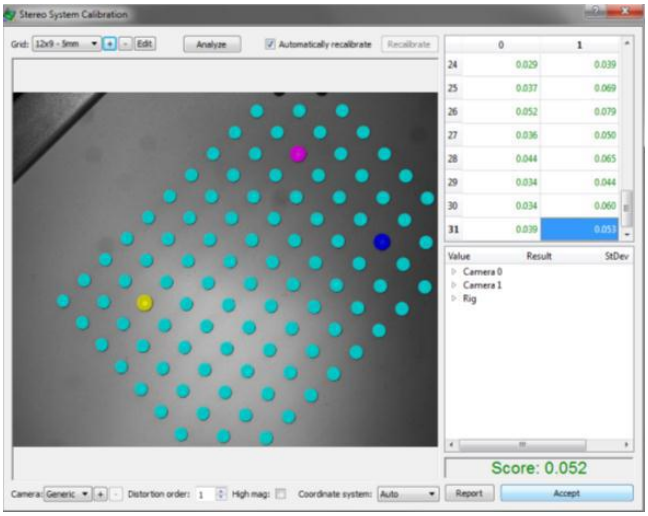

Figure 4.21 Stereo system calibration.

Following calibration, image capture was undertaken automatically at a frame rate of 5 frames per second (200ms intervals) during testing. An area of interest is defined on the reference image consisting of the speckled ‘bowtie’ surface (Figure 4.22a). This step defines the area over which the analysis will be performed and cannot be changed in subsequent images. The ‘subset’ grid was then defined within the area of interest (Figure 4.22b). A subset of 45x45 pixels was used for all analyses due to the consistent speckle pattern used. Since fracture is expected to occur across the centre of the sample, two ‘seed points’ were used to ensure a continuous analysis across as much of the sample surface as possible including post-fracture.

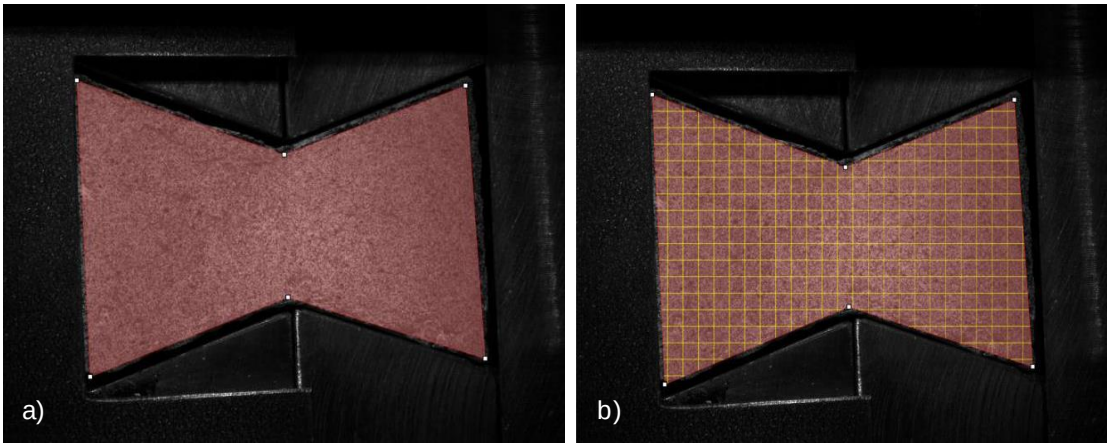

Figure 4.22 Reference image (a) Area of interest and (b) Subset.

A preliminary analysis was then performed using only the reference image to confirm the system recognition of the speckle pattern contained within the area of interest and that an appropriate subset was input. This is confirmed by the output of a continuous (as few gaps as possible) contour plot of the sample surface shape. Since only the reference image is required for checking, no strain or displacement data is shown at this stage.

In addition to using the DIC system to map the full-field strain development on the sample surface during testing, the software has allowed the mechanical behaviour of the loading jaws to be observed. Displacement of the jaws themselves has been tracked relative to markers placed in strategic locations (across jaws and within the captured field of view) shown in Figure 4.23. These markers have been tracked in post-processing giving an indication of jaw separation behaviour.

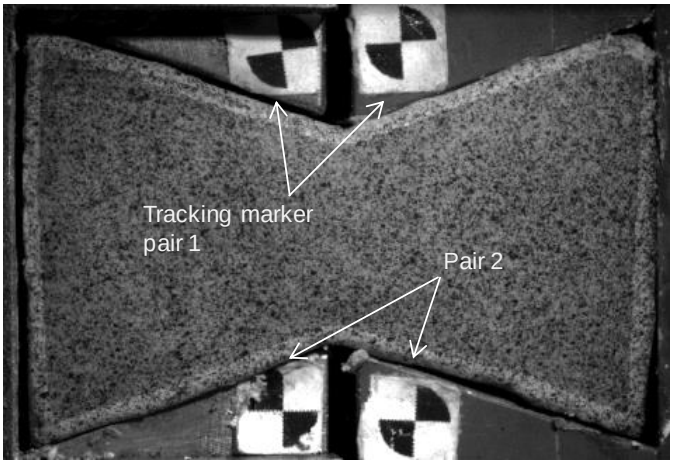

Figure 4.23 Tracking marker locations.

4.4.5.3 DIC analysis

Strain contour plots have been generated for representative direct tension tests at two water contents tested at two strain rates (Figure 4.24-Figure 4.27). Time series are provided to illustrate the development and distribution of strain parallel to the application of tensile stress. Within each time series, a consistent scale has been used to aid comparison and uses the following sign convention: positive strain = extension; negative strain = compression.

4.4.5.3.1 Testing at 1.22mm/min

A sample analysed at 20% water content with a displacement rate of 1.22mm/min is presented in Figure 4.24. It may be seen that tensile strain is initiated at approximately 120s into the test and originates at the lower vertex. After 180s a band of tensile strain is seen to have developed across the central portion of the sample between the vertices of the carriage jaw. However, at 228s a secondary tensile strain localisation is seen to have formed at the lower vertex of the restrained jaw. It is this concentration that is seen to develop into the site of eventual fracture after 240s. Fracturing manifests itself as gaps in the contoured data where correlation is not possible due to disintegration of the speckle pattern. The final fracture formation is shown in the photograph at 258s (Figure 4.24h). This series illustrates the localisation of tensile strain across the centre of the sample though the influence of jaw vertices on the initiation of fracture in a wet of optimum sample is highlighted. Little compressive strain is seen to have developed adjacent to the jaw interior suggesting that the clamping effect is well distributed outside the central sample area.

The same displacement rate was applied to a sample at 10% water content and is presented in Figure 4.25. Beginning at 5min into the test, strain is observed to develop across the sample in a similar manner to Figure 4.24. However, additional strains are seen adjacent to the restrained jaw interior. This is thought to be associated with the alignment of the sample within the jaw space and is discussed later with the aid of data obtained using tracking markers. At 336s, tensile strain is found to have localised about the narrow section of the ‘bowtie’. Importantly, this behaviour is shown to develop symmetrically about the axis of loading. From 342s fracture is observed to propagate towards the centre of the sample until full separation is achieved at 360s.

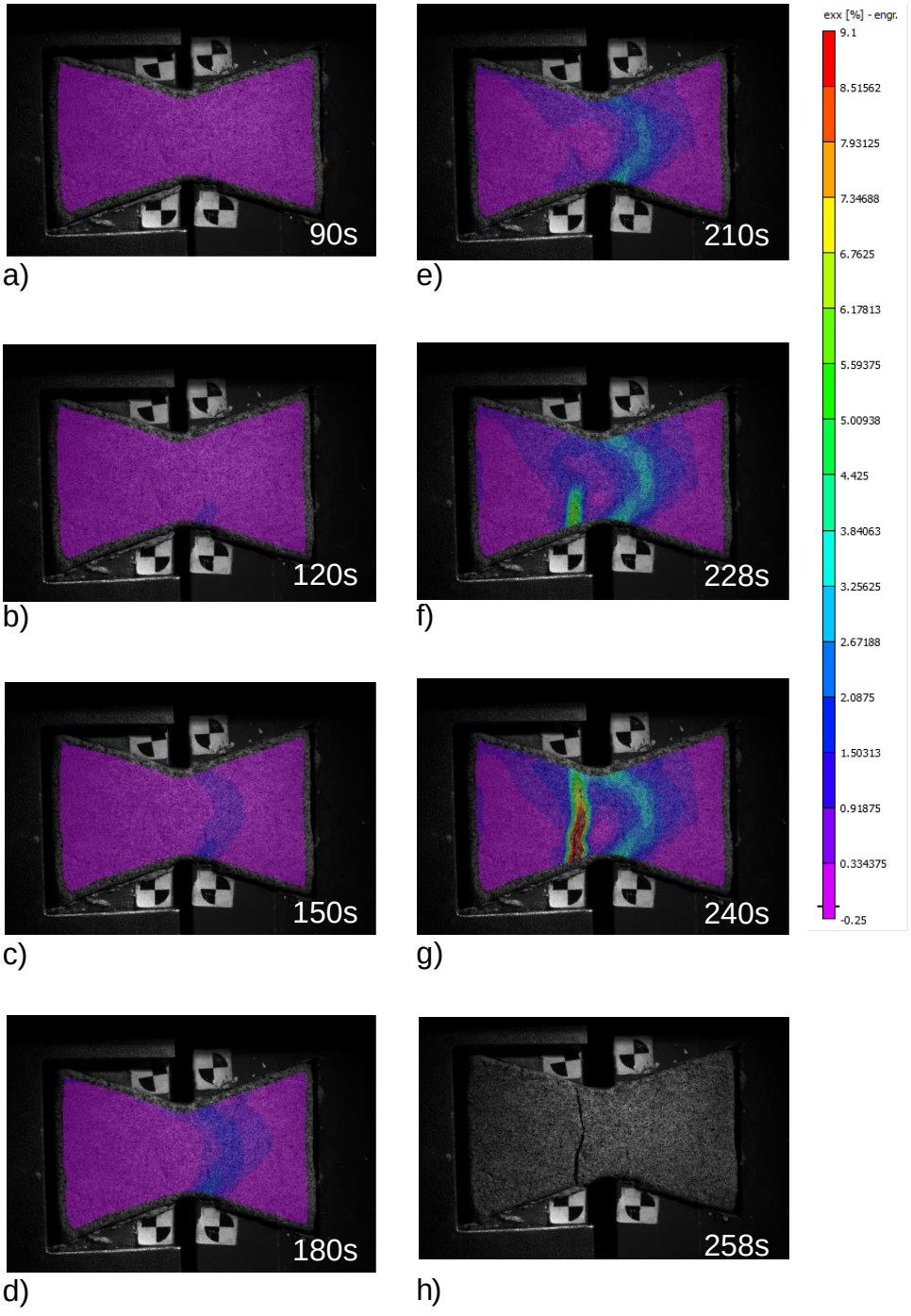

Figure 4.24 xx strain distribution in a sample tested at 20% water content at a rate of 1.22mm/min

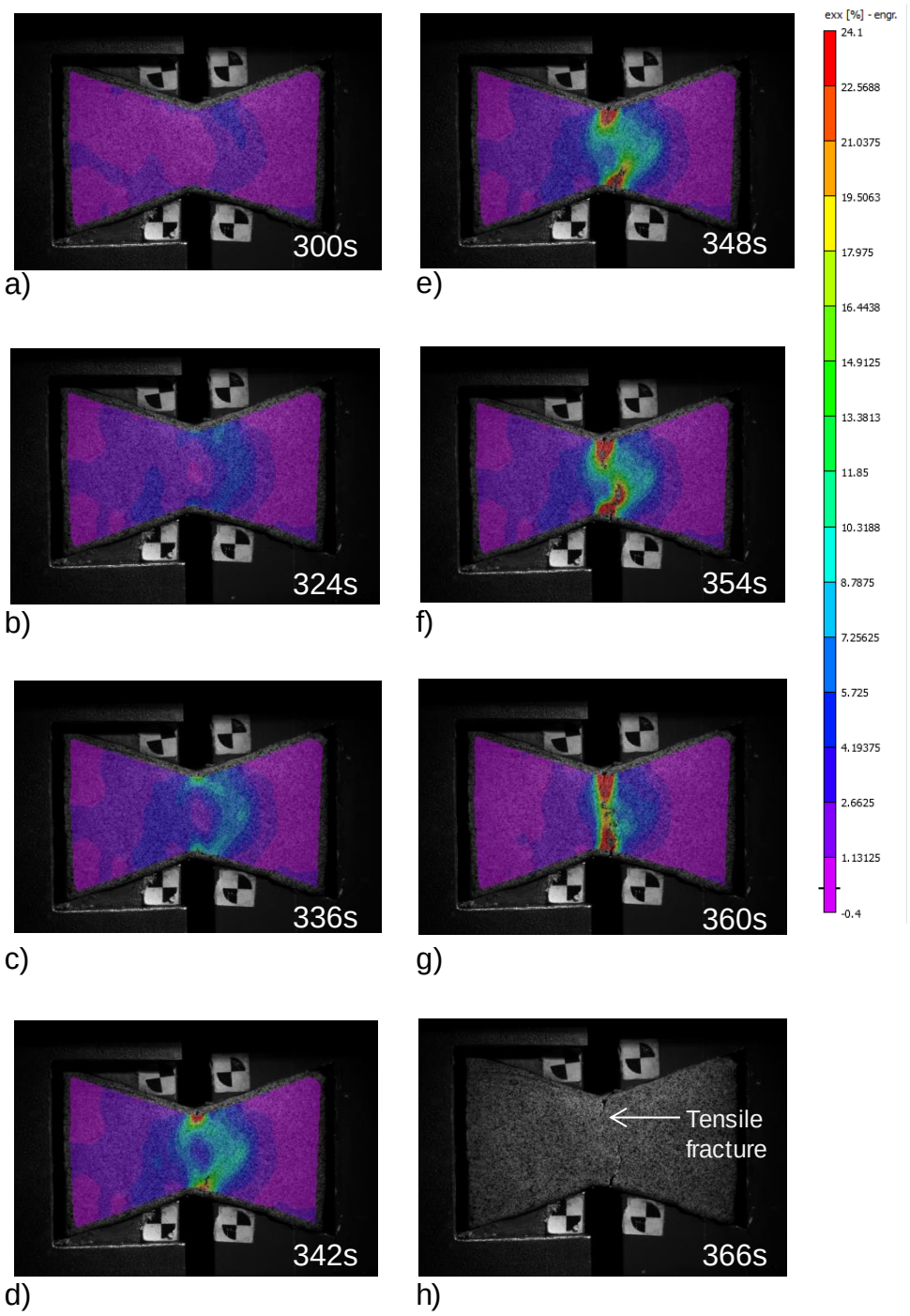

Figure 4.25 xx strain distribution in a sample tested at 10% water content at a rate of 1.22mm/min

4.4.5.3.2 Testing at 0.24mm/min

Two further samples at the same water contents were tested at the slower rate of 0.24mm/min. Figure 4.26 shows no dominant tensile strain concentration for the first 1080s of the test beyond a large region comprising approximately 50% of the sample surface at the middle of the sample. This is in contrast to the behaviour observed when tested at the higher rate. Between 1080 and 1440s, tensile strain concentrations are found to have developed at both sides of the narrow section and are shown to predict the propagation of fracture. The symmetrical development of failure strain at the narrow centre of the 'bowtie' is comparable to that of the 10% water content samples tested at both rates. The drier sample tested at the slow rate shown in Figure 4.27 exhibits the initiation of failure at both sides of the sample yet the upper strain concentration is localised about the left vertex. Unlike the wetter sample tested at the higher rate, the occurrence of this behaviour at only one vertex suggests the influence of misalignment of the sample, a trend observed in samples that have shrunk since formation due to drying.

Based on DIC analyses of samples at a variety of saturations it has been found that ultimate failure reliably occurs in the region between the loading jaws. However, the influence of the jaw vertices is seen to be greatest in wetter samples when testing is conducted at a high rate. That is to say, failure is more consistently observed to develop symmetrically at the narrowest portion of the sample when strained slowly. A full investigation into the effect of strain rate at varying saturation using DIC may be found in Davies (2012). As has been indicated by the distribution of strain in samples at 10% water content, the sample-jaw contact is thought to influence the alignment of loading and has been investigated further.

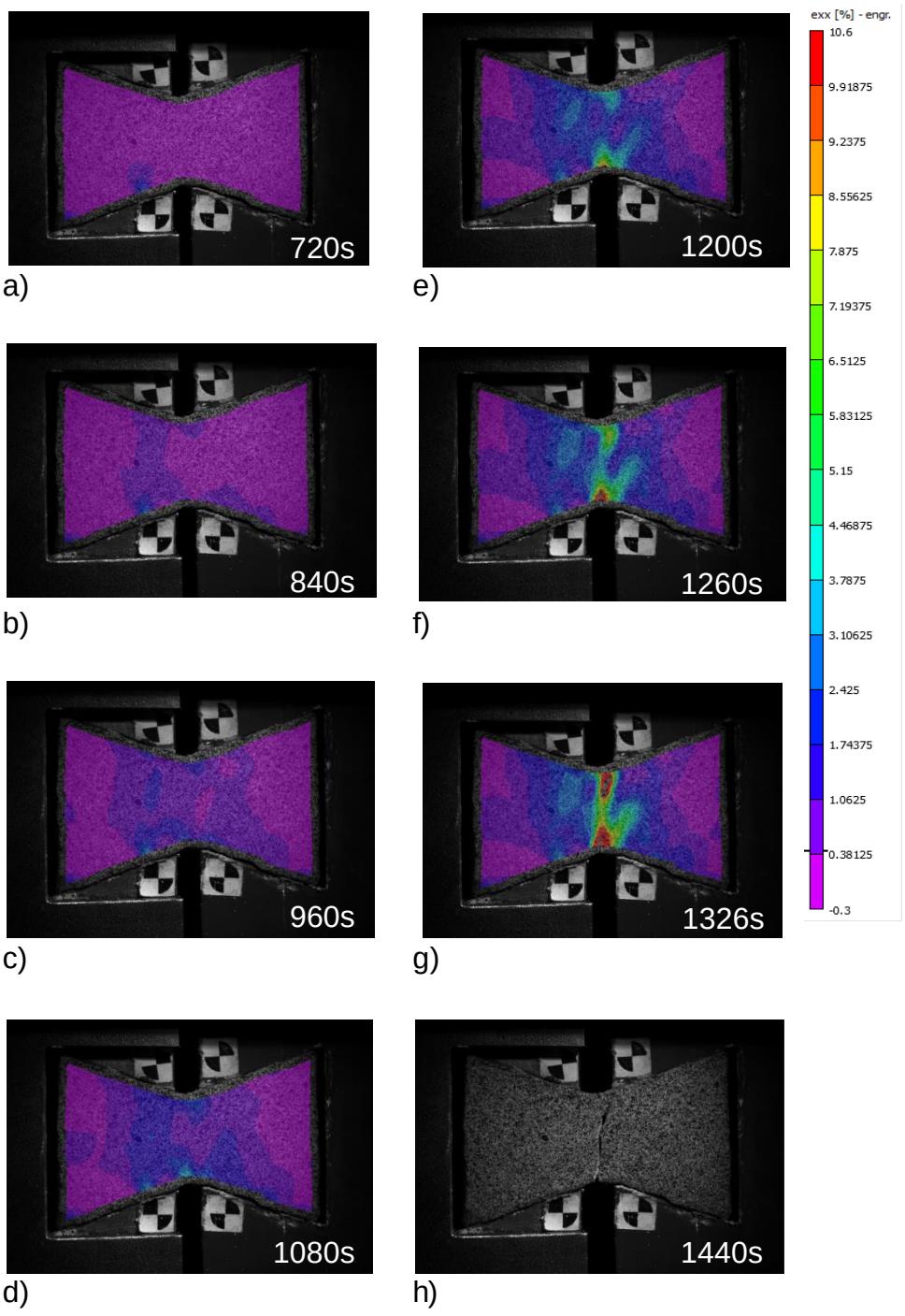

Figure 4.26 xx strain distribution in a sample tested at 20% water content at a rate of 0.24mm/min

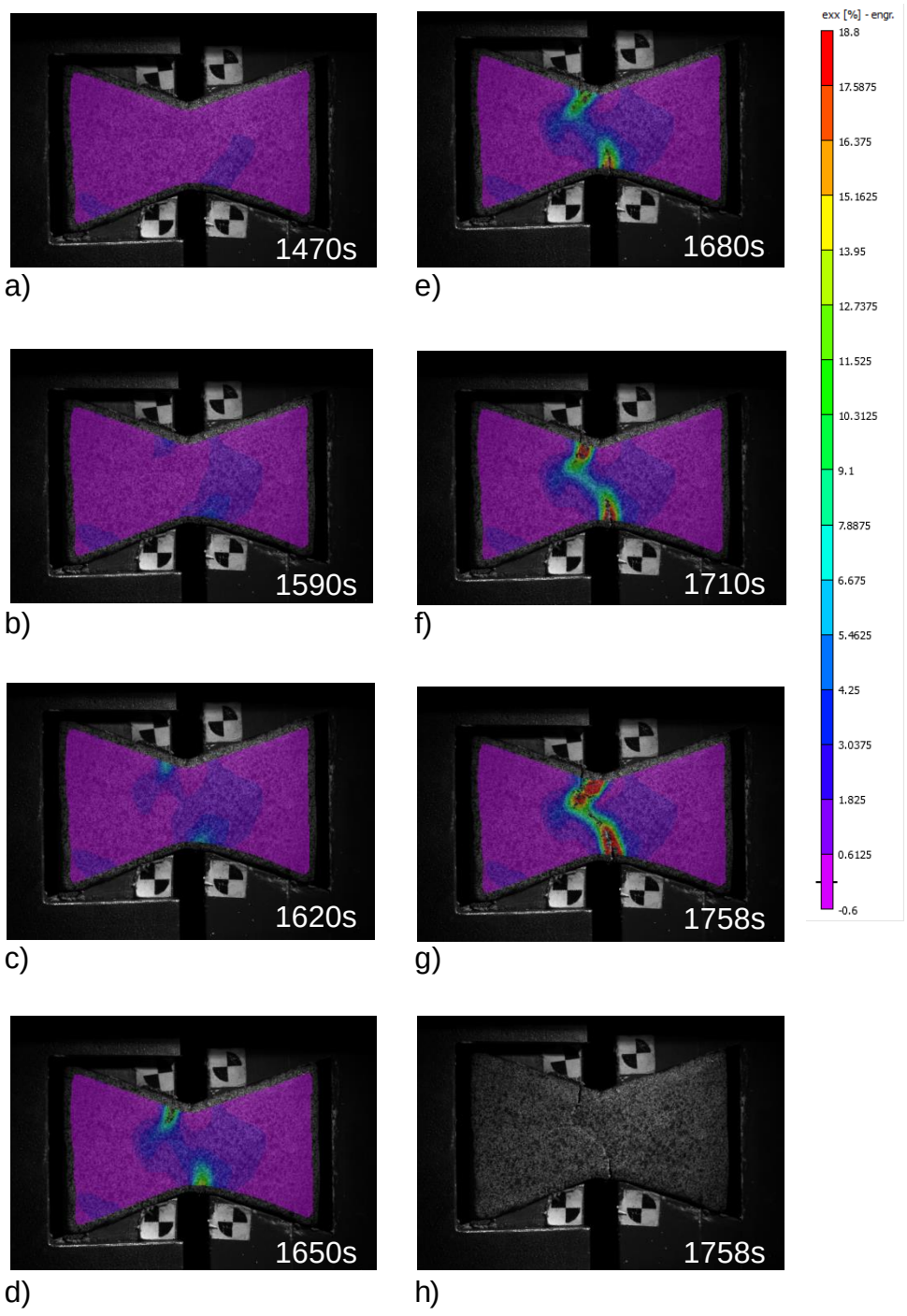

Figure 4.27 xx strain distribution in a sample tested at 10% water content at a rate of 0.24mm/min

4.4.5.3.3 DIC virtual extensometer

The difference in x-displacement between the two jaws for a series of tests on the kaolin-based soil was calculated using tracking data taken at the top (1) and bottom (2) marker pairs shown in Figure 4.23. Tracking at the top and bottom was undertaken to investigate the parallelism of the motion of the carriage jaws and the true rate of applied strain. Direct tension was induced in samples compacted at 22% water content using a motor rate of 1.22mm/min. Representative tracking results are presented in the following graphs alongside the constant, idealised motor displacement.

The results from jaw tracking during testing of a sample at the as-compacted water content are presented in Figure 4.28. It can be seen that the displacement of both sides of the carriage jaw is identical to the input motor speed for the majority of the test. This confirms that the applied motor rate is being translated into sample strain and that the jaws are parting in a perfectly uniaxial manner. The relatively weak, saturated material showed little resistance to the separation of the loading jaws and is noted to fit within the jaws with very little spare space i.e. full soil-jaw contact from the start of jaw motion. Sample failure correlates to approximately 400s where the tracked displacement is seen to deviate from that of the motor speed. The final portion of the tracking data shows an increased displacement rate; this is brought about by the softening of the soil linkage between the two jaws after failure and displacement recovery. The plot shows that the jaws are behaving correctly throughout the test up to the point of failure. There is very little misalignment in the path of the jaws and the sample is undergoing the desired application of external displacement.

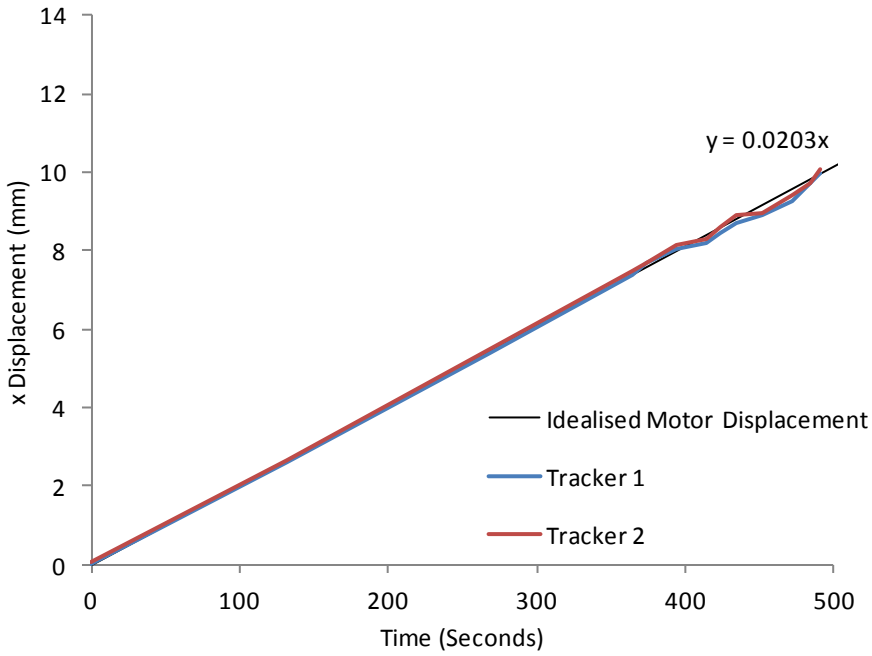

Figure 4.28 Tracking for sample at 22% water content.

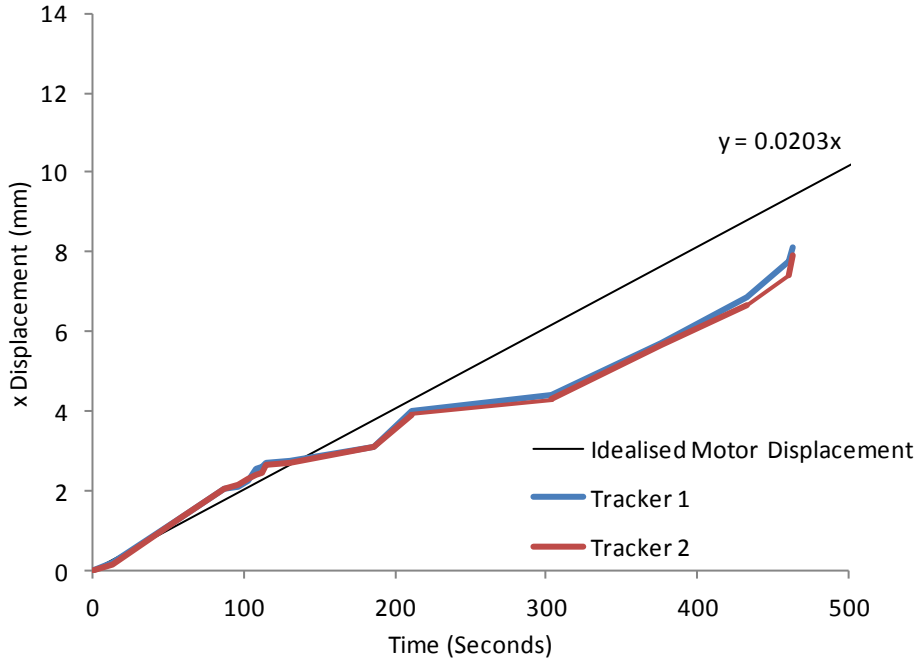

Figure 4.29 Tracking for sample at 5% water content.

In contrast, tracking data for a sample dried to 5% water content is seen to deviate from the intended motor speed after approximately 60-120s (Figure 4.29). At 120s the two sides of the carriage jaw show a brief difference in displacement. This is considered to be the product of sample alignment occurring when the sample comes into contact with the interior of either jaw having previously been free. The freedom of the sample during the initial portion of the test is a trait of samples tested in the drier condition. As part of the drying process, the clay samples underwent considerable shrinkage leading to free space between the untested sample and the loading jaws. The reduced displacement rate evident at 115-185s indicates a resistance to jaw separation due to the stiffness of the sample. At 185s the rapidly increased displacement is the result of slippage between the sample and the interior of the jaw. Another alignment event at approximately 210s sees the stiffness of the sample again reduce the rate of jaw separation. Full sample-loading jaw contact is observed for the remaining time of the test. However, the even displacement of the jaws diverges at 305s. Divergence is indicative of non-uniform jaw separation where one side of the sample is either able to slide against the interior jaw wall or fracturing of the sample has initiated at one side of the centre section. In the case presented in Figure 4.29, fracture has initiated at the top edge seen as a rate increase at tracker pair 1. The fracture continues to propagate until full separation is achieved at approximately 460s when both sides of the jaw rapidly and simultaneously increase in displacement rate. The period of full sample contact and therefore loading is found to be relatively short in comparison to the testing at 22% water content, as would be expected for a more brittle material. However, the ability to assess test configuration during testing has been restricted to the use of such tracking technology, an otherwise complicating procedure in the pursuit of a quick and simple tensile testing method. The facility to record true carriage jaw displacement would meet such a requirement and constitutes a significant recommendation in the further development of the apparatus.

4.5 Indirect Tensile Strength Testing

In the absence of a standardised tensile strength test for soils, the Brazilian test was used as a means of comparing results obtained from the direct test developed in this work.

The application of the Brazilian test to determine the tensile strength of any material requires a number of assumptions: that the material behaves with biaxial linear elasticity in two-dimensions and is homogeneous and isotropic in terms of its strength and elastic properties. It is these assumptions that rule this method inappropriate for use on saturated soils. However, as discussed by Frydman (1964), when soils are in a brittle condition, the method may be justified.

The Brazilian test method adopted herein is that of the ASTM D3967 – 08 (1984) whereby the disc shaped sample is diametrically loaded upon its circumference via the use of flat platens.

4.5.1 Sample preparation

The aforementioned three soil types were used for the purposes of Brazilian testing. In order to best meet the assumptions of the Brazilian test, the soils were tested at low water contents where elastic behaviour is most pronounced.

Test samples were formed from soils manually compacted into U100 cylinders. The same dry densities as samples tested in parallel using the direct method were chosen to allow for a fair comparison. Likewise, the same water content at compaction was used for each sample type i.e. samples tested indirectly and directly possessed the same dry density.

The compacted soil was allowed to air dry until considered suitable for dry cutting. Disc samples were cut to a thickness-to-diameter ratio of 0.5 (within the ASTM recommended 0.2-0.75 range). At this point, half the discs were then wrapped in plastic film and left to equilibrate for 24 hours. The remaining discs were allowed to continue drying for a further 7 days before being wrapped and allowed to equilibrate. Cemented soil discs were wrapped immediately after compaction and left to cure for 7 and 21 days prior to air drying, in the same

manner as samples produced for direct testing. Cemented soil discs were cut and tested within a 4 hour interval.

4.5.2 Testing procedure

As recommended by the ASTM (1984), a constant rate of loading such that the sample fails between 1-10 min was employed. This was back-calculated from tensile strengths obtained during preliminary testing. On average, all tests took 7-8min from initial loading to failure. Compression loading was provided using an Instron 5585H universal testing machine fitted with platens conforming to section 5.2.1 of ASTM D3967 – 08. The sample specific loading rates are provided alongside the general test conditions in Table 4.2. Mean water contents stated represent those established through oven drying and mass balance immediately following the completion of each test.

Table 4.2 Brazilian test conditions.

Test #	Material	Mean water content (%)	Mean dry density (Mg/m^3)	Curing time (days)	Loading rate (kN/min)	# Tests conducted
1	Artificial mix	7.4	1.65	-	0.12	3
2	Artificial mix	15.2	1.65	-	0.06	4
3	Nafferton clay	5.7	1.56	-	0.20	3
4	Nafferton clay	17.9	1.56	-	0.12	4
5	Cemented soil	1.0	1.87	21	0.10	3
6	Cemented soil	13.1	1.87	7	0.06	4

Samples were loaded until brittle failure was observed by way of vertical fracture across the sample diameter. Following ASTM guidance, tensile strength was calculated from P, the load corresponding to failure and the thickness and diameter of the sample using Equation 4.3.

$$\sigma_t = \frac{2P}{\pi D t} \quad \textbf{4.3}$$

The failure load is defined as the maximum applied load measured and is recorded immediately prior to the abrupt loss of stiffness where it is no longer possible to maintain a constant loading rate. It is important to note that up until this failure load, the sample is believed to be fully intact and may therefore be

assumed to behave linear elastically. Such behaviour is supported by the trends observed in the load-strain relationships presented in the following section.

4.5.3 Testing results

The average tensile strengths of each soil type under the 6 saturation conditions are provided in Table 4.3.

Table 4.3 Results of Brazilian tests.

Test #	Material	Mean water content (%)	Mean failure load (kN)	Mean tensile strength (kPa)	Standard deviation (%)
1	Artificial mix	7.4	0.91	116.00	5.74
2	Artificial mix	15.2	0.62	79.20	14.51
3	Nafferton clay	5.7	1.62	206.77	20.26
4	Nafferton clay	17.9	0.52	66.24	11.87
5	Cemented soil	1.0	0.71	90.74	3.52
6	Cemented soil	13.1	0.40	50.81	8.84

Load and vertical strain data recorded externally using the testing rig load cell and displacement transducer for representative tests of each sample condition are presented in Figure 4.30. Load take-up and post-failure data has been removed for clarity.

It may be seen that there are two dominant trends in the load-strain behaviour. Samples tested at the lower water contents (Tests 1, 3 and 5) exhibit a relatively stiff response to loading and show a broadly linear trend. This is with the exception of Test 1, the wetter of the low water content samples which is seen to deviate from a linear elastic trend beyond 0.6% strain. These drier samples were found to fail at higher compressive loads than those samples at higher water contents. Tests 2, 4 and 6 show an increasingly softer response with increased loading- a more plastic behaviour.

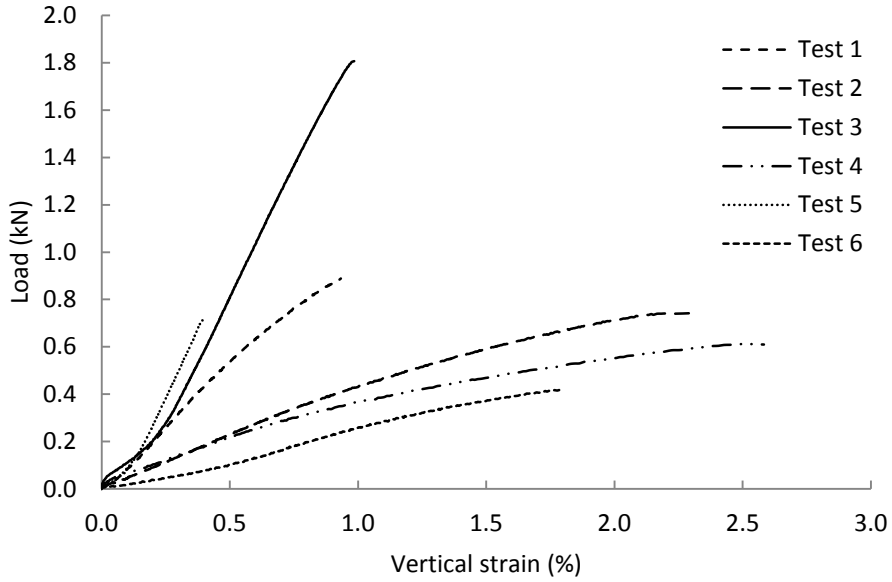

Figure 4.30 Representative load-vertical strain relationships for all test conditions.

4.5.4 Brazilian test DIC

The digital image correlation technique described in section 4.4.4 was used to evaluate the validity of the Brazilian tests conducted on soils. The pale kaolin based material (artificial mix) provided the ideal, pale colour for application of the DIC technique and was used in a 'dry' (D) and relatively 'wet' (W) condition. The results of each individual test are presented in Table 4.4.

Table 4.4 DIC test IDs and results.

Test ID	Water content (%)	Tensile strength (kPa)
D1	8	112.26
D2	6	113.14
D3	9	122.62
W1	16	60.83
W2	14	94.44
W3	15	86.10
W4	16	75.40

Samples were prepared in a similar manner to those used in direct tensile testing. Black aerosol paint was applied to the face of the soil discs to produce a fine speckle pattern with approximately 50/50 paint coverage to pale clay. A 3D system was setup comprising two high resolution digital cameras fitted with

telephoto lenses of 28mm focal length as shown in Figure 4.31. The system was calibrated using a 6mm calibration plate prior to testing. Calibration confirmed a camera separation of 249.0mm with a distance of 276mm from the sample position. Cold source lighting was added to ensure sufficient contrast between the speckle pattern and the soil colour. An exposure of 42.5ms was found to produce a consistently sharp image while avoiding the risk of over exposure during the tests and image capture was conducted at an interval of 500ms.

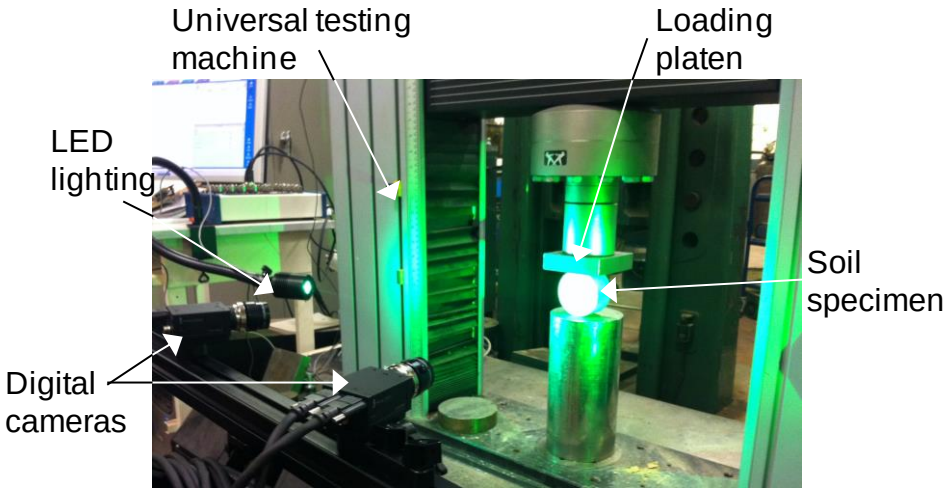

Figure 4.31 Brazilian test DIC setup.

Before testing of soil discs, the setup was confirmed to correctly interpret displacement from processed images using the following method. Markers were placed on the front edge of both the upper and lower loading platen. A rubber dummy sample was then mounted between the platens and a constant load applied while image capture was performed. Using inspection tools available in the post-processing software, vic-3D, the distance between the markers was measured at 9 stages of the test. These measurements are plotted in Figure 4.32 alongside the displacement data recorded by the loading machine transducer. It can be seen that the two methods correlate very well.

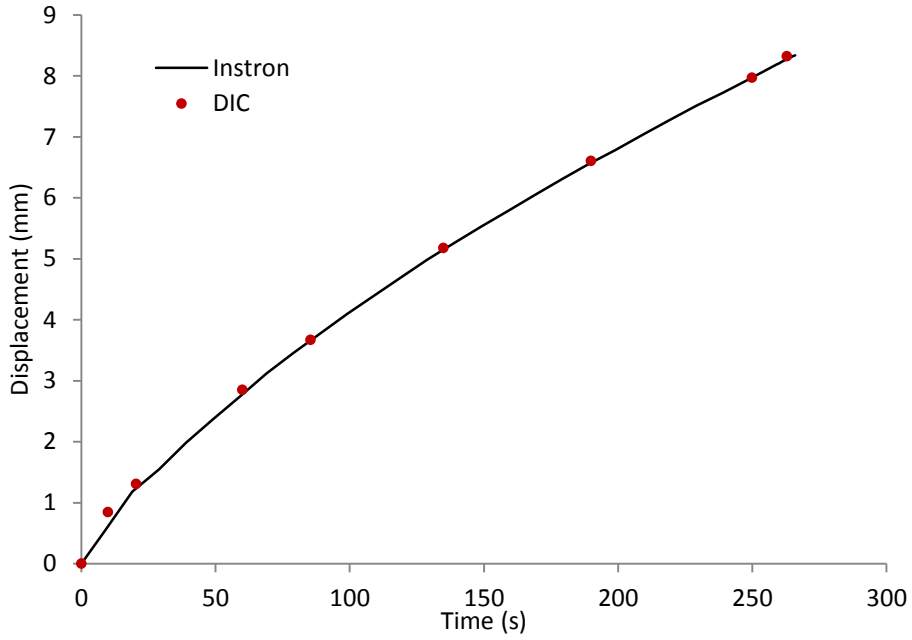

Figure 4.32 Correlation of platen displacement measurement methods.

A time series of contoured strain plots has been produced by post-processing and show the development of the full-field strain across the face of discs from representative tests. A constant percentage strain scale has been applied for each contour plot to aid comparison between individual plots. These plots adopt the following sign convention: positive strain = extension; negative strain = compression.

4.5.4.1 'Dry' clay strain development

Vertically orientated strains developed during testing of a sample at 9% water content are presented in Figure 4.33. It can be seen that vertical compressive strain is initiated at the loading points of the disc. These compressive zones then increase in size and intensity for the duration of the test. It is important to note that the distribution of compressive strain is restricted to a relatively narrow region diametrically positioned between the loading points. The increase in strain magnitude is seen to accelerate approaching failure at 378s. The same time series is presented showing horizontal strain in Figure 4.34. Tensile strain is seen to initiate immediately at the loading points and is bounded by regions of horizontal compression. Similar to the vertical compressive strain behaviour, the tensile strain zones are found to develop in intensity for the duration of the test.

However, tensile strain is found to propagate along a much narrower path across the loaded diameter.

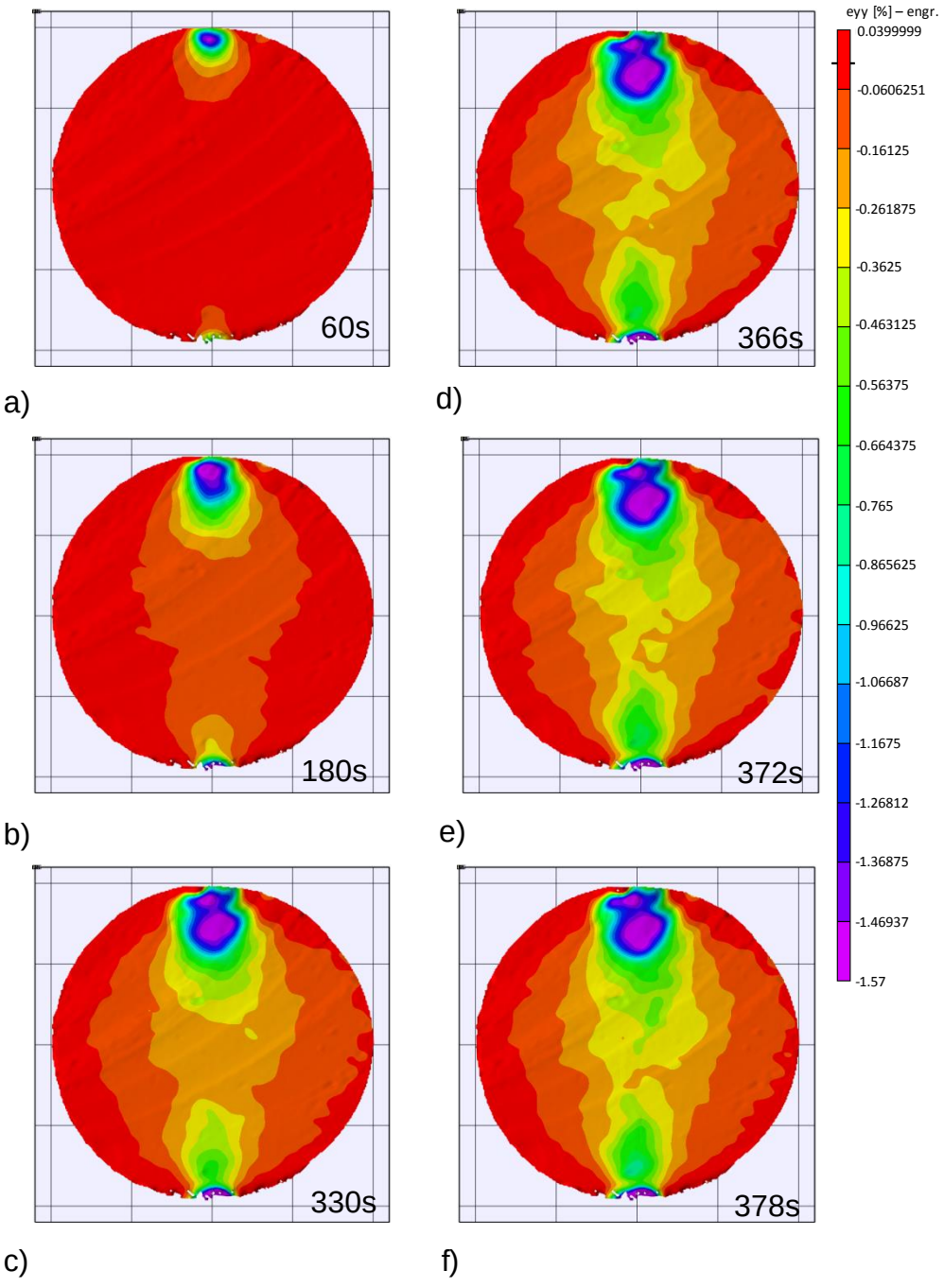

Figure 4.33 D3 yy strain development.

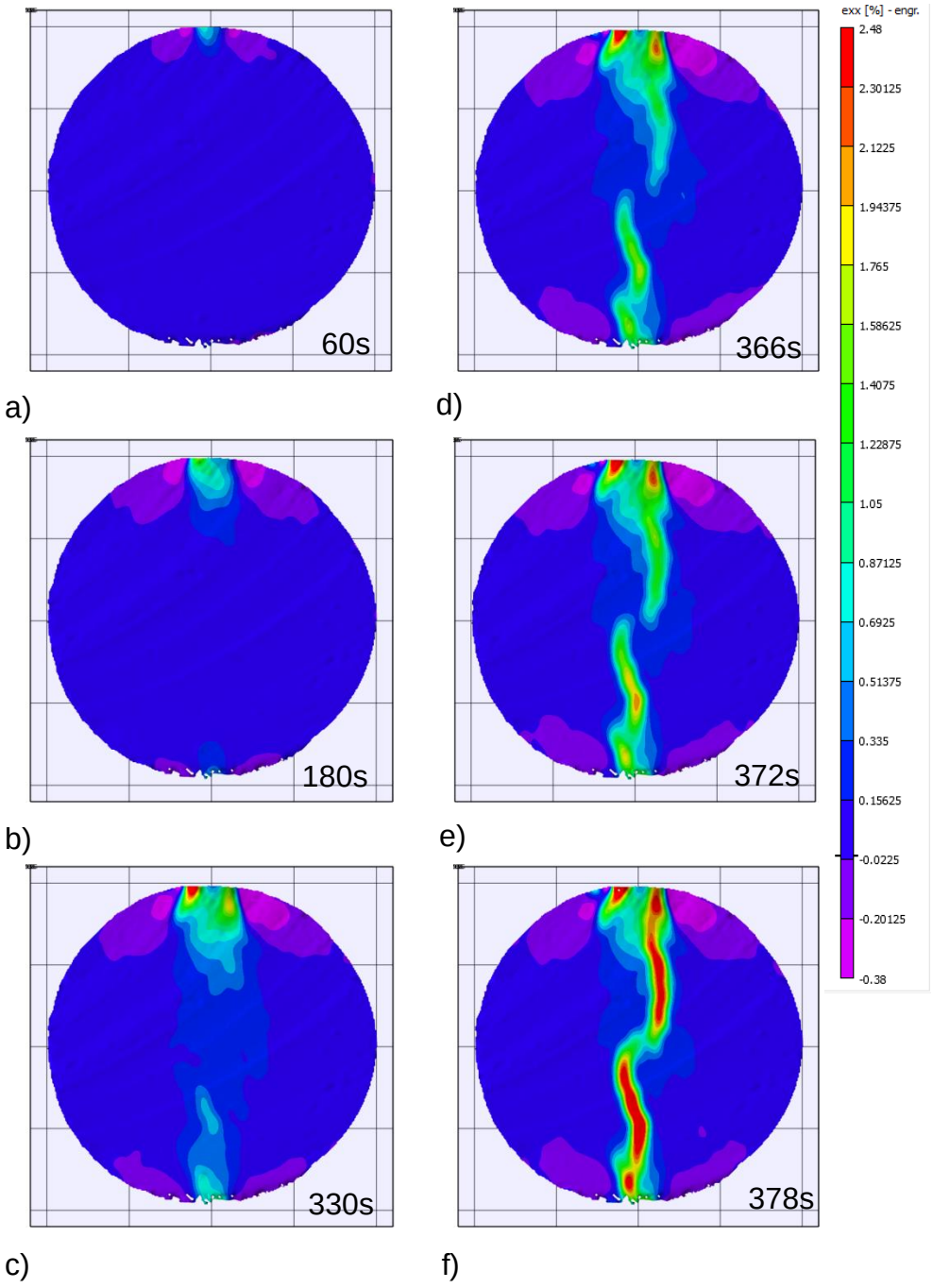

Figure 4.34 D3 xx strain development.

The pre-failure horizontal strain distribution for all three ‘dry’ tests is provided in Figure 4.35. Once again, the same scale has been applied for the purposes of comparison. Maximum tensile stresses may be seen to have developed across the loaded diameter in tests D1 and D3. Test D2, at the lowest water content of all tests, shows the maximum tensile strain to be confined approximately 8mm below the upper loading point. This suggests fracture initiation and therefore

maximum tensile stress to have developed at this point. This is contrary to the assumptions upon which the indirect tensile strength is calculated.

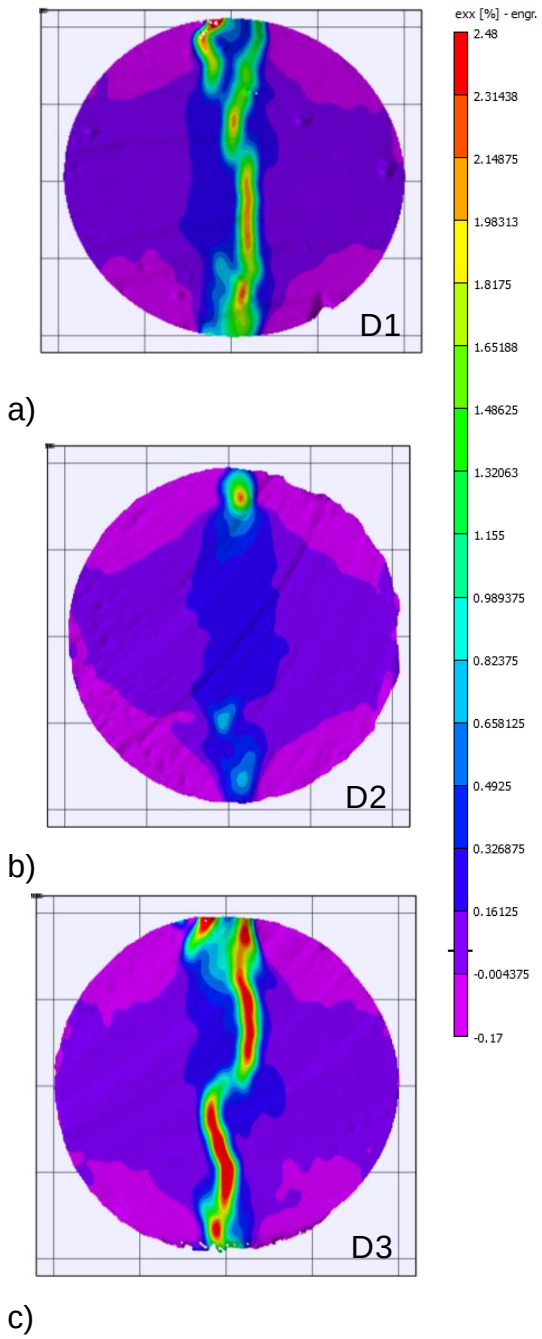

Figure 4.35 xx strain development in 'dry' samples.

Initiation of non-central failure has been highlighted in the use of flat platen loading during Brazilian rock testing monitored via DIC (Stirling et al., 2013). Uniform sandstone described as being linear elastic, homogeneous and isotropic was tested using three different loading methods: flat platen (ASTM, 1984), curved platen (ISRM, 1978) and flattened disc (Wang & Xing, 1999). The

DIC technique was used to investigate the influence of loading method and thickness-diameter ratio on the inferred development and distribution of compressive and tensile stresses. It was shown that the application of load to the disc circumference via a point contact resulting from the use of flat platens produced localised tensile stress generation in close proximity to the loaded ends of the disc. These locations are associated with the greatest degree of localised crushing. It was proposed that brittle failure originated at these isolated regions of tensile strain and not at the disc centre as per the theoretical ideal. The central initiation of failure was most reliably produced when using flattened disc circumferences. This work is provided in the Appendix for reference.

Over all, the trends in the observed strain field in the tested clays are found to be similar to those found in rock samples tested in the same manner, a traditionally more appropriate material on which to perform Brazilian testing. Therefore, on the basis of measured strain behaviour, the performance of the kaolin based soil at 6-9% water content is concluded to be acceptable for indirect tensile strength testing.

4.5.4.2 'Wet' clay strain development

The time-series of vertical and horizontal strains for test W4 are presented in Figure 4.36 and Figure 4.37 respectively. The plots span a longer time period than the previous time series due to a lower loading rate being used in the testing of 'wet' samples. As would be expected, compressive vertical strain is seen to originate at the loaded points of the disc. The main observed difference is that as loading continues, the width of the compressive strain region increases in response to the flattening of the loaded circumference. Maximum vertical strain is found to be almost 300% greater at failure in the testing of the 'wet' condition sample. This is a result of greater plastic deformation. Once more, the accumulation of strain is found to accelerate on approaching the failure load.

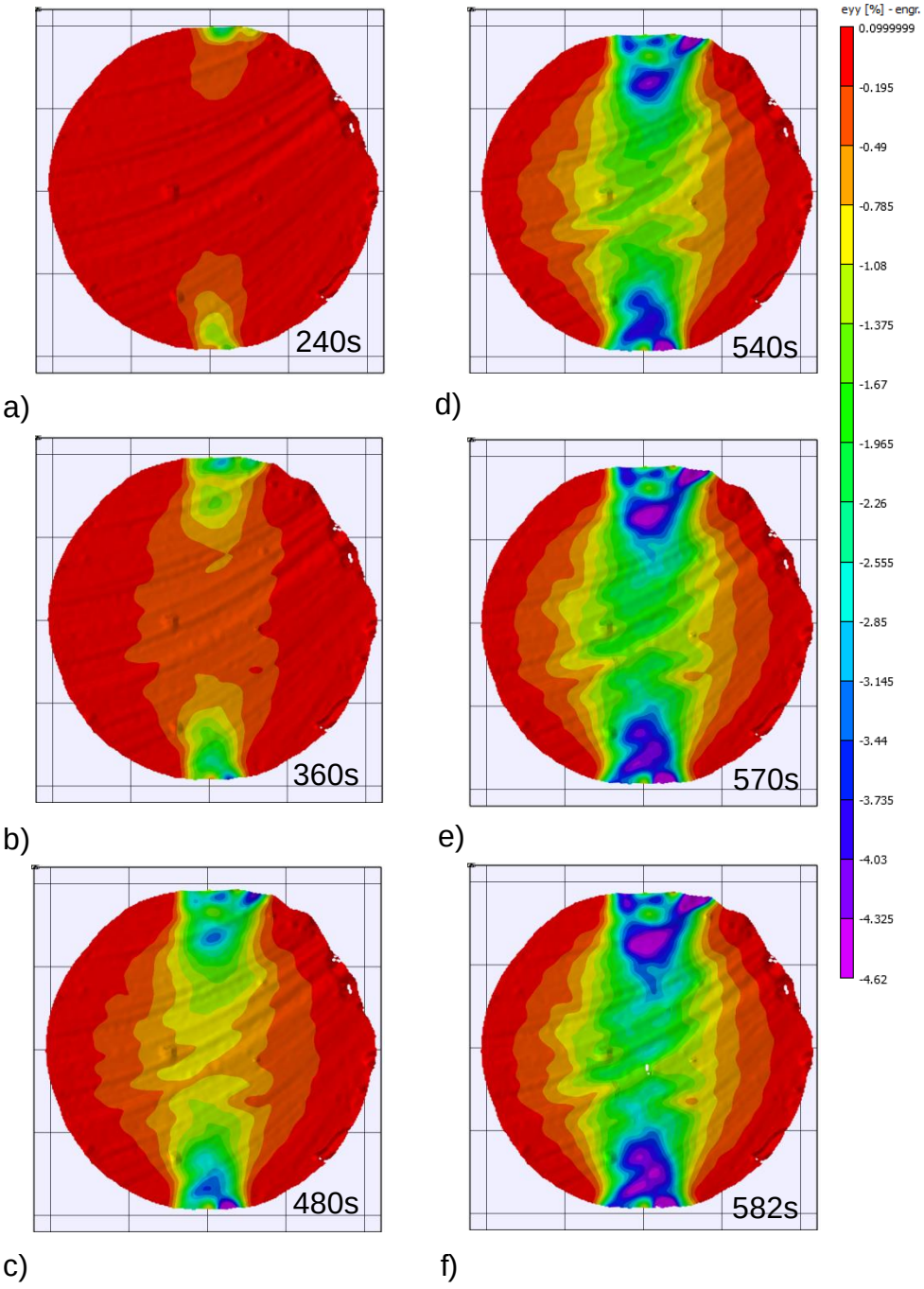

Figure 4.36 W4 yy strain development.

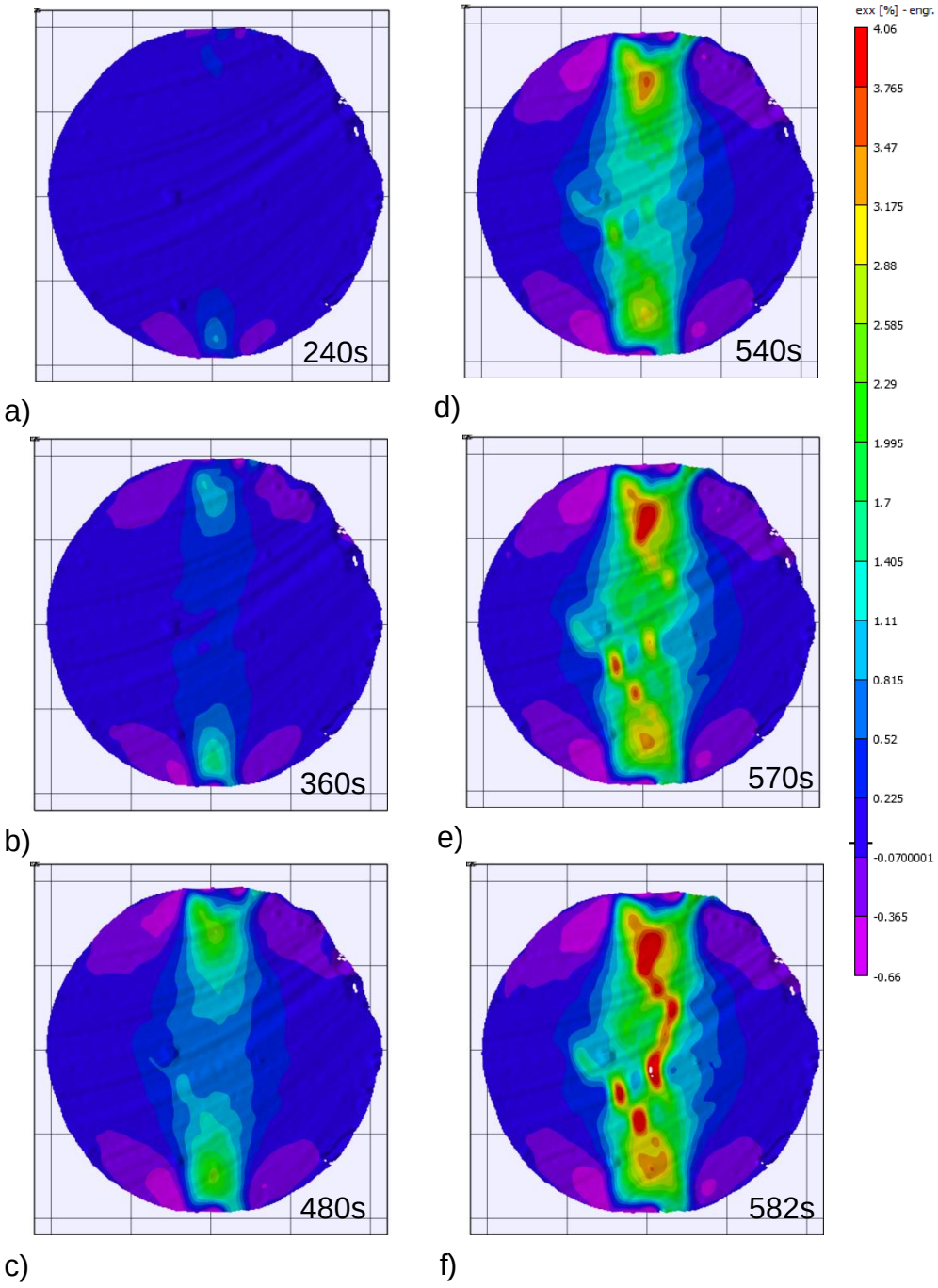

Figure 4.37 W4 xx strain development.

Tensile horizontal strain is again seen to initiate toward the upper and lower loading points, bounded by regions of slightly compressive strain. As the test continues, these tensile strains develop in magnitude and progress toward the centre of the disc. The broad diametric band seen in the vertical strain is found to build as the flattening occurs. Stirling et al. (2013) showed a very similar behaviour in the use of pre-cut, flattened disc ends in the testing of rock materials. Importantly, maximum horizontal extension is situated not at the

loading points but across the central portion of the disc. It was found as part of the rock testing schedule that by distributing the applied compressive load over flattened portions of the disc circumference, crushing was minimised and the most common location of failure initiation was at the centre. Although the soil discs were initially loaded across a circular circumference, the plastic deformation observed during the early stages of loading produced a very similar loading geometry to that proposed by Wang and Xing (1999) as discussed in Stirling et al. (2013). The horizontal strain distribution at failure for all four ‘wet’ tests is provided in Figure 4.38. The distribution of maximum tensile strain is contained within the band defined by the extremes of the flattened disc ends.

The ability of the image correlation processing software to track the distortion of the speckle pattern relies upon the integrity of the surface upon which the pattern is captured. An inability to calculate strain is visually expressed by an omission in the contoured data. Commonly, this occurs around the edge of the sample where material is least confined or where excessive strain occurs, i.e. crushing at the point of loading. However, this behaviour may be seen to occur in the zones of maximum tensile strain at failure in Figure 4.37 and Figure 4.38. This suggests deformation indicative of centralised disc fracture, a requirement for the reliable calculation of indirect tensile strength. Such behaviour was not seen in ‘dry’ sample tests due to the high fracture propagation velocity of the brittle material being greater than that of the image capture rate.

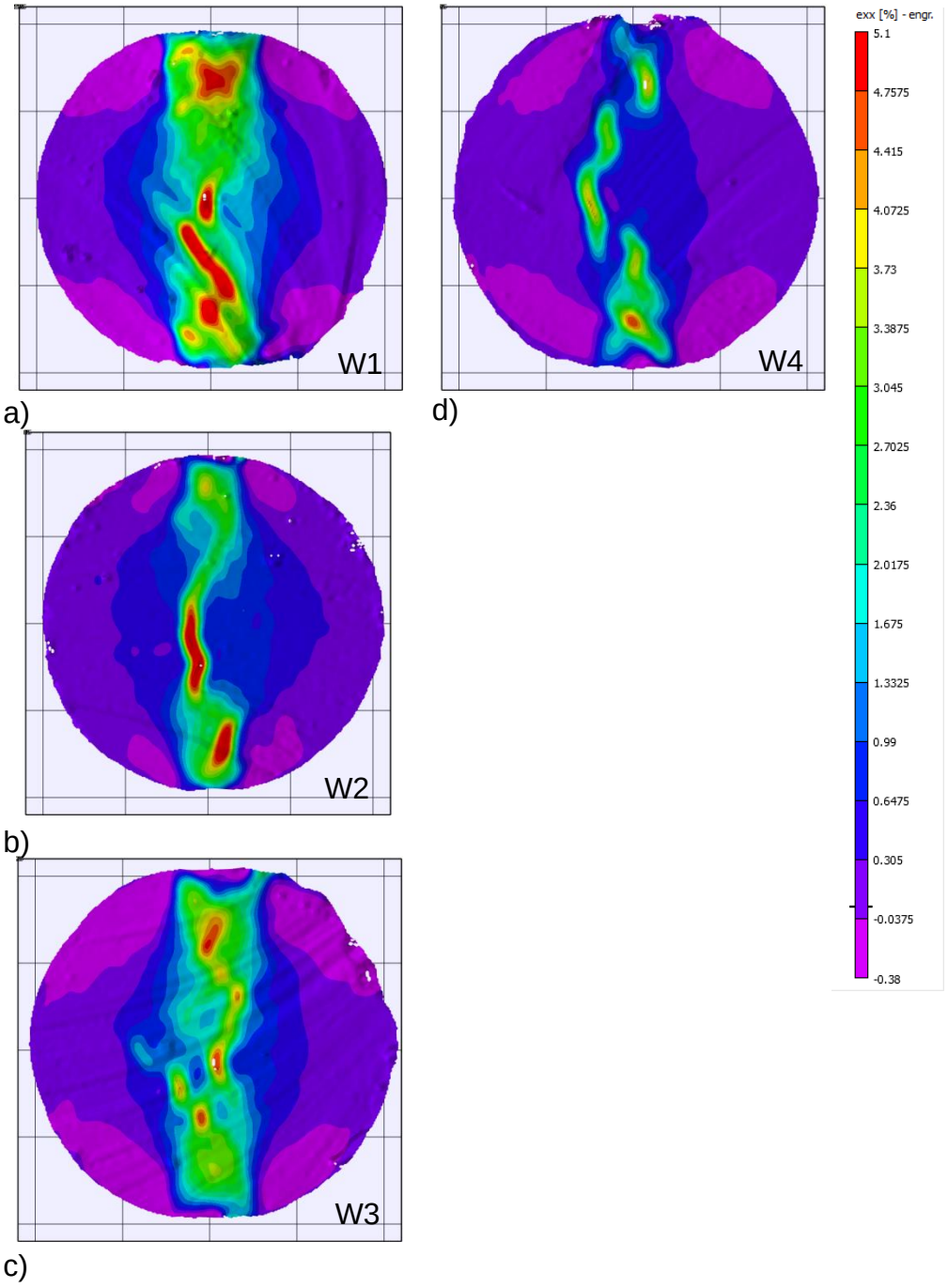

Figure 4.38 xx strain development in 'wet' samples.

On the basis of DIC assessment it has been possible to draw a number of parallels to the behaviour of materials traditionally used in Brazilian testing. Although there exist differences between the distribution of full-field strains in drier, more brittle soil discs to those of a higher water content, both have shown characteristic traits associated with the use of flat platen loading and modification of the disc geometry itself. This geometry modification is further investigated to establish the validity of tests where plastic deformation upon loading has resulted.

4.5.5 Frydman criterion

As has been described by Frydman (1964), when performing Brazilian tests on soil discs, appreciable deformation occurs at the point of loading in the form of flattening; a plastic behaviour. However, elasticity is still assumed throughout due to this plastic deformation being confined to the loaded circumference and not dominating the centre of the disc where the critical tensile stress is generated and indirectly calculated.

Acknowledgement of expected disc deformation is required to assess the validity of the classic relationship in Equation 4.3. Frydman (1964) concludes that the tensile stress generated in the centre of the deformed disc is given by Equation 4.4. The term $g(\sigma_x)$ acts to factor the standard expression for tensile stress by relation to the half width of the flattened area of the disc, a, and the half distance between these flattened areas, y_1. These parameters are illustrated in Figure 4.39.

$$\sigma_x = g(\sigma_x)\frac{2P}{\pi dt} \tag{4.4}$$

where,

$$g(\sigma_x) = -\frac{d}{2a}\left\{2f - \sin 2f - \frac{2y_1}{d}\log\tan\left(\frac{\pi}{4}+\frac{f}{2}\right)\right\} \tag{4.5}$$

where,

$$f = \tan^{-1}\frac{a}{y_1} \tag{4.6}$$

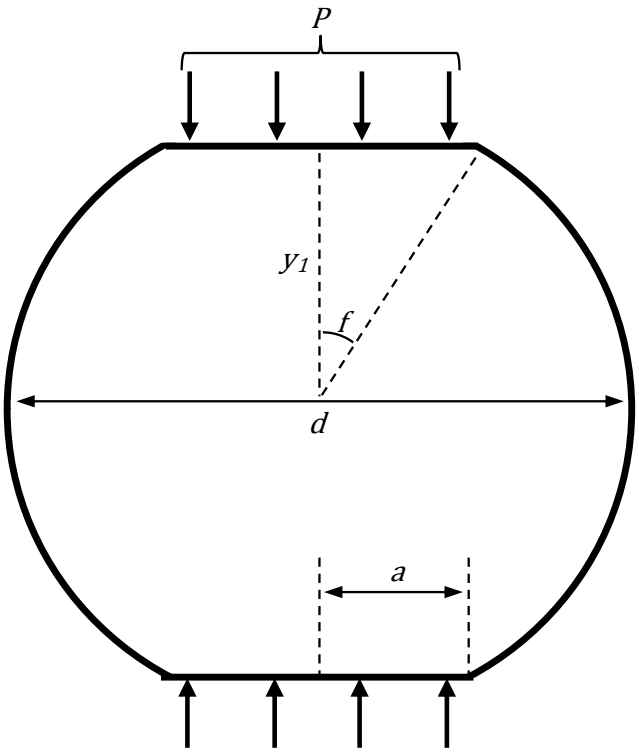

Figure 4.39 Flattened disc under load (after Frydman 1964).

It follows that as the ratio between the width of the flattened area and the distance between them increases, the condition expressed in Equation 4.3 is approached. Frydman (1964) asserts that should this ratio be ≤ 0.27 then it is appropriate to assume $g(\sigma_x) = 1$ within the accepted accuracy of the test.

As described in section 5.5.4, the DIC technique was used to assess the generation of the full strain field on the face of artificial soil samples. The high rate photography used in this process enabled dimensions of the discs immediately prior to failure (<500ms) to be recorded. Widths were measured at the upper and lower loading points and averaged. The distances between the flattened ends of the discs were recorded externally by the loading equipment. Figure 4.40 shows the recorded images before loading and at failure. The flattening of the loading points can clearly be seen in Figure 4.40b. The data relating to the Frydman criterion is presented in Table 4.5.

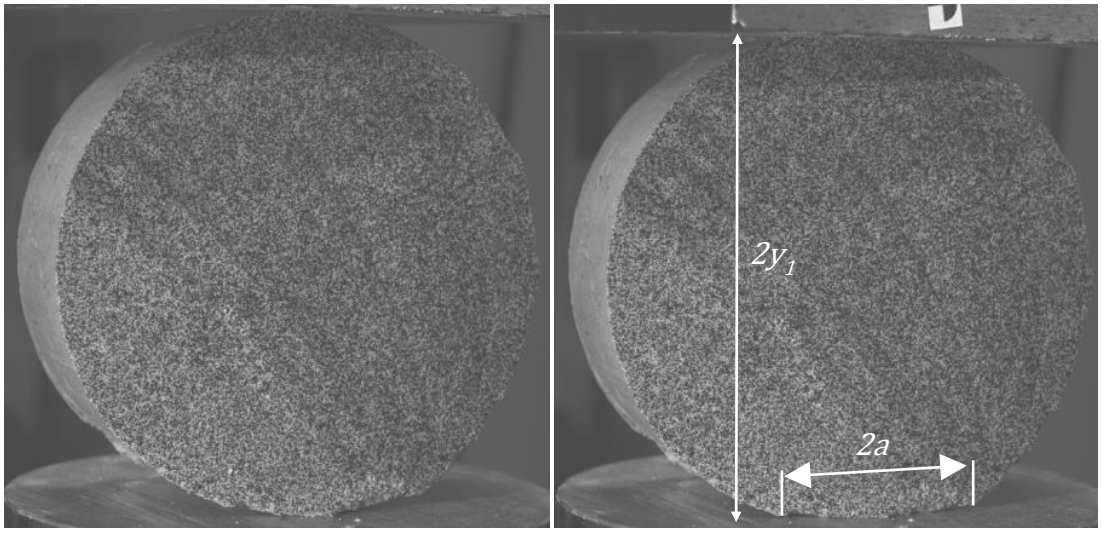

a) b)

Figure 4.40 Flattening of disc under loading (a) circular disc prior to loading and (b) flattened disc at failure.

The ratio y_1/a used to describe the degree of soil disc deformation can be seen to correlate well with the water content of each sample, where lower ratios are found for drier samples showing more brittle behaviour (Table 4.5). It is noted that all test ratios remain below the 0.27 value and therefore the simple tensile strength expression stated in the ASTM standard has been used with confidence.

Table 4.5 Frydman Brazilian test validity data.

Test ID	Water content (%)	Flattened area width (mm)			Distance between flattened areas, $2y_1$ (mm)	y_1/a
		Upper	Lower	Mean, $2a$		
SKB_D1	8	7.68	12.45	10.07	1.24	0.12
SKB_D2	6	11.88	12.32	12.10	0.93	0.08
SKB_D3	9	13.39	12.76	13.07	1.68	0.13
SKB_W1	16	29.01	28.98	29.00	6.02	0.21
SKB_W2	14	16.99	15.69	16.34	2.44	0.15
SKB_W3	15	22.53	19.45	20.99	3.39	0.16
SKB_W4	16	25.19	23.02	24.10	4.78	0.20

4.6 Final Comparison

The ultimate aim of conducting Brazilian tests is to compare the tensile strength values obtained with those measured alongside using the newly developed direct tensile strength equipment under identical material states i.e. density and water content. A comparison between the strength values measured using the direct and indirect methods is presented in Figure 4.41. The Nafferton clay is found to have the maximum strength difference of 40% measured at 18% water content. It is believed that this deviation is related to the greater heterogeneity inherent in any natural deposit. However, overall strength values are shown to compare very well with neither method consistently over or underestimating the tensile strength across the three soil types.

The correlation between the established indirect and the newly developed direct method is only possible at relatively low water contents due to restrictions on the application of the Brazilian method and its assumptions. With the additional evaluation conducted using the DIC technique, the direct tension test is considered to provide an adequate method for the simple and reliable measurement of tensile strength across a wide range of soil types and saturation conditions.

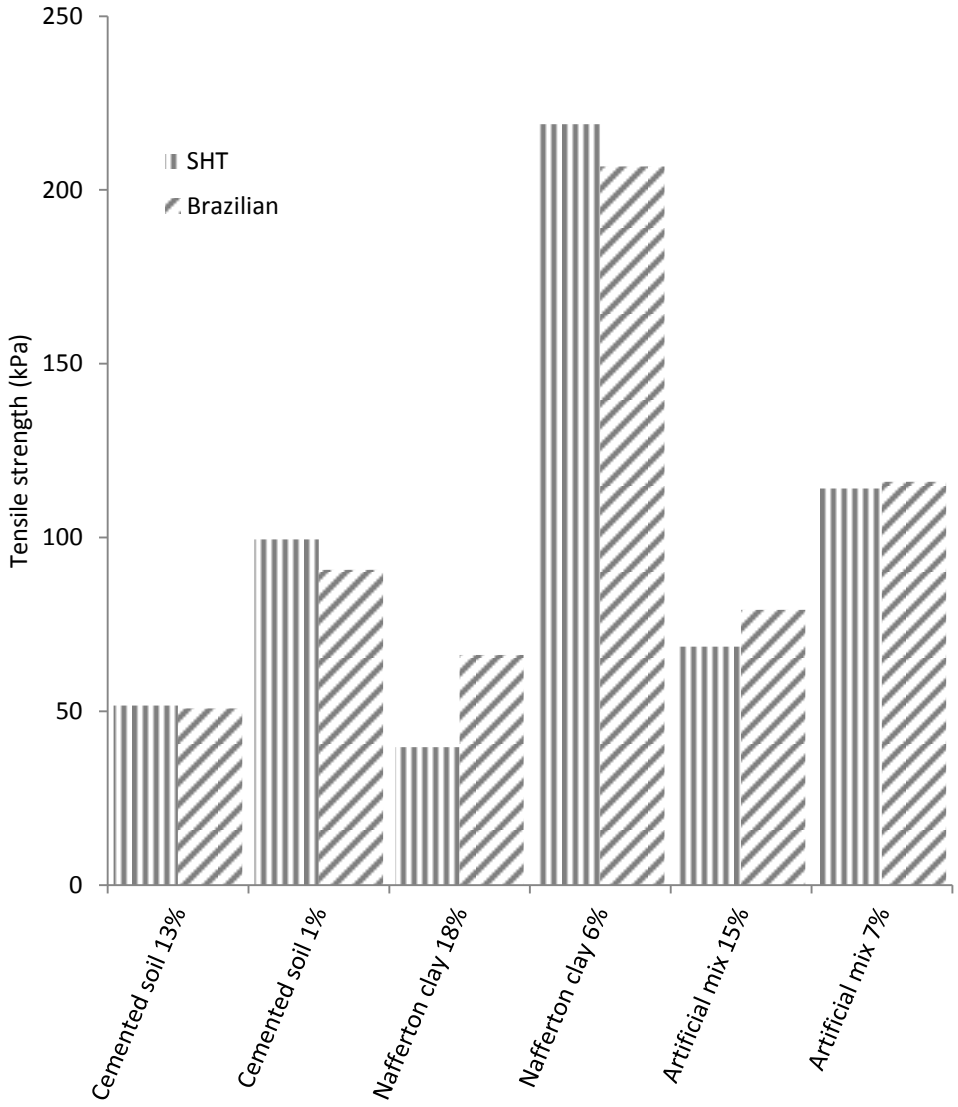

Figure 4.41 Tensile strength comparison between indirect and direct testing methods.

4.7 Future developments

As illustrated by the brace relocation described in Section 4.2.2, the development of such a new piece of equipment is an ongoing process whereby observations made in the practical handling of the apparatus and in the resulting data inform the modification of various aspects of the design. For example, the later testing of the Nafferton clay was conducted with the carriage jaw displacement measured using a frame mounted LVDT and dial gauge. Although simple calculation of the carriage displacement may be conducted using the intended electric motor speed and time, it was acknowledged that strain is accommodated in the deformation of the load ring gauge giving the appearance in the data of an increased straining of the sample. In future testing, it is considered advantageous to measure the jaw displacements directly in addition to automated recording of this together with horizontal load via a load cell in order to eliminate human error caused by the reading of multiple dial gauges.

The direct testing apparatus in its present form does not allow saturation or pore pressure to be measured, nor controlled during testing. This ability tends to be the preserve of triaxial systems where the sample is enclosed and subject to applied back pressure. Although this feature is lacking in the apparatus, the simplicity and speed of sample preparation and testing is considered one of the major advantages of the set up. Should the user wish to establish the tensile strength relationship to suction, one must depend on an established SWRC and its associated assumptions and level of accuracy. At present, there is no intention to develop this aspect beyond the current procedure for establishing the gravimetric water content immediately following testing. It is recognised that the sample is subject to drying during the testing and this may be minimised by development of a chamber subject to controlled environmental conditions.

It has been highlighted by the DIC analysis that the bedding, associated with the testing of samples dry of the compaction water content, is a common cause of non-parallel jaw movement and irregular jaw-sample contact during the early stages of each test. Where samples are to be tested at their ‘as compacted’ water contents, the mould defines the optimum and maximum sample size. However, as the samples dry, this results in a decrease in the cation layer and

increased net attractive forces between clay particles i.e. shrinkage. The extent of this behaviour varies from soil to soil and so no mould may be manufactured to account for this phenomenon, nor for every possible drying increment. Hence, it is suggested that the position of the loading jaws be adjustable in order to minimize the space between the sample and the interior of the jaws at the start of the test. This may be achieved through slotted bolt positions allowing the jaw segments to be set according to Figure 4.42.

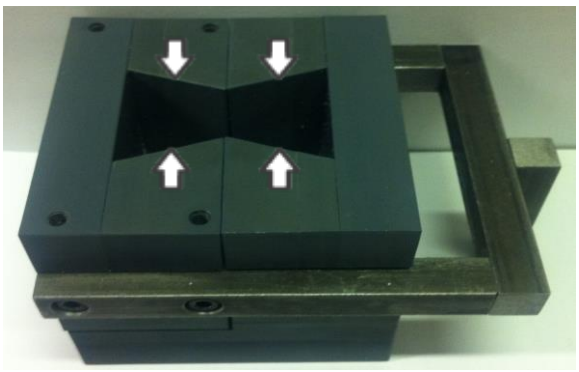

Figure 4.42 Suggested jaw adjustment option.

Lastly, the primary intention of the developed apparatus is to investigate tensile strength in the context of desiccation cracking. However, at present, no confining stress may be applied to the sample and so only unconfined strength such as that experienced at the ground surface may be investigated. The application of a normal confining load similar to that used in direct shear testing has been considered but not, as yet, designed or implemented. Such a facility would allow the change in tensile strength to be considered with respect to depth, a scenario particularly relevant to regions where embankment cracking extends well into the compacted core or in situations where vulnerable layers are installed at depth e.g. landfill liners.

4.8 Concluding Remarks

A necessity to understand and define the relationship between tensile strength and water content of the considered fill material was identified in the literature and subsequently adopted in the modeling methodology. Hence, this chapter set out to describe the development of a simple and reliable test to measure this important relationship. The design of the apparatus has undergone a degree of tuning as part of this process and an appropriate procedure for the repeatable preparation and production of soil specimens has been established.

The validity of results obtained by the tensile testing is recognised to be vital to the successful outcome of this work. Therefore, a series of evaluative approaches have been employed, the first being the testing of multiple soil types. The use of artificially mixed material based on Kaolin for its uniform composition and pale colour, allowed controllable and repeatable testing to be conducted. Additionally, this material facilitated evaluation of the test performance at variable water contents and displacement rates via application of the Digital Image Correlation technique. The results of this study showed the effect of soil water content on the gripping of the specimen and provided positive evidence of tensile failure initiation at the constricted section of the specimen. The secondary validation approach was to compare the direct tensile strength test results to those gained from an established indirect testing method. Brazilian testing was conducted on the same materials; however, limitations of the test restricted the conditions under which the materials could be tested at. The need for brittle failure in Brazilian testing not only supports the development of the direct method but also brought about the need to validate the indirect soil testing itself. Once more, the DIC technique was able to confirm appropriate failure conditions in light of a parallel rock case-study. The findings of the DIC analysis were supported by a subsequent analytical procedure.

The dependence of tensile behaviour upon the water content of cohesive soils has been investigated and an expression for this relationship has been established for inclusion in the numerical model. Although, not required in the modeling of one-way de-saturation, additional work presented in this chapter is the evidence of soil tensile strength deterioration upon cyclic drying-wetting.

Such a relationship is considered useful in the modeling of cracking under transient environmental conditions.

Chapter 5 Model Behaviour

5.1 Introduction

This Chapter details the behaviour of the numerical model (as developed in Section 3.3) and assesses its ability to simulate realistic cracking behaviour as described in Chapter 2 and observed in indicative laboratory experiments. The model is first evaluated according to well constrained parameters and drying conditions before being subjected to sensitivity study. The mechanical properties of the model are investigated first where all hydrological properties of the material remain fixed. As such the influence of basal restraint upon the generation of reaction (tensile) stress is investigated alongside the use of the experimentally derived tensile strength (Section 4.4). The effect of tensile strength magnitude and heterogeneity is presented, as may be measured for any given soil, although additionally the importance of the tensile strength function is evaluated given the chosen interface element inclusion approach. Finally, the hydrological aspects of the model have been investigated. Where possible, variation in these properties has been considered on the basis of measured ranges and those reported for other clayey soils in the literature.

5.2 Baseline model behaviour

This section describes how the simulation behaves using previously presented laboratory and field reference data and as such, may be considered as the baseline model for the sensitivity study to follow.

5.2.1 Hydraulic baseline behaviour

Since an ability to simulate water loss is fundamental to capturing soil behaviour during drying and desiccation, it is appropriate to consider the hydrological aspects of the model before presenting the mechanical performance. Figure 5.1 presents the gravimetric water content change during the course of laboratory Test 5 as originally presented in Section 3.3.1. The baseline model was run using a drying flux magnitude of 5.1×10^{-7} m/s corresponding to the start of Test 5. Water content during the course of Test 5 was established by way of mass balance and as such represents the drying of the soil mass as a whole. Similarly, the global water content change in the entire mesh was required for direct comparison. In order to achieve this, saturation averaged from all zones was converted to gravimetric water content via the initial porosity/saturated water content and the specific gravity of the soil. A similar trend between the measured and simulated global water content change may be seen in Figure 5.1 though the numerical curve is acknowledged to not pass through the majority of experimental data points beyond the initial 2 hours of drying. This indicates that a slower water loss was simulated with the greatest deviation between modelled and measured data being in the region 14-20 hours into drying. However, both curves may be divided into having two approximately linear components (as highlighted in Figure 5.1) that show a similarly timed transition at 11-16 hours between primary and residual drying phases. The final values achieved by the experiment and simulation are within 2% water content which is considered a reasonable correlation given the method by which each water content value was calculated.

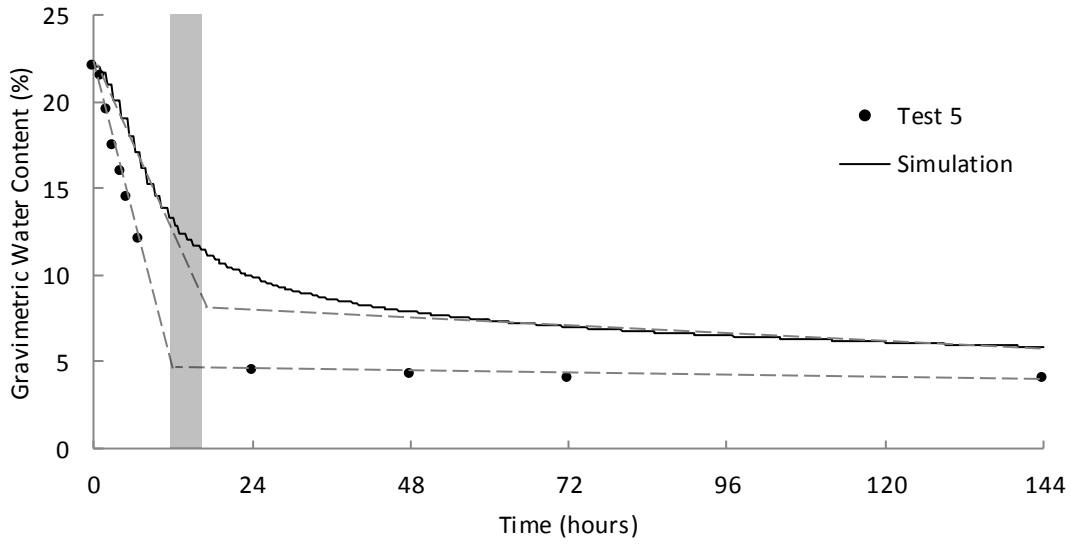

Figure 5.1 Modelled and measured water content change with progressive drying.

Tied into the reduction in water content is the generation of matric suction as described by the SWRC provided in Section 3.3.5. The initially 1-dimensional drying from the upper mesh boundary gives rise to a non-linear suction profile with progressive drying. Figure 5.2 shows the progressive development of the suction profile taken at a vertical line at the midpoint of the grid width. Note that a logarithmic suction scale has been employed to best display the large range over which suctions were shown to develop. Due to this, the initial suction profile is given at time 7.2×10^{-3} s as the profile at 0 s is negative (positive pore-water pressure) towards the bottom of the mesh after initialisation of stresses (Section 3.3.7) and so was unable to be plotted on the selected scale. The first profile shows a range of 4 orders of magnitude with the smallest suction at the bottom of the mesh indicating the presence of a wetter region as would be expected furthest from any evaporative boundary and adjacent to the lowest impermeable boundary (steel mould/impermeable grid region).

Progressive drying up to 2 hours shows a smoothening out and a more uniform suction profile being generated with an overall increase in mean suction across the full grid height. After this, a broadly linear suction distribution is observed below the upper 15mm although an increasingly pronounced increase in suction is evident in proximity to the drying flux boundary. The depth over which this non-linear region extends is shown to shallow as the suction magnitude continues to increase. Finally after 48 hours of drying, little change in the profile

is found to have occurred and a highly desiccated crust of <5 mm thickness above an evenly distributed suction profile is shown after the full 6 days of simulated drying.

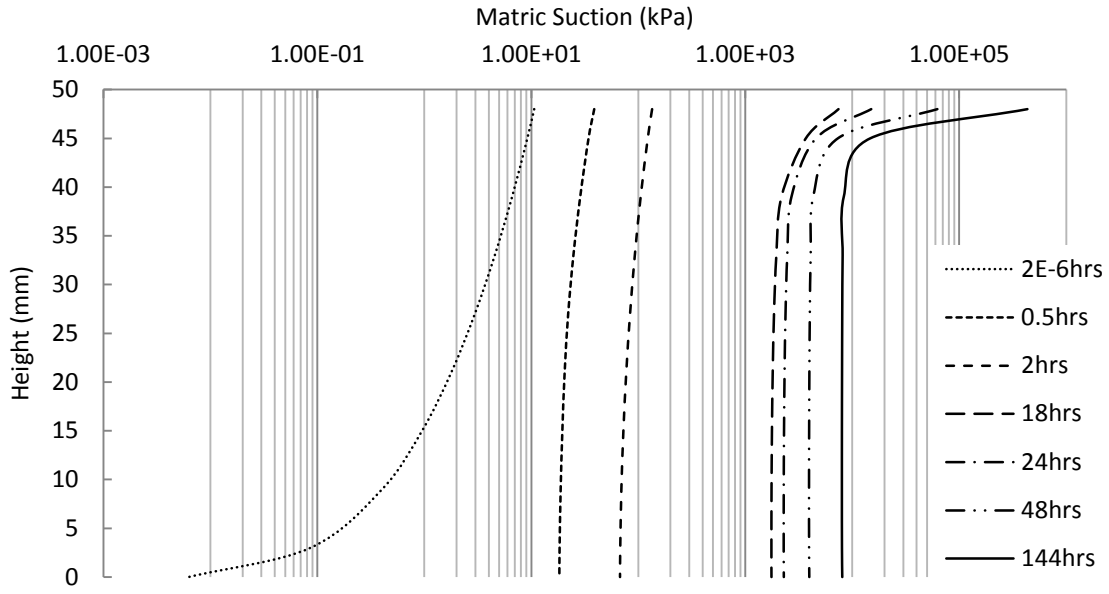

Figure 5.2 Vertical suction profile at the middle of the mesh throughout simulated drying.

The features that have been highlighted in the suction profile show two stages of profile development. Firstly, the range of suction magnitudes at a given time are shown to reduce to a more linear distribution where free water held under lower negative pressures is most easily removed. Beyond this stage, the remaining water is held under much higher suctions and correspondingly, the relative (unsaturated) permeability coefficient is markedly reduced leading to the more shallowly orientated curve in the water loss plot (Figure 5.1). The extremely low resultant permeability causes less water to be able to be removed from deeper in the clay and so an increasingly thin crust of elevated suction is produced. The result is the formation of a hydraulic barrier at the interface between the atmosphere and the soil which inhibits both the further removal of water by evaporation in the presented model as well as potential hydration by rainfall at the immediate surface. Such behaviour is considered to increase the degree to which crack infiltration will contribute to the overall infiltration potential of the desiccated soil surface according to crack hydrology (Section 2.6.1).

The development of each stage emphasises the highly non-linear behaviour in the resultant suction profile. However, such a profile is often treated linearly (Peron et al., 2009; Amarasiri et al., 2011). Vogel et al. (2005) on the other hand, attempted to negate this issue in their discrete 2-dimensional model by specifying a thickness of clay relative to the rate of evaporation such that water content gradients are avoided. The development of a suction gradient is therefore particularly prominent in the simulation of thick layer desiccation which may be considered more analogous to the field case.

This simulation resulted in the formation of cracking, though prior to describing the geometric nature of simulated cracking, crack initiation is presented in relation to the soil-water characteristics of the modelled clay. Figure 5.3 presents the SWRC used in the baseline model. The suction at which crack initiation occurred was established by correlating the flow-time at first interface separation (anywhere throughout the mesh) with the contemporaneous recorded surface (uppermost grid-point) suction value. The point along this curve at which crack initiation occurred (labelled) is positioned close to the air entry value, the very early stages of de-saturation. This is in agreement with numerous reported studies e.g. Peron et al. (2006); Rodriguez et al. (2007); Peron et al. (2009); Tang et al. (2010).

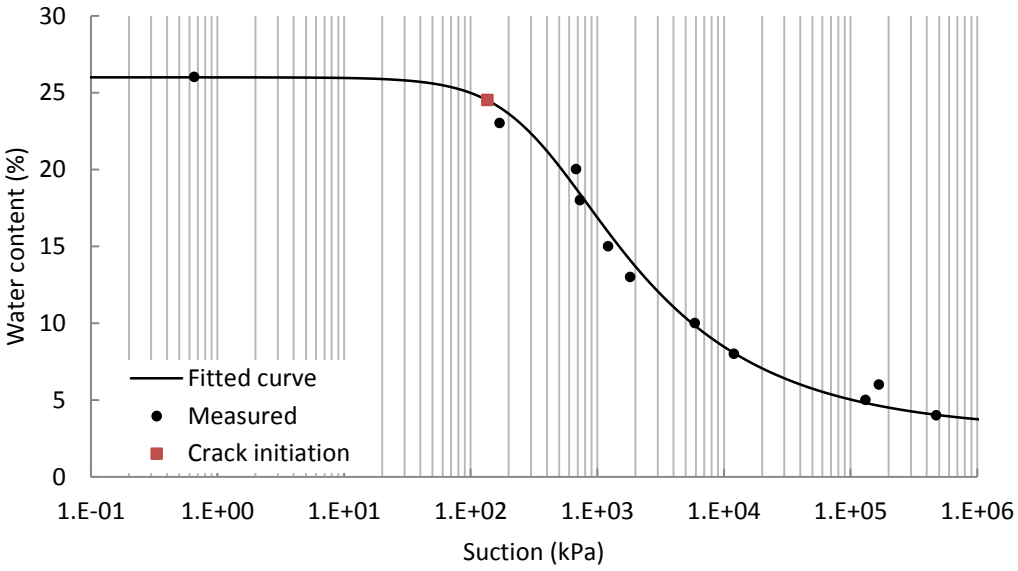

Figure 5.3 Surficial position on SWRC at crack initiation.

The mechanism by which water was simulated to have evaporated from the surface of the clay is presented in Figure 5.4. For clarity, the vectors have been plotted for a right-hand portion of the grid and in the absence of the grid lines. Therefore, the region located below the clay grid is not visible as no flow is able to take place in this region. A dominant, vertically upward trend is evident in the vectors due to the orientation of the discharge boundary condition on the upper surface. It may be seen that the magnitude of the vectors diminishes with depth into the grid. At this point in flow-time (6 days), little flow is shown to be taking place toward the interior of the mesh as this region is hydraulically isolated by the highly desiccated, high suction crust as discussed with reference to Figure 5.2. Incorporation of the secondary discharge boundary condition is clearly shown in Figure 5.4 by the presence of horizontally, outward trending flow vectors positioned along the outer most right-hand boundary and either inner edge of opened cracks. However, it may be seen that the internal extent of these secondary flow conditions is limited to only 2-3 elements from the new mesh boundaries. This is likely due to the smaller magnitude of the secondary discharge function and its occurrence during drier simulation states when relative hydraulic conductivity is reduced. Hence, the influence of this condition is limited to the removal of moisture from lower positions within the grid where water would otherwise be isolated from the effects of the upper surface discharge.

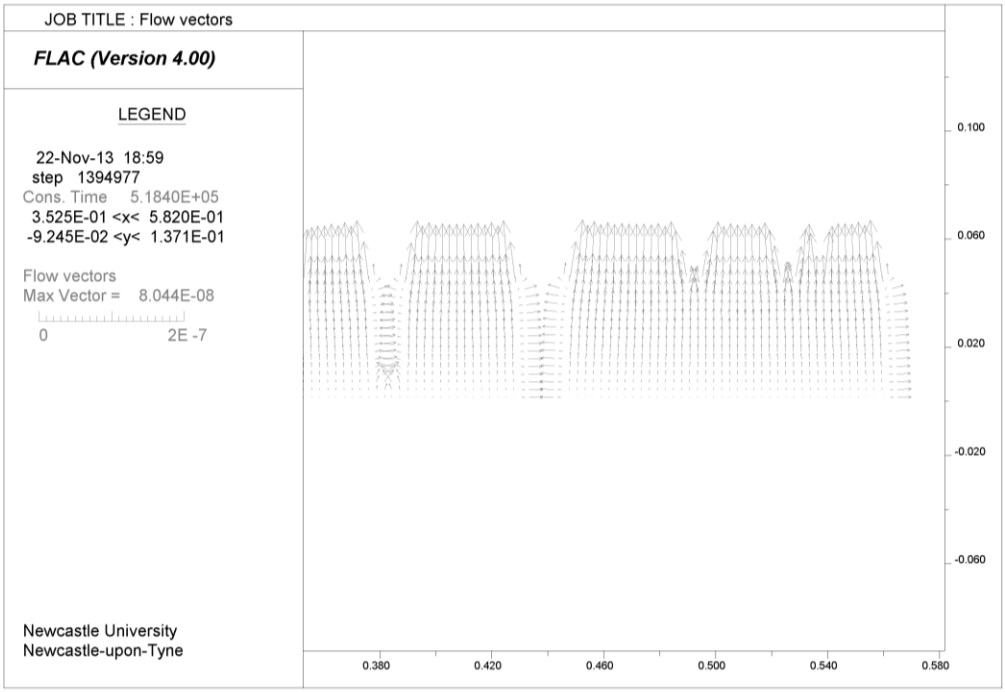

Figure 5.4 Flow vectors after 6 days of drying.

5.2.2 Mechanical baseline behaviour

Further to the described hydraulic features of the simulation, drying has given rise to the generation of a stress field conducive to the development of desiccation cracking. The ability of the model to capture this behaviour is described herein. As described in Chapter 2, the generation of tensile stresses that exceed the critical soil tensile strength is fundamental to the initiation of cracking. The aforementioned drying mechanics has given rise to the horizontal stress fields presented in Figure 5.5. A consistent colour contour scale has been selected; however, the stress distribution at 0 hours is best depicted in the description of initial model conditions in Section 3.3.7 (specifically Figure 3.26). Stress is expressed in units of Pa according to the following sign convention: Positive stresses indicate tension; negative stresses indicate compression.

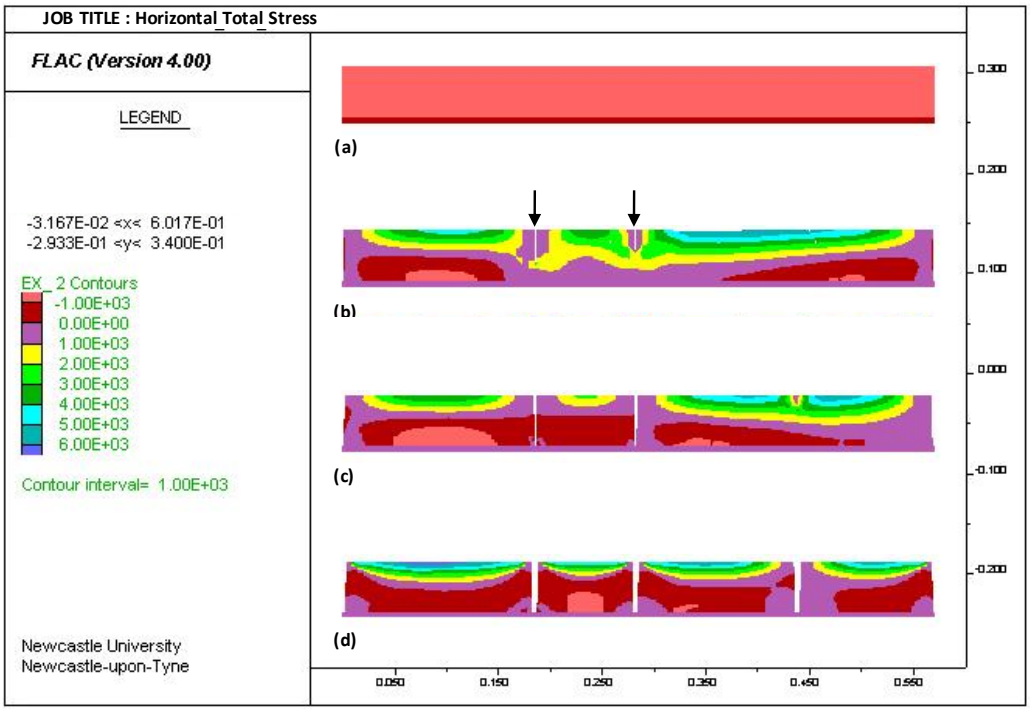

Figure 5.5 Horizontal total stress contours after (a) 0 hours, (b) 30 minutes, (c) 1 hour and (d) 2 hours of drying.

It is apparent from Figure 5.5b that after 30 minutes, horizontal stress in the order of 5-6kPa has been generated at the upper surface of the grid where the effects of drying are most pronounced. The regions of greatest tensional stress are found not to extend to the lateral boundaries due to a stress relief effect brought about by the shrinkage displacement of the upper grid corners. Hence, greater tensional stresses are found to generate toward the horizontal centre of

the grid. However, it is clearly shown in Figure 5.5b that stress relief has been brought about by the tensile failure of two interface elements (highlighted). These have perturbed an otherwise continuous surface region of tensional stress. The greatest reduction in tensile stress about the two simulated cracks may be seen at the surface with the region about the crack tips retaining proximal tensile stresses in excess of ~2kPa. Surficial stresses away from the existing cracks are found to be much greater than those between them indicating a relaxation interaction. Also shown in Figure 5.5b is a compression feature immediately adjacent to the clay-mould interface. This feature is most apparent towards the two ends of the clay grid, though once again does not extend to the lateral grid boundaries where the grid is subject to the greatest free displacement.

From the position of the maximum surficial tensile stress shown in Figure 5.5b, the location of any further cracking may be estimated on the basis of tensile failure. Therefore, at this stage, cracking is predicted to occur to the right-hand side of the existing cracks. After 1 hour of drying (Figure 5.5c), a third crack is initiated and perturbs this region of elevated surface tensional stress. Interestingly, the third crack is not located simply at the position of maximum tensile stress but instead further toward the right-hand lateral boundary. This is a function of the incorporation of randomised tensile strength in the specification of interface properties and will be discussed later in this section. As the initial cracks have grown to fully penetrate the thickness of the clay, the depth of surficial tensional stresses has reduced. This is related to the continued removal of water from the upper surface and the resulting elevation of suction in an increasingly shallow region.

Upon further drying (Figure 5.5d), three fully penetrating cracks may be seen after a simulated flow-time of 2 hours. Increasingly shallow, horizontally bridging regions of surface tensile stress are observed to have formed of increased magnitude. These regions diminish towards the crack walls where the widening of cracks acts to inhibit the generation of horizontally orientated stress. This behaviour is much like that of isolated soil blocks with the removal of influence from one another upon ultimate separation. This is unlike earlier in the simulated drying time when partially penetrating cracks interacted and

influenced the stress field nearby. Note the diminished magnitude of the compressive zone at the clay base as well as its larger distribution along the clay-mould interface. Within each separate clay block, it is observed that an increasing stress gradient is formed towards the surface, as was shown in the suction profiles in Figure 5.2; this is related to the development of a desiccated crust.

The key effect of stress relief is controlled by the ability of the grid to deform according to shrinkage behaviour at boundaries and the growth (widening and deepening) of cracks. Grid-point displacement throughout the grid may be used to illustrate the simulated shrinkage behaviour. Final displacement vectors after the full 6 day drying reference period are presented in Figure 5.6. The greatest vector magnitudes are observed around the grid boundaries (clay block ends, upper drying surface and crack walls). Clearly, the segregation of the grid by the ability to develop discontinuities has enabled the clay to continue to shrink and develop an otherwise unattainable desiccated geometry.

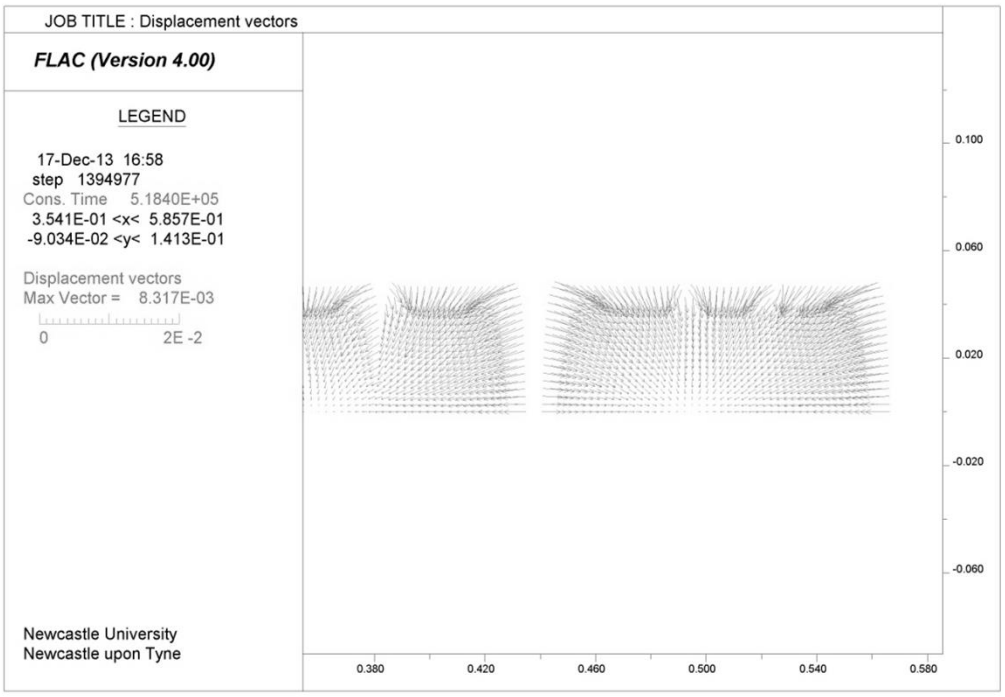

Figure 5.6 Displacement vectors after 6 days of drying

In addition to displacement vectors, displacement in the principle 2D directions is presented in Figure 5.7. Vertical consolidation of up to 4.5mm may be seen in Figure 5.7a as well as the influence of mesh separation with maximum vertical displacements experienced toward the centre of the intact clay regions.

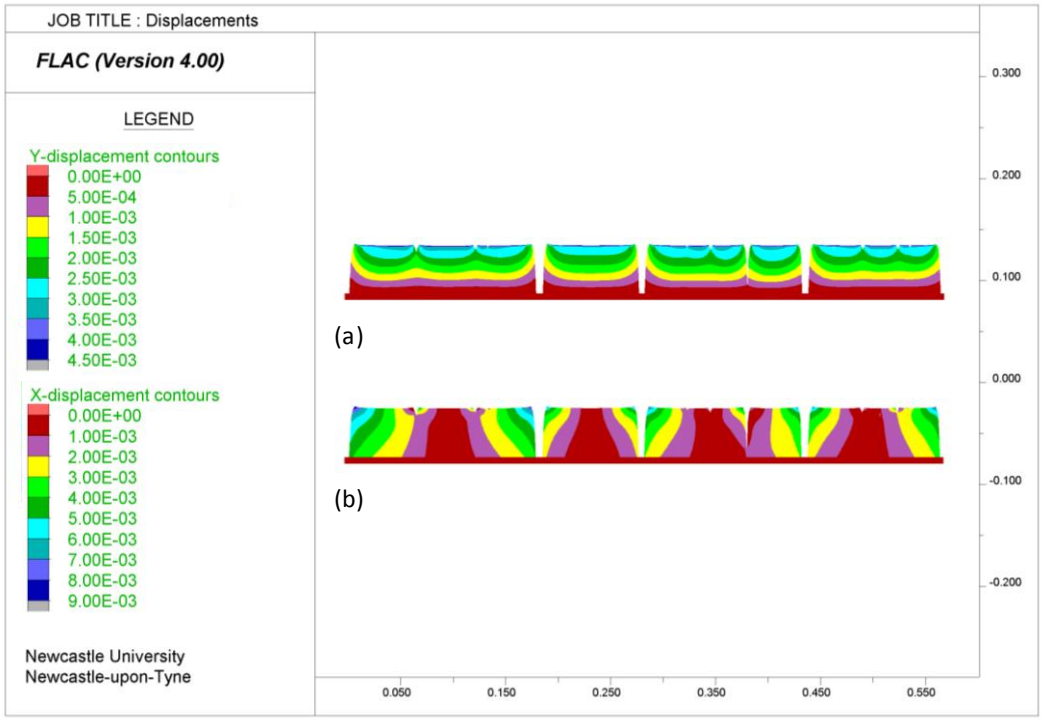

Figure 5.7 Final displacement contours after 6 days of drying in the (a) y-direction and (b) x-direction.

Figure 5.7b shows purely the horizontal displacement which constitutes a significantly larger proportion of the total shrinkage strain. Particularly of note here is the relationship between the x-displacement either side of the crack. It is apparent that the absolute displacement on a given crack wall (or lateral boundary) is related to the relative size of the intact block (continuous length of grid) the side of which the crack forms. It is inferred that the size of the intact block is further relative to the tensile stress magnitude present within it i.e. larger intact clay blocks have undergone less stress relaxation than smaller ones. Hence it may be seen that for a given crack, greater displacement is observed on the crack wall adjacent to the greater tensile stress present at the time of crack propagation. This results in crack asymmetry being captured in the presented simulation.

The least vertical settlement combined with the greatest horizontal shrinkage is produced at crack-soil surface intersections as seen in Figure 5.6 and Figure 5.7. Such behaviour gives rise to a concave, intact clay ped surface and is linked to the development of curling in unconstrained shrinkage. This type of feature is common among polygonal desiccation features (Konrad & Ayad, 1997) and some linear laboratory experiments (Nahlawi & Kodikara, 2002). In the field, horizontal cracking at shallow depth is observed to result from the curling stress within the desiccated crust (Dyer et al., 2009). FE and FD modelling of this specific phenomenon has been undertaken by other researchers; however, this is limited to scenarios of very thin soil layers (12.5-20mm) (Kodikara et al., 2004; Hu et al., 2006) and is not the focus of this work given the greater thickness of the soil layer under investigation and the absence of such behaviour in the indicative laboratory experiments using the compacted fill.

As mentioned, the order in which cracks occur with the developing horizontal stress field is related to this stress exceeding the tensile strength of the embedded interfaces. It is important here to illustrate the distribution in the specified tensile strengths used. The method, as previously described in Section 3.3.4.1, makes use of a random number FISH command that generates a number from a normal distribution about 0.0 with a standard deviation of 1.0. A random number is generated and assigned to each of the 94 vertical interfaces across the grid; Figure 5.8 shows this distribution. The custom function then modifies the mean and standard deviation by multiplying the returned number by a factor and adding an offset equal to the water content dependent tensile strength. An example tensile strength distribution is depicted in Figure 5.9.

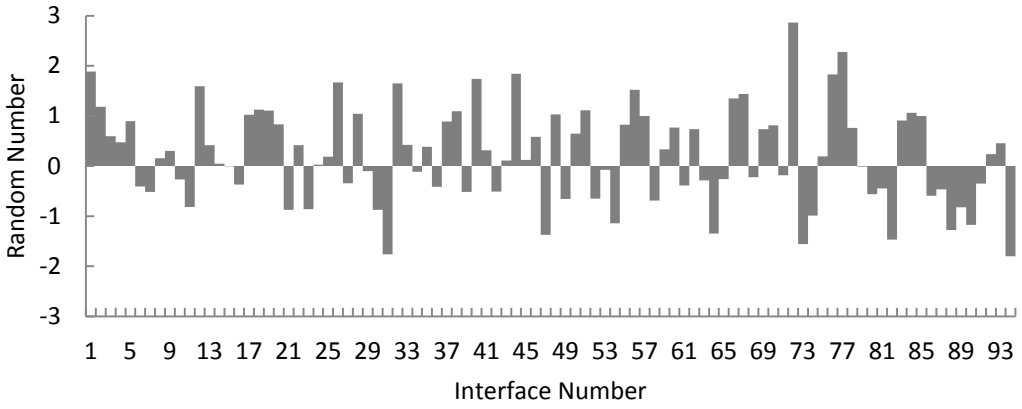

Figure 5.8 Interface specific random number distribution.

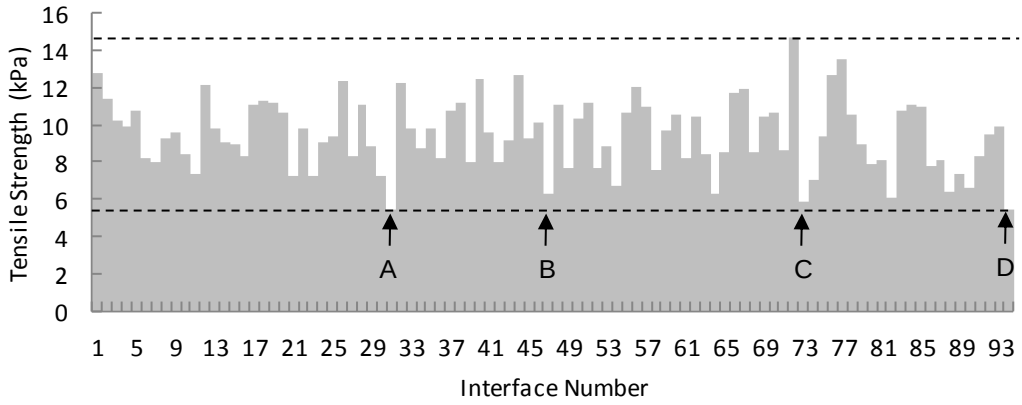

Figure 5.9 Randomised tensile strength distribution.

As was shown in Figure 5.5, interfaces located at A and B are found to be the sites of first crack initiation. This is due to these interfaces possessing prominently lower strengths than neighbouring interfaces. These interfaces are the first sites where drying induced tensional stress exceeds the simulated clay strength and crack deformation is subsequently localised. Interestingly, the interfaces positioned at C and D are weaker than that at B; however, these interfaces are inhibited from opening by the tensional stress being buffered by the soil's ability to undergo deformation freely at the right-hand lateral boundary. Interface D is number 94 and is the furthest right-hand interface, immediately adjacent to the grid boundary. Although possessing a similarly low tensile strength as at A, this interface will remain extremely unlikely to open. Interface C has been shown to open following interface B as the total horizontal stress increased with continued drying.

It is clearly possible to estimate the order in which cracks are simulated to occur based on information about the tensile strength heterogeneity and an appreciation of the stress relief effects that freely shrinking boundaries and crack walls provide. Figure 5.10 illustrates the crack pattern development with cracks A-C corresponding to those interfaces identified in Figure 5.5 and Figure 5.9. It would be true to surmise that cracking tends to occur toward the middle of the grid in so far as the interface at D in Figure 5.10b is observed to follow the primary cracking of A-C despite interface D possessing the same strength as an interface of approximately equal distance to C on the opposite, free boundary side (Figure 5.9).

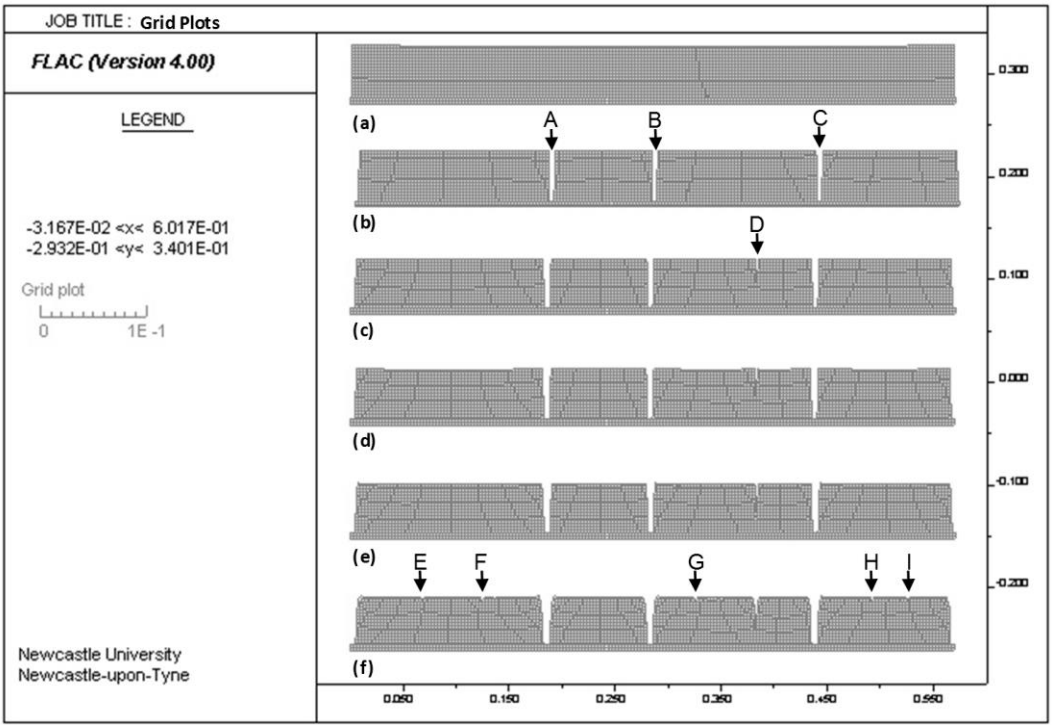

Figure 5.10 Development of grid geometry during progressive drying after (a) 1 hour, (b) 2 hours, (c) 18 hours, (d) 24 hours, (e) 48 hours and (f) 144 hours.

The cracks identified as A-D are shown to continue to develop and widen with continued drying. However, crack D is noted to remain partially penetrating throughout the full 6 days of simulated drying. This is thought due to its proximity to the widening crack C. Sufficient shrinkage is observed by the growth of the existing cracks after the formation of cracks A-D to inhibit any further significant cracking. Figure 5.10f shows the cracked grid geometry after the full 6 days. Minor cracking is observed at interfaces E-I and exist within the thin desiccated crust identified previously. At the state presented in Figure

5.10f, the grid is considered to represent the clay having reached a shrinkage limit according to the non-linear elastic constitutive model employed with little further water loss expected according to Figure 5.1.

Figure 5.11 and Figure 5.12 show the crack widths and depths respectively for the ultimate cracked state. Crack widths and depths are found to align well with the order in which they occurred. For example, cracks A-C (Figure 5.10) that initiated after only 18hours of drying show the largest widths, followed by crack D whose width is found to be proportional to the crack depth achieved at the end of drying. The final depths of cracks A-C are shown to be less than the initial 50mm thickness of the pre-dried grid due to being measured after vertical settlement by drying driven shrinkage. The later stages of cracking shown in Figure 5.10f are shown to be of approximately uniform width (4.01-4.57mm) and depth (0.04-0.21). Such crack sizes are infinitesimally small and are recognised to be undiscernible as discrete cracks. However, such behaviour may be considered analogous to the crumbling of clay at the soil surface upon extreme desiccation. A fourth phase of cracking with widths ranging 2.01-2.62mm are <0.01mm deep and assigned to the crumbling phenomenon.

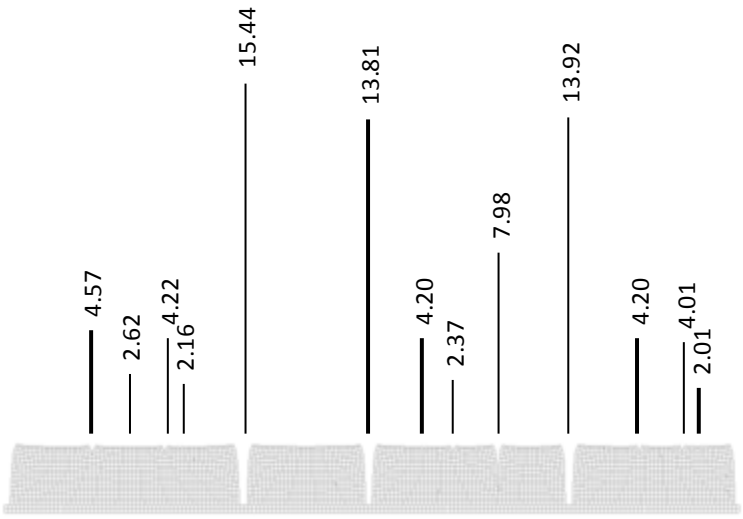

Figure 5.11 Final crack widths at upper surface (mm).

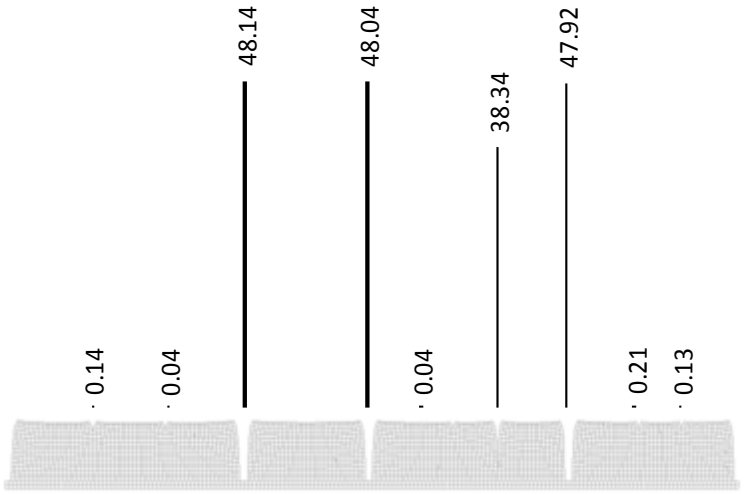

Figure 5.12 Final crack depths (mm).

As described in Section 2.4.1, a common means by which to assess the extent of cracking is by using the Crack Intensity Factor (CIF). This allows quantification of the surface shrinkage in terms of the growth of cracks relative to the total surface (original un-cracked state). The CIF herein has been calculated as:

$$CIF = \frac{\sum L_C + L_s}{L_0} \times 100 \quad \textbf{5.1}$$

where L_c is the surface crack width, L_s is the end shrinkage and L_0 is the original length (0.57 m). Equation 5.1 was incorporated into a FISH function that was implemented on an hourly flow-time basis.

This data is presented in Figure 5.13 and shows three distinct stages. For clarity, the transition between the first and second stages has been plotted separately in Figure 5.14. The first stage captures a period of rapid shrinkage incorporating crack initiation and end shrinkage. This behaviour slows over hours 2-14 before transitioning to a period of constant opening of existing cracks. The end of crack initiation (stage I) may be noted to coincide with the transition between primary and residual water loss (Figure 5.1). Lastly, the stepwise trend, shown during stage III in Figure 5.13, captures the sporadic initiation of cracks <5mm in width, as presented in Figure 5.11. This latter stage is associated with the deterioration of the desiccated crust and as such is prominent in the calculation of CIF due to only the upper most surface (grid-

point) geometry being included in Equation 5.6. Therefore, it is important to remember that the final stage apparent in the CIF time-series takes no account of the penetrative extent of cracking; this is best interpreted from stage I data.

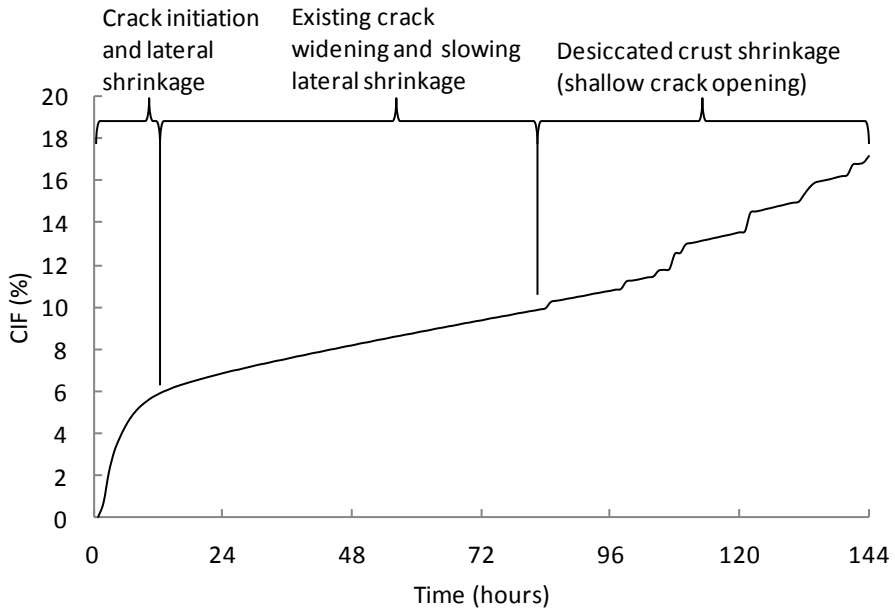

Figure 5.13 Baseline development of CIF.

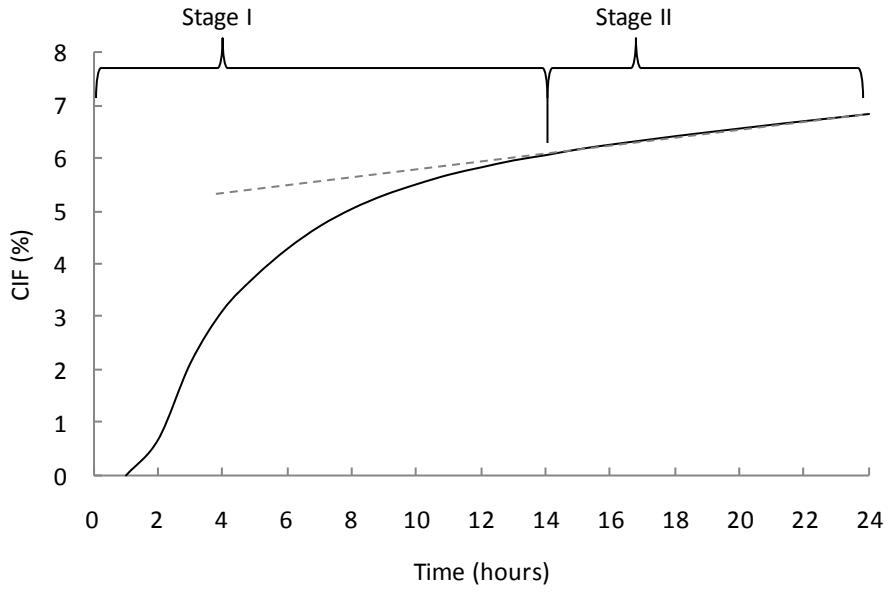

Figure 5.14 Development of CIF over first 24 hours.

A similar factor termed the ‘surface crack ratio’ was employed by Tang et al. (2010) who noted that the ratio increased rapidly with decreasing water content in the early stages of cracking followed by a rapid decline in the increase increment with further drying. However, the surface crack ratio was

characterised as reaching a stable value beyond critical water content whereas the behaviour exhibited in Figure 5.13 shows the model to have captured a further stage of closely spaced, shallow micro-cracking synonymous with crumbling which is unlikely to be considered in experimental studies. The scale of these features means that this surface deterioration would likely not be as apparent in a physical model. The magnitude of the modelled CIF at the end of steady crack development is comparable to those reported in the literature for clays of similar plasticity e.g. CIF 9-13% (Tang et al., 2008).

Lastly, the development of shear properties at the clay-mould interface is presented in Figure 5.15. As was described in Section 3.3.4.2, the nature of the clay-mould contact was established by means of experimentation using an adapted direct shear apparatus. The relationship between shear strength and stiffness with decreasing water content was established from these data and functions of these relationships input to the model. As was shown in Figure 5.1, the period of greatest global water loss was between 0-20 hours. Therefore, it may be expected that the greatest change in the properties at the base of the grid occurs within this period. It is evident in Figure 5.15 that both interface shear strength and stiffness reach residual values after c.48 hours. This is as a result of the properties being governed by water content which is observed to change most slowly at the base of the clay due to its distance from the primary upper discharge boundary and the development of secondary drying boundaries. After c.48 hours, according to the recorded development of the basal interface, the isolated clay blocks (crack bound sections of the grid) are able to slide/displace along the simulated mould under lower compression stress and post-cracking shrinkage occurs.

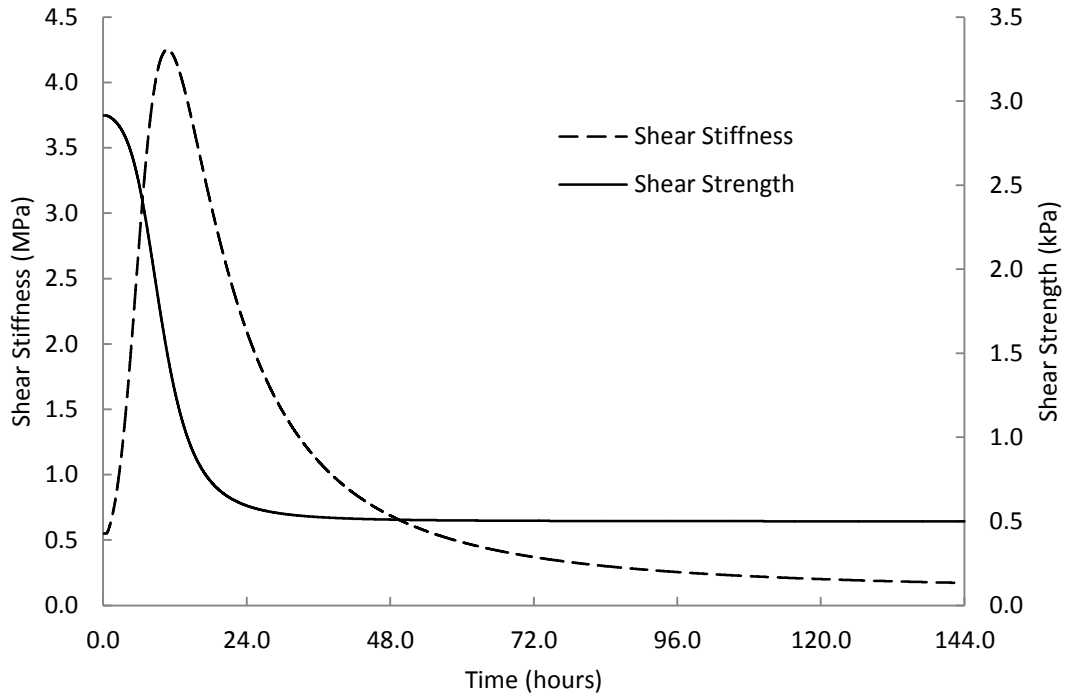

Figure 5.15 Development of basal shear properties

5.2.3 Baseline model conclusions

The drying processes outlined in Section 3.4 and summarised in Figure 3.28 (pg. 165) have successfully been incorporated and demonstrated to function under laboratory constrained conditions. It has been shown that the developed model is capable of capturing the fundamental characteristics of a drying clay block beyond crack initiation, crack growth and the formation of a desiccated crust. Crucially, the feedback mechanism between the drying generated stress and the development of cracking has been simulated. No quantitative comparison may be made between the numerical component of this work and the indicative laboratory experiments due to low data resolution of the physical model. However, a qualitative comparison between the modelled and physically cracked clay block may be made from Figure 5.16. It may be seen that a similar shrinkage geometry and crack spacing is captured despite the random, unrepeatable nature of the clay tensile properties between the two cases.

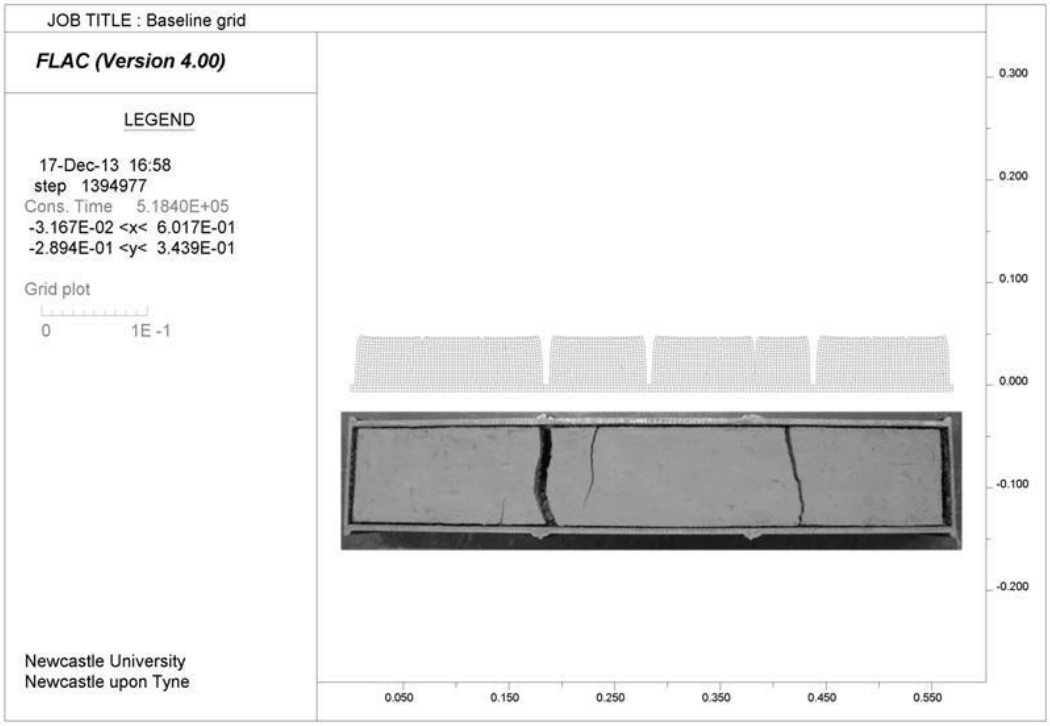

Figure 5.16 Indicative experiment state (plan view) and modelled grid geometry (vertical section) after drying to residual conditions.

5.3 Mechanical conditions

The following section investigates the sensitivity of the model to mechanical properties and functions by quantitatively assessing their influence on cracking. These include:

- Continuum constitutive model - the change in stiffness upon drying;
- Mesh boundaries - lateral and basal conditions; and
- Crack orientated interfaces – their tensile strength and heterogeneity.

5.3.1 Elastic stiffness

The constitutive law employed in this work is explained in Section 3.3.3 and describes a non-linear elastic rule with the modulus a function of water content. This is designed to capture the increase in material stiffness of the clay with progressive drying. In order to investigate the influence of the elastic modulus function on cracking, the baseline, measured relationship is compared to a similar trend reported in the literature and a reduced empirical function.

An expression for the change in modulus with suction was reported by Kodikara et al. (2004) after testing conducted on Werribee clay by Nahlawi (2004):

$$H = 24.0\varphi^{0.95} \quad \textbf{5.2}$$

This was later recast by Kodikara and Choi (2006) using the SWRC into the form of Equation 5.3 and by establishing that the clay remained saturated below the plastic limit, a Poisson's ratio of 0.45 was assumed and Equation 5.4 was used to represent the change in Young's modulus with water content.

$$H = 3 \times 10^{10}\omega^{-4.070} \quad \textbf{5.3}$$

$$E = H(1 - 2v) \quad \textbf{5.4}$$

This function is presented in Figure 5.17 in addition to the baseline, empirical trend and an artificially reduced version of the measured relationship modified by reducing the intercept variable by 50% while maintaining the original exponent. This latter function was devised to test the scenario where little gain in stiffness is experienced upon drying. All other baseline conditions were maintained.

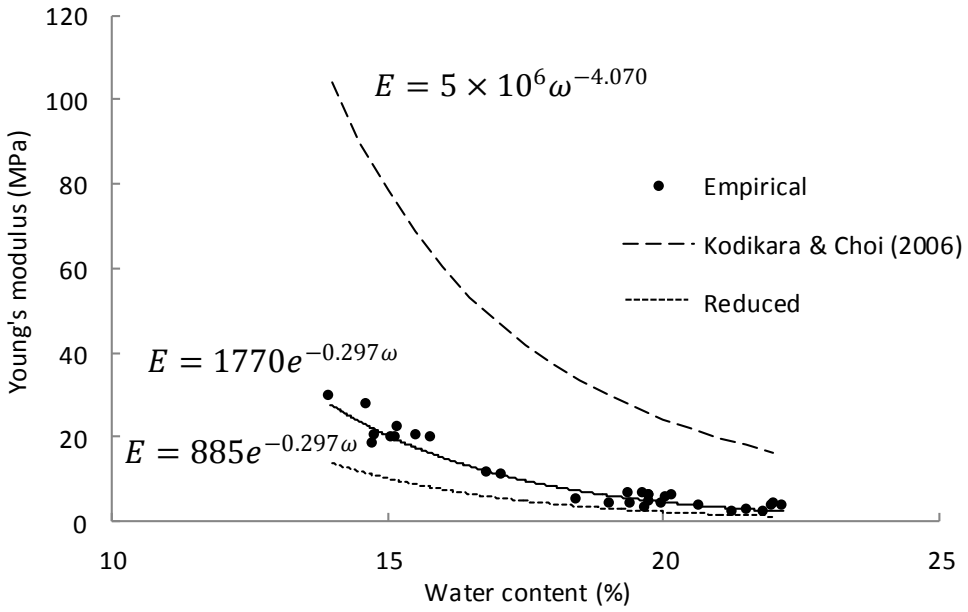

Figure 5.17 Tested relationships between Young's modulus and water content.

The resulting geometries from each simulation are presented in Figure 5.18 in order of decreasing ultimate stiffness. It is evident that the more extreme stiffening trend reported by Kodikara et al. (2004) produced no initiation of cracking in this model and limited end-shrinkage. Tensile stresses generated by shrinkage due to simulated drying were insufficient to exceed the tensile strength of any single crack interface. However, cracking was initiated in the baseline case and it is observed that the same crack interfaces that fully penetrate the baseline mesh have also been exploited by drying in the reduced stiffening version of this case. For any given stage in the drying time, the lower elastic modulus has resulted in greater shrinkage strain. This has led to the widening of these cracks and a greater degree of end shrinkage.

The CIF time-series data is provided in Figure 5.19 and captures the development of cracking at the surface for the three simulations. The magnitude of the CIF obtained from the use of the higher modulus function is relatively low at a maximum of 2.6% and represents only the dislocation of the clay ends; this is achieved early in the 6 day drying period in only 10 hrs. The baseline case, as previously discussed displays the initiation of major cracking followed by a broadly linear increase in their surface aperture. Similarly, the less stiff case displays this behaviour; however, the magnitude of CIF during stage I crack initiation and shrinkage is approximately double that of the baseline, empirical

function. Lastly, the onset of stage III surface disintegration is observed to have occurred 47 hrs sooner than that in the baseline case.

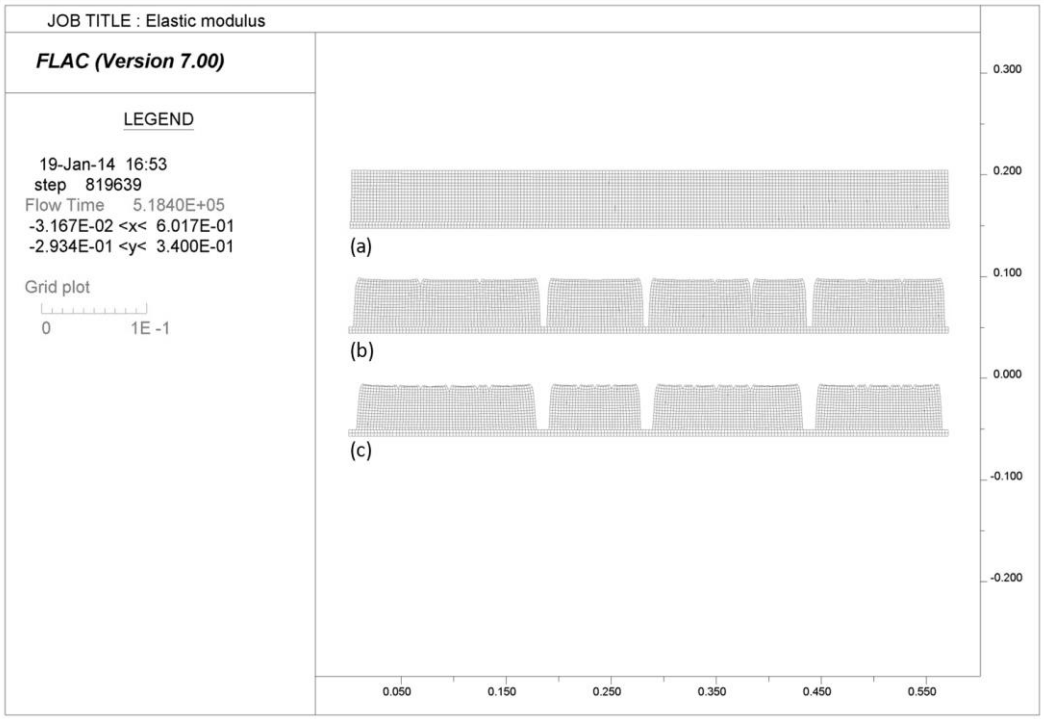

Figure 5.18 Crack geometries resulting from elastic modulus functions (a) Kodikara & Choi (2006), (b) empirical and (c) reduced empirical.

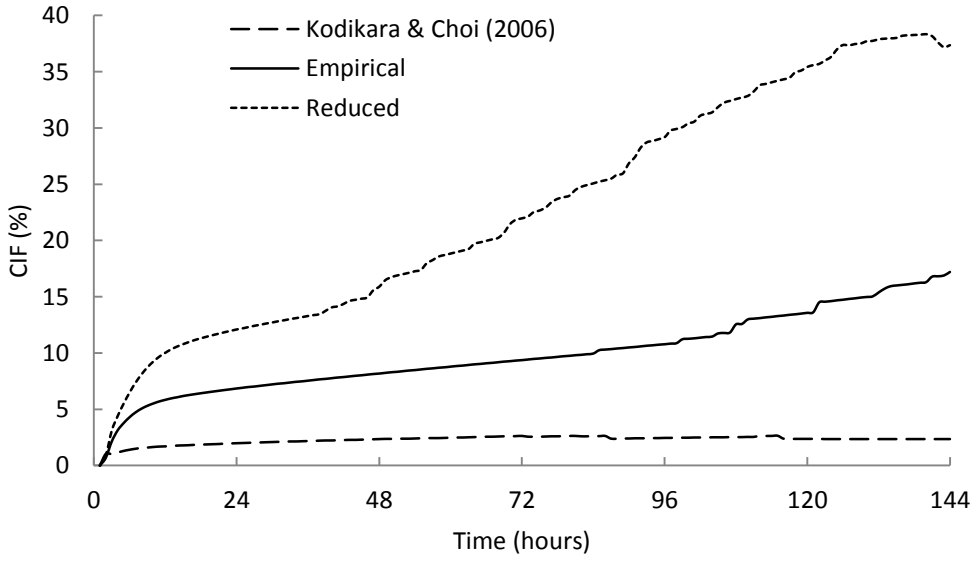

Figure 5.19 Effect of elastic modulus function on the development of CIF

Although no cracking was simulated here using the power-law function reported by Kodikara et al. (2004), cracking was captured in the DEM by Amarasiri et al. (2011) using this function. The outcomes of both models cannot be directly

compared as besides using an array of different properties, geometry and solution method, the initial conditions differ greatly. Amarasiri et al. (2011) modelled the drying and cracking of clay slurry and reported cracking to initiate at water contents in excess of 90%. At such high water contents, the elastic modulus is considerably lower than that experienced within the water content range of compacted fill.

The stiffness function employed in this work clearly has a significant influence on the generation of cracking. The difference in cracking extent is more apparent with progressive drying time according to the CIF time-series. However, the modulus is a function of water content and not time. Since the greatest change in global water content has been shown to occur in the first c.24 hrs (Figure 5.1), it is considered within this period that the stiffness function is understood to have had greatest influence with regard to primary crack initiation.

5.3.2 Crack interface conditions

The inclusion of crack (vertically) orientated interface elements was, as described in Section 3.3.4.1, on the basis of a tension bond criterion. Hence, the governing property that determines their behaviour is tensile strength, the critical stress acting perpendicularly to the interface plane. The following sub-sections investigate the influence of the magnitude of this property and the degree to which the standard deviation in the employed randomisation of strengths affects the development of cracking.

5.3.2.1 Tensile strength magnitude

The effect of tensile strength magnitude on cracking was investigated by adapting the experimentally derived relationship. The exponential description of the relationship between tensile strength and water content (Section 3.3.4.1) was modified by increasing and decreasing the intercept variable while maintaining the original exponent. The chosen variations on the measured trend are presented in Figure 5.20. It may be seen that at any given point upon the measured trend line, the tested values represent +/- a given percentage value of that given point. That is to say, it is the rate in which tensile strength increases with drying that has been modified as opposed to maintaining the

exponential rate while shifting the trend up or down the strength axis. This approach was believed to capture a more realistic development of tensile strength from a relatively low, residual magnitude at high water contents. Should the magnitude of values have been increased or decreased consistently along the measured line, unrealistically high and potentially negative strengths would have been prescribed at high water contents. Such behaviour was not observed in any of the conducted tensile strength testing. As was presented in Figure 3.12 (pg. 145 Crack interfaces), the least deviation from the best-fit line was observed at the wet end of the data.

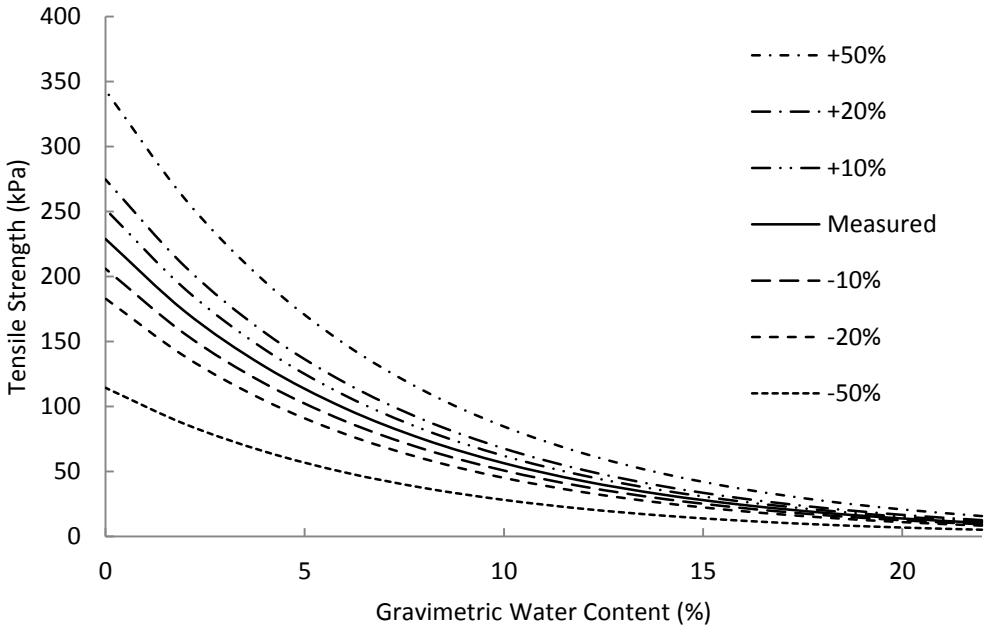

Figure 5.20 Tested tensile strength relationships.

Besides the use of consistent baseline model properties between tests, it is important to note that the spatial distribution of random variation in interface tensile strength values was maintained in accordance with Figure 5.8.

The crack model geometries captured following the full 6 day drying period are presented in Figure 5.21. At least qualitatively, the cracking geometry may be seen to have been affected relatively little by a - 10% change in the tensile strength, though a +10% change produces one less full crack. This trend is as expected with larger tensile stresses required to initiate cracking in higher tensile strength simulation. However, the simulation at +20% has reverted to three fully and one partially penetrating cracks, similar to that of the 0 and -10%.

The position of these cracks is observed to have been influenced with cracks appearing towards the freely shrinking boundaries. In line with the requirement of lower tensile stress to initiate cracking in the lower tensile strength cases, four fully penetrating cracks are evident when a -20% magnitude is applied. The greatest difference from the baseline model is seen by the +/- 50% simulations. Very different cracking morphologies are apparent in these tests with many more narrow and partially penetrating cracks in the lower tensile strength test than in the coherent, clod-like appearance of the strongest simulation.

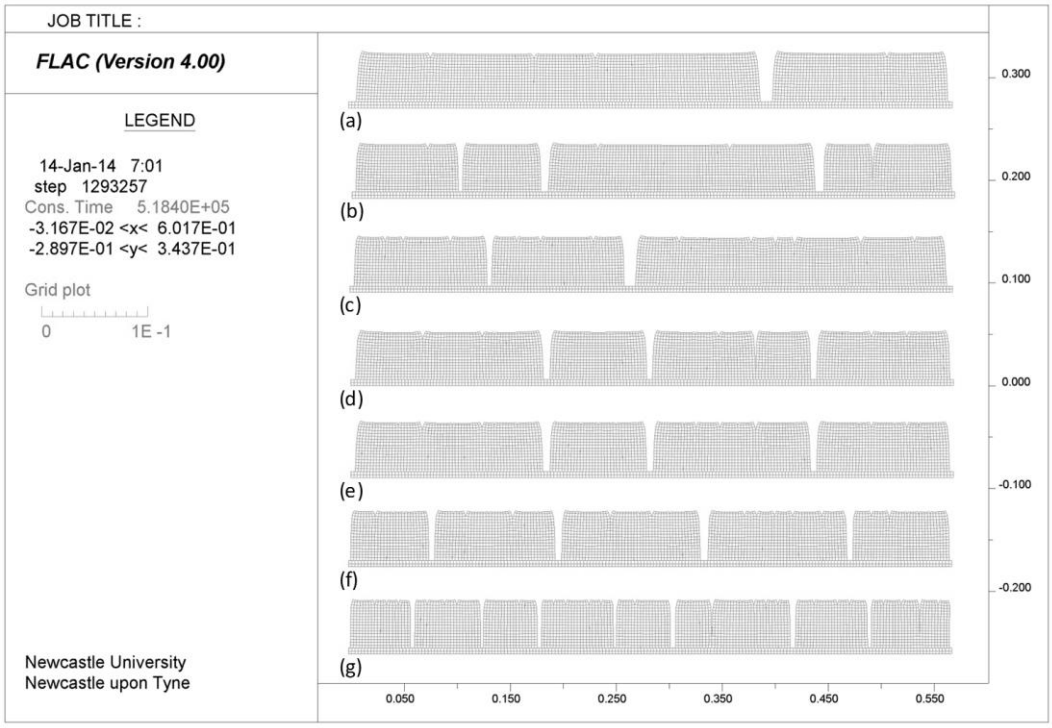

Figure 5.21 Crack geometries resulting from varied tensile strength magnitude (a) +50%, (b) +20%, (c) +10%, (d) 0%, (e) -10%, (f) -20% and (g) -50%.

The CIF time-series data for the above simulations are presented in Figure 5.22. As was identified in the final crack geometry plots, simulations conducted with +/-50% variation in tensile strength magnitude present the extreme cases. Simulation using a -50% trend resulted in a 3% higher CIF after stage I than in the use of +50%. Furthermore, the rate of CIF increase associated with the widening of existing cracks in stage II is shown to be greater in the weaker case and the onset of stage III disintegration is observed to have occurred 44 hrs earlier. The higher rate of widening is attributed to the presence of a greater number of cracks. The earlier onset of surface disintegration is a consequence

of lower surficial stresses required to break the interface bonds, the same mechanism that produced the original, deeper cracking. The CIF outlier to the expected pattern between the extreme cases is at +10%. With only two fully penetrating cracks, stages I and II show CIF development below that of +20% as well as unexpectedly large surface deterioration. It is not fully understood why this has occurred although at such a minor variation from the baseline case, it is proposed that numerical rounding in the solution scheme may be responsible.

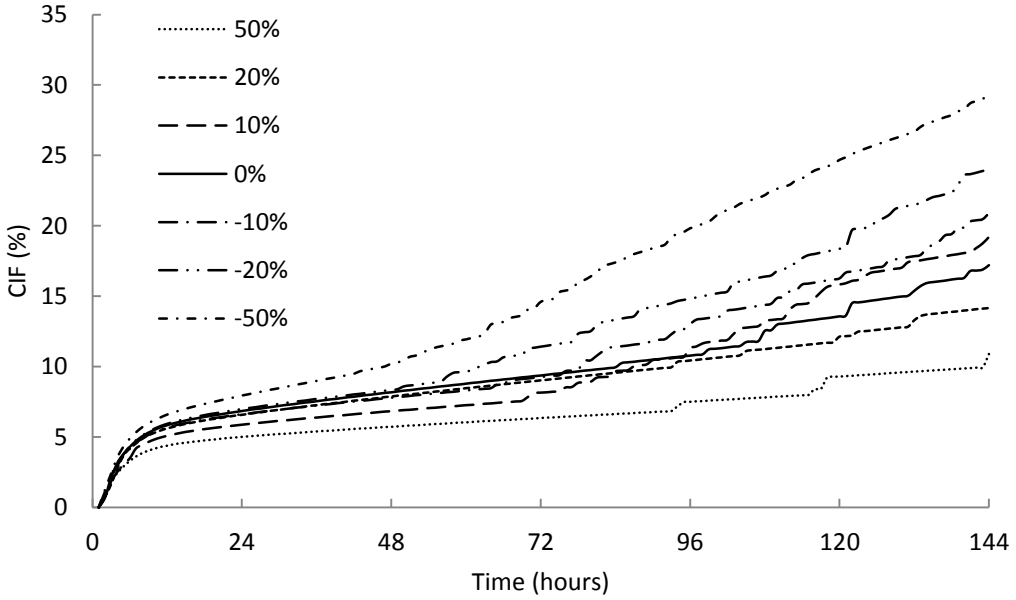

Figure 5.22 Effect of tensile strength magnitude on the development of CIF.

The tensile strength magnitude employed has been found to influence the cracking style of the model output with a trend towards higher strength producing fewer, wide cracks with little surface disintegration. Conversely, a trend towards lower strength has been found to produce a larger number of narrow, closely spaced cracks with a large component of crust disintegration.

5.3.2.2 Tensile strength heterogeneity

In the baseline case, each crack orientated interface is prescribed a tensile strength randomised about a mean, measured value according to tensile strength testing (Chapter 4). However, to assess the influence of heterogeneity (the degree to which values deviate randomly from the mean), the standard deviation was varied.

The FISH random number generator command was used to return an integer, R, from a Gaussian distribution with a mean of 0.0 and a standard deviation of 1.0. The randomised tensile strength value was then calculated from Equation 5.5 where sd represents the desired standard deviation and the mean tensile strength as a function of water content is given by ${\sigma_t}^M$.

$$ {\sigma_t}^R = {\sigma_t}^M \left[{\sigma_t}^M R \left(\frac{sd}{10} \right) \right] \qquad \textbf{5.5} $$

For the purposes of this study, tensile strength heterogeneity was assessed using standard deviations of 1, 2.5, 5, 7.5 and 10. In addition, a scenario of homogeneity is also included i.e. an interface tensile strength dependent solely upon the local water content variation. The random number series is consistent across all simulations and is presented in Figure 5.8 (page 240). For an example ${\sigma_t}^M(\omega) = 10$ kPa, the resulting tensile strength distributions according to the investigated deviations are provided in Figure 5.23. It is important to note that calculated negative strengths are specified as zero and Figure 5.23 depicts all interfaces experiencing uniform water content though this is understood to be unlikely for any given time.

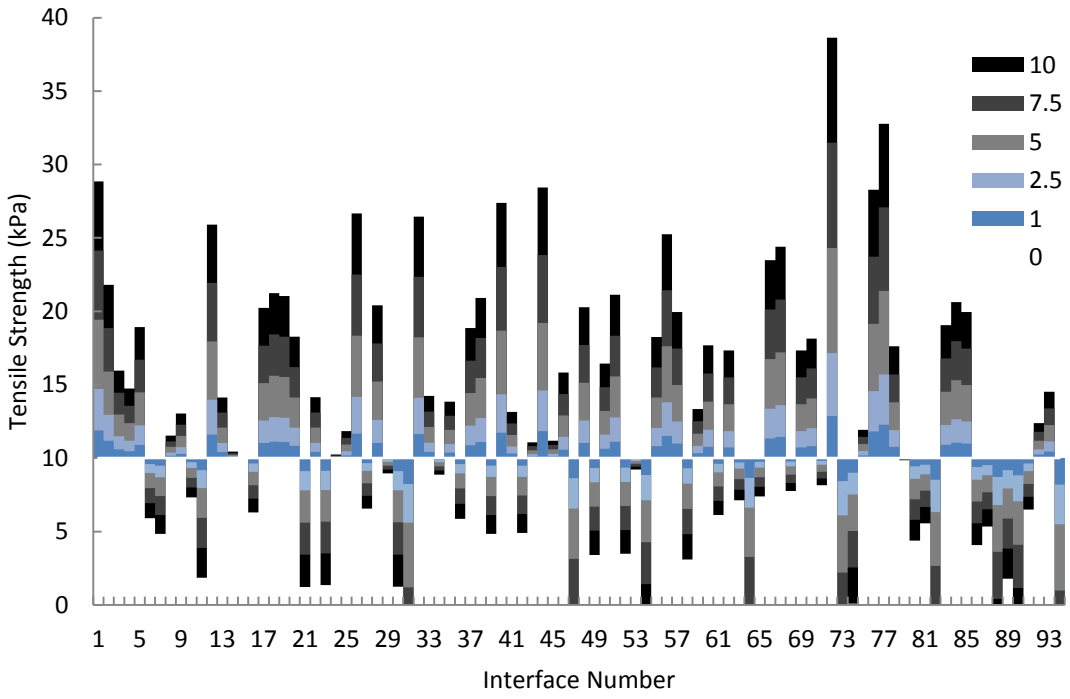

Figure 5.23 Example tensile strength distributions at various standard deviations

At this point, it is highlighted that tensile strength heterogeneity is the result of both the presence of flaws according to Griffith (1924) and potentially just a importantly, heterogeneity in water content distribution. Within any natural material, as within manmade materials, structural flaws exists to varying extent and scales; however, the spatial variability in the ability of the soil surface to exchange water vapour is recognised to bring about water content variation. The scale upon which this variation exists will be dynamic and transient, needless to say, it has been demonstrated in Chapter 4 that a sufficient difference in tensile strength results from relatively minor differences water content. Therefore, by incorporating tensile strength heterogeneity into the modelling procedure, this is thought to reflect the presence of a randomised variation in water content distribution.

The geometries produced by simulations under the described conditions are provided in Figure 5.24. The extreme cases of standard deviations equal to 0 and 10 show clearly different crack morphologies, but most interestingly is the commonality between intervening values of standard deviation. This will be discussed further in light of the recorded CIF time-series.

Where sd = 0, the essentially 1-dimensional drying from the pre-cracked upper surface of the clay leads to an approximately homogenous tensile strength distribution at any given time due to an almost uniform water content across the surface. Under the influence of horizontal stress relaxation produced by the free lateral boundaries, maximum tensile stress is formed at the centre of the bar. This is in agreement with the analytical tensile failure approaches in the absence of tensile strength heterogeneity (Section 2.7.2) (Kodikara & Choi, 2006; Hu et al., 2006; Peron et al., 2007; Kodikara & Costa, 2013). As such, it is not surprising that crack initiation has been shown to occur at the centre of the grid. However, no sequential infilling of subsequent cracking is evident. This is considered due to sufficient crack strain accommodation for the subsequently increasing tensile strength not to be met by further development of tensile stress with progressive drying.

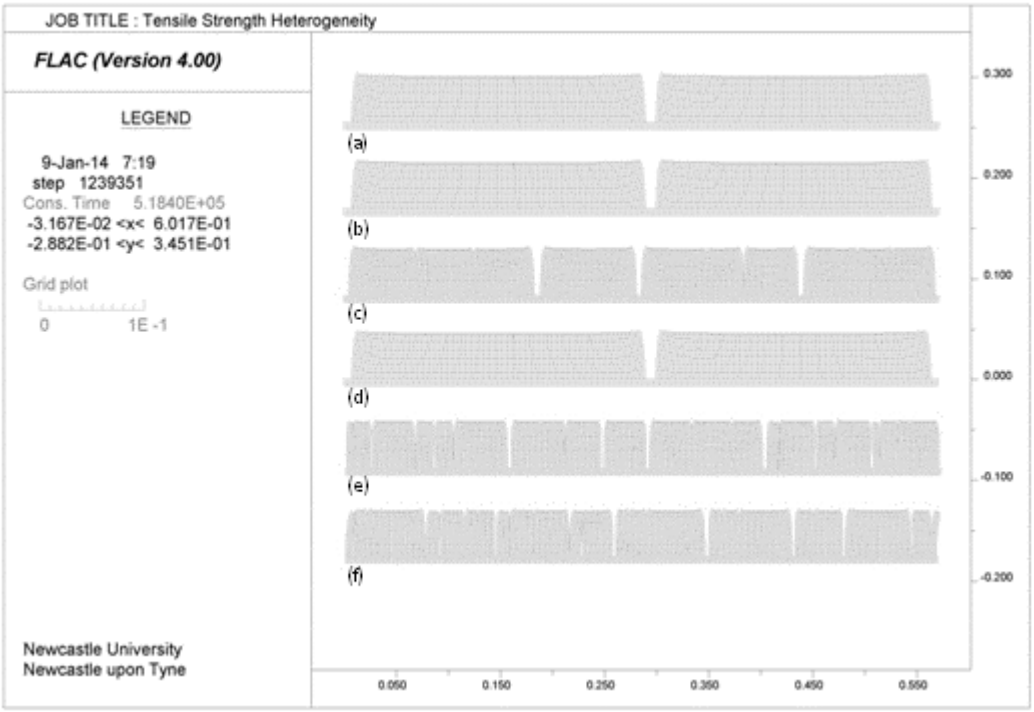

Figure 5.24 Crack geometries resulting from varied tensile strength standard deviations equal to (a) 0, (b) 1, (c) 2.5, (d) 5, (e) 7.5 and (f) 10.

The simplistic crack geometry of the $sd = 0$ case is further identified in the recorded CIF data, as provided in Figure 5.25. Here, the initiation of the crack is clearly identifiable during stage I, after which the remaining drying time shows stage II shrinkage associated with crack widening and end shrinkage.

With the introduction of a small standard deviation of 1, no change to the style of cracking is found in both Figure 5.24b and Figure 5.25. This level of tensile strength deviation throughout the clay is not sufficient to produce anything other than idealised, theoretical behaviour. However, when $sd = 2.5$ (baseline case), the development of a realistic crack morphology is captured (Figure 5.24c) with three identifiable stages of CIF development. With further increase in standard deviation to 5, cracking is identical to the numerical case with no heterogeneity; the reason for this is not clear. By increasing the standard deviation further to 7.5 and 10, cracking is shown to be much more pervasive in manner with very similar trends in CIF development (Figure 5.25). A stage I crack initiation phase is still observed though this is followed by an approximately linear increase at 0.12%hr^{-1}. This is likely due to a sufficient number of interfaces being weak enough under a given drying state for constant crack initiation and growth to occur.

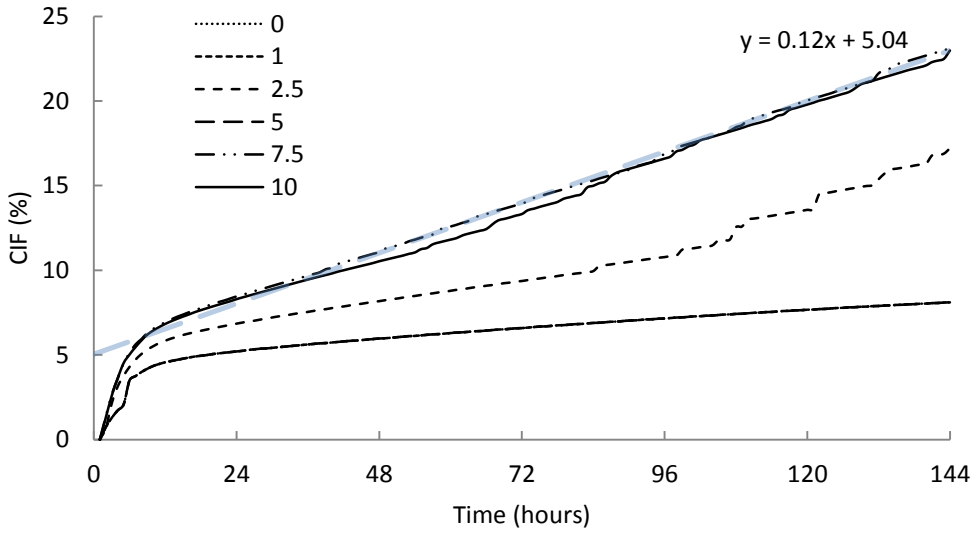

Figure 5.25 Effect of tensile strength standard deviation on the development of CIF.

By comparing the results of this study to the crack morphology observed in the indicative laboratory experiments (Figure 5.16), a standard deviation of 2.5 is believed appropriate for the clay under consideration. This is by no means a conclusive methodology to establish the correct degree of heterogeneity for the modelling of all cracking soils but is a necessary component of any crack modelling work that includes the randomisation of tensile strength throughout a

drying medium. Such a feature is understood to be central to the ability of the model to capture appropriate crack initiation rate and distribution.

5.3.2.3 Constant tensile strength

In addition to the above studies whereby each interface tensile strength behaves according to the accepted trend of increasing strength with decreasing water content, the effect of constant, homogenous tensile strength is presented. In this case a constant tensile strength value of 10 kPa was prescribed for all crack interface elements and maintained throughout drying.

The resulting model geometry is presented in Figure 5.26 alongside data showing the separation of each interface across the mesh. It is found that all crack interfaces have separated with an average separation of 1.86mm as highlighted. The majority of interfaces have separated within the range of 0.8-1.8mm and were produced by the near simultaneous exceeding of the constant tensile strength. However, 9 cracks are observed to have developed >2mm width with three of these exceeding 5mm. This behaviour is contrary to both the predicted theory for a continuous medium where in the absence of tensile heterogeneity, crack growth should not localise and to that of the free ended bar as depicted in Figure 5.24a. The occurrence of these anomalous cracks is thought to be a numerical issue, the product of rounding during the time-stepping procedure.

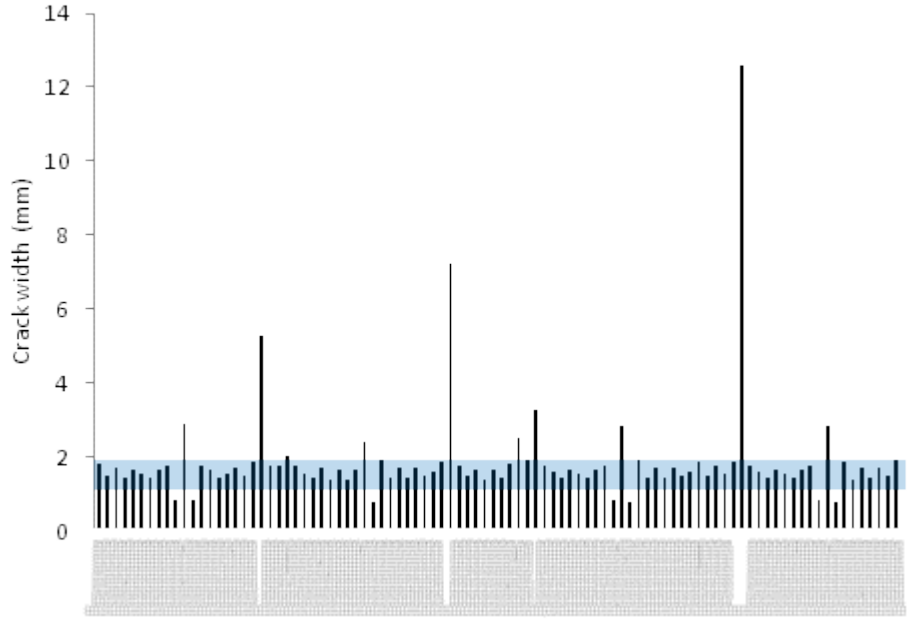

Figure 5.26 Final crack distribution using constant tensile strength (10kPa).

The broadly linear development of CIF at 0.21%hr^{-1} shown in Figure 5.27 is indicative of the relatively constant separation of interfaces. The stepwise transitions highlighted indicate the initiation of the anomalously dominant crack features. The magnitude of CIF that has developed during the 6 days of drying is much larger than that of the baseline case with no indication of eventual cessation in this time. The interface behaviour in this study may therefore be likened to continual stage I CIF development and does not conform to the rapid establishment of a stable crack pattern with drying.

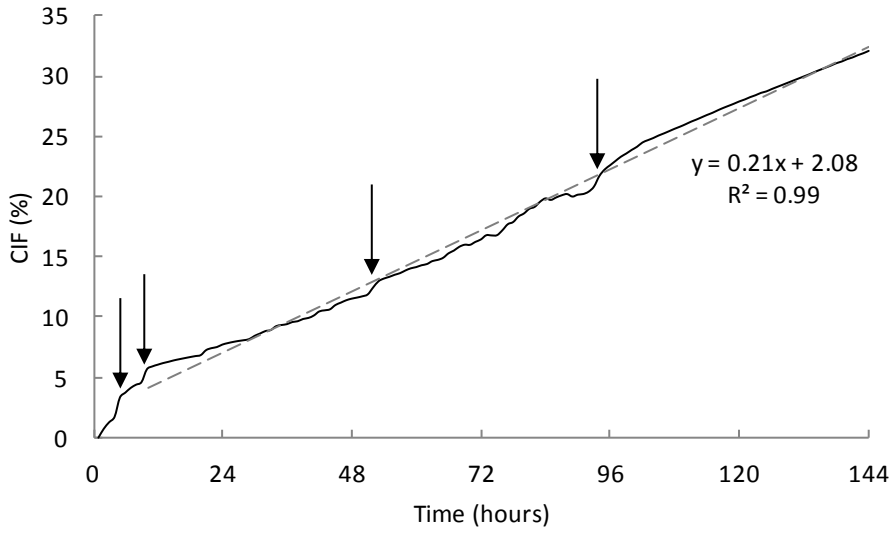

Figure 5.27 Development of CIF with constant tensile strength.

5.3.3 Mechanical boundary effects

The mechanical boundary conditions employed in the modelling of any geotechnical scenario play a fundamental role in the generation of an accurate stress-strain field and are directly linked to the initiation of cracking. In this section, the baseline model has been tested for the influence of both the lateral and basal boundary conditions. The lateral boundary analysis has investigated behaviour where shrinkage from the end of the simulated mould is both facilitated and restricted. The influence of the boundary condition at the clay base has also been investigated via the two bounding extreme cases. This boundary has been found to have the greatest influence upon the development of cracking.

5.3.3.1 Basal interface condition

To investigate the influence of the basal boundary condition on crack development, the baseline model scenario was compared to fully fixed and free conditions. Where in the baseline scenario, the clay-mould interface is subject to measured shear conditions, a fixed boundary in the x-direction is considered to approach a vertically continuous case where the thickness of the clay is infinite and lateral displacement is limited by the presence of further clay to depth. However, it is recognised that in the fixed case, zero displacement is an extreme of this scenario. The free case is highly idealised and may be considered only representative of specialised laboratory scenarios such as in the use of Teflon (Peron et al., 2005) or glass (Lecocq & Vandewalle, 2003; Vogel et al., 2005) mould constructions or highly lubricated surfaces (Groisman & Kaplan, 1994; Nahlawi & Kodikara, 2006).

The resulting mesh geometries from each case are presented in Figure 5.28. The crack geometries of the fixed and shear condition cases are found to be very similar with the same number and spacing of cracks. However, when fixed, shrinkage has clearly been restrained at the clay block ends and crack tips limiting allowable accommodation of crack growth at depth. The free shrinkage case (Figure 5.28c) shows a dramatically different geometry with no fully penetrating cracks forming and maximum shrinkage being accommodated at the block edges.

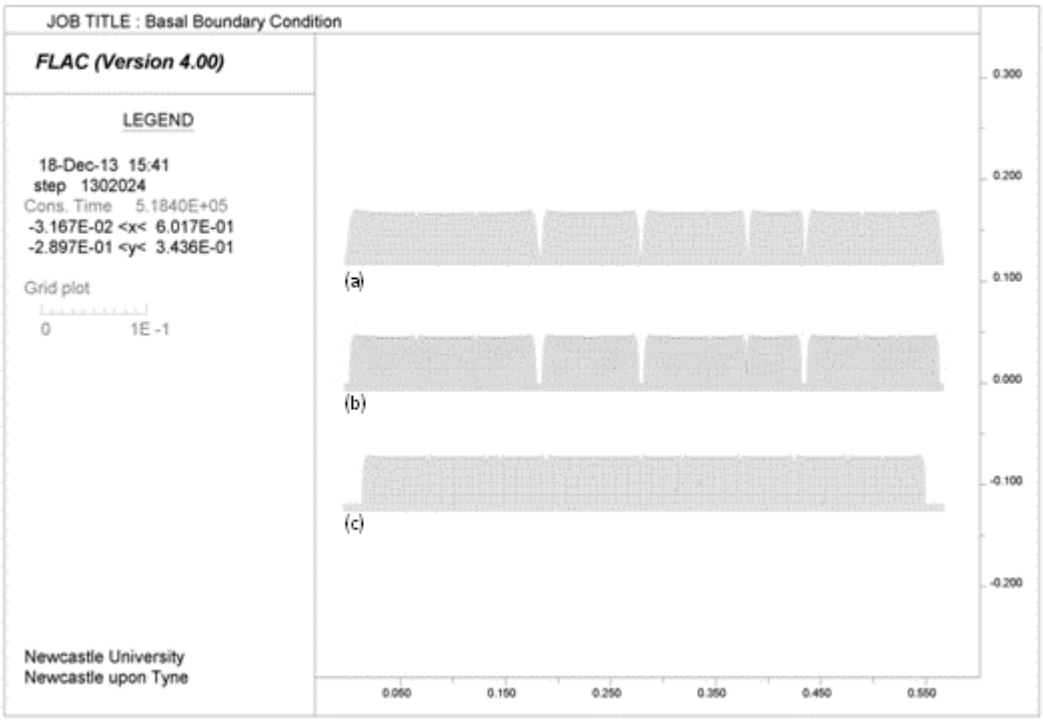

Figure 5.28 Crack geometries resulting from (a) fixed, (b) shear boundary and (c) free basal conditions.

The crack intensity factor time-series presented in Figure 5.29 highlights the similarity in cracking behaviour between the fixed and restrained cases. As can be seen, the common CIF trend deviates only at the onset of stage III where initiation of shallow cracking in the fixed case initiated approximately 14 hours earlier. With no basal restraint, less total shrinkage is shown to occur during stage I and II of the CIF development as indicated by the lack of penetrative cracking in the final geometry. However, of the three cases, the free case shows the earliest onset of desiccated crust disintegration (stage III).

This study clearly demonstrates the necessity of basal restriction in the development of deep cracking. This finding is not entirely surprising and is born out in experimental works (Hu et al., 2006; Peron et al., 2009). The results do indicate the ability of the model to capture this mechanism and furthermore show evidence of an inevitable development of a disintegrating crust under all restraint conditions upon prolonged drying. The inclusion of moisture dependent restraint and ultimate detachment compared to traditional fixed base methodologies is found to influence crack growth; crack widths are larger relative to free lateral shrinkage during laboratory scale simulation. It is expected that this influence would be more exaggerated with decreasing clay

layer thickness as greater shrinkage is known to occur with proximity to the drying boundary.

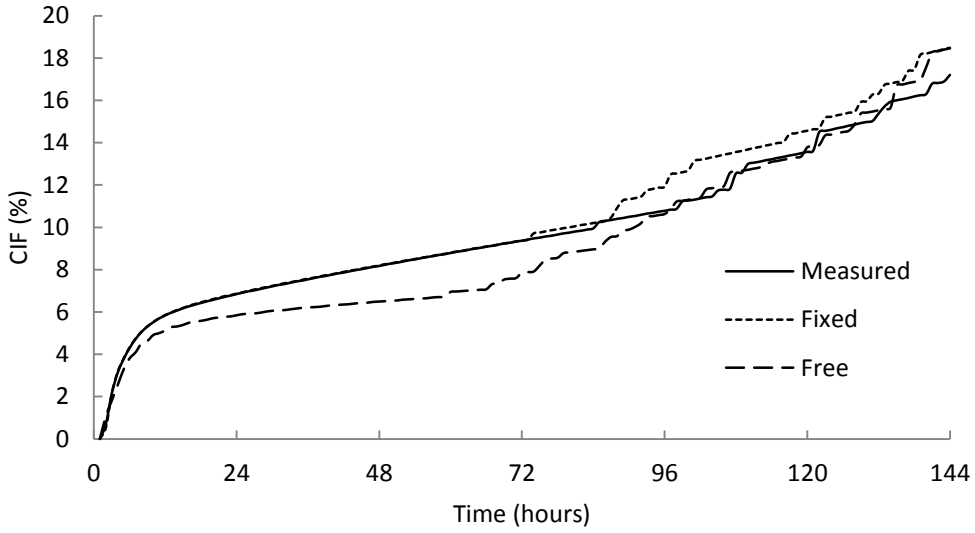

Figure 5.29 Development of CIF with fixed, free and measured basal boundary conditions.

5.3.3.2 Lateral boundary condition

To investigate the influence of different lateral boundary conditions on crack development, the baseline model scenario where boundaries are free to shrink from the inner mould surface was compared to the same simulation but with a fixed x-direction condition. This setup may be considered to represent continuation of the clay beyond the horizontal grid limits whereby symmetrical generation of stress-strain conditions are understood to occur. However, this is not the intended scenario under investigation as this would be more accurately simulated under plain strain analysis. For ease of comparison, plain stress conditions have been maintained. Additionally, in the fixed case, the boundary remained free in the y-direction allowing vertical shrinkage to occur as observed in the baseline case.

The final cracked geometries of both cases are presented in Figure 5.30. In the fixed case, fully penetrating cracks developed at the weakest interface sites as in the free case. However, these cracks are wider and have accommodated the shrinkage that otherwise manifested itself as additional crack opening in the free case. Additionally, a narrow, fully penetrating crack is shown to be located at the furthest right-hand interface. Where horizontal stress relief is facilitated in the use of a free lateral boundary, a fixed boundary has not allowed this such that the local horizontal tensile stress has exceeded the interface tensile strength.

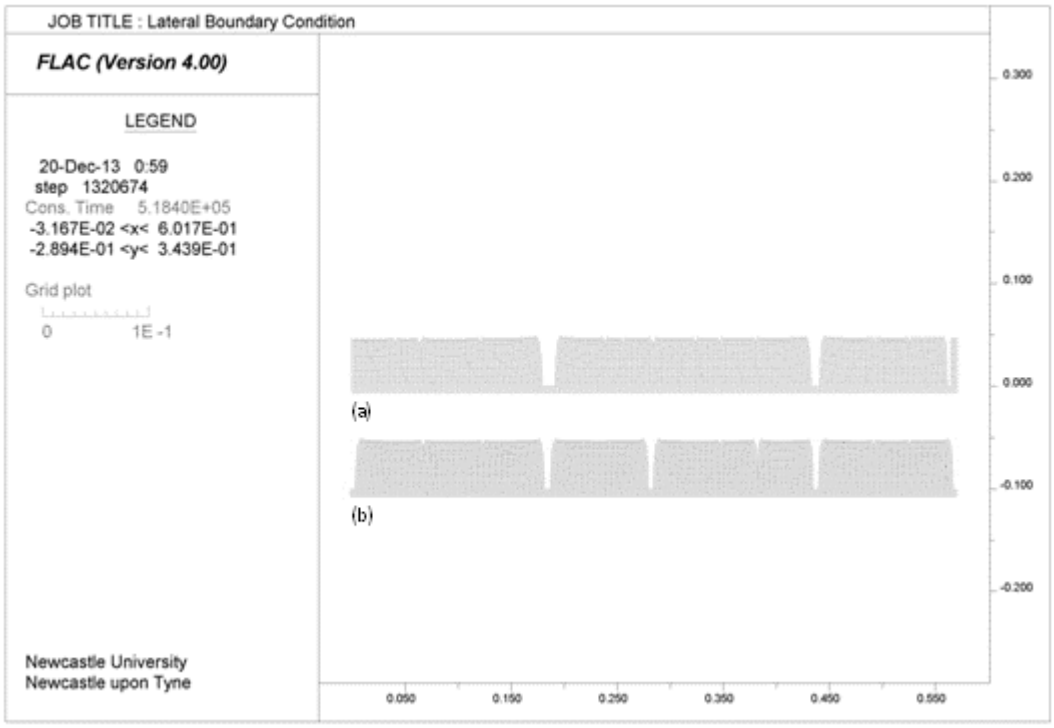

Figure 5.30 Crack geometries resulting from (a) free and (b) fixed lateral boundary conditions.

The crack intensity is presented in Figure 5.31 where it may be seen that primary crack onset is similarly timed although the behaviour deviates upon approach of stable shrinkage. The free case has allowed for a greater degree of surface opening as depicted by the steeper gradient. However, it is interesting to note the difference in development of shallow cracking between the two cases. The third, shallow cracking stage is initiated earlier in the fixed case and is related to an elevated surface tensile stress within the desiccating crust. These conditions are not generated until later in the simulated flow-time of the free case due to the combined action of end shrinkage stress relief (contributing to the overall higher CIF) and the perturbations in the surface crustal stress caused by the initiation of centrally located cracking.

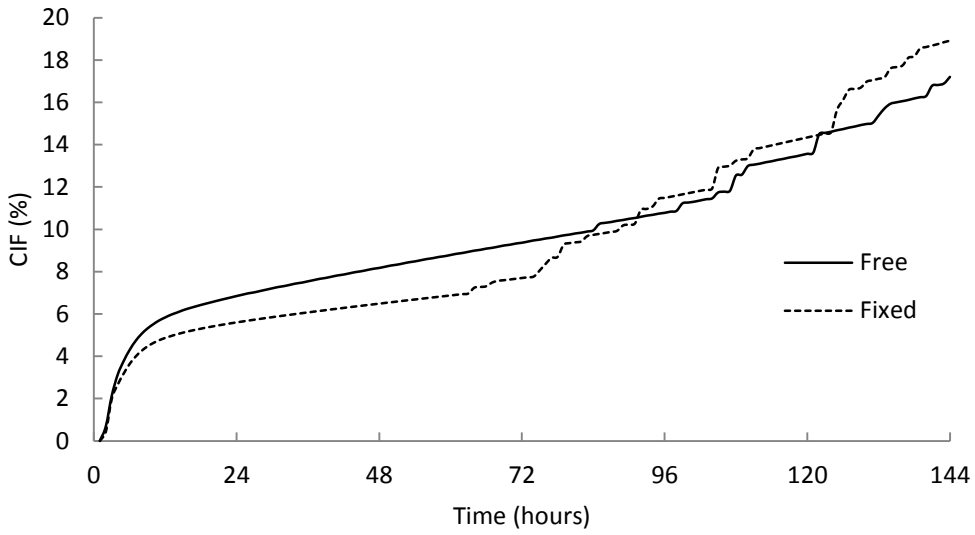

Figure 5.31 Development of CIF with free and fixed lateral boundary conditions.

Although the fixed case is not directly comparable to an infinite boundary condition, this exercise may indicate a tendency towards more widely spaced cracks of greater aperture in addition to more pronounced disintegration of the desiccated upper-most layer.

5.4 Hydrological conditions

The following studies investigate the influence of hydrological conditions on the drying and cracking behaviour of the developed model alone. Hence, for consistency, the mechanical conditions outlined in the baseline case will be maintained throughout these simulations. An attempt to utilise field and laboratory conditions and parameter magnitudes has been made; however, with respect to variation in the SWRC of the compacted fill, the absence of variable data has led to representative values being sought from the literature where possible.

5.4.1 Drying rate

Drying was simulated by the application of a discharge condition at exposed boundaries of the clay grid. FLAC defines this discharge rate as a constant value that represents the maximum extraction of available water. With the reduction in water availability with progressive drying, the effective rate of water discharge will reduce.

Typical drying curves from a slurried state are provided in Figure 5.32 and illustrate the two stage process. Initially, a constant and broadly linear stage of water removal is observed followed by a stage of reducing drying rate up until residual water content is reached. The transition between these stages is correlated with the saturated shrinkage limit presented by Haines (1923) in Figure 2.16. By applying a single, constant discharge rate in the modelling approach, this enables the linear initial portion of the drying curve to be captured. However, the drying curves of compacted soils show a slightly less well defined transition between the constant evaporation and falling rate stages, as illustrated in Figure 5.33. Such behaviour is exhibited in the simulations and discussed further within this section.

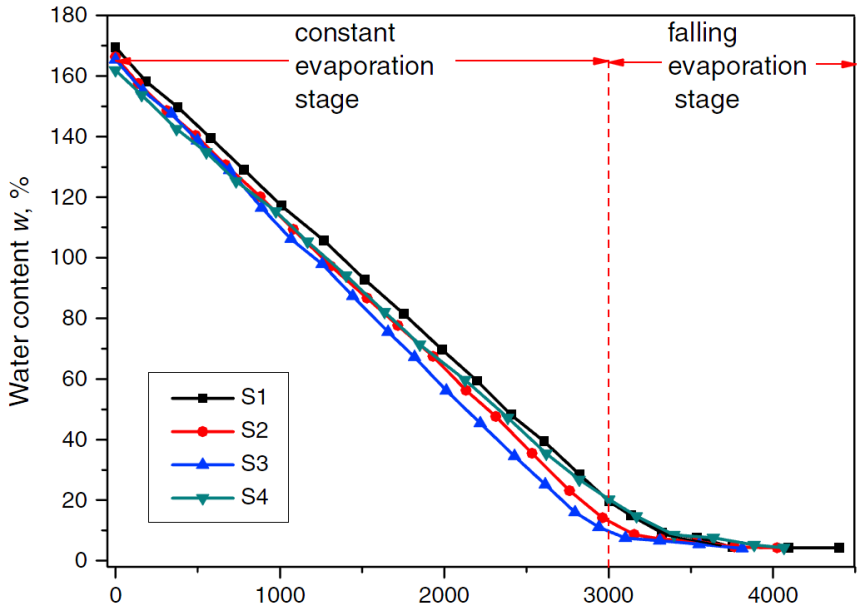

Figure 5.32 Desiccation curves from soil slurry (after Tang et al., 2011).

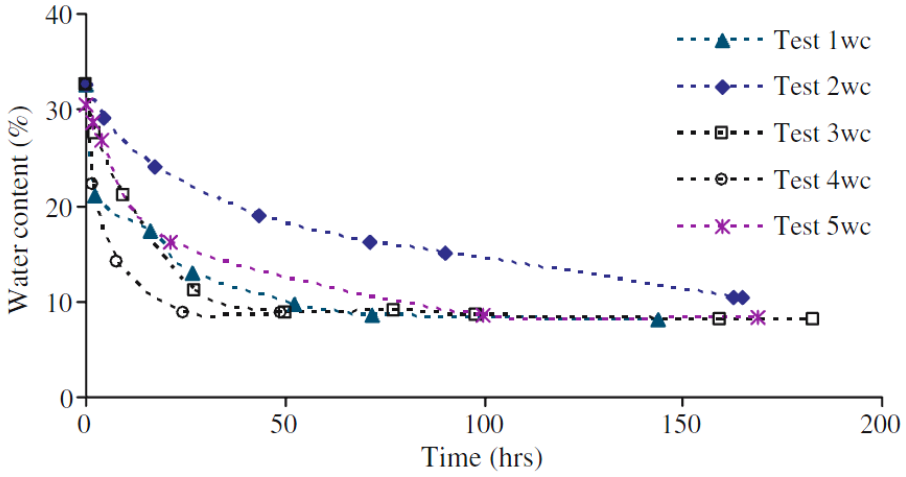

Figure 5.33 Desiccation curves from compacted soil (after Nahlawi & Kodikara, 2006).

Table 5.1 shows the discharge rates tested. These rates, of equal interval, have been selected to incorporate the minimum rate established in the indicative laboratory experiments (Test 1) up to a maximum rate equal to the difference between the baseline and this minimum. Given the parametric study methodology, all model other conditions have been maintained as per the baseline scenario.

Table 5.1 Drying rates tested

Discharge rate (ms^{-1})	Equivalent physical rate (ms^{-1})
1×10^{-6}	-
8×10^{-7}	-
6×10^{-7}	5.9×10^{-7} (Test 5)
4×10^{-7}	3.7×10^{-7} (Test 4)
2×10^{-7}	2.1×10^{-7} (Test 1)

The clearest illustration of the influence prescribed drying rate has on the drying of the clay grid is given by the global water content change with drying time presented in Figure 5.34. In all five of the curves, the two stages of primary drying transitioning to residual drying may be observed with only 1.4% (6.9-5.5%) water content difference after 6 days of drying. As would be expected, the lowest gradient is seen to be produced by the lowest applied drying rate. However, with increasing applied drying rate the increment by which the gradient of water loss increases is not linear. This may be explained by considering that although a higher applied rate of water removal can be specified, with a decreasing effective saturation front developing from the upper surface, unsaturated permeability will correspondingly reduce. This effect indicates the influence of the developing desiccated crust which acts as a hydraulic barrier that moderates the flow of water through an increasingly unsaturated zone.

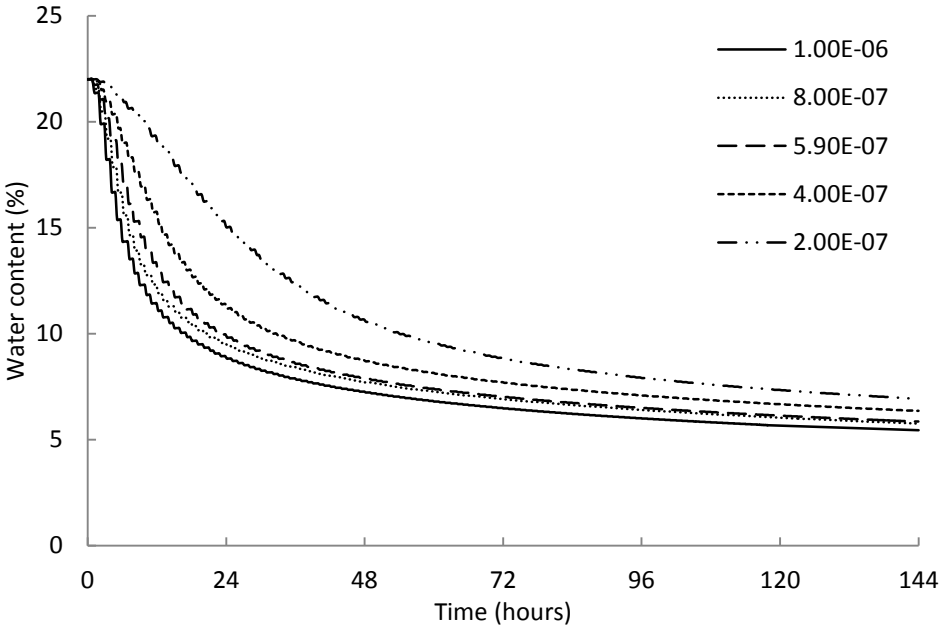

Figure 5.34 Drying curves for each applied drying rate.

The effect of applied drying rate on the resultant cracked geometry is presented in Figure 5.35. Cracking is clearly more pervasive with higher applied drying rates. Given the common SWRC employed throughout these simulations, greater cracking is thought to occur due to a greater increase in suction leading to tensile stresses exceeding the tensile strength more rapidly with higher drying rates. After 6 days of drying, a maximum of three fully penetrating cracks are formed, this crack number ceiling is considered to be a function of the length of the model grid. It is evident that shallow surface cracking features are only found when dried at a rate of 4×10^{-7}ms^{-1} or above, a solitary, fully penetrating crack is shown after drying at a rate of 2×10^{-7}ms^{-1}. With the formation of only widely spaced, deep cracking at lower drying rates, the formation of a heavily desiccated crust is shown to be less dominant in the formation of cracking.

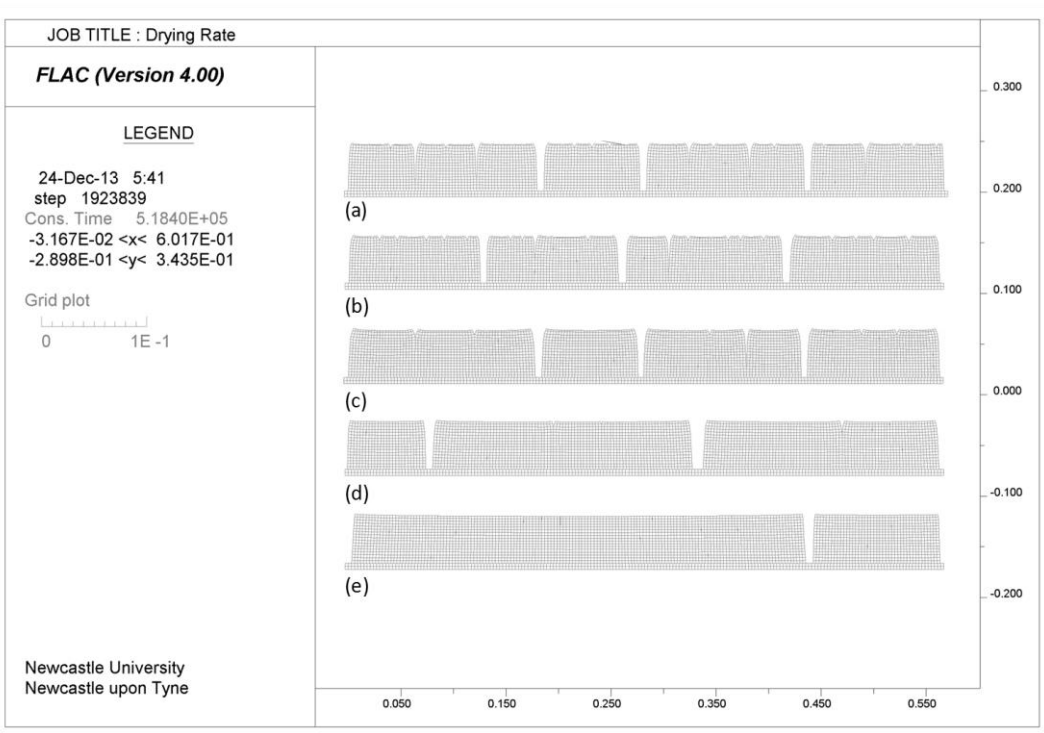

Figure 5.35 Crack geometries resulting from varied drying rates (ms^{-1}) (a) 1×10^{-6}, (b) 8×10^{-7}, (c) 6×10^{-7}, (d) 4×10^{-7} and (e) 2×10^{-7}.

The CIF time-series for each applied drying rate is provided in Figure 5.36. Owing to the magnitude of the CIF beyond 123 hours recorded when modelling a rate of $1 \times 10^{-6} ms^{-1}$, data for this simulation beyond this time has been excluded from Figure 5.36; the full time-series may be found in Figure 5.37.

Stage I crack initiation and primary shrinkage is shown to differ between the simulations in two principle ways. Firstly, the rate in which the CIF trends are found to increase is clearly greater for higher applied drying rates. Secondly, the duration of this stage is seen to reduce with increased rate. These characteristics are directly linked to the trend in water loss previously described. The more rapid the water removal, the quicker the generation of elevated suctions toward the drying surface which in turn results in a higher degree of cracking (higher CIF). Similarly, the onset of stage III surface deterioration is shown to occur earlier for higher rate simulations with the lowest rate CIF curve never reaching this stage. A further stage in CIF development is shown beyond a simulated flow-time of 123 hours at the highest rate (Figure 5.37). This stage exhibits a perfectly linear increase in CIF at $48\%hr^{-1}$. The uniform nature of this stage is likely the result of all crack orientated interface elements having

separated, leaving the uppermost element row able to shrink isotropically at a rate proportional to the suction generated. Therefore, this late behaviour is purely a numerical artefact of the model geometry.

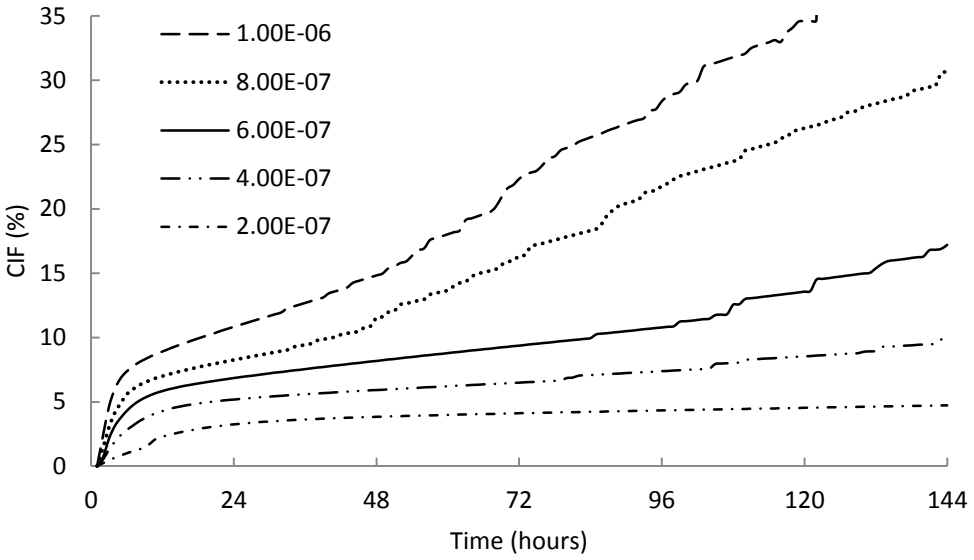

Figure 5.36 Development of CIF with each applied drying rates.

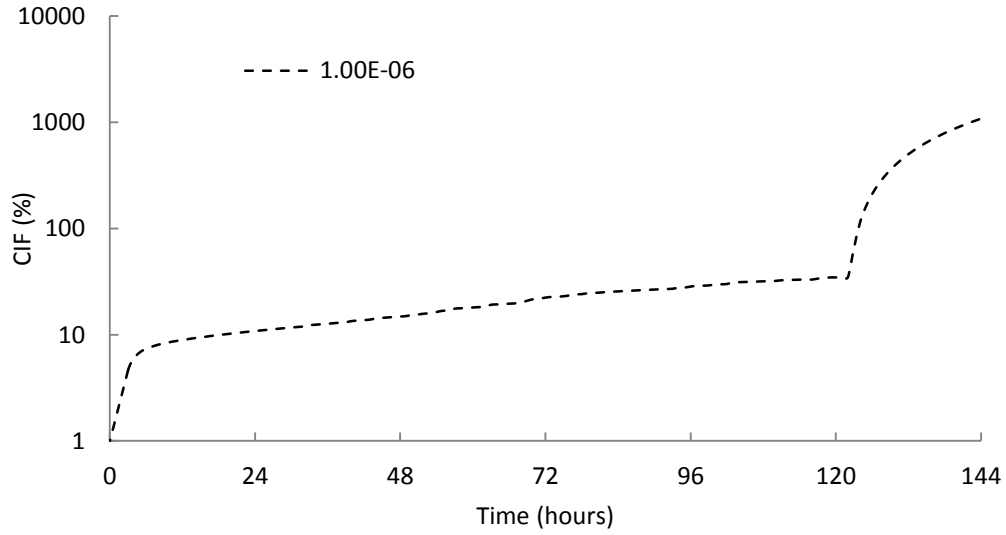

Figure 5.37 Development of CIF with an applied drying rate of 1×10^{-6} ms^{-1}.

5.4.2 Saturated permeability

The unsaturated hydraulic conductivity (k) is determined as a fraction of the hydraulic conductivity of the medium under saturated conditions (k_s). The weighting of this fraction is governed by the moisture content of the soil as given by van Genuchten (1980) and is derived using the van Genuchten m parameter and the effective saturation (θ_e) given as follows:

$$k = k_s\sqrt{\theta_e}\left(1-\left(1-{\theta_e}^{1/m}\right)^m\right)^2 \quad \textbf{5.6}$$

The van Genuchten m parameter influences the shape of the SWRC description and as such is related to the 'rate' of de-saturation according to $m = 1 - 1/n$ (Mualem, 1976). The saturated hydraulic conductivity may be considered to govern the overall magnitude of the conductivity range experienced by a drying soil and hence has a large effect on the hydraulic conductivity experienced by the soil prior to the cracking water content.

Hydraulic conductivity values were selected with regards to the laboratory reference value of 1.12×10^{-10} ms^{-1}. Selected conductivity magnitudes are presented below:

Table 5.2 Tested hydraulic conductivity values and associated total flow times.

'Permeability'		Flow time (hours)
Saturated Mobility coefficient (m^2(Pa.s)$^{-1}$)	Saturated hydraulic conductivity (ms^{-1})†	
5×10^{-13}	5×10^{-11}	144
1×10^{-12}	1×10^{-10}	144
5×10^{-12}	5×10^{-10}	144
1×10^{-11}	1×10^{-9}	144
5×10^{-11}	5×10^{-9}	50
1×10^{-10}	1×10^{-8}	26

†dynamic viscosity of water constant at 1×10^{-3} Pa.s at 20℃

It is important to note that model runs were conducted for a simulated flow time of 144 hours (6 days). However, conductivity values of 5×10^{-9} and 1×10^{-8} ms^{-1} (highlighted in Table 5.2) did not run to completion due to numerical instability as a result of excessive localised deformation. The flow times provided in Table 5.2 represent the last intact stage of the model run. As described in Section 3.2.1.3, quadrilateral elements that make up the model mesh are sub-divided into triangular pairs. If both of these sets of triangular elements are badly distorted then FLAC reports an error (ITASCA, 2002). Thus, the finite difference mesh is unable to manage the large element distortions. The incomplete model runs confirm that the model is unable to run with a saturated hydraulic conductivity greater than 5×10^{-9} ms^{-1}.

The incomplete simulations at relatively high conductivities have been included alongside successful simulations in the water loss data presented in Figure 5.38. During the early stages of drying, the rate of water loss is approximately consistent across all simulations (highlighted). However, the data diverges after primary drying and a marked difference is observed between the final water contents achieved by each simulation. The general trend of greater water loss with increased saturated hydraulic conductivity is clearly depicted. Interestingly, the influence of saturated hydraulic conductivity is most evident during the transitional stage as primary drying is continued longer when a higher conductivity value is applied. There exists little range in the rates of water loss during residual drying i.e. 0.01-0.05 %/hr-1 during the latter 3 days. Hence, the period of influence is restricted to the transitional drying stage. Those tests that did not complete the full specified flow time indicate the continuation of this trend but the data cannot conclusively confirm this behaviour.

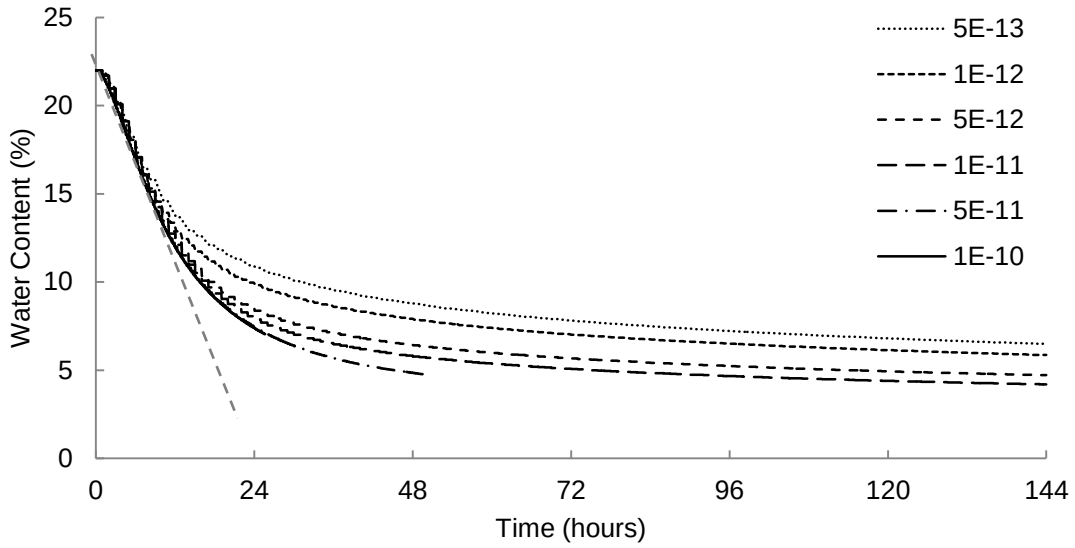

Figure 5.38 Water content change for varied saturated mobility coefficient values.

To evaluate the influence of the resultant primary drying phase cessation on the initiation of cracking, the surface suction at initiation is plotted for each case in Figure 5.39. Cracking is initiated at relatively low suction values when higher saturated hydraulic conductivities are applied with the surface of the clay remaining saturated. However, cracking is observed to initiate about the AEV at de-saturation when lower conductivities are applied. The difference in suctions generated at the surface of the clay is a direct result of water removal rate and as such may be linked to behaviour observed in the study of applied drying rate (Section 5.4.1).

With higher conductivity, more rapid transport of water toward the drying boundary may occur, thus inhibiting the generation of elevated surface suctions and producing the greater global mesh drying seen in Figure 5.38. However, applied lower conductivity inhibits the dissipation of suctions, with the early generation of these surface suctions, the feedback mechanism will lead to further reduced relative permeability. A hydraulic barrier in the form of the desiccated crust is effectively produced. Therefore elevated suctions local to the surface are established despite lower global mesh drying.

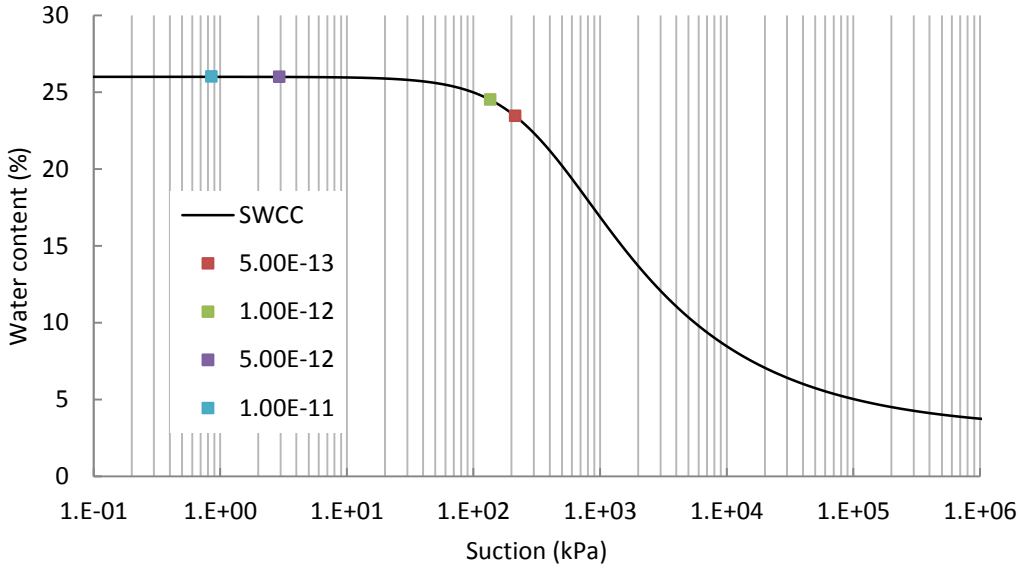

Figure 5.39 Surface suction at crack initiation with varied saturated mobility coefficient values.

The final geometries for the listed successful simulations are presented for comparison in Figure 5.40. The most striking change between the cracked geometries is the increase in crack number with decreasing hydraulic conductivity. Saturated mobility coefficients of 1×10^{-11} and 5×10^{-12} $m^2(Pa.s)^{-1}$ both show a single, fully penetrating crack which are shown to differ in width on the basis of CIF (Figure 5.41). No shallow surface cracking/crumbling behaviour is observed in these simulations which indicates the lack of a desiccated crust; this is in agreement with the lower final water content and surface suction discussed earlier. Geometry (c) is the baseline case and is shown to exhibit both fully penetrating cracking and stage III surface disintegration as a result of crust formation due to elevated surface suction. The minimum saturated hydraulic conductivity case shows a greater number of deep cracks (Figure 5.40d) and the earliest onset of surface disintegration that totals the highest CIF recorded (Figure 5.41).

This study highlights the ability of the model to capture two dominant drivers in the tensile cracking mechanism. Where cracking has propagated to the clay-base contact, crack growth is determined by the tensile reaction stress generated by the basal restraint. With the formation of a shallow, hydraulically isolated layer due to locally decreased unsaturated permeability, elevated suctions in this region generate a high eigen-stress gradient that leads to tensile lateral stresses at the surface and crack initiation.

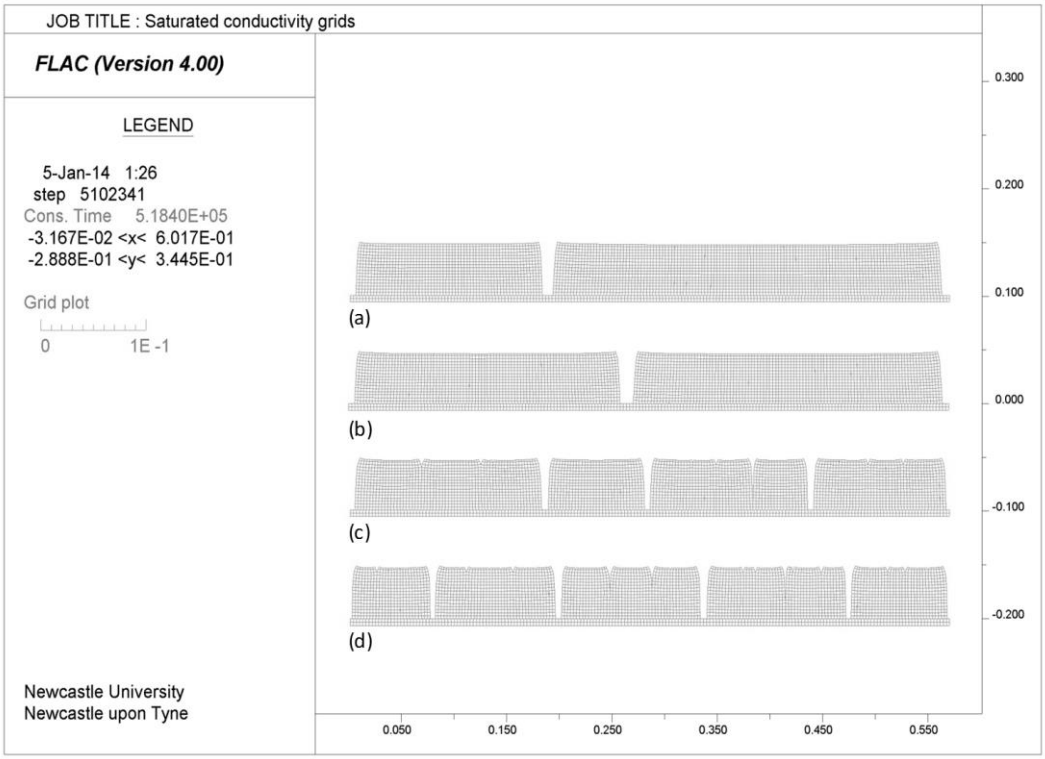

Figure 5.40 Crack geometries resulting from saturated mobility coefficient values (m^2/(Pa.s)) (a) 1×10^{-11}, (b) 5×10^{-12}, (c) 1×10^{-12} and (d) 5×10^{-13}.

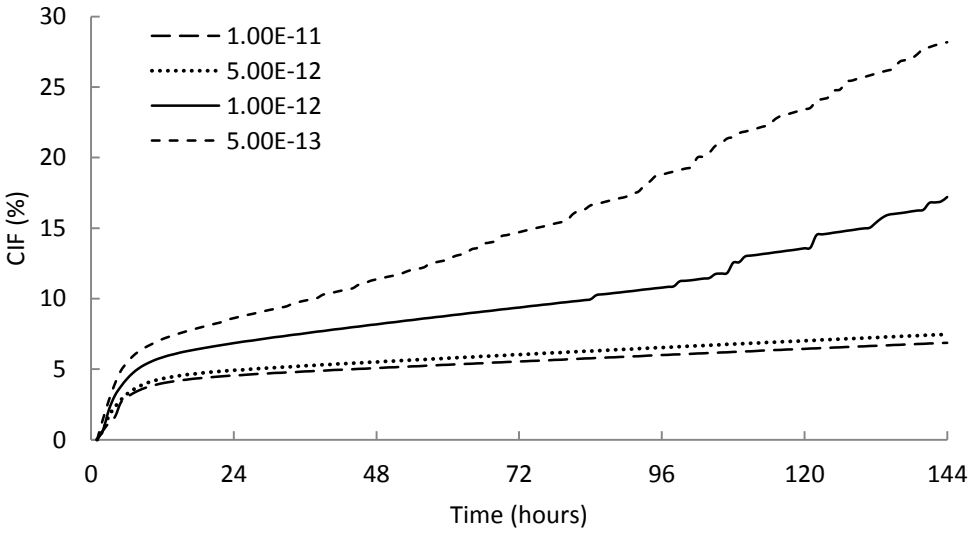

Figure 5.41 Development of CIF with varied saturated mobility coefficient values.

5.4.3 Soil-water retention parameters

The relationship between decreasing water content and the resulting increase in negative pore water pressure is fundamental to the generation of shrinkage stresses. FLAC tp-flow incorporates a description of the soil-water retention via the van Genuchten expression whereby effective water content is related to suction/head by three curve fitting parameters, α, n and m. The functions of each parameter are described in Section 2.2.5; however, in using the Maulem - van Genuchten approximation (where $m = 1 - 1/n$), the SWRC fitting parameters are reduced to the α and n coefficients (van Genuchten, 1980). These directly relate to the air-entry value (the suction at which the curve deflects from saturation due to the entry of air into the largest pore spaces) and the steepness of the curve (the rate at which the soil de-saturates under a given suction range, considered relative to the PSD) respectively.

The following work investigates the influence of these hydraulic soil properties, via the variation of van Genuchten curve parameters, on the cracking behaviour simulated by the developed model.

5.4.3.1 Air-entry value (α coefficient)

The AEV derived from the measured SWRC data (as presented in Figure 3.18 on page 153) constituted the baseline value about which a lower and upper bounding set of values were selected. These are provided in Table 5.3.

Table 5.3 Tested air entry values.

α coefficient (m^{-1})	P_0 (kPa)	Equivalent Soil Type†		
			AEV (kPa)	
0.28	35.7	Silt	20	(Huang, 1994)
0.028	357.1	Indian Head Till	200	(Vanapalli, 1994)
0.0028	3571.4	Regina Clay	2500	(Fredlund, 1964)

†as cited in Vanapalli et al., 1999

The measured value of 357.1 kPa may be compared in magnitude to other compacted glacial tills such as Indian Head Till in Canada (Vanapalli, 1994). Air entry (P_0) values 1 order of magnitude greater and less than the measured value were chosen. These values are comparable to those measured for other soil types such as a coarser, silt material where the pore-size distribution

possesses larger pores allows air entry at lower suctions as well as high plasticity clay where pore-sizes are much smaller and higher suctions are required. The remaining baseline SWRC parameters were maintained in order to isolate the effect of SWRC air entry. This gives rise to the curves presented in Figure 5.42.

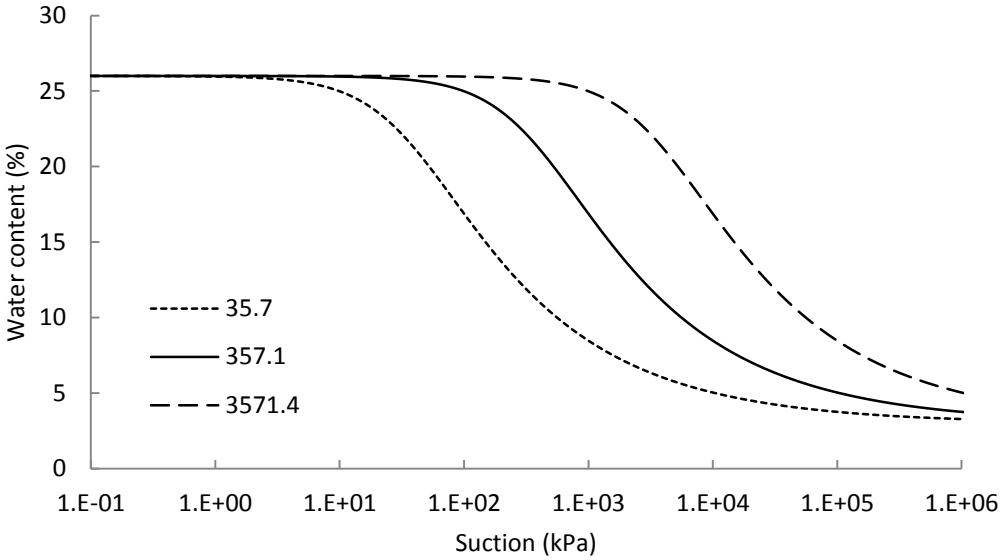

Figure 5.42 SWRC showing tested air entry values.

The global water loss with progressive drying for each simulation is presented in Figure 5.43. Primary drying is shown to have occurred at a greater rate in simulations conducted using a lower AEV. However, in using a reduced AEV, primary drying is seen to transition to residual drying most quickly. More rapid drying in this simulation would be physically expected given the inherently lower suction needed for draining of the pore space. Despite this, the same final water content is achieved by the minimum and maximum AEV simulations after 6 days of drying. An elevated AEV is shown to produce more subtly changing water content with drying time. Here, primary drying is slower and residual water content is not conclusively reached after the baseline 6 day drying period.

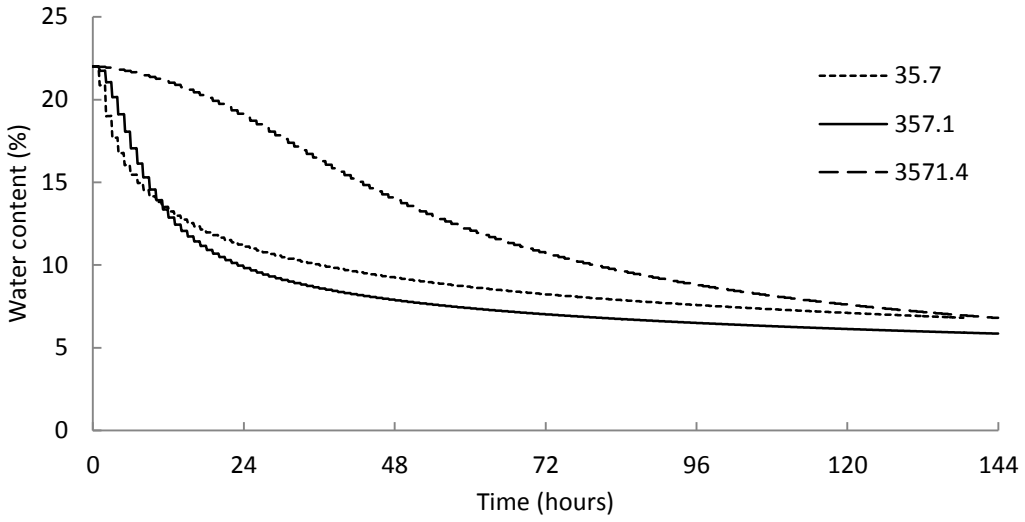

Figure 5.43 Drying curves for each air entry value.

The ultimate geometries for the three simulations are presented in Figure 5.44. Each geometry shows extremely differing crack morphology and it is important to recognise that Figure 5.44c is significantly unlikely to physically occur. The cracked geometry produced using a lower AEV shows little end shrinkage and shallow, partially penetrating cracks. Figure 5.44b is the baseline case as described in Section 5.2. The high AEV simulation (Figure 5.44c) shows extensive cracking characterised by wide (10.4-22.7mm), fully penetrating interface separation. At approximately 125mm from the left-hand edge, an arch structure may be discerned. This is the product of two interface elements failing adjacent to a previously separated interface and due to a lack of confinement, the resulting free columns have collapsed. This is a direct result of the mesh-interface geometry. In addition to excessive ped shrinkage, the arch structure indicates that tensile stresses have continued to be developed such that the stress relaxation effect of the central interface opening is exceeded.

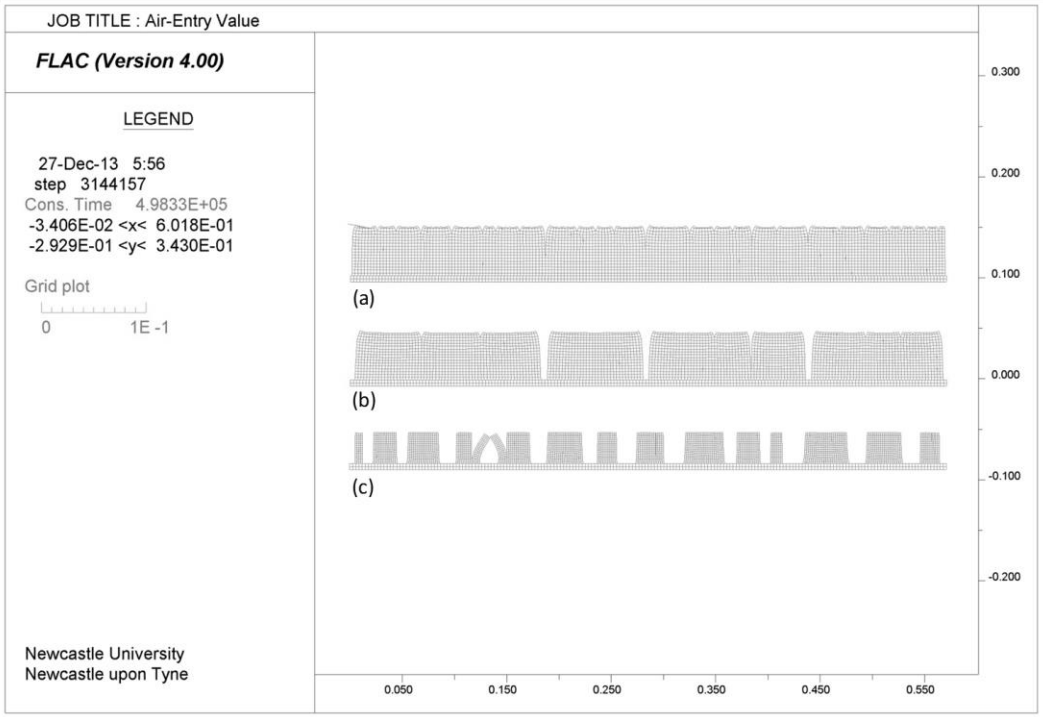

Figure 5.44 Crack geometries resulting from AEV equal to (a) 35.7 kPa, (b) 357.1 kPa and (c) 3571.4 kPa.

The three contrasting crack morphologies are further identified by the recorded CIF time-series data plotted in Figure 5.45. A common phase of end shrinkage is observed at the start of stage I CIF development (<3hrs). The application of a low AEV shows stage III, surface disintegration in the absence of stage II behaviour which may be approximated by a linear rate of 0.26%/hr. This is observed to be more than double that of the baseline rate of approximately 0.12%/hr indicating a significantly greater degree of desiccated crust formation. The CIF data from the simulation conducted with a high AEV shows a considerably extended period of stage I crack initiation and growth lasting circa 4 days before steady widening of existing cracks. This simulation shows no sign of crust disintegration.

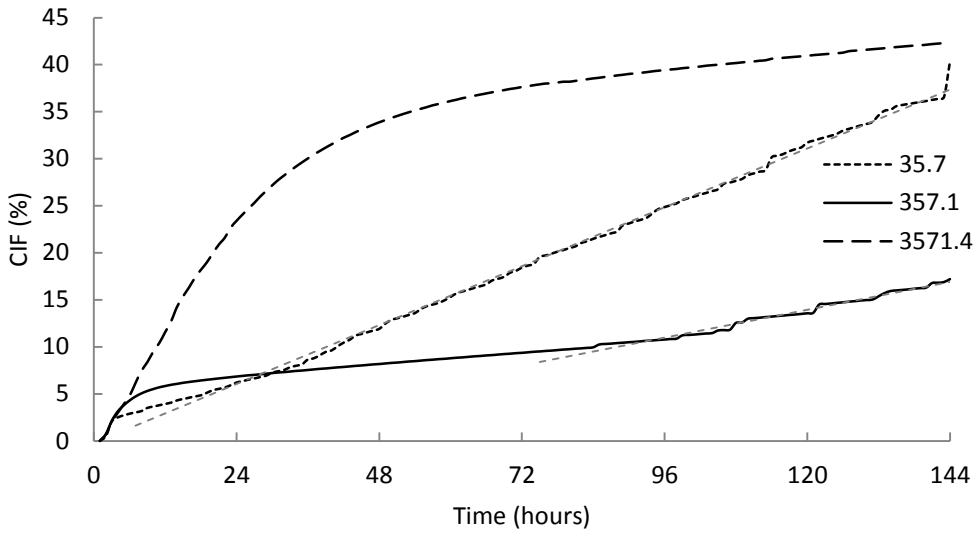

Figure 5.45 Development of CIF with varied air entry values.

The evidence presented in Figure 5.43 suggests that for the high AEV case, the clay remained at higher water content for longer than the previous simulations. This led to a much slower, steadier de-saturation up to the higher suction range. The slow removal of water maintained a relatively high hydraulic conductivity at the surface, reducing the development of a desiccated, hydraulic barrier/crust. This allowed greater removal of water from within the clay interior whereupon higher suctions were progressively achieved leading to an increased horizontal tensile stress field resulting in pervasive, penetrating cracking. This is in contrast to the use of lower AEVs where the onset of de-saturation at lower suctions accelerated the development of a low hydraulically conductive crust leading to shallow crustal stage III cracking.

5.4.3.2 Rate of de-saturation (n coefficient)

The rate of de-saturation is largely governed by the pore-size distribution of the material. Where the distribution is small, de-saturation of similarly sized pore spaces occurs rapidly leading to a steeper SWRC characterised by a higher van Genuchten n coefficient than materials possessing a broad pore-size distribution.

The study into the effect of the n coefficient on the modelled development of cracking ideally would have used values representative of the analogous materials stated in the preceding AEV investigation. However, upon repeated

modelling trials, it became clear that the model is extremely sensitive to this parameter. The baseline, measured n value for the compacted till is 1.3; however, beyond bounding values of 1.35 and 1.275 resulted in numerical instability as a result of excessive localised deformation as discussed in Section 5.4.2. A procedure of progressively narrowing trials provided the successful values depicted in Figure 5.46.

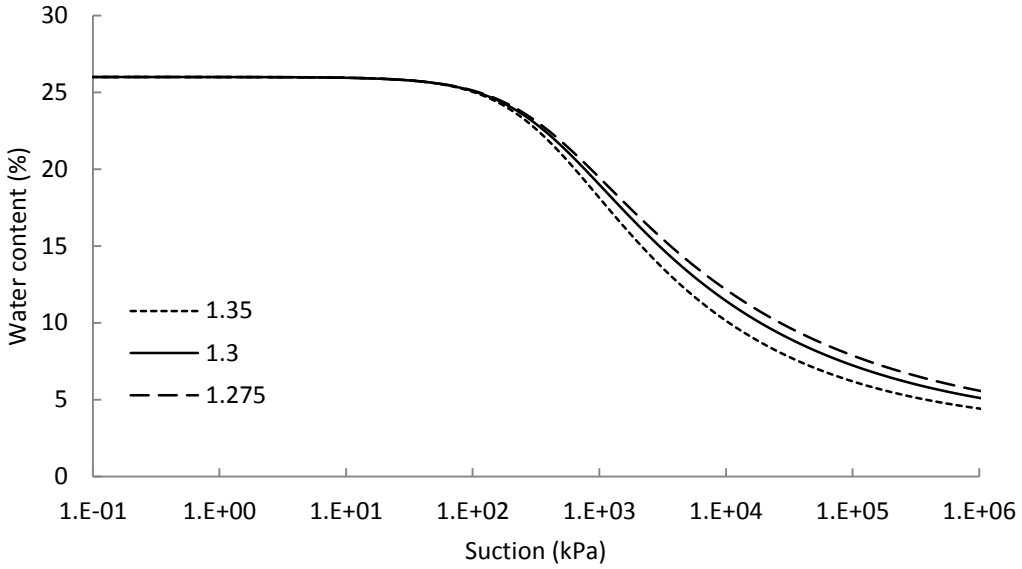

Figure 5.46 SWRC showing tested n values

It is thought that simulation using high n values results in too rapid a de-saturation throughout the soil profile relative to the drying flux imposed. High flow is caused by the high gradient in water content change at relatively low suctions where relative hydraulic conductivity will remain high. This high flow rate is comparable to the problematic simulations conducted using applied high saturated hydraulic conductivity. The use of too low a n value is understood to generate extremely elevated suctions locally within the surface element row, given the prescribed drying flux, leading to excessive element distortion.

The drying curves recorded for the three simulations (Figure 5.47) show little difference in trend as would be expected for the relatively small difference in SWRC applied. Nevertheless, the influence of varied n coefficient on the direction of influence in terms of overall drying may be discerned. As mentioned earlier, this parameter describes the rate with which the medium de-saturates upon reaching the common AEV between simulations. It is therefore of little

surprise that a larger n coefficient produces a greater degree of drying characterised by a steeper and longer duration of primary drying ultimately leading to lower residual water content.

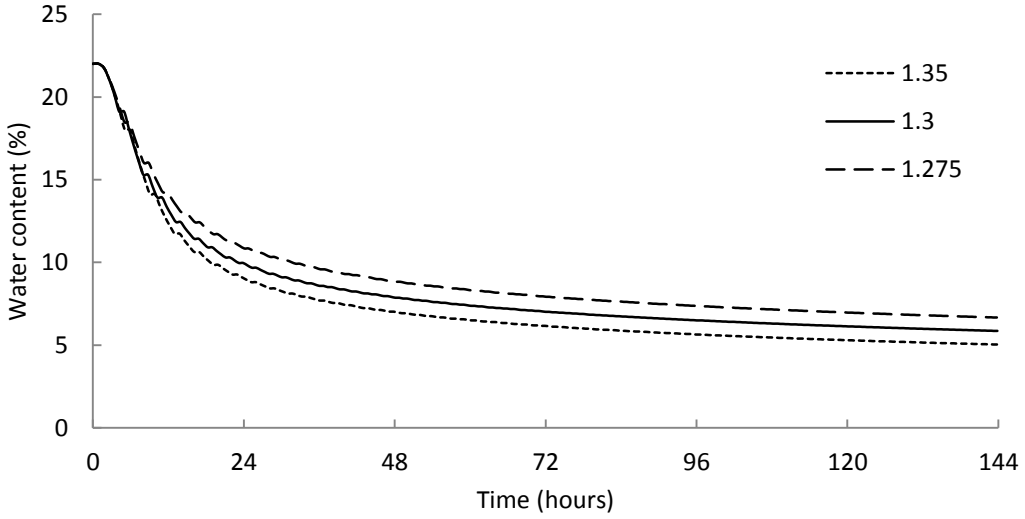

Figure 5.47 Drying curves for each n coefficient value.

The subtle variation between the feasible simulations is further evident in the cracked mesh geometries provided in Figure 5.48. There is clearly a tendency for common crack positioning (a function of the tensile strength distribution) though the differences are better captured by the CIF development in Figure 5.49. Here, it may be seen that although the intervals between the feasible n values are not equal, a trend toward less fully penetrating cracking is produced through the use of a larger n, steeper SWRC. However, this is manifested as only a 1% lower CIF at the end of stage I. The most striking difference is the onset of stage III, surface deterioration. Progressively greater crust deterioration is evident upon using a less steep SWRC. In the greater drying scenario produced by the use of a high n coefficient, water removal is more evenly distributed through the clay profile. On the other hand, although a lower overall water removal is observed using a low n coefficient, for any given water content, a higher magnitude of suction is calculated. Therefore, higher surface tensile stresses are modelled to result from the implementation of a shallow, more slowly de-saturating SWRC following air entry.

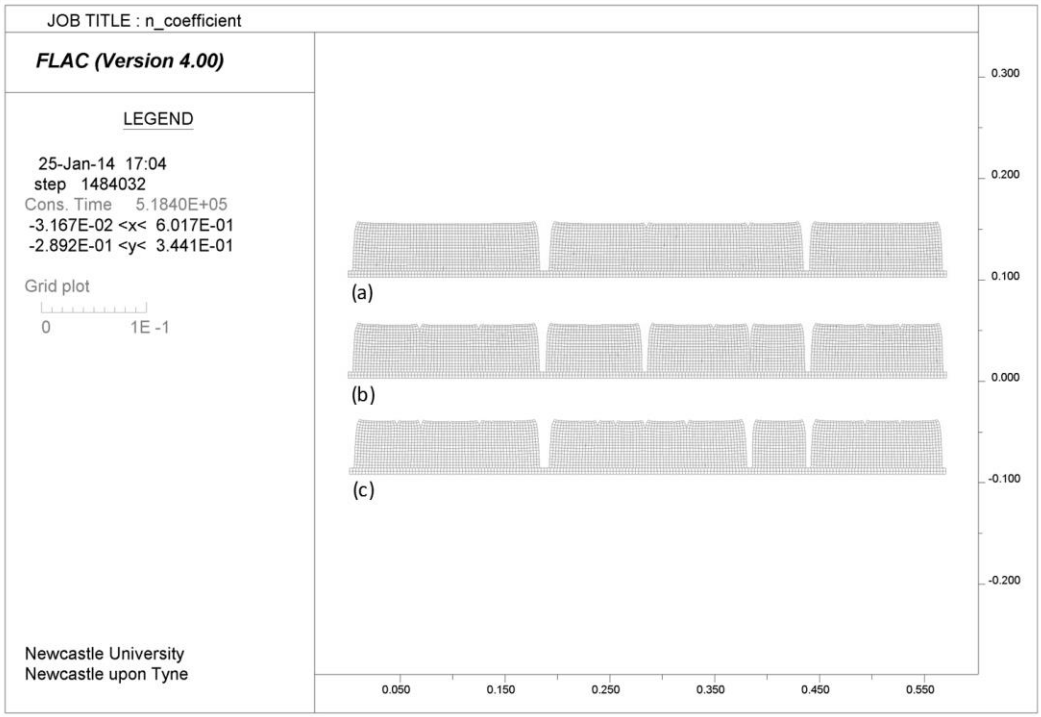

Figure 5.48 Crack geometries resulting from n coefficients equal to (a) 1.35, (b) 1.3 and (c) 1.275.

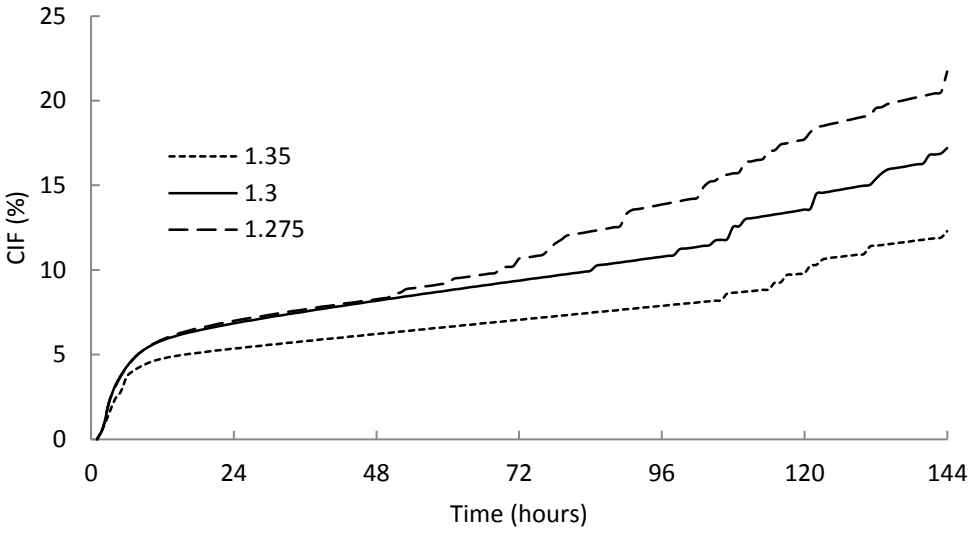

Figure 5.49 Development of CIF with varied n coefficient values

5.5 Concluding remarks

Cracking produced under baseline conditions was shown to develop according to the following process:

1. Drying of the clay grid from the upper boundary is initially rapid and results in an approximately constant removal of water along with simultaneous linear shrinkage (clay end dislocation).
2. Drying generates increasingly negative pore pressure from the exposed upper surface. Linear shrinkage is restrained by the influence of the clay-base contact.
3. Tensile horizontal stresses grow in the upper half of the grid, the largest of which are produced away from the free ends of the clay. Approaching air-entry, this tensile stress exceeds the tensile strength of the clay first where tensile strength is lowest relative to the developing tensile stress distribution.
4. Continued drying causes continued shrinkage of the clay in the form of crack propagation and Stage 3 was observed to repeat until the tensile stress no longer exceed the increasing tensile strength. The clay-base interface is essentially free toward the end of this stage.
5. De-saturation increases the stiffness of the clay according to the exponential function included in the constitutive model. This inhibits the continuation of shrinkage and crack growth.
6. Further drying generates elevated suctions at the upper surface and reduces the relative hydraulic conductivity. This occurs to the point of creating a barrier to the withdrawal of residual water from deeper in the clay layer.
7. The hydraulic gradient between elevated surface suctions and those of a lower magnitude further from the surface produces a restraint effect, eigen-stress. Once more, the tensile strength may be exceeded and extremely shallow cracking results.

The sensitivity of the presented model to variation in mechanical and hydrological parameters was investigated. Overall shrinkage was observed to be heavily influenced by the rate of clay stiffness increase employed; this led to the greatest difference seen in primary cracking (typically >10mm in depth) as

assessed by the use CIF. Displacement boundary conditions were demonstrated to have differing effects. The basal restraint condition was shown to make the difference between solely linear shrinkage with the later development of a desiccated crust and deep cracking occurring at all. Therefore, basal conditions were found to be influential in the simulation of primary cracking. However, study into the effect of lateral boundary conditions demonstrated little difference in the style of cracking. The main difference between fixed and free lateral boundary simulations was the distribution of cracking with the effect of stress relief due to free shrinkage being diminished in the fixed case.

Constant tensile strength investigation demonstrated the importance of including a water content dependent function in the simulation of localised deep cracking. The magnitude of the resultant strength parameter was shown to influence the number of deep cracks yet overall shrinkage accommodated by these cracks was comparable across the clay layer. Upon prolonged exposure to drying, a greater deteriorated crust effect was observed in the weaker strength simulations. The degree of variability in the distributed tensile strengths was also shown to influence the number of primary cracks yet the overall shrinkage accommodated by these was found to be very different. A greater degree of crack widening was observed in simulations conducted with higher standard deviation in the random distribution function.

The increasing rate of drying flux applied to the modeled clay produced a predictable increase in crack number, overall surface shrinkage and crustal deterioration. Similarly, an increase in saturated hydraulic conductivity resulted in less primary cracking developing and reduced likelihood of crust formation and deterioration. Like the drying rate study, this is related to the ability of the model to capture unsaturated flow behaviour in relation to the efficiency of water removal. Investigation into the air-entry SWRC parameter captured the inability of a coarser material to generate sufficient suctions required to produce primary cracking. However, excessive air-entry suctions were shown to be produced in the simulation of very sensitive clays resulting in unrealistically pervasive primary cracking and excessive shrinkage. The most sensitive modeling parameter was shown to be the n coefficient. Only a narrow range of coefficient

values was found acceptable without excessive elemental deformation at the drying surface. The modelled range of values showed little effect on the development of primary cracking although crust formation increased in the simulation of a more gradually de-saturating SWRC shape due to the generation of higher suctions.

An order of parameter priority for the modeling of desiccation cracking is provided as an outcome of the sensitivity analysis. The mechanical boundary conditions have been shown to influence the overall geometry of primary cracking; however, it is the hydrological parameters that determine the extent to which cracking is initiated and propagated. Drying rate ultimately governs the occurrence of cracking as it is directly related to the removal of water and the implicit generation of suction induced tensile stresses. The secondary tier is occupied by the soil hydraulic parameters that determine the unsaturated permeability. These are fundamentally based upon the soil micro-structure and essentially the particle-particle configuration as this controls the maximum (saturated) permeability, suction under which the soil desaturates and the rate at which this proceeds.

Chapter 6 Conclusions

6.1 Tensile strength testing

A direct, undrained tensile test has been developed and shown to be a relatively quick and simple means of investigating the tensile behaviour of three different soils up to strengths in the order of 200kPa. However, test specimen preparation represented the greatest time constraint on the proposed method. Photogrammetry analysis has enabled the performance of the test apparatus-specimen interaction to be evaluated. It was observed that specimen failure was consistently by means of tensile loading and that the compression component applied by the restraining action of the apparatus jaws was negligible in comparison to the generated tensile strains about the narrowed central section. This is with the exception of testing at a relatively high displacement rate (1.22 mm/min) on specimens of high water content, in the range of the plastic limit and above. Under these conditions, the action of the jaw vertices was observed to be most prominent in the initiation of failure. Therefore, it may be concluded that the proposed testing method is most appropriate when testing is conducted at slower rates (in the order of 0.24 mm/min) and in the drier range of specimen saturation. However, sample alignment issues are prevalent at low water contents due to the volume loss behaviour inherent in the clay specimen. A future modification to the jaw design has been proposed to address this. This work has produced the expression that described the increasing magnitude of tensile strength with progressive drying that has been successfully implemented in the cracking numerical model.

Despite the modelling component of this thesis focusing on the de-saturation direction alone, the effect of drying-wetting cycles on tensile strength behaviour was included. While drying was conducted by bench air-drying in the laboratory, wetting was achieved using a humidifying chamber. Tensile strength tests were conducted along the drying - wetting - re-drying paths. It was shown that the wetting path was characterised by lower strengths than the initial drying path. This was attributed to hysteretic behaviour in addition to a fundamental change in the micro-structure of the specimen - drying induced fissuring, leading to increased porosity and weakening of the clay fabric. Upon re-drying, a hysteric influence was indicated by a more marked increase in strengths again with drying than observed on the wetting path, although evidence of a permanent

change in the structure of the clay toward lower strengths was seen from initial drying. This suggests that cracking prone clay will have a tendency toward a larger magnitude of cracking early on (larger tensile stresses required to initiate failure) under environmental cycles. The progressively reduced strength of the clay with repeated cycling would result in the majority of shrinkage to be accommodated by these cracks with a simultaneous deterioration of the matrix structure. Although not investigated fully in this work, it is anticipated that a residual drying-wetting path be achieved following sufficient repeated cycles.

Finally, the indirect (Brazilian) test has been employed to enable comparison between the developed direct apparatus and the established testing method. The limited water content range under which indirect testing is appropriate has constrained the specimen conditions tested, further highlighting the advantage of the direct test. In order to demonstrate an acceptable level of confidence in the indirect testing of soil specimens, DIC was employed once more in the manner adopted in production of the work provided in the Appendix. Similarity between the testing of the example soils and the behaviour of rock samples was seen, although softening at the point of loading during the course of wetter specimen tests was evident. An analytical expression to define the degree of flattening at failure was employed to investigate this and the data was deemed acceptable in relation to the theoretical basis upon which the indirect tensile strength was calculated. Ultimately, this enabled a quantitative comparison between the tensile strength values obtained between the direct and indirect testing methods. An excellent correlation was presented. This supports the reliability of the direct test results for the low water content range although validation at higher ranges remains impossible in the absence of data from competing tests under the same conditions and with the same materials.

6.2 Cracking model

The use of FLAC 2D two-phase flow has allowed the inclusion of fundamental matrix hydraulic relations within a continuum mesh via the definition of the fill SWRC. This is considered a necessary step forward from previous works that have routinely employed prescribed, often linear, hydraulic gradients in the modelling of desiccation processes. Additionally, the interface element facility has allowed the expression of discontinuity generation in the continuum mesh according to an appropriate cracking criterion ($\sigma_3 > \sigma_t$). In addition to crack initiation identified by the use of interfaces, propagation is accommodated which has allowed feedback into the stress redistribution. This has allowed crack propagation to influence the generation of future crack development.

The discharge flux boundary facility has been found to be insufficient in capturing the true extent of water content reduction in the indicative laboratory experiments. However, water removal rate during the period of modelled crack initiation is comparable between modelled and physical drying. Crack initiation has been identified to occur immediately prior to air entry according to the input SWRC. This is in agreement with experimental experience throughout the literature. The dynamic drying boundary extension function has simulated the evolving geometry of the cracking surface. However, the prescription of a single, initial flux value is recognised to be a fundamentally limiting factor in the modelling of soil-atmosphere interactions. There is an increasing body of work that has advanced this field in recent decades. Inclusion of these more realistic evaporative flux functions would be a highly recommended advance on the current model. This would ideally incorporate the action of vegetation in the manner of root-water uptake in addition to the role of mechanical reinforcement.

In terms of the mechanical response of the model to baseline conditions, tensile stresses are simulated to develop from the drying surface, extending from the horizontal centre of the grid and buffered toward the lateral ends by the action of free shrinkage. Tensile strength heterogeneity throughout the clay has been shown to capture the asymmetric distribution of crack initiation and has also led to asymmetrical shrinkage. Additionally, the realistic process of proximal crack suppression has been successfully captured.

The CIF as a tool to quantitatively assess the development of cracking has allowed the following desiccation processes of the model to be identified. The first stage of the model response to drying is shrinkage; this was vertical but predominantly horizontal under the restraint of shear conditions at the clay-mould contact. This was rapidly followed by the meeting of the crack initiation criterion - at the position where horizontal tensile stress exceeded local tensile strength along the exposed drying surface. Continued drying and resultant shrinkage caused this crack(s) to propagate toward the base leading to complete separation of the clay block. This process repeated sequentially across the clay until developing tensile stress no long exceeded the increasing strength. As drying continued, surface suctions increased forming effectively a hydraulically non-conductive shallow layer, or crust. This was found to inhibit the withdrawal of water from deeper in the profile. Within this shallow zone of elevated suctions tensile stresses were generated by extreme hydraulic gradient, rather than the influence of basal restraint and may again meet the crack initiation criterion. Due to the limited depth of influence, these cracks were sub-mm in scale. In the context of desiccation cracking in compacted fill, these features are negligible and their influence on the infiltration potential of the clay is considered comparable to the unsaturated matrix itself. However, the ability of the model to capture the deterioration of a highly desiccated surface supports the combined interface element and two-phase flow methodology described in this work.

The expansion of the model geometry is suggested as the next logical step to further this work in addition to a more comprehensive calculation of the evaporative flux. A grid used to represent in situ slope cracking would require the removal of the imposed basal conditions yet the depth of the clay layer would have to be extended well beyond the influence of any fixed lower boundary condition. Under these circumstances, it is believed that the hydraulic gradient leading to differential shrinkage would be the dominant mechanism in the generation of tensile stress. The main limiting factor to the extrapolation of the presented method is the restriction in interface orientation and complexity i.e. purely vertical cracking would be a recommended initial step.

6.2.1 Model sensitivity

Investigation into the sensitivity of the model to variation in boundary and interface conditions, continuum properties and hydrological parameters was conducted. The salient findings from these studies are summarised here.

The non-linear elastic constitutive model employed, as might be expected, resulted in a reduced cracking extent when a higher elastic modulus trend with drying was prescribed. The lower shrinkage strains induced by the generation of negative pore-water pressure due to drying led to a reduced likelihood of crack initiation. The influence of variation of this property on the modelled cracking was dominantly the growth of crack aperture i.e. the magnitude of shrinkage required to be accommodated by the cracks, rather than a change to the number of primary cracks or crust development.

Studies into the implementation of tensile strength in the model were centred on the data obtained as part of experimental work reported in this thesis. Modelling conducted in the absence of an increase in tensile strength with progressive drying, constant throughout the grid showed a tendency to produce evenly distributed cracking at all available sites. This physically unrealistic behaviour provided justification for the inclusion of both the experimentally established trend of increasing strength with drying and the necessity for strength heterogeneity. It was found that with an increased tensile strength trend magnitude, occurrence of crack initiation was reduced although cracks that did initiate propagated and opened to greater final widths than diffuse cracks produced at lower strengths. Additionally, less crustal deterioration was also established with increased strengths. Therefore, it may be said that modelled strain localisation occurs to a greater degree in material of higher overall strength. The degree of heterogeneity included in the model was found to influence not only strain localisation but also crack asymmetry throughout the clay.

The influence of basal restraint (lower boundary condition) on the cracking behaviour has been shown to be considerably greater than that of the lateral boundaries. Laboratory cracking has been commonly attributed to the clay-base interface with continuum numerical models confirming the greater magnitude of

generated tensile stresses in the fixed case. The model presented has similarly identified the tendency for cracking only to occur with the inclusion of restraint. However, the model's ability to capture the generation of a desiccated crust upon prolonged desiccation in the entirely free case is considered original. This has only been possible with the ability to simulate unsaturated flow throughout a grid capable of forming discontinuities. There was found to be little difference between the fully fixed and shear basal interface conditions in terms of cracking behaviour. This was attributed to high basal interface shear strength and stiffness during the near saturated period immediately prior to the initiation of cracking. Hence, future modelling may be conducted on the basis of a fixed lower boundary under the simulated drying conditions without the need to carry out specialised, modified mould-clay shear box testing. However, this conclusion is not considered applicable to the modelling of thinner soil layers where it is believed that basal restraint would play a more important role in the generation of reaction forces. Lateral mechanical boundary conditions were shown to have little difference on the cracking behaviour other than to affect the distribution (spacing) of cracks because of lateral stress relaxation in the free shrinkage scenario. This supports the case for extrapolation of the modelling approach to in situ conditions, as would be a significant and recommended next step based on the findings of this work.

The drying rates employed were shown to have a great effect on the cracking geometry produced. The series of rates modelled showed that with an increase in applied drying rate (discharge flux), more primary, deep cracking resulted as well as the earlier the onset of crustal formation and deterioration. Saturated hydraulic conductivity was found to have a large influence over the formation of desiccated crust. With a higher saturated conductivity, a greater volume of water was simulated to have been removed throughout the clay layer profile leading to more primary, deep cracking and little to no crust formation. However, in the modelling of low saturated conductivity, the relative permeability range was reduced. This resulted in less drying from the clay interior and substantial, shallow crust disintegration.

Lastly, the sensitivity of the model to variation in the van Genuchten (1980) SWRC fitting parameters was investigated. Study into the effect of low air entry

suction (10s kPa) on the development of cracking showed steady, continuous crack initiation that was exclusively crustal in nature along with rapid de-saturation. The model was found to be highly sensitive to AEV in the order of 1000s kPa resulting in highly unrealistic interface geometries. However, full depth cracking was evident from the simulation and was associated with water removal being maintained from the full profile of the clay layer. Therefore, the model is shown to capture penetrative, deep cracking associated with soils of higher AEV i.e. soils of small pore sizes typical of high clay contents. Of all the parameters assessed, the model was found to be most sensitive to the n coefficient. This coefficient is related to the steepness or rate of the de-saturation portion of the SWRC. Numerical instability associated with excessive localised deformation meant that only a narrow range of values typical of a material with a relatively broad pore-size spectrum (e.g. glacial till) could be simulated. Little difference was observed in the development of primary, cracking as this occurs about the AEV, which is unaffected by the parametric study of n values. However, it was indicated by the direction of behavioural trend that soils with a more uniform pore-size distribution (rapid de-saturation) produce little in the way of crustal formation. This is related to such soils drying to residual water content at lower suctions. Conversely, more slowly de-saturating soils with larger pore-size distributions generate higher suctions with continued steady drying at the surface and result in a highly desiccated, disintegrated surface. This modelled response is believed to have captured true behaviour typical of the modelled compacted fill verses a more uniformly graded medium.

6.3 Further model development

The application of a single, constant drying boundary condition has been identified as a limitation of the modelling method presented. It is suggested that this be further developed to account for the principle drivers of evaporation in the laboratory case i.e. temperature and humidity. A boundary condition based upon actual laboratory measured values of these parameters represents a significant improvement to the realism of the modelled case. However, ultimately, the facility to apply a single discharge rate will remain due to the limitations of the software employed though this value may be constrained in

terms of vapor exchange rather than overall system mass balance. Furthermore, the initial conditions employed (homogenously saturated) are recognized to be an initial step in the development of the presented model. As tensile strength heterogeneity has been identified as being a significant control on crack initiation and extent, the initial water content distribution plays an important role in cracking extent. It is suggested that upon establishing an appropriate cracking pattern (i.e. validated against cracking laboratory experiments), the heterogeneity used to apply spatial variability directly in the tensile strengths could be used to back-calculate the likely water content distribution in the compacted sample. Further study into the effect of as-compacted water content distribution is recommended.

A considerable next step in the development of the model is considered to be the incorporation of re-wetting into the simulation. The presented work in this thesis pertains to the single drying path and as such covers the initial cracking mechanism. However, it is recognised that soil desiccation is one part of the cyclic environmental conditions experienced in many climates around the world. Reversal of the discharge boundary method presented is thought to be the first step to incorporating recharge resulting from rainfall and further consideration of the influence of cracks (i.e. crack bottom ponding) would further add to the complexity of the modelled physical, transient system. In this way the dynamic crack magnitude could be captured and studied with respect to the overall infiltration potential of the soil surface condition during varied climatic conditions.

Lastly, up-scaling of the presented model to slope-scale is a natural progression from the incorporation of the aforementioned developments. Mesh inclination would allow the influence of slope geometry to be assessed in terms of crack asymmetry and inter-dependency. Field scale simulation is foreseen to necessitate the use of recorded meteorological data and thereby accounting for transient wetting and drying conditions as well as allowing the application of predicted weather patterns in the context of various climate change scenarios.

Reference List

Abu-Hejleh, A. N. & Znidarcic, D., 1995. Desiccation theory for soft cohesion soils. *Journal of Geotechnical Engineering,* 121(6), 492-502.

Ahuja, L. R. & Hebson, C., 1992. Root zone water quality model. *GPSR Tehnical Report No. 2.*

Akazawa, T., 1953. Tension test method for concretes. *R.I.L.E.M. Bulletin* 16, 13-23.

Albrecht, B. A. & Benson, C. H., 2001. Effect of desiccation on compacted natural clays. *Journal of Geotechnical and Geoenvironmental Engineering,* 127(1), 67-75.

Allaire, S. E., Roulier, S. & Cessna, A. J., 2009. Quantifying preferential flow in soils: A review of different techniques. *Journal of Hydrology* 378, 179-204.

Alonso, E. E., Gens, A. & Josa, A., 1990. A constitutive model for partially saturated soils. *Geotechnique* 40(3), 405-430.

Alsayed, M. I., 2002. Utilising the Hoek triaxial cell for multiaxial testing of hollow rock cylinders. *International Journal of Rock Mechanics and Minning Sciences* 39, 355-366.

Aluwihare, M. & Watanabe, K., 2003. Measurement of evaporation on bare soil and estimating surface resistance. *Journal of Environmental Engineering ASCE* 129(12), 1157-1168.

Amarasiri, A. L. & Kodikara, J. K., 2011. *Numerical modeling of desiccation cracking using the cohesive crack method and random material property variations.* Melbourne, Australia, s.n.

Amarasiri, A. L., Kodikara, J. K. & Costa, S., 2011. Numerical modelling of desiccation cracking. *International Journal for Numerical and Analytical Methods in Geomechanics* 35, 82-96.

Anderson, M. G., Hubbard, M. G. & Kneale, P. E., 1982. The Influence of Shrinkage Cracks on Pore-Water Pressures Within a Clay Embankment. *Quarterly Journal of Engineering Geology and Hydrogeology* 15, 9-14.

ASTM Committee on Fracture Testing, 1961. The slow growth and rapid propagation of cracks. *Materials Research and Standards* 1(5), 389-393.

ASTM, 1983. *Standard testing method for plane-strain fracture toughness of metallic materials. (E399-83).* Philadelphia: American Society for Testing and Materials.

ASTM, 1984. Standard test method for splitting tensile strength of intact rock core specimens. *In annual book of ASTM standards,* 336-341.

ASTM, 2000. *Standard test methods for measurement of hydraulic conductivity of saturated porous materials using a flexible wall permeameter (D5084).* Philadelphia: American Societry for Testing and Materials.

ASTM, 2003. *Standard test method for measurement of soil potential (suction) using filter paper.* s.l.:American Society for Testing and Materials International.

Aubry, D., Chouvet, D., Modaressi, A. & Modaressi, H., 1986. *GEFDYN : Logiciel d'Analyse de Comportement Mécanique des Sols par Eléments Finis avec Prise en Compte du Couplage Sol-Eau-Air,* s.l.: Ecole Centrale Paris.

Ayad, R., Konrad, J.-M. & Soulié, M., 1997. Desiccation of a sensitive clay: application of the model CRACK. *Canadian Geotechnical Journal* 34, 943-951.

Azam, S., Ito, M. & Khan, F., 2013. Influence of cracks on soil water charateristic curve. In: B. Caicedo et al. eds. *Advances in Unsaturated Soils.* London: Taylor & Francis Group, 217-220.

Basnett, C. & Brungard, M., 1992. The clay desiccation of a landfill composite lining system. *Geotechnical Fabrics Report, Industrial Fabrics Association International,* 38-41.

Bassam, L., 2007. *Roads: Motorway Lane Closures. Answer to Earl Attlee,* s.l.: Lords Hansard 21 Nov 2007: Column WA84.

Bear, J., 1972. *Dynamics of fluid in porous media.* New York: Dover Publications, Inc..

Bear, J. & Bachmat, Y., 1990. *Introduction to Modeling of Transport Phenomena in Porous Media.* 4 ed. Haifa, Israel: Kluwer Academic Publishers.

Beven, K. & Germann, P., 1982. Macropores and water flow in soils. *Water Resources Research* 18(5), 1311-1325.

Bishop, A. W. & Garga, V. K., 1969. Drained tension tests on London Clay. *Geotechnique* 19, 309-313.

British Standards, 1990. *Methods of test for Soils for civil engineering purposes 1377- Part 2: Classification tests.* London: British Standards Institution.

British Standards, 1990. *Methods of test for Soils for civil engineering purposes 1377- Part 4: Compaction related tests.* London: British Standards Institution.

British Standards, 1990. *Methods of test for Soils for civil engineering purposes 1377- Part 7: Shear strength tests (total stress).* London: British Standards Institution.

Bronswijk, J. J. B., 1988. Modeling of water balance, cracking and subsidence of clay soils. *Journal of Hydrology* 97, 199-212.

Brooks, R. H. & Corey, A. T., 1964. Hydraulic properties of porous medium.. *Colorado State University (Forts Collins), Hydrology Paper,* Nr. 3.

Brutsaert, W., 1966. Some methods of calculating unsaturated permeability. *Transactions of the ASCE* 10, 400-404.

Carneiro, F. & Barcellos, A., 1953. Tensile stength of concretes. *R.I.L.E.M. Bulletin* 13, 99-125.

Chan, K. Y. & Hodgson, A. S., 1981. Moisture regimes of a cracking clay soil under furrow irrigated cotton. *Australian Journal of Experimental Agriculture and Animal Husbandry* 21(112), 538-542.

Correlated Solutions Ltd., 2010. Vic-3D Testing Guide.

Corte, A. & Higashi, A., 1960. *Experimental research on desiccation cracks in soil. Research report 66,* s.l.: US Army Snow and Ice and Permafrost Research Establishment.

Croney, D. & Coleman, J. D., 1954. Soil structure in relation to soil stuction (pF). *Journal of Soil Science* 5, 75-84.

Cui, Y.-J., Ta, A. N., Hemmati, S., Tang, A. M. & Gatmiri, B., 2013. Experimental and numerical investigation of soil-atmosphere interaction. *Engineering Geology* 165, 20-28.

Daniel, D. E. & Wu, Y.-K., 1993. Compacted Clay Liners and Covers for Arid Sites. *The Journal of Geotechnical Engineering* 119(2), 223-237.

Davies, C., 2012. *Evaluation of the SHT tensile testing equipment for use on cohesive soils using digital imaging correlation technology.* MSc thesis. Newcastle University, UK: s.n.

Dijkstra, T. A. & Dixon, N., 2010. Climate change and slope stability: Challenges and approaches.. *Quarterly Journal of Engineering Geology and Hydrogeology* 43(4), 371-385.

Driscoll, R. & Crilly, M., 2000. *Subsidence damage to domestic buildings. Lessons learned and questions asked.* London: Building Research Institute.

Durner, W., 1994. Hydraulic conductivity estimation for soils with heterogeneous pore structure. *Water Resources Research* 30(2), 211-223.

Dyer, M., Utili, S. & Zielinski, M., 2009. Field survey of desiccation fissuring of flood embankments. *Water Management* 162(WM3), 221-232.

Fairhurst, C., 1964. On the validity of the 'Brazilian' test for brittle materials. *International Journal of Rock Mechanics and Mining Sciences and Geomechanics Abstracts* 1(4), 535-546.

Farrell, D. A., Greacen, E. L. & Larson, W. E., 1967. The effect of water content on axial strain in a loam soil under tension and compression. *Proceeds of the Soil Science Society of America* 32, 445-450.

Feddes, R. A. et al., 1988. Modelling soil water dynamics in the unsaturated zone - state of the art. *Journal of Hydrology* 100, 69-111.

Fleureau, J. M., Kheirbek-Saoud, S., Soemitro, R. & Taibi, S., 1993. Behaviour of clayey soils on drying-wetting paths. *Canadian Geotechnical Journal* 30(2), 287-296.

Fredlund, D. G., 1964. Comparison of soil suction and one-dimensional consolidation characteristics of a highly plastic clay. *MSc thesis, University of Alberta, Canada.*

Fredlund, D. G. & Pham, H. Q., 2006. *A volume-mass constitutive model for unsaturated soils in terms of two independent stress state variables.* Carefree, Arizona, American Society of Civil Engineers, 105-134.

Fredlund, D. G. & Rahardjo, H., 1979. *Soil mechanics for partially saturated soils.* s.l.:Wiley.

Fredlund, D. G. & Rahardjo, H., 1985. Theoretical context for understanding unsaturated residual soil behaviour. *Preceedings of the 1st International Conference on Geomechanics in Tropical, Lateritic and Saprolitic Soils, Brasilia* 1, 295-306.

Fredlund, D. G. & Rahardjo, H., 1993. *Soil mechanics for unsaturated soils.* New York: Wiley.

Fredlund, D. G. & Xing, A., 1994. Equations for the soil-water characteristic curve. *Canadian Geotechnical Journal* 31, 521-532.

Freed, Y. & Banks-Sills, L., 2007. Crack growth resistance of shape memory alloys by means of a cohesive zone model. *Journal of the Mechanics and Physics of Solids* 55(10), 2157-2180.

Frydman, S., 1964. The applicability of the Brazilian (indirect tension) test to soils. *Australian journal of applied science* 15, 335-343.

Gardner, W. R., 1958. Some steady state solutions of the unsaturated moisture flow equation with application to evaporation from a water-table. *Soil Science* 85, 228-232.

Gerke, H. H. & Genuchten, v., 1993. Evaluation of a first-order water transfer term for variably saturated dual-porosity flow models. *Water Resource Research* 29(4), 1225-1238.

Gerke, H. H. & van Genuchten, M. T., 1993. A dual-porosity model for simulating the preferential movement of water and solutes in structured porous media. *Water Resource Research* 29, 305-319.

Goulding, R. B., 2006. *Tensile strength, shear strength and effective stress for unsaturated sand. PhD thesis.* Missouri, Columbia: University of Missouri.

Green, W. H. & Ampt, C. A., 1911. Studies on soil physics: flow of air and water through soils. *Journal of Agricultural Science* 4, 1-24.

Griffith, A. A., 1921. The phenomena of rupture and flow in solids. *Philosophical Transactions of the Royal Society of London Series A* 221, 163-198.

Griffith, A. A., 1924. *Theory of rupture.* Delft, Holland, 55-63.

Groisman, A. & Kaplan, E., 1994. An experimental study of cracking induced by desiccation. *Europhysics Letters* 25(6), 415-420.

Haines, W., 1923. The volume-changes associated with variations of water content in soil. *Journal of Agricultural Science* 13, 296-310.

Hannant, D. J., Branch, J. & Mulheron, M., 1999. Equipment for tensile testing of fresh concrete. *Magazine of Concrete Research* 51(4), 263-267.

Heibrock, G., Zeh, R. M. & Witt, K. J., 2003. *Tensile Strength of Compacted Clays.* Weimar, Germany, Preceedings of the international conference 'From Experimental Evidence towards Numerical Modelling of Unsaturated Soils', 395-412

Ho, D. Y. F. & Fredlund, D. G., 1982. Increase in strength due to suction for two Hong Kong soils.. *Preceedings of the Conference on Engineering and Construction in Tropical and Residual Soils, Honolulu,* 263-295.

Hoogmoed, W. B. & Bouma, J., 1980. A simulation model for predicting infiltration into cracked clay soil. *Journal of the Soil Society of America* 44, 458-461.

Huang, S.-Y., 1994. Evalution and laboratory measurement of the coefficient of permeability in deformable, unsaturated soils.. *PhD thesis, University of Saskatchewan, Canada.*

Hughes, P., Glendinning, S. & Mendes, J., 2007. Construction, Testing and Instrumentation of an infrastructure testing embankment. *Proceedings of the Expert Symposium on Climate Change Modelling, Impacts & Adaptations, Singapore,* 159-166.

Hulme, M. et al., 2002. *Climate Change Scenarios for the United Kingdom: The UKCIP02 Scientific Report,* Norwich (United Kingdom): Tyndall Centre, School of Environmental Sciences.

Hu, L., Peron, H., Hueckel, T. & Laloui, L., 2006. Numerical and phenomenological study of desiccation of soil. *Advances in unsaturated soil, seepage and environmental geotechnics. ASCE geotechnical special punlication 192(17)*, 166-173.

Ibarra, S. Y., McKyes, E. & Broughton, R. S., 2005. Measurement of tensile strength of unsaturated sandy loam soil. *Soil and Tillage Research* 81, 15-23.

Irwin, G. R., 1958. Fracture. In: S. Flugge, ed. *Encyclopedia of Physics.* Berlin: Springer, 551-590.

ISRM, 1978. Suggested methods for determining tensile strength of rock materials. *International Journal of Rock Mechanics and Mining Sciences* 15, 99-103.

ISRM, 1988. Suggested Methods for Determining the Fracture Toughness of Rock. *International Journal of Rock Mechanics and Mining Sciences and Geomechanics Abstracts* 25(2), 71-96.

ITASCA, 2002. *FLAC User's Guide.* s.l.:ITASCA: Minnesota, USA.

ITASCA, 2004. *UDEC Users' Guide,* Minnesota, USA: ITASCA.

ITASCA, 2011. *UDEC User's Guide.* s.l.:ITASCA: Minnesota, USA.

Jenkins, G. et al., 2010. *UK Climate Predictions Briefing Report,* s.l.: UK Climate Impacts Programme.

Jones, L. D. & Jefferson, I., 2012. Expansive soils. In: J. Burland, T. Chapman, H. Skinner & M. Brown, eds. *ICE manual of geotechnical engineering. Volume I: Geotechnical engineering principles, problematic soils and site investigation.* London: ICE Publishing, 413-441.

Kim, T. -H. & Hwang, C., 2003. Modeling of tensile strength on moist granular earth material at low water content. *Engineering Geology* 69, 233-244.

Kleppe, J. H. & Olsom, R. E., 1985. Desiccation cracking of soil barriers. In: A. I. Johnson, R. K. Frobel, N. J. Cavalli & C. B. Pettersson, eds. *Hydraulic Barriers in Soil and Rock. ASTM STP 874.* Philadelphia: ASTM, pp. 263-275.

Kodikara, J., Barbour, S. L. & Fredlund, D. G., 1998. An idealized framework for the analysis of cohesive soils undergoing desiccation: Discussion. *Canadian Geotechnical Journal* 35, 1112-1114.

Kodikara, J. & Costa, S., 2013. Desiccation cracking in clayey soils: mechanisms and modelling. In: L. Laloui & A. Ferrari, eds. *Multiphysical Testing of Soils and Shales.* s.l.:Springer-Verlag Berlin Heidelberg, 21-32.

Kodikara, J. K., Barbour, S. L. & Fredlund, D. G., 2000. Desiccation cracking of soil layers. *In: Proceedings of the Asian Conference in Unsaturated Soils, UNSAT ASIA, Singapore,* 693-698.

Kodikara, J. K. & Choi, X., 2006. A Simplified Analytical Model for Desiccation Cracking of Clay Layers in Laboratory Tests. *ASCE Geotechnical Special Publication* 2, 2558-2569.

Kodikara, J. K., Nahlawi, H. & Bouazza, A., 2004. Modelling of curling in desiccating clay. *Canadian Geotechnical Journal* 41(3), 560-566.

Konrad, J.-M. & Ayad, R., 1997. An Idealized framework for the analysis of cohesive soils undergoing desiccation. *Canadian Geotechnical Journal* 34, 477-488.

Konrad, J.-M. & Ayad, R., 1997. Desiccation of a sensitive clay: field experimental observations. *Canadian Geotechnical Journal* 34, 929-942.

Kosmas, C., Moustakas, N., Kallianou, C. & Yassoglou, N., 1991. Cracking patterns, bypass flow and nitrate leaching in Greek irrigated soils. *Geoderma 4*9, 139-152.

Krishnayya, A. V. G. & Eisenstein, Z., 1974. Brazilian tensile test for soils. *Canadian Geotechnical Journal* 11, 632-642.

Krishnayya, A. V. G., Eisenstein, Z. & Morgenstern, N. R., 1974. Behaviour of compacted soil in tension. *Journal of the Geotechnical Engineering Division* 100, 1051-1061.

Krishnayya, G., 1973. *Analysis of cracking of earth dams*

Lachenbruch, A. H., 1961. Depth and spacing of tension cracks. *Journal of Geophysical Research* 66(12), 4273-4292.

Lau, J. T. K., 1987. *Desiccation cracking of clay soils. MSc Thesis.* Saskatoon, Canada: Department of Civil Engineering. University of Saskatchewan.

Lecocq, N. & Vandewalle, N., 2003. Dynamics of crack opening in a one-dimensional desiccation experiment. *Physics A* 321, 431-441.

Lu, N. & Likos, W. J., 2004. *Unsaturated Soil Mechanics.* New York: John Wiley and Sons.

Lu, N., Wu, B. & Tan, C. P., 2005. A tensile strength apparatus for cohesionless soils. In: A. Tarantino, ed. *Advanced experimental unsaturated soil mechanics.* Trento, Italy, 105-110.

Lu, N., Wu, B. & Tan, C. P., 2007. Tensile strength characteristics of unsaturated sands. *Journal of Geotechnical and Geoenvironmental Engineering* 133(2), 144-154.

Maulem, Y., 1976. A new model for predicting the hydraulic conductivity of partially saturated porous media. *Water Resources Research* 12(3), 513-522.

McKee, C. R. & Bumb, A. C., 1984. *The importance of unsaturated flow parameters in designing a monitoring system for hazardous wastes and environmental emergencies.* Houston, Texas, Hazardous Materials Control Research Institute.

McKee, C. R. & Bumb, A. C., 1987. Flow-testing coalbed methane production wells in the presence of water and gas. *Special publication. Formation Evaluation,* 599-608.

Mendes, J., 2011. Assessment of the impact of climate change on an instrumented embankment: an unsaturated soil mechanics approach. *PhD thesis. Durham University.*

Miller, C. J., Mi, H. & Yesiller, N., 1998. Experimental analysis of desiccation crack propagation in clay liners. *Journal of the American Water Resources Association* 34(3), 677-686.

Miller, C. J. & Mishra, M., 1989. Modeling of leakage through cracked clay liners 1: State of the Art. *Water Resources Bulletin* 25(3), 551-555.

Mitchell, A. R. & van Genuchten, M. T., 1993. Floof irrigation of a cracked soil. *Soil Science Society of America Journal* 57(2), 490-497.

Montgomery, R. J. & Parsons, L. J., 1989. *The Omega Hills final cap test plot study: Three year data summary..* Washington D.C., National Soild Waste Management Association.

Morris, P. H., Graham, J. & Williams, D. J., 1992. Cracking in drying soils. *Canadian Geotechnical Journal* 29, 263-277.

Mualem, Y., 1976. A new model for predicting the hydraulic conductivity of unsaturated porous media. *Water Resource Research* 12(3), 513-522.

Musielak, G. & Banaszak, J., 2007. Non-linear heat and mass transfer during convective drying of kaolin cylinder under non-steady conditions. *Transport in Porous Media* 66, 121-134.

Musielak, G. & Sliwa, T., 2012. Fracturing of clay during drying: modelling and numerical simulation. *Transport in Porous Media* 95, 465-481.

Nahlawi, H., 2004. *Behaviour of a reactive soil during desiccation, MEng. Thesis.* s.l.:Department of Civil Engineering, Monash University, Australia.

Nahlawi, H., Chakrabarti, S. & Kodikara, J., 2004. A Direct Tensile Strength Testing Method for Unsaturated Geomaterials. *ASTM Geotechnical Testing Journal* 27(4), 1-6.

Nahlawi, H. & Kodikara, J., 2002. *Experimental observations on curling of desiccating clay.* Recife, Brazil, 553-556.

Nahlawi, H. & Kodikara, J. K., 2006. Laboratory experiments on desiccation cracking of thin soil layers. *Geotechnical and Geological Engineering* 24, 1641-1664.

Nelson, J. D. & Miller, D. J., 1992. *Expansive soils: Problems and practice in foundation and pavement engineering.* New York: Wiley.

Novak, V., Simunek, J. & van Genuchten, M. T., 2000. Infiltration of Water into Soil with Cracks. *Journal of Irrigation and Drainage Engineering* 126(1), 41-47.

Nyambayo, V. P. & Potts, D. M., 2005. A New Permeability Model for Shrinkable Soils Undergoing Desiccation. *Proceedings of the International Conference on Soil Mechanics and Geotechnical Engineering* 2, 831-836.

Nyambayo, V. P., Potts, D. M. & Addenbrooke, T. I., 2004. The Influence of Permeability on the Stability of Embankments Experiencing Seasonal Pore Water Pressure Changes. *Advances in Geotechnical Engineering: The Skempton Conference, Thomas Telford, London,* 898-910.

Ohkubo, S., Fukui, K. & Kimura, A., 2002. Dynamic quality and constitution equation for Dotan soil. *Tunnel and Underground* 21(1), 45-50.

Ono, N., Mochizuki, A., Kurosaki, H. & Ueno, K., 2003. *Trial tests with compressive and tensile strength measuring apparatus*, 337-338.

Parker, J. C., Lenhard, R. J. & Kuppusamy, T., 1987. A parametric model for constitutive properties governing multiphase flow in porous media. *Water Resources Research* 23(4), 618-624.

Peron, H., Delenne, J. Y., Laloui, L. & El Youssoufi, M. S., 2009. Discrete element modelling of drying shrinkage and cracking of soils. *Computers and Geotechnics* 36, 61-69.

Peron, H., Hueckel, L., Laloui, L. & Hu, L. B., 2009. Fundamentals of desiccation cracking of fine-grained soils: experimental characterisation and mechanisms identification. *Canadian Geotechnical Journal* 46(10), 1177-1201.

Peron, H., Hu, L. B., Laloui, L. & Hueckel, I., 2007. *Mechanisms of desiccation cracking of soil: Validation.* Rhodes, Greece, Taylor & Francis.

Peron, H., Hu, L., Laloui, L. & Hueckel, T., 2007. *Numerical and experimental investigation of desiccation of soil.* Nanjing, China, 3rd Asian Conference on Unsaturated Soil.

Peron, H., Laloui, L. & Hueckel, T., 2005. An experimental evidence in desiccation cracking in sandy silt. In: Tarantino, ed. London: Taylor & Francis, 475-481.

Peron, H., Laloui, L., Hueckel, T. & Hu, L., 2006. Experimental study of desication of soil. *ASCE Geotechnical Special Publication* 147, 1073-1084.

Peron, H., Laloui, L., Hu, L.-B. & Hueckel, T., 2013. Formation of drying crack patterns in soils: a deterministic approach. *Acta Geotechnica* 8, 215-221.

Peters, W. H. & Ranson, W. F., 1982. Digital imaging techniques in experimental stress analysis. *Optical Engineering* 21(3), 427-431.

Pham, H. Q., Fredlund, D. G. & Barbour, S. L., 2005. A study of hysteresis models for soil-water characteristic curves. *Canadian Geotechnical Journal* 42, 1548-1568.

Philip, L. K., Shimell, H., Hewitt, P. J. & Ellard, H. T., 2002. A Field-based Test Cell Examining Clay Desiccation in Landfill Liners. *Quarterly Journal of Engineering Geology and Hydrogeology* 35, 345-354.

Pietsch, W., 1968. Tensile strength of granular materials. *Nature* 217, 736-737.

Pietsch, W. & Rumpf, H., 1967. Adhesion, capillary pressure, liquid volume and angle of contact of a liquid bridge between two spheres. *Chemie Ingenieur Technik* 39(15), 885-893.

Rice, J. R., 1968. A path independent integral and the approximate analysis of strain concentrations by notches and cracks. *Journal of the Mechanics and Physics of Solids* 35, 379-386.

Richards, L. A., 1931. Capillary conduction of liquids through porous mediums. *Physics* 1, 318-333.

Ridley, A., McGinnity, B. & Vaughan, P., 2004. Role of Pore Water Pressures in Embankment Stability. *Geotechnical Engineering* 157(GE4), 193-198.

Ringrose-Voase, A. J. & Sanidad, W. B., 1996. A method for measuring the development of surface cracks in soils: application to crack development after lowland rice. *Geoderma* 71, 245-261.

Rodriguez, R., 2002. *Estudio experimental de flujo y transporte de cromo, niquel y manganeso en residuos de la zona minera de Moa (Cuba): Influencia del comportamiento hidromecanico.* Technical University of Catalonia, Spain.

Rodriguez, R., Sanchez, M., Ledesma, A. & Lloret, A., 2007. Experimental and numerical analysis of desiccation of a mining waste. *Canadian Geotechnical Journal,* Volume 44, pp. 644-658.

Romkens, M. J. M. & Prasad, S. N., 2006. Rain Infiltration into Swelling/Shrinking/Cracking Soils. *Agricultural Water Management* 86, 196-205.

Rooke, D. P. & Cartwright, D. J., 1976. *Compendium of Stress Intensity Factors.* London: Her Majesty's Stationary Office.

Rouainia, M., Davies, O., O'Brien, T. & Glendinning, S., 2009. Numerical Modelling of Climate Effects on Slope Stability. *Engineering Sustainability* 162(ES2), 81-89.

Schubert, H., 1975. Tensile Strength of Agglomerates. *Powder Technology* 11, 107-119.

Schubert, H., 1984. Capillary forces - modelling and application in particulate technology. *Powder Technology* 37(1), 105-116.

Sih, G. C., 1973. *Handbook of Stress-Intensity Factors: Stress-intensity factor solutions and formulas for reference.* Bethlehem, Pennsylvania: Institute of Fracture and Solid Mechanics. Lehigh University.

Silvestri, V., Sarkis, G., Bekkouche, N. & Soulie, M., 1992. Evapotranspiration, Trees and Damage to Foundations in Sensitive Clays. *Canadian Geotechnical Conference* 2, 533-538.

Simoni, A. et al., 2004. Preliminary result from pore pressure monitoring on an unstable clay slope. *Engineering Geology* 73, 117-128.

Simunek, J., Jarvis, N. J., van Genuchten, M. T. & Gardenas, A., 2003. Review and comparison of models for describing non-equilibrium and preferential flow and transport in the vadose zone. *Journal of Hydrology* 272, 14-35.

Smethurst, J. A., Clarke, D. & Powrie, W., 2006. Seasonal Changes in Pore Water Pressure in a Grass-covered Cut Slope in London Clay. *Geotechnique* 56, 523-537.

Snyder, V. A. & Miller, R. D., 1985. Tensile strength of unsaturated soils. *Journal of the Soil Science Society of America* 49, 58-65.

Stirk, G. B., 1954. Some aspects of soil shrinkage and the effect of cracking upon water entry into the soil. *Australian Journal of Agricultural Research* 5(2), 279-296.

Stirling, R. A., Simpson, D. J. & Davie, C. T., 2013. The application of digital image correlation to Brazilian testing of sandstone. *International Journal of Rock Mechanics and Mining Sciences* 60, 1-11.

Sture, S. & Kim, T. H., 2002. *Experimental study: Influence of moisture on tensile strength in granular soil.* Riyad, Saudi Arabia.

Sutton, M. A. et al., 1983. Determination of displacements using an improved digital correlation method. *Image and Vision Computing* 1(3), 133-139.

Tada, H., Paris, P. C. & Irwin, G. R., 2000. *The Stress Analysis of Cracks Handbook.* 3rd ed. American Society of Mechanical Engineers.

Take, W. A. & Bolton, M. D., 2002. The use of centrifuge modelling to investigate progressive failure of overconsolidated clay embankments.

Tamrakar, S. B., Mitachi, T. & Toyosawa, Y., 2007. Factors affecting tensile strength measurement and modified tensile strength measuring apparatus for soil. In: T. Schanz, ed. *Experimental Unsaturated Soil Mechanics.* Springer Berlin Heidelberg, 207-218.

Tamrakar, S. B., Mitachi, T., Toyosawa, Y. & Itoh, K., 2005. *Development of a new soil tensile strength test apparatus.* Austin, Texas, American Scociety of Civil Engineers.

Tamrakar, S. B., Toyosawa, Y., Mitachi, T. & Itoh, K., 2005. Tensile strength of compacted and saturated soils using newly developed tensile strength measuring apparatus. *Soils and Foundations* 45(6), 103-110.

Tang, C. -S. et al., 2011. Desiccation and cracking behavior of clay layer from slurry state under wetting-drying cycles. *Geoderma* 166, 111-118.

Tang, C.-S., Cui, Y.-J., Tang, A.-M. & Shi, B., 2010. Experiment evidence on the temperature dependence of desiccation cracking behaviour of clayey soils. *Engineering Geology* 114, 261-266.

Tang, C. -S. et al., 2008. Influence factors of geometrical structure of surface shrinkage cracks in clayey soils. *Engineering Geology* 101, 204-217.

Toride, N., Inoue, M. & Leij, F. J., 2003. Hydrodynamic dispersion in an unsaturated dune sand. *Soil Science Society of America Journal* 67(3), 703-712.

Towner, G. D., 1961. Influence of soil-water suction on some mechanical properties of soils. *Journal of Soil Science* 12(1), 180-187.

Towner, G. D., 1987. The Mechanics of Cracking of Drying Clay. *Journal of Agricultural Engineering Research* 36, 115-124.

Towner, G. D., 1987. The Tensile Stress Generated in Clay through Drying. *Journal of Agricultural Engineering Research* 37, 279-289.

Trabelsi, H. et al., 2010. *Some investigations about the tensile strength and the desiccation process of unsaturated clay.* 14th International Conference on Experimental Mechanics.

Trabelsi, H., Jamei, M., Zenzri, H. & Olivella, S., 2012. Crack patterns in clayey soils: experiments and modeling. *International Journal for Numerical and Analytical Methods in Geomechanics* 36(11), 1410-1433.

Tresca, H., 1864. Memoire sur l'ecoulement des corps solides soumis a de fortes pressions. *comptes Rendus Academie des sciences* 59, 754.

van Genuchten, M. T., 1980. A closed-form equation for predicting the hydraulic conductivity of unsaturated soils. *Soil Science Society of America Journal* 44(5), 892-898.

Vanapalli, S. K., 1994. Simple test procedured and their interpretation in evaluating the shear trength of an unsaturated soil. *PhD thesis, University of Saskatchewan, Canada.*

Vanapalli, S. K., Fredlund, D. G. & Pufahi, D. E., 1999. The influence of soil structure and stress history on the soil-water characteristics of a compacted till. *Geotechnique* 49(2), 143-159.

Vanicek, I., 2013. The importance of tensile strength in geotechnical engineering. *Acta Geotechnica Slovenica* 1, 5-17.

Venkataramana, K., Hanumantha Rao, B. & Singh, D. N., 2009. A critical review of the methodologies employed for determination of tensile strength of fine-grained soils. *Journal of Testing and Evaluation* 37(2).

Villar, L. F. S., Camps, T. M. P., Azevedo, R. F. & Zornberg, J. G., 2009. *Tensile strength changes under drying and its correlations with total and matric suctions.* IOS Press.

Vogel, H. -J., Hoffmann, H. & Roth, K., 2005. Studies of crack dynamics in clay soil 1. Experimental methods, results and morphological quantification. *Geoderma* 125, 203-211.

Vomocil, J. A., Waldron, L. J. & Chancellor, W. J., 1961. Soil tensile strength by centrifugation. *Proceeds of the Soil Science Society of America* 25, 176-180.

von Mises, R., 1913. Mechanik der festen korper im plastisch deformablen zustand. *Nachrichten von der Gesellschaft der Wissenschaften zu Gottingen, Mathematisch-Physikalische Klasse,* 582-592.

Waldron, L. J., McMurdie, J. L. & Vomocil, J. A., 1961. Water retention by capillary forces in an ideal soil. *Soil Science Society of America Proceedings* 25, 265-267.

Wang, J.-J., Zhu, J.-G., Chiu, C. F. & Zhang, H., 2007. Experimental study on fracture toughness and tensile strength of a clay. *Engineering Geology* 94, 65-75.

Wang, Q. Z. & Xing, L., 1999. Determination of fracture toughness KIC by using the flattened Brazilian disc specimen for rocks. *Engineering Fracture Mechanics* 64, 193-201.

Willden, R. & Mabey, D. R., 1961. Giant desiccation fissures on the Black Rock and Smoke Creek Deserts, Nevada. *Science* 133(3461), 1359-1360.

Williams, J., Prebble, R. E., Williams, W. T. & Hignett, C. T., 1983. The influence of texture, structure and clay mineralogy on the soil moisture characteristic. *Australian Journal of Soil Research* 21, 15-32.

Yesiller, N., Miller, C. J., Inci, G. & Yaldo, K., 2000. Desiccation and cracking behavior of three compacted landfill liner soils. *Engineering Geology* 57, 105-121.

Zeh, R. & Witt, K. J., 2005. *Suction-controlled tensile strength of compacted clays.* Osaka, Japan, 16th ICSMGE.

Zhan, T., Ng, C. & Fredlund, D. G., 2006. Instrumentation of an Unsaturated Expansive Soil Slope. *Geotechnical Testing Journal* 30(2), 1-11.

Appendix: Published work and conference papers

Stirling, R. A., Simpson, D. J. & Davie, C. T., 2013. The application of digital image correlation to Brazilian testing of sandstone. *International Journal of Rock Mechanics and Mining Sciences,* Volume 60, pp. 1-11.

Technical Note: **The application of Digital Image Correlation to Brazilian testing of sandstone**

1. Introduction

The conventional Brazilian test indirectly establishes the tensile strength of brittle materials assuming biaxial linear elasticity in two-dimensions. Theoretically, the sample is considered to fail within the central portion of the disc, where the tangential stress ($\sigma_{\theta y}$) will overcome the uniaxial tensile strength under the application of a radially compressive stress (σ_{ry}) (Figure 1), [1].

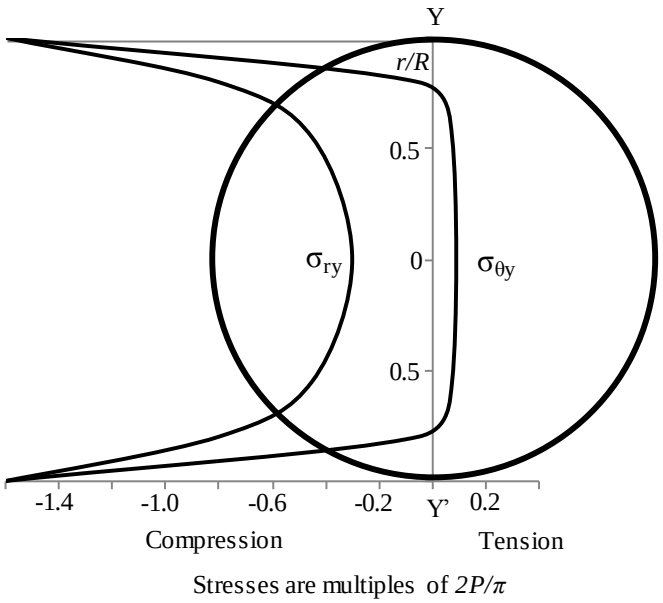

Figure 1: Stress distribution along line YY' in the Brazilian test where, r=radial distance, R=disc radius and P=applied load (after Fairhurst, [2]).

Fairhurst [2] proposed that the tensile strength calculated from Brazilian test results is highly dependent upon the loading method used. The ASTM adopts the use of flat platens, where loading is applied to the disc at diametrically opposing points (Figure 2a), with recommended thickness (t) /diameter (D) ratios ranging between 0.2 – 0.75 [3]. The ASTM method has been criticised as sample crushing resulting from stress concentration has been found to initiate failure at the loading points rather than at the centre of the disc, which is critical in ensuring the validity of the test [4] and [5]. Several authors, including Andreev [6] and Yu, et al. [1] have attempted to mitigate the crushing behaviour through the positioning of 'cushions' and spacers of materials of various stiffness relative to the sample under investigation to decrease the localised stress. This has been shown to reduce the crushing effect of point loading, however adds a layer of complexity. In contrast, the ISRM recommends the application of load

through a curved platen of radius 1.5 times that of the sample whose t/D ratio should be 0.5 (Figure 2b) [7]. This method requires the manufacture of loading platens of differing curvature depending upon the diameter of the sample disc being tested in order to retain a consistent loaded section of the circumference.

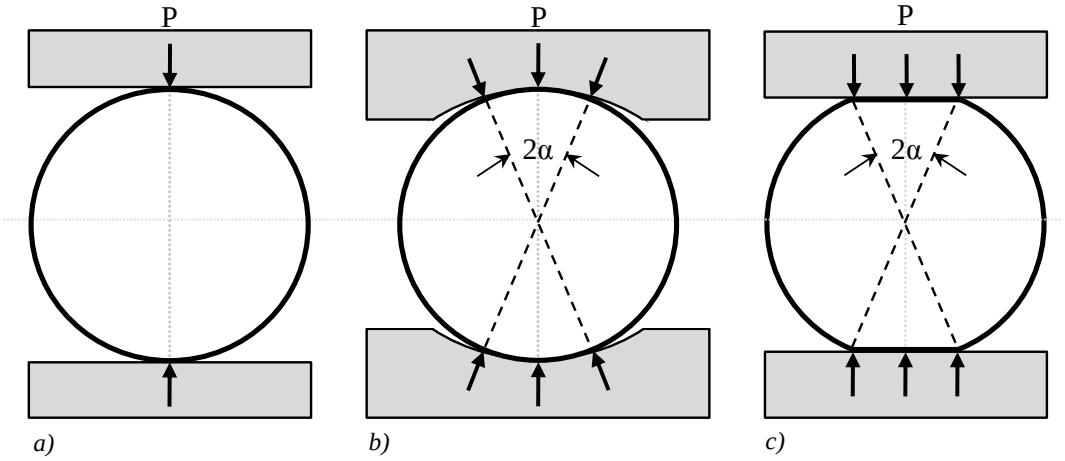

Figure 2: Loading methods a) Flat-point [3], b) Arch-arch [7] and c) Flat-flat [8]

In order to address these issues, Wang & Xing [8] proposed a modified flattened Brazilian disc that allows a good contact between the sample and flat loading platens (Figure 2c) while minimising the crushing associated with point loading. Wang & Xing [8] found that, providing these flattened, parallel surfaces form an angle of $2\alpha \geq 20°$, fracturing will develop from the centre of the disc during testing, thus ensuring the reliability of results [5] and [1].

These three loading methods are presented in Figure 2. The area of the disc over which the load (P) is applied is indicated. Figure 2b and c share a common angle, 2α, which defines the boundaries of the loaded area, though the area loaded in Figure 2b is greater (as it is applied though the use of curved platens) than that of the flattened disc geometry of Figure 2c [2].

Attempts to observe the development of local compressive and extensional strains during Brazilian tests have been carried out using strain gauges adhered to the surface of specimens in both the horizontal and vertical orientation by [9], [10] and later by [11] and [12]. Whilst this method can provide accurate results, they are time consuming and cumbersome to prepare and may not be suitable for weak, friable lithologies. Strain measurements are also highly localised and can be affected by the stiffness of the gauge and adhesive.

The 3D Digital Image Correlation (DIC) system is a method for identifying the distribution and development of strains without the need for direct sample contact. The theoretical basis of the DIC technique was first proposed by Chu, et al [13] and has since been used in many fields of material testing, although its application in geo-mechanics is not well publicised [14]. Using high-resolution image capture, the displacement of an applied speckle pattern coated on the surface of a sample is tracked on the basis of pixel distortion before being converted into a measure of strain.

In using two calibrated parallax cameras, this apparatus can measure the development of strains in the vertical and horizontal axes to a high degree of accuracy whilst also enabling measurement of out-of-plane displacements. Its advantages also include its ease of use following setup, measurement of the full strain field and compatibility with soft or friable specimen surfaces to which more traditional means of local strain measurements would not adhere.

The work herein aims to demonstrate the application of DIC as a substitute to more traditional strain gauges in Brazilian testing. This study initially applies the DIC technique to qualitatively and quantitatively assess the influence of loading geometry on strain localisation across the sample face. A comparative study is presented whereby the effect of ASTM, ISRM and flattened disk loading styles (presented by Wang & Xing, [8]) is examined with respect to localised straining behaviour at the top and bottom of the disk and location of fracture initiation. A second study considers varying disc t/D ratio in order to assess out-of-plane displacement.

2. Material description

The material tested in this work was Springwell sandstone, originally sourced from the Springwell Quarry in Gateshead, Tyne and Wear, UK. The brown-yellow fine grained sandstone consists of sub-rounded to sub-angular, well sorted grains and forms part of the middle Pennine coal measures deposited in the Upper Carboniferous period.

The rock comprises predominantly quartz (85%), clay mineral (8%), alkali feldspar (5%) and mica (2%) [15]. The rock is ideal for these tests as it has been found to show no preferred orientation and has been described as “medium strong, linear elastic, homogeneous and isotropic in terms of both its strength and elastic properties” [16]. A summary of physical and mechanical properties is provided in Table 1.

Table 1: Physical and mechanical properties of the Springwell sandstone, (after [16]).

Property Measured	**Symbol**	**Value**	**Unit**
Porosity	n	10.74	%
Dry density	γ_d	2226	Kg/m^2
Uniaxial compressive strength	σ_u	44.113	MPa
Young’s modulus	E	7.527	GPa
Poisson’s ratio	v	0.261	-
Indirect tensile strength	σ_t	3.725	MPa

3. Experimental procedure

Samples were cored from the parent block with an 81.5mm external diameter diamond core barrel. This resulted in a consistent sample set known to have

originated from the same vertical sequence and within a $1m^3$ volume. Disturbance during transportation was minimised as sample preparation and testing were carried out in-house. The discs were finished on a surface grinder to ensure their faces were flat to the required degree of parallelism and that the t/D ratio was accurate to within 0.01. Both the ASTM and ISRM methods require the use of circular discs as shown in Figure 3a. Samples that required the flattened disc geometry for comparison between loading methods were cut to the specification of Wang & Xing [8] as shown in Figure 3b. The rock disks were oven dried for a period of 48 hours.

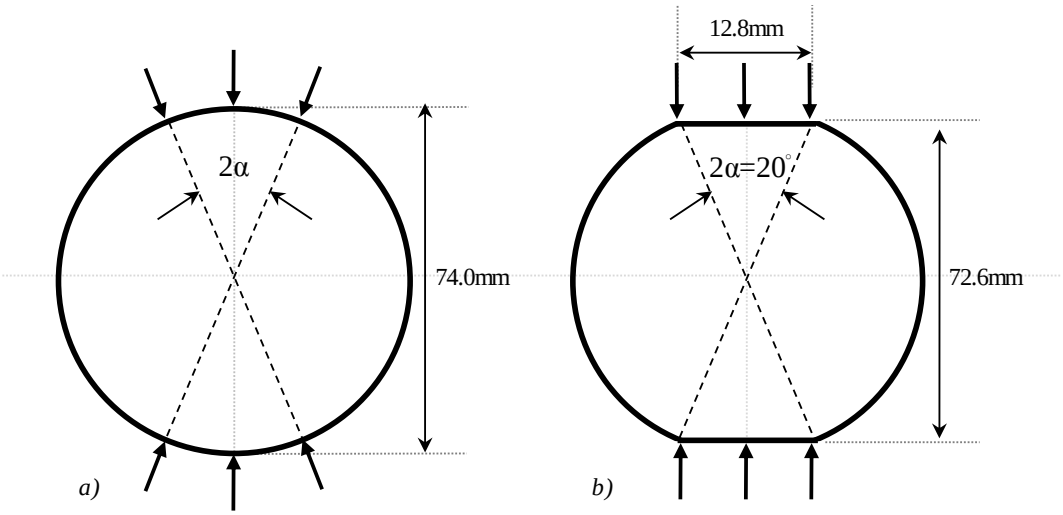

Figure 3: Rock disc geometries; a) ISRM and ASTM and b) Flattened (after [8])

The testing schedule consisted of two stages, the first being a comparative study of the loading methods stated in the ISRM and ASTM standards and that proposed by Wang & Xing, [8], using the DIC technique to observe the development of strain with the aim of identifying the location of crack initiation and loading induced out-of-plane deformation. A t/D ratio of 0.5 was maintained for the purpose of comparison between tests. The second stage was aimed at investigating the effect of varying thickness with reference to the ASTM recommended t/D ratio range and the ability of DIC to observe out-of-plane deformation. The test ratios and adopted nomenclature are provided in Table 2.

Table 2: Sample geometries and loading methods

Test ID	*t/D* Ratio	Testing Method	# Samples Tested	Loading Rates (kN/min)
I0.5_	0.5	ISRM [7]	3	3.225
A0.5_		ASTM [3]	3	
W0.5_		Wang & Xing [8]	4	
A0.1_	0.1	ASTM [3]	3	0.645
A0.2_	0.2		3	1.290
A0.75_	0.75		3	4.839

All testing was conducted using an Instron 5585H universal testing machine. This device is able to apply either a constant loading rate or rate of displacement. Both the ISRM and ASTM standards recommend stress controlled testing, applying a constant rate of load such that samples will fail within a reasonable timeframe. In order to achieve failure in accordance with the standards, a loading rate of 3.225kN/min was back-calculated from the average tensile failure strength of Springwell sandstone (3.73 MPa) as observed by Alsayed [16] for a desired time to failure of approximately 5 minutes. This rate was used during all stage 1 tests. Rates used during stage 2 tests are shown in Table 2 and are derived from the thickness of the samples tested.

Work conducted by Andreev [6] has highlighted the inaccuracy in the application of different materials in cushioning the transfer of load to the disc. In addition to this, the suggested use of cardboard and plywood in the ASTM standard is arbitrarily defined and in the interest of consistency between methods, no cushioning was used in this work. Furthermore this work adopts the following sign convention: positive strain = compression; negative strain = extension.

4. Digital image capture and processing

The Vic-Snap photogrammetry system was employed to monitor the samples in a contactless manner [17]. Two cameras were mounted on a tripod and profile bar then centred symmetrically about the sample position. The cameras were fitted with telephoto lenses of 28mm focal length and a 2mm relative aperture. In order to provide the desired degree of out-of-plane resolution for a sample at around 500mm distance from the cameras, an approximately 30° angle of incidence was chosen, as suggested in the user guide [17]. The DIC setup is shown in Figure 4.

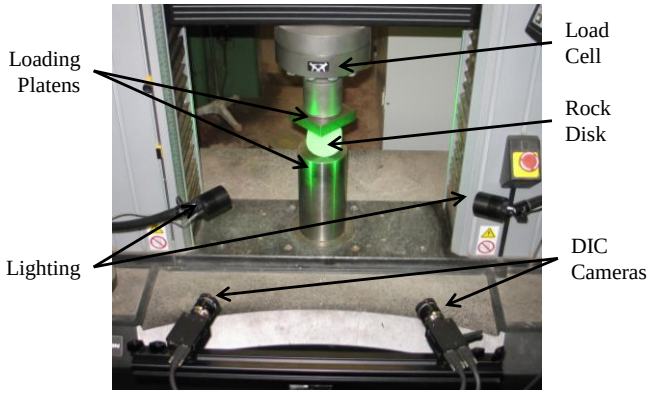

Figure 4: DIC and testing rig setup

In preparing the samples for DIC, a black-on-white speckle pattern was applied to the prepared face using fine aerosol paint to achieve a 50:50 coating that was both non-repetitive and isotropic [17]. Upon DIC system setup, this pattern was confirmed to meet the 2-30 pixel per speckle requirement and additional LED (cold source) lighting was used in order to maintain sufficient contrast of the pattern. Minor flaws in the contoured output may result from the accumulation of paint, highlighting the importance of an even speckle pattern. Image capture was conducted at intervals of 50ms (20fps). This was deemed

sufficient to record sample deformation. A reference image was captured prior to application of load in order that subsequent relative sample deformation could be computed.

Following compilation of test images, an area-of-interest (AOI) was marked on the reference image consisting of the speckled face of the sample (Figure 5). An analysis grid large enough to ensure a sufficiently distinctive pattern was included within the AOI to allow for correlation. A single level of grid discretisation was used for all analyses as this relates to the use of a consistent speckle pattern. In addition to this, two analysis seed points, from which analysis begins, were placed within the AOI where least deformation was expected i.e. away from loading contacts and the disc centre. Two seed points were used to ensure the continuation of analysis either sides of the potential fracture. It must be noted that due to the prescription of this grid and only complete squares being analysed, a varying area around the circumference of the AOI is lost despite a fine grid spacing being set (Figure 5). This resulted in the flattened geometry of W0.5_ samples not being apparent in the post-processed output. Once the analysis specification was made using the reference image, all subsequent deformation of the speckle pattern in the test images was then tracked using the system software, Vic-3D [17]. The DIC data is converted to a triangular mesh defined on the tangential plane of the sample surface and strains are computed in much the same way as conventional Finite Element analyses.

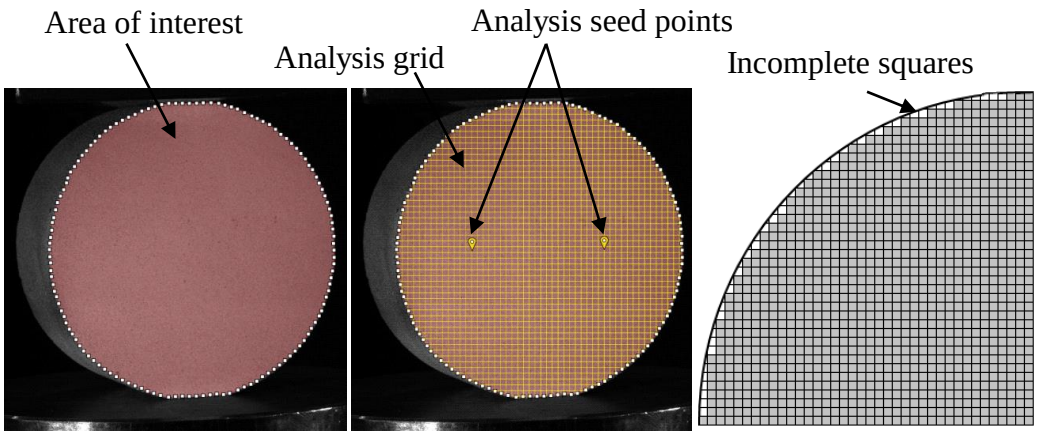

Figure 5: Reference image and analysis area selection.

5. Loading method comparison

All samples were loaded until the resulting fracture was seen to propagate through the whole specimen diameter. Following ASTM and ISRM guidance, tensile strengths (σ_t) of samples were calculated using Equation 1. This expression assumes the material to display linear elasticity until failure and that maximum tensile stresses are therefore induced normal to the loaded diameter such that failure is initiated at the centre of the disc. The scenario is essentially treated as a two-dimensional problem. The validity of the two-dimensional solution traditionally used in calculating the tensile strength has also been investigated by Wijk, [18]. Three-dimensional corrections to the traditional solution have been proposed, although the complexity of the process and

assumptions made make this approach prohibitive for the majority of routine tensile testing and thus they are not considered here.

$$\sigma_t = \frac{2P}{\pi Dt}\sigma_t = \frac{2P}{\pi Dt} \quad (1)$$

$$\sigma_t = k\frac{2P}{\pi Dt}\ \sigma_t = k\frac{2P}{\pi Dt} \quad (2)$$

The tensile strength of samples cut with the flat loading geometry was calculated using the adapted Equation 2 with the introduction of coefficient, *k,* which is related to the angle, *α* (Figure 3b). When 2*α=20°*, k=0.9644 [5]. Secant elastic moduli, E_{sec}, were calculated from local horizontal strain data measured using the DIC. Table 3 shows the calculated tensile strength and DIC measured stiffness of all samples tested during stage 1 of this study.

Table 3: Tensile strength of Springwell sandstone with different loading methods

Test	Testing Method	Failure Load, *P* (kN)	Tensile Strength, σ_t (MPa)	DIC Modulus, E_{sec} (GPa)
A0.5_A	ASTM [3]	14.30	3.32	8.83
A0.5_B		14.99	3.49	10.51
A0.5_C		13.77	3.20	9.44
I0.5_A	ISRM [7]	14.71	3.42	10.59
I0.5_B		13.93	3.24	10.73
I0.5_C		10.10	2.35	8.22
W0.5_A	Wang & Xing [8]	17.92	4.02	9.35
W0.5_B		18.49	4.15	7.27
W0.5_C		15.16	3.40	10.21
W0.5_D		18.54	4.16	9.29

Tensile strengths were derived from the load (*P*) corresponding to failure as observed from the externally measured load-strain relationship (Figure 6). Failure is defined by an abrupt loss of stiffness often accompanied by a fracture (although not necessarily visually apparent) and where a constant loading rate may no longer be maintained. Prior to the failure load, no fractures have developed and samples are assumed to behave in a linear elastic manner. This is supported by the load-strain relationships in Figure 6.

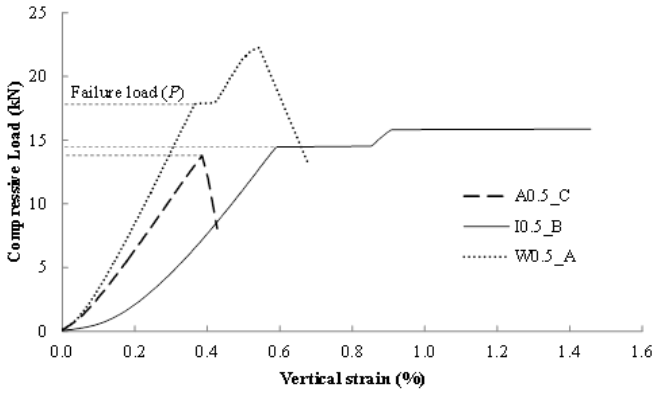

Figure 6: Representative load-strain results

The failure load marked the end of tests carried out in accordance with ASTM standards, as the samples fell apart and could carry no more load. The load-strain behaviour of samples tested following ISRM guidance and Wang & Xing, [8] flattened geometry typically showed a temporary plateau following failure where load remained approximately constant and rapid vertical compressive straining was observed as the Instron attempted to maintain a constant loading rate. In these cases, the load imposed upon the sample continued to rise following this plateau until testing was stopped manually. This is thought to be an effect of the sample being constrained by the testing platens and beginning to shear.

Omitting post-failure behaviour, caused by sample constraint, the externally measured load-strain relationship of the Springwell sandstone is presented for each test in Figure 7. These results show a relatively high level of consistency in apparent stiffness and load at failure within each testing method, with the exception of test I0.5_C which was likely caused by an unseen flaw within that sample. Samples tested using the flattened disc specification provided by Wang & Xing [8], indicate a stiffer response to load, with samples failing at marginally higher loads and undergoing less strain than those following the ASTM and ISRM standards. Failure loads, and therefore tensile strengths, of the ASTM and ISRM tests were similar, as too was the apparent stiffness prior to failure. However, the externally measured strain behaviour of the samples upon initial loading differed greatly, with significantly higher vertical strain being observed in ISRM testing. This may be partially due to total displacements incorporating additional compliance in the case of the ISRM curved platens. However the effect of bedding-in is seen in the externally measured strains of all three testing methods where initially softer responses are seen at the onset of loading.

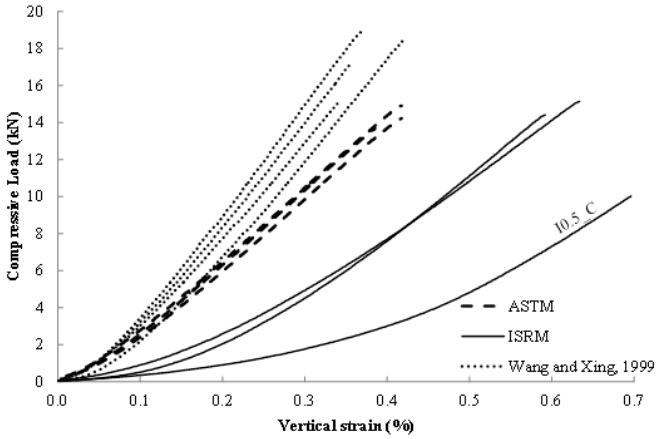

Figure 7: Load-corrected displacements recorded externally for all tests

For the purposes of comparison, representative tests of each loading method have been selected for analysis. Vertical strain between the top and bottom of the disk were measured locally using DIC and are presented alongside externally measured load-strain data in Figure 8. The DIC method is recognised to have excluded the area immediately around the circumference of the disk due to the prescription of an analysis grid subset. Therefore, as is the case with all local strain measuring tools, total vertical strains calculated using this software do not include those associated with bedding-in, localised crushing at the loaded surfaces or apparatus compliance. This has resulted in more competent load-strain behaviour being captured than is seen using only external measurements. By using the DIC to measure horizontal extensional strains, comparable tensile stiffness of between 7.3 and 10.7GPa can be calculated for all tests regardless of loading method. Values presented in Table 3 are found to be of a comparable magnitude to that established under compressive testing shown in Table 1.

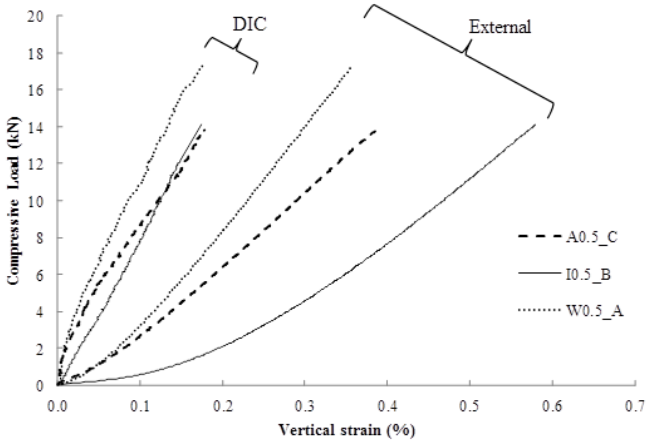

Figure 8: Load-corrected displacements recorded internally (DIC) and externally for representative samples

Post-fracture behaviour has been captured photographically via the DIC system and is shown in Figure 9. The fracture geometry of a representative ASTM sample after reassembly is shown in Figure 9a. Owing to the high fracture

velocity, propagation could not be captured using DIC. Asymmetrical notches can clearly be seen at the sample top and bottom as a result of circumferential crushing brought about by point loading. The curved platen loading geometry of the ISRM specification holds the sample in place post-failure, allowing image capture of the fracture as shown in Figure 9b. The dominant fracture is typically accompanied by secondary fractures that open from the circumference at the outer points of contact with the curved platens.

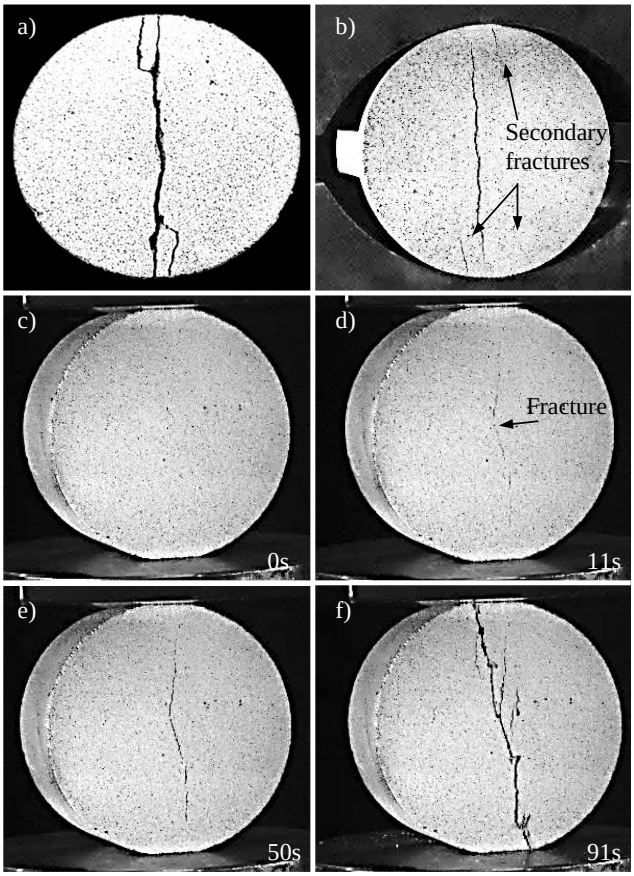

Figure 9: Disc samples during and post-failure a) Sample A0.5_A post failure, b) I0.5_B at onset of fracture and c-f) W0.5_A fracture growth post-failure

The growth of fracture in tests using the flattened disc geometry of Wang & Xing [8] was easily captured due to the relatively slow stepwise propagation. Figure 9c shows a representative flattened disc immediately prior to failure with no fracture visible. Subsequent images, at the times shown, depict the propagation of the highlighted fracture, which originates across the centre of the disc in Figure 9d and opens diametrically. The final fractured state is presented in Figure 9f and shows the stepped geometry that incorporates the central fracture. Failure load (P) was taken at the instant the initial central fracture opened according to the load-displacement data. However it should be noted that the load continued to increase as the fracture propagated steadily through the sample until the fracture spanned the whole sample diameter.

Local strain was calculated during post-processing of the DIC images captured during all tests. For the purposes of comparison, representative tests of each loading method have been selected as in Figure 8 and contour plots of

percentage horizontal and vertical strains are presented in Figure 10. Plots represent the captured state immediately prior to failure and therefore fractures have not yet developed.

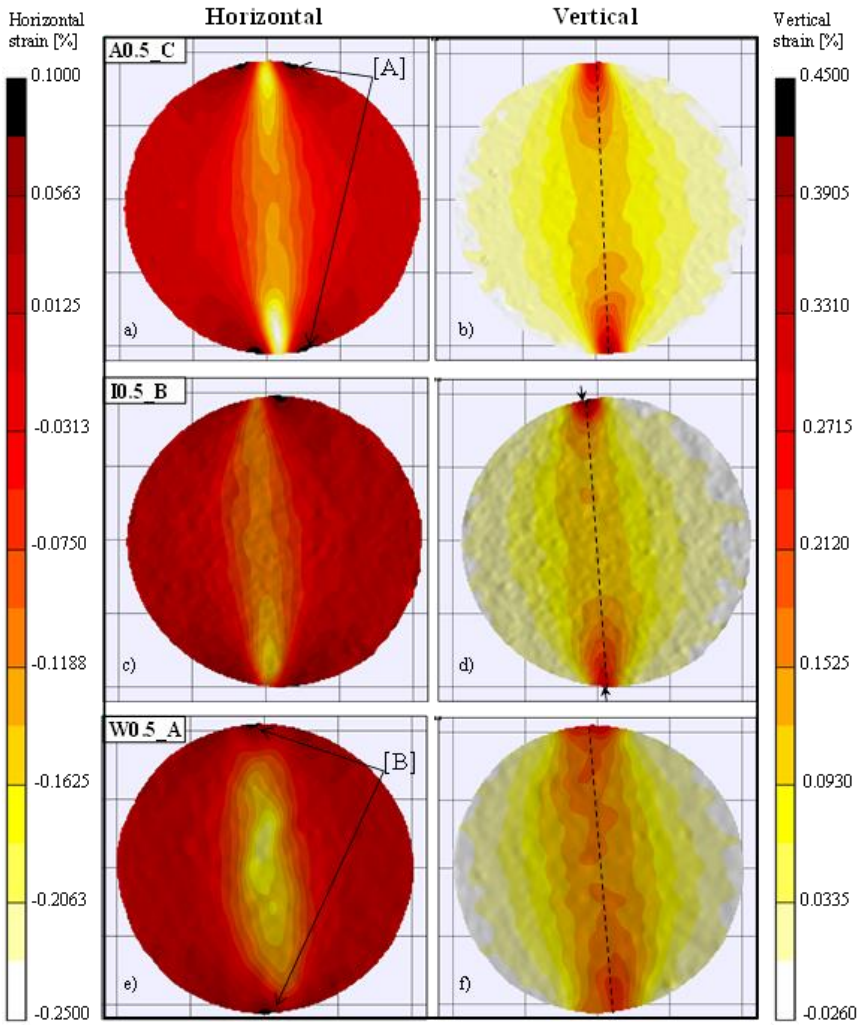

Figure 10: Strain distributions immediately prior to failure a-b) ASTM, c-d) ISRM and e-f) Flattened

In theory, samples are expected to fail within the central portion of the disc. By examining the development of local strains using DIC, it is possible to compare the locations of strain concentrations between loading methods.

Qualitative assessment of Figure 10a, showing the ASTM loading method, highlights two regions of dominant horizontal extension located to the top and bottom of the disc. These areas are seen to be within a relatively narrow band of extension occurring across the vertical diameter. Compressive strains caused by loading the top and bottom points of the disc can be clearly seen in Figure 10b. Greatest vertical compressive strain occurs exactly at the edges of the disc, whereas horizontal extension is located inward of these areas. The regions of high vertical compression are accompanied by the maximum horizontal compression located at [A] in Figure 10a. This is thought to be evidence of crushing behaviour as greatest compression is shown here in both

orientations and corresponds well with the observed fracture pattern in Figure 9a.

For the ISRM arch-platen loading method, a sub-diametric region of horizontal extension and associated vertical compression in Figure 10c & d is shown respectively. Areas of greatest compression are seen to be located to the top and bottom of the disc, as seen in the ASTM method. However, with the use of curved-platens, these areas are seen not to be perfectly, diametrically opposed where load is transferred to the sample off-centre, as in Figure 10d. This eccentric behaviour has also been observed by several authors and is a function of an imperfect interface between the sample curvature and that of the loading platen [9]; [11]; [8] and [5]. The lateral extent of the sub-vertical strain concentration is shown to be comparable to that of ASTM testing despite a theoretically greater contact area due to the use of curved platens.

For the flattened disc procedure provided by Wang & Xing [8], horizontal compression is seen to be located at the loaded ends of the disc at [B] in Figure 10e, although in this case this is not associated with the extensional maximum. Instead, the dominant region of horizontal extension can be clearly observed to have formed at the centre of the disc, representing the best compliance with suggested theory. In contrast to the standard methods, upon loading at flattened disc ends, a broader distribution of vertical compressive strains is evident with reduced magnitude at the loading positions (Figure 10f). This is due to load being applied over a greater area of the disc circumference to that of the ASTM method, although theoretically the contact area is comparable to the ISRM loading method. In order to quantitatively compare the development of tensile strain and hence, comment upon the likely associated generation of tensile stress, strain profiles have been taken from across the loaded diameter (depicted in Figure 10b, d and f) and are presented in Figure 11.

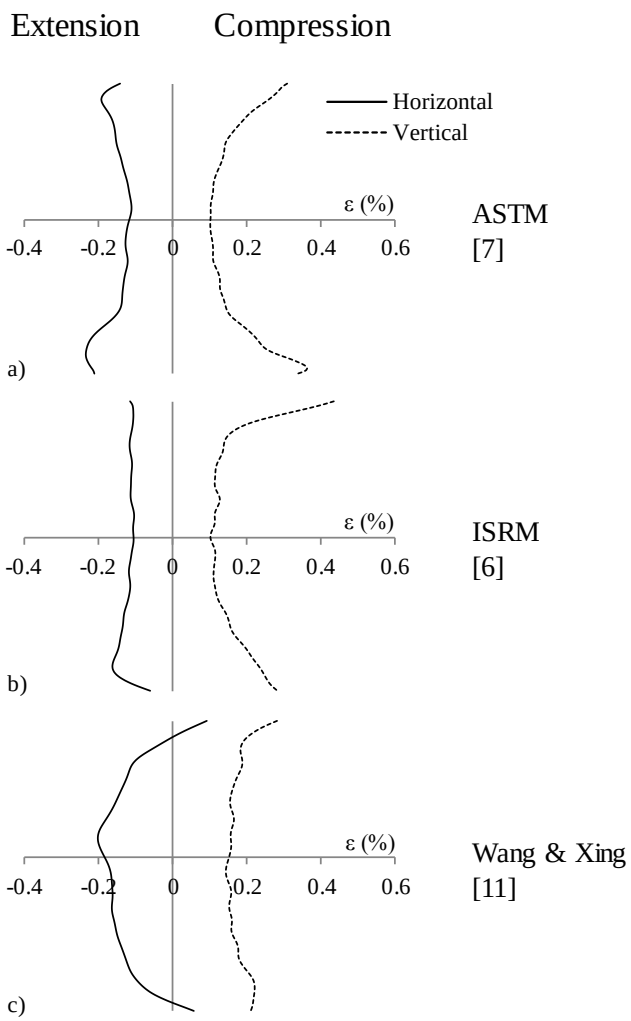

Figure 11: Strain profiles across loaded diameter immediately prior to failure.

It can be seen in Figure 11a, showing the ASTM loading method, that exclusively compressive vertical strain has developed across the sample with the greatest vertical strain of 0.36% exhibited to have developed at the loading points, as would be expected. Horizontal strain is entirely extensional over the disc diameter across which the sample was loaded.

Along this profile two regions where extensional horizontal strain increases are visible and it can be seen that these correlate with the area of maximum compressive strain. The minimum horizontal strain, -0.11% is found to be located at the centre of the disc. Assuming linear elasticity, two distinct regions of maximum tensile stress are found to be located approximately 5mm inward from each loading point. This would suggest that fracture of the disc ultimately initiated in one of these regions, which is counter to the observations made by Yanagidani, et al. [10], using more traditional local strain gauges and is counter to the Brazilian test theory.

A similar vertical compressive trend may be seen in Figure 11b) where curved-platens were used. The maximum vertical compressive strain, and therefore it is assumed stress, is found at the loading points, with the greatest strain of 0.44% at the top of the disc. The distribution of horizontal strain is found to be more

even across the disc diameter with an average of -0.1%. Greatest horizontal extension is measured in the lower half with a maximum strain of -0.16%. This suggests that for the tests carried out, failure initiated within the sample close to the lower contact.

The maximum horizontal extension found within the flattened disc using Wang and Xing's [8] method is located to the centre (Figure 11c), which is in significant contrast to the results for tests using ASTM and ISRM methods. As with these loading methods, vertical strain is found to be greatest towards the points of loading (0.28%) though is generally more evenly distributed across the sample owing to the larger area over which the load is imposed. However, horizontal strain is seen to be compressive at these points, brought about by the restraint offered by the relatively large contact area. Extensional straining is seen to develop increasingly from the sample ends to a maximum at the approximate centre of the flattened disc. This indicates the greatest tensile stress concentration to be located here and corresponds with the observed initiation of fracturing and to Brazilian test theory.

Although samples tested in accordance with the ISRM and those with flattened geometries share a similar theoretical loading area, as defined by the angle 2α, the two methods produce very different results. Several authors including Wang, et al., [5] and Jianhong, et al., [11] have stated that although the theoretical purpose of the curved loading platens is to distribute load over a known area, in practice confidence in the ability to maintain this area throughout the test is limited. This is borne out by the results of this work (Figure 10c and d). The Wang & Xing [8], method is believed to reduce this uncertainty when used with stiff, well cemented materials, as the sample ends can be cut and ground to be parallel with a high degree of accuracy, all but removing 'bedding-in' errors, as can be seen in Figure 7.

Further to these results, the DIC was able to calculate the development of out-of-plane displacement during each test. Figure 12 displays the final surface profiles taken vertically at the centre of samples immediately prior to failure. It can be seen that tests conducted to ASTM specification consistently exhibit an outward (positive) protruding region towards the top and bottom of the disc, in the area proximal to loading contact. Again, this is likely related to sample crushing. Tests conducted to the ISRM standard exhibit a similar behaviour, though limited to a single end of the disc. It may be noted that ISRM tests are located higher on the vertical axis as samples were mounted within the additional curved platens relative to the DIC cameras. Surface profiles for tests conducted on flattened discs using Wang & Xing [8] specification show a more level face indicating that less sample crushing was occurring due to the load being applied over flat and parallel surfaces. This increased contact area may also have resulted in greater restraint of the sample leading to a lesser degree of sample movement from the z=0mm reference position at the start of testing.

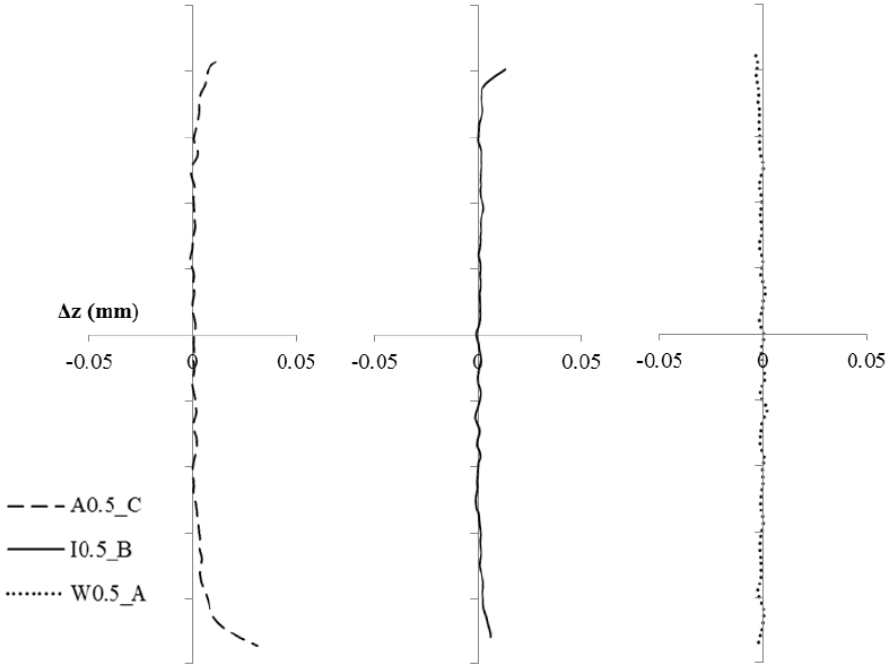

Figure 12: Vertical surface profiles of representative samples immediately prior to failure.

6. Effect of disc thickness

Brazilian tests were carried out to ASTM standard on sandstone disks of varying thickness-diameter ratios. The ASTM standard suggests a ratio range of 0.2-0.75 and these extremes were tested in addition to the 0.5 ratio used in Section 0. To investigate the ability of the DIC system to measure out-of-plane displacement on the disk face, a ratio of 0.1 was also tested as this was anticipated to exhibit greatest displacement in this orientation. Loading rates were calculated to induce failure at a consistent time based upon the sample thicknesses used, as stated in Table 2. All discs were observed to fail in the conventional manner via vertical fracture at approximately 4 minutes. Tensile strengths were then calculated from the failure loads using Equation 1 and are presented in Table 4. It can be seen that a broadly constant tensile strength is attained though the magnitude of load at failure is proportional to the area upon which the disk was loaded, dependent upon thickness.

Table 4: Tensile strengths of Springwell sandstone tested with different disk thickness.

***t/D* ratio**	**Test**	**Failure Load, *P* (kN)**	**Tensile Strength, σ_t (MPa)**	**DIC Modulus, E_{sec} (GPa)**
0.1	A0.1_A	2.71	3.15	5.11
	A0.1_B	2.55	2.97	4.66
	A0.1_C	2.72	3.16	5.54
0.2	A0.2_A	5.76	3.35	5.85
	A0.2_B	5.37	3.12	10.99
	A0.2_C	6.45	3.75	7.44
0.5	A0.5_A	14.30	3.32	8.83
	A0.5_B	14.99	3.49	10.51
	A0.5_C	13.77	3.20	9.44
0.75	A0.75_A	18.02	2.79	11.67
	A0.75_B	19.70	3.05	13.68
	A0.75_C	19.60	3.04	10.67

Representative tests have been selected to demonstrate the effect of thickness/diameter ratio on measured out-of-plane displacements. The DIC can be seen to be capable of resolving z-displacements to an accuracy of within ±0.001 mm. Surface profiles have been taken vertically across the diameter and are provided in Figure 13.

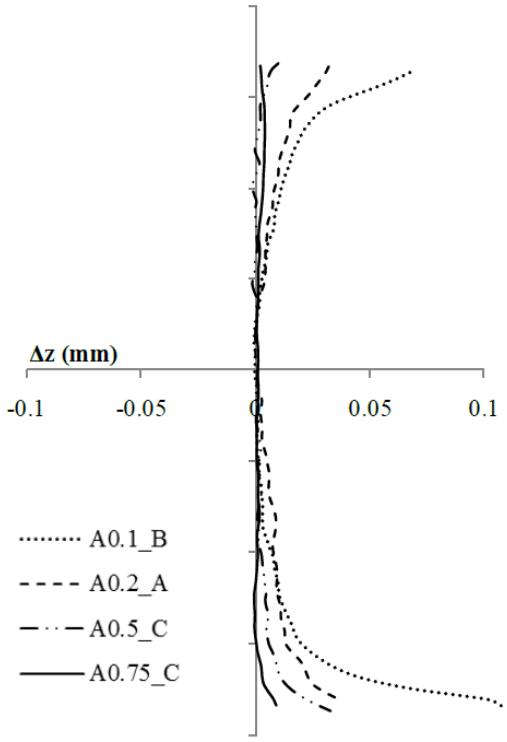

Figure 13: Vertical surface profiles of representative samples immediately prior to failure.

Samples prepared to a ratio of 0.75 exhibit little out-of-plane variation along the diameter except at the bottom of the disk where deflection towards the camera is seen. As the t/D ratio is reduced, the degree of z-plane deformation across the samples diameter increases, particularly towards the top and bottom of the disks proximal to the points of loading. Samples cut to a ratio of 0.1 display the greatest out-of-plane displacements of all samples, measuring between 0.02mm and 0.06mm.

Furthermore, the locations of the maximum z-displacements of all samples correspond closely with the position of the maximum magnitudes of vertical compressive strains (Figure 14) as a result of Poisson's effect and this localised z-displacement trend may also be evidence of crushing in these regions.

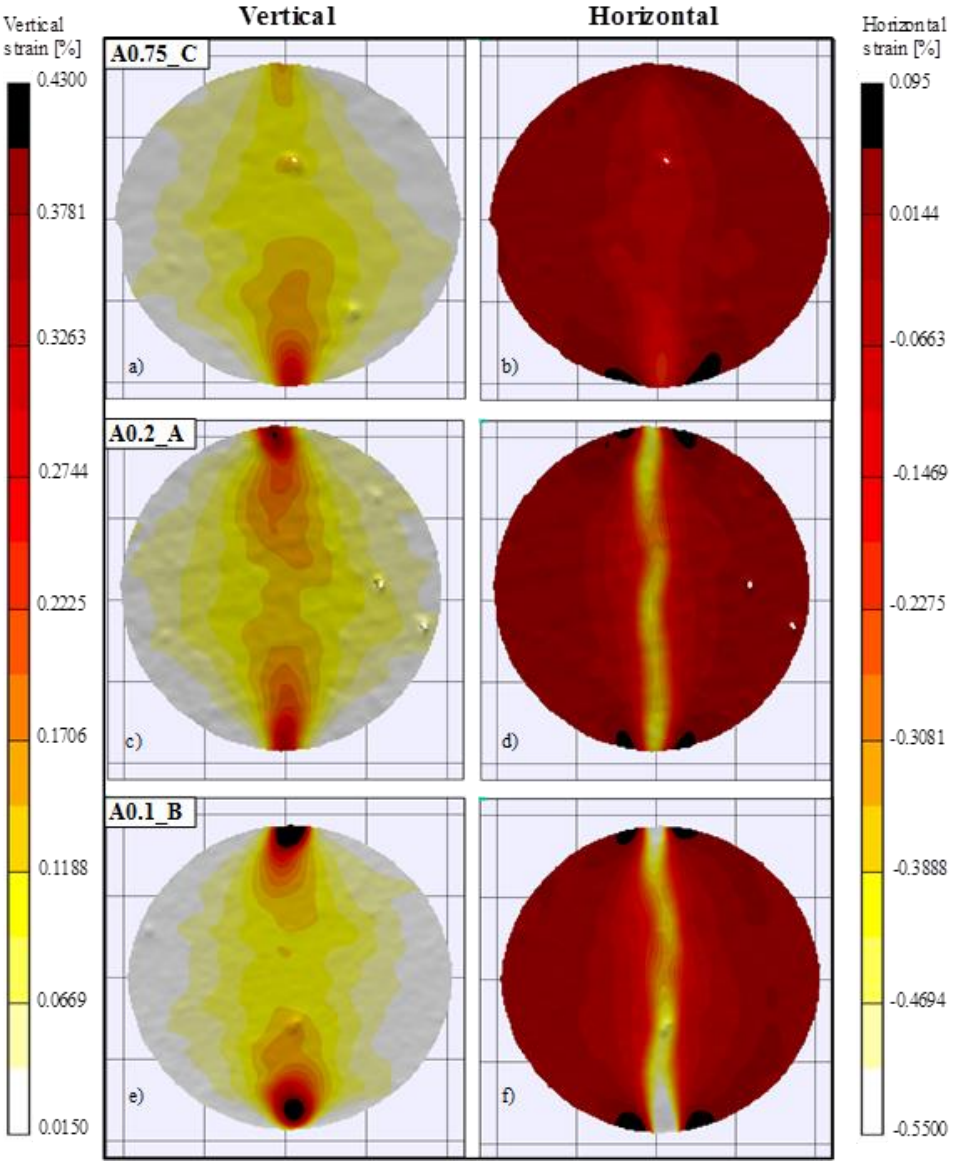

Figure 14: Strain distributions immediately prior to failure for samples of t/D ratios a-b) 0.75, c-d) 0.2 and e-f) 0.1

Total vertical strains through the central vertical section of the samples measured using DIC increase as the t/D ratio reduces, meaning that thinner samples are undergoing greater vertical strains than thicker ones, despite all samples failing at highly comparable tensile stresses. The greatest horizontal and vertical compression measured for each sample is once again seen to be adjacent to the loading points. It can be seen in Figure 14 that the intensity with which horizontal extensional strain is produced increased with reducing t/D ratio.

When image capture speed has enabled the moment of fracture initiation to be captured, it is possible to compare the location of fracture formation to the development of horizontal extensional strain immediately prior to failure. This is in agreement with work conducted by [19] into the use of DIC for investigating desiccation cracking in clay based materials. A strong correlation between the localisation of inferred tensile stress and the location of cracking is seen, an example of which is presented in Figure 15.

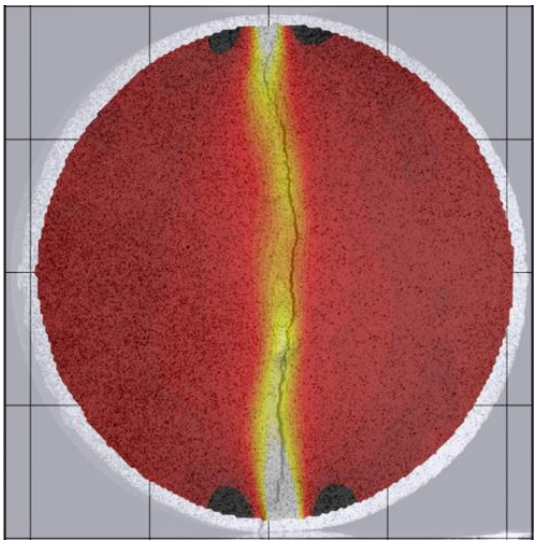

Figure 15: Tensile strain development and fracture correlation in representative sample A0.1_B

7. Conclusions

The 3D DIC system has been shown to be capable of producing high resolution strain mapping across the surface of rock discs undergoing Brazilian testing. By comparing the effects of loading method and sample geometry upon surface strains and out-of-plane deformations, DIC has allowed the following conclusions to be drawn:

1. The ASTM, ISRM and flattened disk loading methods have shown differing horizontal and vertical strain development throughout the course of the tests.
    a) The ASTM and ISRM tests have shown greatest tensile strain concentration to have developed toward the points of loading corresponding to the regions of highest compressive strains in the loaded orientation. This implies that fracture initiation occurs in these regions, though the frame rate employed was insufficient to capture

the instance of failure owing to extremely high fracture velocity. Crushing in these areas was further evidenced by out-of-plane movement.

b) The use of flattened disk geometry has shown a consistently central development of extensional horizontal strains in addition to evenly distributed, vertically compressive strain. The use of DIC confirmed the centralised origin of failure.

2. In using a 3D system, it has been possible to observe out-of-plane displacements increasing with decreasing sample thickness. This behaviour has been found to be greatest at the top and bottom of the sample, coincident with the regions of largest vertical compressive strain. Whilst this does not appear to affect the calculated tensile strength, DIC has enabled this behaviour to be observed counter to the solely 2D deformation assumption inherent in Brazilian testing.

In addition to these conclusions, the following general observations on the application of DIC to Brazilian testing have been made:

1. DIC represents a rapid and simple means of measuring strains across the whole analysed surface. Traditional methods of measuring local strains, for example electrical resistance strain gauges and linear variable differential transformers (LVDT's), are limited to a finite number of linear 2D gauge lengths per sample due to space restrictions. By using DIC to measure the development of small-scale displacements, not only are more realistic strain behaviours observed than would be captured externally, this measurement is made throughout the full strain field in 3D rather than between a limited number of discreet points.

2. In post-processing, strain development may be observed throughout the course of the test. The visualisation options include graphical data, still images and video, increasing the accessibility of data for interpretation.

3. In using DIC, assessment of the point of fracture initiation, and therefore test validity, can be deduced via post-processing of strain data and observation of photographs taken automatically by the DIC system.

4. Traditional local strain gauges require sample contact along with knowledge of the relative stiffness of the gauges themselves. The DIC system is contactless and the stiffness of the paint is considered to be negligible.

5. Preparation of multiple samples for application of DIC may be carried out efficiently with reference to time, although the performance of the analysis is highly dependent upon the user's ability to create a speckle pattern that is both appropriate in size and consistent across samples.

Acknowledgements

The authors would like to thank Fred Beadle, Stuart Patterson and Alex Blenkinsopp for assistance during laboratory work, Dr Peter Helm for help in the preparation of the manuscript and Chris Russell for his encouragement.

References

[1] Yu Y, Zhang J, Zhang J. A modified Brazilian disk tension test. Int. J. Rock Mech. Min. Sci. 2009;46:421-425.

[2] Fairhurst C. On the validity of the 'Brazilian' test for brittle materials. Int. J. Rock Mech. Min. Sci. 1964;1:535-546.

[3] ASTM C496. Standard test method for splitting tensile strength of cylindrical concrete specimens. In Annual Book of ASTM, Standards, vol. 0.042. Philadelphia: ASTM; 1984. p. 336–41.

[4] Hudson JA, Brown ET, Rummel F. The controlled failure of rock discs and rings loaded in diametral compression. Int. J. Rock Mech. Min. Sci. 1972;9:2241–8.

[5] Wang QZ, Wang XM, Jia SQ, et al. The flattened Brazilian disc specimen used for testing elastic modulus, tensile strength and fracture toughness of brittle rocks: analytical and numerical results. Int. J. Rock Mech. Min. Sci. 2004;41: 245–53.

[6] Andreev GE. A review of the Brazilian test for rock tensile strength determination. Part II: contact conditions. Min. Sci. Tech. 1991;13: 457-465.

[7] ISRM. Suggested methods for determining tensile strength of rock materials. Int. J. Rock Mech. Min. Sci. 1978;15:99–103.

[8] Wang QZ, Xing L. Determination of fracture toughness KIC by using the flattened Brazilian disc specimen for rocks. Eng. Fract. Mech. 1999;64:193–201.

[9] Hondros G. The evaluation of Poisson’s ratio and the modulus of materials of a low tensile resistance by the Brazilian (indirect tensile) test with particular reference to concrete. Aust. J. Appl. Sci. 1959;10:243–68.

[10] Yanagidani T, Sano O, Terada M, Ito I. The observation of cracks propagating in diametrically-compressed rock discs. Int. J. Rock Mech. Min. Sci. 1978;15:225–235.

[11] Jianhong Y, Wu FQ, Sun JZ. Estimation of the tensile elastic modulus using Brazilian disc by applying diametrically opposed concentric loads. Int. J. Rock Mech. Min. Sci. 2009;46:568–576.

[12] Dave EV, Braham AG, Buttlar WG, Paulino GH. Development of a flattened indirect tension test for asphalt concrete. J Test Eval 2011;39(3):1-8.

[13] Chu T, Ranson W, Sutton M. Applications of digital-image-correlation techniques to experimental mechanics. Exp. Mech. 1985;25:232-244.

[14] Sutton MA, McNeill SR, Helm JD, Chao YJ. Advances in two-dimentional and three-dimentional computer vision. Photomechanics, Topics App. Phys. 2000;77:323-372.

[15] Wu B, King MS, Hudson JA. Stress-induced Ultrasonic wave velocity anisotropy in a sandstone. Int. J. Rock Mech. Min. Sci. 1991;28(1):101-107

[16] Alsayed MI. Utilising the Hoek triaxial cell for multiaxial testing of hollow rock cylinders. Int. J. Rock Mech. Min. Sci. 2002;39:355-366

[17] Correlated Solutions. Vic-3D Testing Guide. 2010.

[18] Wijk G. Some new theoretical aspects of indirect measurments of the tensile strength of rocks. Int. J. Rock Mech. Min. Sci. 1978;15:149-160

[19] Hedan S, Cosenza P, Valle V, Dudoignon P, Fauchille A, Cabrera J. Investigation of the damage induced by desiccation and heating of Tournemire argillite using digital image correlation. Int. J. Rock Mech. Min. Sci. 2012;51:64-75

Stirling, R. A., Davie, C. T. & Glendinning, S., 2013. Numerical modelling of desiccation crack induced permeability. ***In: 18th International Conference on Soil Mechanics and Geotechnical Engineering***. Paris, France.

Numerical modelling of desiccation crack induced permeability

Modélisation numérique de la perméabilité induite par la fissuration des sols

R. A. Stirling, C. T. Davie & S. Glendinning
Newcastle University, Newcastle-upon-Tyne, UK

ABSTRACT: The development of cracking as a result of desiccation and the apparent increase in permeability of cracked fill is increasingly under investigation. Rainfall infiltration into soil surfaces that experience cracking increases due to the additional, preferential transmission of water. This in turn results in cycles of rapidly elevated pore water pressure and is widely cited as a significant mechanism for strength reduction that leads to embankment failure. A two-phase flow numerical model that allows the partially saturated behaviour of the desiccated medium to be captured is presented based on the finite difference code FLAC 2D. The material properties of the developed model, including soil stiffness and strength, are incorporated as a function of drying. The model has allowed investigation into the factors influencing the incidence and scale of cracking.

RÉSUMÉ : L'infiltration des précipitations dans les sols sensibles à la dessiccation augmente comme résultat de la transmission préférentielle, additionnelle d'eau. Ce phénomène se traduit par des cycles de pression interstitielle rapidement élevée, et est largement cité comme un mécanisme important de la réduction de la résistance qui conduit à la rupture des remblais. Un modèle numérique de l'écoulement diphasique, permettant la prise en compte du comportement partiellement saturé du milieu desséché, est présenté. Ce modèle est basé sur un code de calcul de différences finies, FLAC 2D. Les propriétés du matériau du modèle, y compris la rigidité et la résistance du sol, sont incorporées comme fonction du séchage dans la description de la courbe caractéristique sol-eau. Le modèle a permis également l'évaluation des principaux facteurs qui influencent l'incidence et l'ampleur de la fissuration des sols.

KEYWORDS: Numerical modelling, Unsaturated soils, Soil behaviour

1 INTRODUCTION

Cracking within clay fills has been an accepted phenomenon for many decades. The engineering study of desiccation cracking has been motivated by its impact upon the effectiveness of many earth structures including liners (Philip et al 2002), foundations (Silvestri et al 1992), cuttings and embankments (Smethurst et al 2006) due to an apparent increase in water infiltration.

Desiccation cracking is the product of volumetric shrinking of clays brought about by a reduction in soil-water content. Cracking initiates when tensile stresses generated by increasing suctions exceed the soil strength, which in itself, is controlled by soil water content. Variability in soil-water content is primarily the result of seasonal fluctuation in precipitation/evaporation in addition to the transient demands of vegetation and the infiltration potential of the soil surface and is therefore largely governed by climate.

Predicted climate change scenarios are recognised to have the capacity to more frequently bring about conditions conducive to the increased occurrence of this behaviour because of the increased occurrence of warmer and drier summers experiencing rainfall events of shorter duration and higher intensity (Hulme et al 2002, Jenkins et al 2010).

Progressive failure is thought to be largely governed by permeability which is in turn controlled by the micro- and macro-scale structure of the soil. Previous studies have established that current permeability measurement techniques produce discrepancies between both laboratory and field established values and numerically simulated pore-water pressure values (Smethurst et al 2006, Rouainia et al 2009). These differences have been identified as being caused by permeability values ranging by up to three orders of magnitude (Nyambayo and Potts 2005, Rouainia et al 2009). Albrecht and Benson (2001) identified the same increase in hydraulic conductivity of three orders of magnitude in laboratory testing of small cracked samples when compared to equivalent non-cracked samples of the same material. This supports the notion that it is the presence of pervasive cracks that results in the elevated permeability. An empirically reasoned permeability modification has been employed in the modelling of embankment pore pressures (Nyambayo et al 2004).

Many researchers have attempted to model the mechanisms involved in crack initiation and propagation, particularly with respect to crack pattern. Kodikara and Choi (2006) present a simplified analytical model for laboratory cracking which has subsequently been implemented by Amarasiri et al. (2011) into a distinct element code. Their work describes the modelling of cracking behaviour in slurried clays under given laboratory boundary conditions and incorporates material changes due to drying. More recently, work has been carried out using the finite element method to investigate the development of tensile stresses associated with desiccation (Trabelsi et al 2011, Peron et al 2012). In contrast, this work models partially saturated flow throughout the medium induced by a simulated evaporation boundary and combines this mechanism with the ability to capture a fracturing geometry.

2 TWO-PHASE FLOW

Modelling has been carried out using the commercial finite difference code, FLAC (Fast Lagrangian Analysis of Continua) . The internal programming language, FISH, has allowed material variables to be defined as a function of water content. Given the fundamental influence of water content in desiccation cracking, it is important to be able to capture the partially

saturated behaviour of the medium. To do this, the Two-phase Flow (tp-flow) option available with FLAC was used.

The tp-flow option allows the flow of two immiscible fluids to be modelled whose proportions are representative of soil saturation. Darcy's law is then used to define the wetting and non-wetting fluid flow according to their relative pressures. Capillary pressure is fundamentally linked to the effective saturation and is considered in this work using the van Genuchten approximation (van Genuchten 1980). The relative permeability of each fluid is considered to be a fraction of the saturated coefficient of permeability dependent upon the effective saturation.

Coupled fluid-mechanical modelling was conducted in which volumetric deformation causes changes in fluid pressures. Similarly, changes in effective stress result in volumetric strain, with the pore pressure increment weighted by the level of saturation (Itasca 2002).

3 MATERIAL PROPERTIES

3.1 Continuum properties

For simplicity, the soil was assumed to behave elastically, although non-linear behaviour was captured as described below. Young's Modulus, E (MPa), in partially saturated soils is a function of water content, ω (%), this relationship was derived experimentally for the material modelled using constant water triaxial tests. These data are presented in Figure 1.

The properties required by the software were dry density, bulk and shear moduli. The bulk and shear moduli were calculated using the Young's modulus from Figure 1 and a Poisson's ratio of 0.3 (Tomlinson 2001). These moduli were updated at each time-step of the analysis using code developed in FISH and were based on changes in element water content. The initial dry density of the soil was 1.65Mg/m^3, based upon sampling of a full scale trial embankment at Newcastle University (Hughes et al 2007).

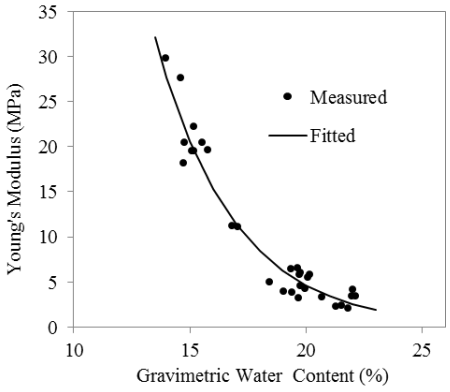

Figure 1 The trend in Young's modulus at varying water content.

3.2 Interface properties

Interfaces were sited vertically throughout the mesh with regular spacing. The use of interfaces enables separation of the mesh into discrete regions between which slip and separation can occur, subject to criteria set by interface properties and so provide locations for potential cracking.

The Interface bond will break when tensile stresses exceed the tensile strength or when shear stresses exceed the shear strength of the individual interface. Separation can then occur along the interface segment (delineated by node pairs) where this condition is met.

The interface properties comprise the friction angle; cohesion; tensile strength and stiffness in both the normal and shear orientations. Interface property values were derived primarily from standard laboratory tests (e.g. direct shear test). However, interface normal and shear stiffness were calculated according to the relative stiffness and size of neighbouring elements. As with continuum stiffness, interface stiffness was updated while stepping using the relationship with water content.

The magnitude of tensile strength for a given soil is widely recognised to be dependent upon the soil water content and therefore, suction present (Heibrock et al 2003, Nahlawi et al 2004, Tamrakar et al 2005, Trabelsi et al 2011). Laboratory testing was conducted using an adapted standard direct shear apparatus on samples of the modelled clay at varying water content. The identified trend input to the model is presented in Figure 2.

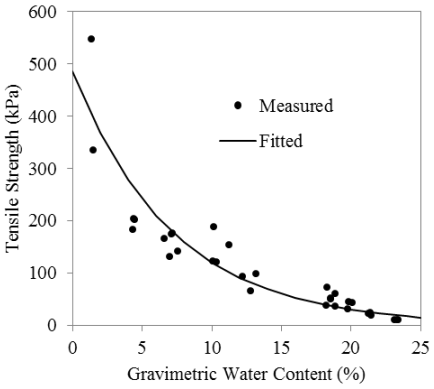

Figure 2 Tensile strength of compacted clay as a function of water content.

In addition to the dependency of interface tensile strength with water content, variability in soil strength was also included using a normally distributed random number facility about the experimentally derived value. This variability was included to enable a degree of the inherent heterogeneity of compacted clay to be better captured. The implications of this method on crack initiation and spacing is discussed later.

Restrained shrinkage at the base of clay has been shown to have a great influence on the generation of the tensile stress that leads to cracking . The clay-mould interface properties incorporated were based upon laboratory trials of compacted clay shrinkage in specially constructed moulds.

3.3 Hydrological Properties

To implement the two-phase flow calculation, van Genuchten properties of the clay were obtained from the soil water retention curve established using the Filter Paper Technique. These data are presented in Figure 3 alongside the implemented fitted van Genuchten approximation.

The curve describes the general trend of increasing suction with decreasing soil water content. It is this increase in suction that is understood to bring about an increase in soil stiffness and strength, in addition to shrinkage strain required for the development of tensile stress.

The saturated mobility coefficient input to FLAC was calculated from the coefficient of permeability and the dynamic viscosity of water. The permeability value used was measured from un-cracked sites on a trial embankment constructed using the modelled clay fill (Hughes et al 2007).

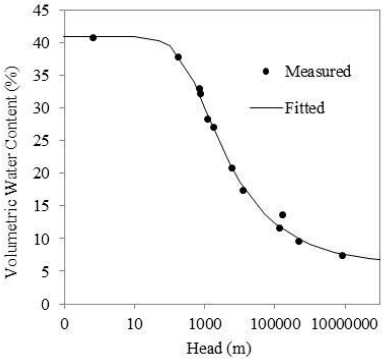

Figure 3 Soil water characteristic curve.

4 NUMERICAL MODEL

The model developed in this work was based on experiments conducted to investigate the desiccation cracking of compacted clay fill in the laboratory. As such, the geometry (Figure 4), material behaviour and initial conditions were based on these experiments.

The modelled mould consisted of a 190x2 element thick region located beneath the mesh representing the clay and was fixed in space. The remaining mesh comprised 190x17 quadrilateral elements, 94 vertically orientated interfaces and 95 horizontal interfaces, the latter forming a single plane between the base of the clay mesh and the mould. All boundaries of the sample mesh remained free to shrink/swell in any orientation. Plane-stress was configured given the finite out-of-plane depth of the modelled scenario.

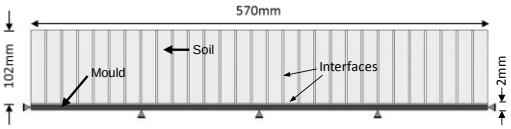

Figure 4 Geometry of the model mesh.

An evaporative drying condition was applied to the exposed, upper surface of the clay. The drying flux was numerically simulated by application of a discharge boundary condition statically located at the upper surface of the model mesh (5a).

During the early stages of experimental drying, shrinkage was observed as both ends of the soil sample, away from the mould ends resulting in an increase in the exposed surface area of the sample. Therefore, in addition to simulated discharge from the upper surface of the sample mesh, the transient behaviour of the exposed end surfaces was accommodated. Furthermore, the evaporative surface area increases upon the onset of cracking and this is also included. At every simulated hour of drying, each interface is assessed for separation (i.e. crack opening). When separation is identified, the exposed 'crack wall' is subjected to the dynamic discharge condition. An example evolution of the drying boundary geometry is illustrated in Figure 5.

The model requires a drying rate to be applied to the surface, this was determined from laboratory experiments where mass loss is considered to be solely that of water.

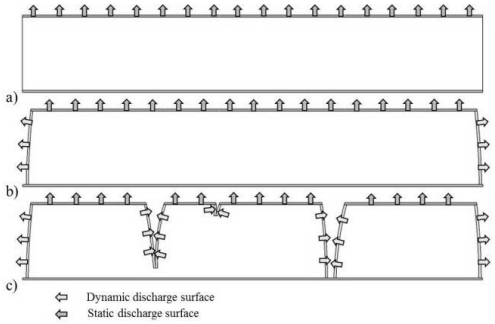

Figure 5 Illustration of the drying boundaries a) Initial upper surface b) Upper surface plus exposed sample ends and c) Upper surface, exposed ends plus crack walls.

5 RESULTS

An example of the output geometry from a typical simulation is provided in Figure 6a alongside a representative laboratory experiment. It can be seen that shrinkage of the modelled clay has taken place, represented by the difference in total length between the mesh simulating the clay and that of the fixed mould. Towards the outer boundaries of the clay mesh, the edge is seen to curve from the vertical. This realistic behaviour is captured by the ability of the model to generate the non-linear negative pore pressure gradient through the depth of the mesh. By applying a drying condition to the outer surface, primarily the upper boundary, this region has been found to develop the greatest suction magnitudes. Additionally, the overall residual height of the mesh following drying is found to have reduced from the pre-drying condition.

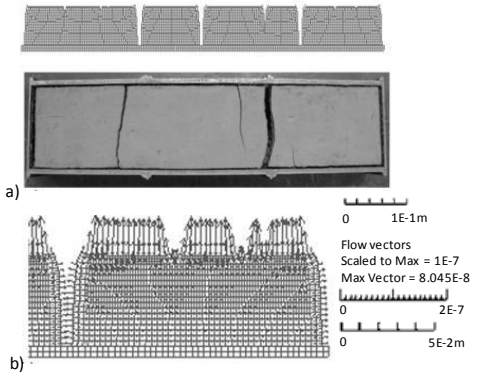

Figure 6 a) Model geometry output (side elevation) and an inset example laboratory experiment (plan elevation) and b) Cracked geometry with flow vectors.

Flow may be seen in Figure 6b to predominantly act in the upward direction throughout the medium. In the vicinity of separated interfaces, flow is shown to occur toward the crack wall contributing to the overall drying mechanism of the model.

The ability to capture the development of tensile stress throughout the medium is vital for the simulation of crack initiation and growth conditions. A representative contour plot of total horizontal stress is presented in Figure 7. Most clearly depicted is the generation of greatest tensile stress localisation about the modelled crack tip. As the propagation of interface separation takes place it is found that the magnitude of this

stress concentration increases. However, upon full separation of the mesh, this tip stress is relieved as propagation is halted. The mesh is then free to shrink further subject to the basal friction condition.

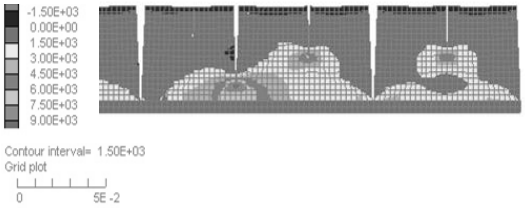

Figure 7 Distribution of total stress in the horizontal orientation.

The formation of shallow compressive stress concentrations at the upper surface, such as that shown between existing cracks in Figure 7 is considered to be the indicator of crack initiation loci. The progressive development of such surface stress concentrations away from previous crack formation is evidence of sequential crack formation. The incorporation of tensile strength variability across the many interfaces has allowed this phenomenon not to dominate, therefore avoiding symmetry in the resultant crack pattern. Simultaneous growth of primary cracking at spacing relative to the progressive development of surface stress is evident in Figure 6a, shown by the fully penetrating cracks. The initiation of minor cracks at the surface has led to stress relaxation and inhibited further pervasive cracking.

Growth of basal tensile stress concentrations are shown to result from the imposed shear conditions at the clay-mould interface. These are found to contribute to the propagation of interface separation approaching the base of the clay. However, clay tensile strength is consistently exceeded at the evaporative outer boundary initially.

6 CONCLUSIONS

This work is set in the context of cracking due to seasonal drying in compacted, engineered fills used in the construction of infrastructure embankments.

The model presented is capable of replicating the non-linear, partially saturated state that results from the application of a drying flux. Through incorporating interface elements, the model is not only able to model the stress field generated through drying but is capable of simulating the cracking behaviour of an engineered fill undergoing desiccation. It is recognised that the placement of predefined, potential cracking sites has the inherent tendency to bias the distribution of cracking. However, attempts have been made to include a degree of heterogeneity in tensile strength throughout a finely discretised mesh. Through this, a combination of spontaneous and sequential crack initiation processes is captured much like the development of primary and second order cracking recorded in the field.

The use of a dynamic, evaporative boundary condition is incorporated in an attempt to capture the transient nature of surface permeability under drying.

ACKNOWLEDGEMENTS

The authors would like to thank Stuart Patterson for help with laboratory work, Dr Joao Mendes for triaxial data and Dr Peter Helm for his helpful advice in the use of the numerical software.

REFERENCES

Albrecht B. A. and Benson C. H. 2001 Effect of desiccation on compacted natural clays. *J. Geotechnical and Geoenvironmental Eng*. 127 (1), 67-75

Amarasiri A. L., Kodikara J. K. and Costa S. 2011 Numerical modelling of desiccation cracking. *Int. J. Numerical and Analytical Methods in Geomech*. 35, 82-96

Heibrock G, Zeh, R. M. and Witt K. J. 2003 Tensile strength of compacted clays. *Preceedings of the international conference 'From Experimental Evidence towards Numerical Modelling of Unsaturated Soils.* Weimar, Germany

Hughes P., Glendinning S. and Mendes J. 2007 Construction, testing and instrumentation of an infrastructure testing embankment. *Proceedings of the Expert Symposium on Climate Change Modelling, Impacts & Adaptations*, Singapore, 159-166

Hulme M., Jenkins G. J., Lu X., Turnpenny J. R., Mitchell T. D., Jones R. G., Lowe J., Murphy J. M., Hassell D., Boorman P., McDonald R. and Hill S. 2002 Climate change scenarios for the United Kingdom: The UKCIP02 Scientific Report, Tyndall Centre for climate change research, Norwich

ITASCA 2002 FLAC User's Guide. ITASCA, Minnesota

Jenkins G., Murphy J., Sexton D., Lowe J., Jones P. and Kilsby C. 2010 UK climate projections: Briefing report. 2. UK Climate Impacts Programme

Kodikara J. K. and Choi X. 2006 A simplified analytical model for desiccation cracking of clay layers in laboratory tests. *ASCE Geotechnical Special Publication* 2, 2558-2569

Nahlawi H., Charkrabarti S. and Kodikara J. 2004 A direct tensile strength testing method for unsaturated geomaterials. *ASTM Geotechnical Testing Journal*. 27 (4), 1-6

Nyambayo V. P. and Potts D. M. 2005 A new permeability model for shrinkable soils undergoing desiccation. *Proceedings of the International Conference on Soil Mech. and Geotechnical Eng.* 2, 831-836

Nayambayo V. P., Potts D. M. and Addenbrooke T. I. 2004 The influence of permeability on the stability of embankments experiencing seasonal pore water pressure changes. *Advances in Geotechnical Eng.: The Skempton Conference*, Thomas Telford, London, 898-910

Peron H., Laloui L., Hu B. L. and Hueckel T. 2012 Formatio of drying crack patterns in soils: a deterministic approach. Acta Geotechnica, 1-7

Peron H., Hueckel L., Laloui L. and Hu L. B. 2009 Fundamentals of desiccation cracking of fine-grained soils: experimental characterisation and mechanisms identification. *Can. Geotechnical J*. 46, 1177-1201

Philip L. K., Shimell H., Hewitt P. J. and Ellard H. T. 2002 A field-based test cell examining clay desiccation in landfill liners. *Q. J. Eng. Geol. and Hydrol*. 35, 345-354

Rouainia M., Davies O., O'Brien T. & Glendinning S. 2009 Numerical modelling of climate effects on slope stability. *Eng. Sustainability*, 162 (ES2), 81-89

Silvestri V., Sarkis G., Bekkouche N. and Soulie M. 1992 Evapotranspiration, trees and damage to foundations in sensitive clays. *Can. Geotechnical Conference*. 2, 533-538

Smethurst J. A., Clarke D. and Powrie W. 2006 Seasonal changes in pore water pressure in a grass-covered cut slope in London clay. *Geotechnique*. 56, 523-537

Tamrakar S. B., Toyosawa Y., Mitachi T. and Itoh K. 2005 Tensile strength of compacted and saturated soils using newly developed tensile strength measuring apparatus. *Soils and Foundations*, 45 (6), 103-110

Tomlinson M. J. 2001 Foundation design and construction. 7th ed. Pearson Education, Harlow, England

Trabelsi H., Jamei M., Zenzri H. and Olivella S. 2011 Crack patterns in clayey soils: Experiments and modelling. *Int. J. Numerical and Analytical Methods in Geomech.*, 36 (11), 1410-1433

van Genuchten M. T. 1980 A closed-form equation for predicting the hydraulic conductivity of unsaturated soils. *J. Soil Soc. Am*. 44 (5), 892-898

Stirling, R. A., Hughes, P. N., Davie, C.T. & Glendinning, S., 2014. Cyclic relationship between saturation and tensile strength in the near-surface zone of infrastructure embankments. ***To be presented at: 6th International Conference on Unsaturated Soils (UNSAT2014): Research & Applications***. *Sydney, Australia*.

Cyclic relationship between saturation and tensile strength in the near-surface zone of infrastructure embankments

R.A. Stirling, P.N. Hughes, C.T. Davie & S. Glendinning
Newcastle University, Newcastle-upon-Tyne, UK

ABSTRACT: The near surface properties of engineered fill have a significant impact on its engineering behaviour. A common way in which soil will change is through cracking due to the effects of desiccation, vegetation and climate. This has an impact on soil mass permeability, strength and stiffness and hence slope failure susceptibility. Knowledge of the tensile strength and degree of saturation relationship is essential to understand the development of desiccation cracking. This paper presents a study to establish the cyclic relationship between tensile strength and soil water content in a re-moulded glacial till. Testing was conducted using a direct tensile strength test modification to standard direct shear apparatus. As with the soil-water retention, the relationship between soil water content and tensile strength shows hysteretic characteristics. Furthermore, this relationship was found to develop upon repeated drying and re-wetting cycles. This has implications for the degradation of near surface material on engineered infrastructure slopes.

1 INTRODUCTION

Knowledge of the tensile strength properties of geomaterials is important in a number of engineering applications. Engineered fills in embankments, cuttings and dams, landfill liners and other earth structures are susceptible to tensile failure, particularly in the near surface "vadose" zone where evapotranspiration and seasonal wetting and drying can induce shrink-swell cyclicity.

Much work has been conducted into the generation of tensile stresses due to restrained shrinkage relatively recently including the following principle contributors, Kodikara et al. (2004)(2004), Hu et al. (2006) and Peron et al. (2009). The development of tensile stress is generally accepted as arising from non-uniform drying or any frictional boundary effect up to a magnitude that may exceed the tensile strength of cohesive soils leading to what is increasingly understood to be a dominant criterion for the initiation and propagation of desiccation cracking (Peron, et al., 2009). Therefore the capacity to characterise the tensile strength/stiffness behaviour of geomaterials is of importance.

There exist a number of tensile tests available for the characterisation of geomaterials. These can be separated into two categories, direct and indirect tests. Direct tests include modification of triaxial testing apparatus (Tang and Graham, 2000; Heibrock et al., 2003; Witt and Zeh, 2007) and modification of direct shear testing apparatus (Nahlawi et al., 2004; Tamrakar et al., 2005; Trabelsi et al., 2012). Indirect tests include the Brazilian tensile test (Frydman, 1964; Krishnayya and Eisenstein, 1974) & Hollow Cylinder Triaixial test (Alsayed, 2002). Each of these approaches have their advantages and limitations although direct testing is generally preferred as requiring relatively simple sample preparation and testing procedures making this class of test both effective and economical. However, serious consideration must be given to the potential for squeezing of low stiffness material by shear keys and loading jaws leading to uneven stress distributions and hence inaccurate stress measurement.

In this work, a direct tensile strength test has been used to investigate the effect of drying-wetting cycles on the development of the tensile strength – water content relationship. This has been conducted in the context of observed degradation of compacted engineered fill at the near surface of infrastructure embankment structures.

2 TESTING METHOD

2.1 Equipment

An adaptation of existing direct shear apparatus was developed in order to test direct tensile behaviour. The test rig chosen for modification was a conventional 100 mm x 100 mm Wykeham Farrence direct shear test rig. The modifications to the rig consisted of two PVC loading jaws that when combined form a sample aperture in the shape of two mirrored isosceles trapeziums, commonly referred to as a 'bow-tie'. These jaws can be inserted into the carriage where the shear box is usually placed. A schematic of the loading jaws is presented in Figure 1a, how this device then fits into a conventional direct shear rig is shown in Figure 1b. The advantage of this system is that the loading jaws can be quickly removed allowing the rig to be returned to its original purpose as the need arises.

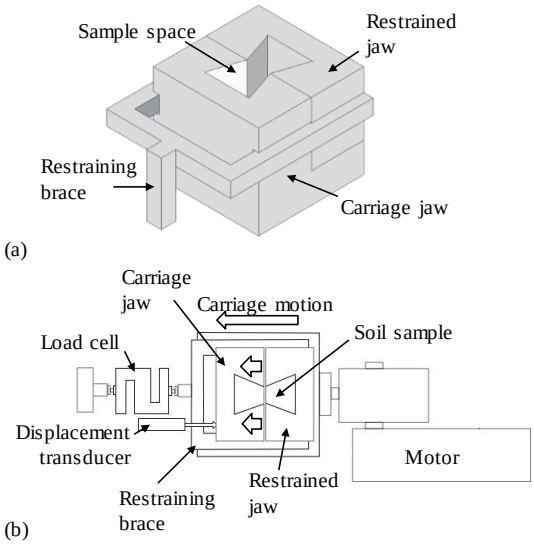

Figure 1. Tensile test apparatus comprising (a) loading jaws and (b) schematic of testing rig.

2.2 Material

The material investigated was an engineered fill comprising glacial till representative of embankments in the north of the UK. Such soils are prone to shrink-swell behaviour which contributes to the progressive failure of infrastructure embankments as well as desiccation cracking phenomena.

The Atterberg limits, tested in accordance with BS 1377 (1990), were 43% and 21% for Liquid and Plastic Limits respectively which classifies the material as intermediate plasticity. Compaction characterisation was conducted to BS 1377 (1990) using normal Proctor (light) compaction which found the maximum dry density to be 1.71 Mg/m^3 at a 15% optimum water content. Lastly, the particle distribution of the material was established and is provided in Figure 2 where the soil is shown to be relatively well-graded in the portion >2μm.

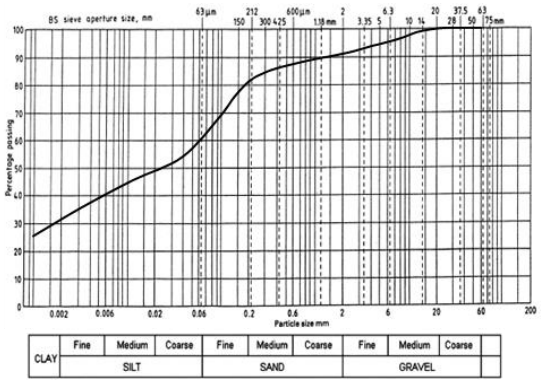

Figure 2. Engineered fill particle size distribution.

2.3 Sample preparation

The above fill material was prepared by air drying to residual moisture content before being passed through a 5 mm sieve. This process is known to alter the natural PSD of the natural material; however, it was deemed impractical to test soils whereby individual grains constituted greater than 2% of the total volume of the sample (78.3 ml).

Following drying, water was then added to bring the soil in a mechanical mixer to a predetermined water content (23%) and the bulk sample was then wrapped in two layers of uPVC film and left to equilibrate for at least 24 hours. After this period, a sub-sample of soil was weighed such that when a sample is produced using a bespoke steel press, a desired average dry density (1.65 Mg/m^3) was achieved. This process allowed the rapid production of samples with consistent water contents, densities and dimensions.

Samples were subsequently air dried again until the desired water content was reached. On reaching the required water content, samples were then re-sealed for 24 hours to ensure an even re-distribution of water within the specimen prior to testing. Where samples were required to be tested along the wetting path, samples were first allowed to dry to their residual value (where no mass change was observed). A humidity chamber was then employed in order to gradually increase these samples' water content. The insulated chamber measured approximately 450 mm x 300 mm x 300 mm and contained a 20-30mm water bath within which was placed up to 3 ultrasonic water foggers. This maintained a high relative humidity enabling the samples to absorb moisture gradually as a more rapid approach would inevitably lead to destruction of the soil fabric and likely sample disintegration. For a typical dried sample to be returned to a water content of 20%, a period of approximately 7 days was required.

2.4 Testing procedure

Specimens are placed in the loading jaws and a constant motor speed selected. The carriage is then propelled leading to separation of the loading jaws. The resultant load is transmitted through the sample and recorded continually until the two halves of the sample are completely separated and the load reading returned to a residual value. It may be noted that non-zero stress values are recorded post specimen failure indicating, as in any mechanical system, a level of internal system friction/inefficiency.

A range of displacement rates are available by using an existing direct shear rig. However, a motor rate of 0.61 mm/min was used. Due to the

stiffness of some samples, the true displacement rate has been found to deviate from the applied rate. Hence, true displacement was measured directly as the carriage jaw was displaced.

3 RESULTS

3.1 Tensile stress-strain behaviour

The tensile stress-strain data gained from testing the clay fill along the initial drying path are presented in Figure 3. At the start of each test, a period of sample seating may be seen in the form of low sustained stresses with developing strain. It can be seen that samples tested at moisture contents below 15% show a somewhat linear stiffness with slight stiffening prior to the ultimate strength being reached. At the ultimate strength, samples were found to fail with an instantaneous fracture across the neck of the sample. Subsequently, stress is shown to drop sharply; however, in the wetter sample at 22% (approx. plastic limit) a strain softening behaviour is apparent post-failure at a substantially lower ultimate strength. This is shown by the gradual decrease in stress upon returning to the residual value with continued straining. These samples exhibit a less well defined brittle fracture and eventually divide following a period of neck thinning in a ductile manner.

3.2 Drying-wetting-drying path

The testing program was conducted with the ultimate aim of investigating the tensile strength change with cyclic drying and re-wetting of clay embankment fill. To this end, the following data is presented showing this relationship along an initial drying, wetting and subsequent re-drying path (Figure 4).

The initial drying path shows a typical trend of exponentially increasing tensile strength with decreasing water content. This data has been curve fitted with an R^2 value of 0.84, the highest fit of all the strength-water content data. Upon wetting, a similarly exponential trend may be fitted. However, the wetting relationship follows much lower strength values and at water contents >20%, negligible tensile stress is maintained. The second drying path exhibits higher tensile strengths than that of the wetting trend yet is considerably weaker than the initial drying curve.

4 DISCUSSION

Tensile strength is increasingly understood to be a crucial parameter in the study of desiccation crack initiation and stable crack propagation in cohesive soils. Traditionally, the relationship between tensile strength and water content established along an initial drying path has been considered as a main influence on the temporal and spatial distribution of crack initiation during progressive soil drying. How-

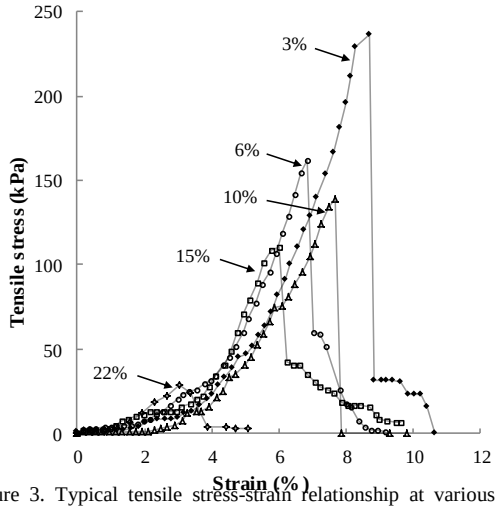

Figure 3. Typical tensile stress-strain relationship at various water contents.

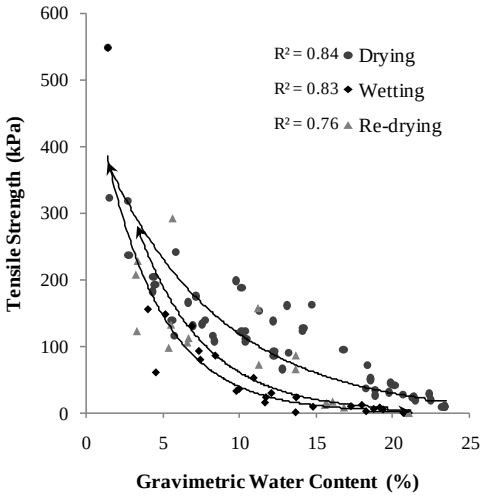

Figure 4. Tensile strength relationship upon initial drying, wetting and re-drying.

ever, this relationship has been found to undergo translation toward the origin of both σ_t and ω axes upon cyclic wetting and drying.

The development of tensile strength in clay soils with changing water content is understood to be related to (but not solely a result of) an inherent change in matric suction. In granular soils, suction is the governing mechanism behind resistance to tensile stresses, in compacted clay fills soil fabric is considered to play a significant role.

Crack initiation is assumed to occur by induced tensile stress brought about by restrained shrinkage due to surface desiccation exceeding the soil tensile strength under a given condition. A cracking analysis on this basis would indicate that crack initiation would occur at a given tensile strength which exists at specific water content. The following discussion precedes under the supposition that cracking may or may not have occurred in the initial drying of the subject soil. Should the cracking condition have been met under initial drying then sufficient stress 'relaxation' behavior may well take place whereby subsequent generation of tensile stress may not exceed critical tensile strength and no further cracking can proceed. Notwithstanding, the use of a single, initial drying relationship is understood to result in an underestimation in the later development of crack networks.

By investigating the cyclic tensile strength-water content relationship, deterioration in the clay is evident. Hysteretic phenomena are familiar in the study of soil wetting. In the context of soil-water retention, upon wetting, lower suction is developed at a given water content than would be generated upon drying. This effect may well contribute to explaining the reduced strength shown along the wetting path. However, it is believed that deterioration of the soil fabric is the primary means of strength reduction. The development of micro-flaws during the initial desiccation stage has led to an increment of non-recoverable destruction in the structure of the compacted clay fabric. The second drying stage illustrates this loss in soil integrity. Tensile strengths are higher on drying than wetting once again though are considerably lower than on the initial drying path. The return of the curve to higher strength values on drying indicates the influence of hysteretic soil-water-air phenomena. The large contrast between the two drying paths signifies a more fundamental deterioration.

On establishing lower tensile strengths as a result of cyclic wetting and drying, the criterion by which crack initiation is believed to occur is met by the generation of lower tensile stresses. This would lead to an increased occurrence of cracking (e.g. development of an inter-connected network) with progressive drying-wetting cycles. The authors anticipate a residual tensile strength – water content relationship after repetition of drying and wetting whether this be partial or complete in either direction. As previously described, some hysteretic influence is believed to remain.

5 CONCLUSION

By developing an approach to measure the tensile strength of a typical, compacted clay embankment fill at a variety of water contents, the development of this relationship upon cycles of drying and wetting has been identified. The implication of this work is a better understanding of the tensile strength deterioration process with repeated wetting and drying in clay fills and specifically how this influences the initiation of tensile failure at the near-surface.

REFERENCES

Alsayed, M. I. 2002. Utilising the Hoek triaxial cell for multiaxial testing of hollow rock cylinders. *International Journal of Rock Mechanics and Minning Sciences* 39: 355-366.

British Standards Institution. Methods of Test for Soils for Civil Engineering Purposes. BSI, Milton Keynes, 1990, BS 1377.

Frydman, S. 1964. The Applicability of the Brazilian (Indirect Tension) Test of Soils. *Australian Journal of Applied Science* 15: 335-343.

Heibrock, G., Zeh, R. M. & Witt, K. J. 2005. Tensile Strength of Compacted Clays. In: T. Schanz, ed. Unsaturated Soils: Experimental Studies. s.l.:Springer Berlin Heidelberg, pp. 395-412.

Hu, L., Peron, H., Hueckel, T. & Laloui, L. 2006. Numerical and phenomenological study of desiccation of soil. *Advances in unsaturated soil, seepage and environmental geotechnics*. ASCE 148: 166-173.

Kodikara, J. K., Nahlawi, H. & Bouazza, A. 2004. Modelling of curling in desiccating clay. *Canadian Geotechnical Journal* 41(3): 560-566.

Krishnayya, A. V. G. & Einsenstein, Z. 1974. Brazilian Tensile Test for Soils. *Canadian Geotechnical Journal* 11: 632-642.

Nahlawi, H., Chakrabarti, S. & Kodikara, J. 2004. A Direct Tensile Strength Testing Method for Unsaturated Geomaterials. *Geotechnical Testing Journal* 27(4): 1-6.

Peron, H., Hueckel, L., Laloui, L. & Hu, L. B. 2009. Fundamentals of desiccation cracking of fine-grained soils: Experimental characterization and mechanisms identification. *Canadian Geotechnical Journal* 46: 117-1201.

Tamrakar, S. B., Toyosawa, Y., Mitachi, T. & Itoh, K. 2005. Tensile strength of compacted and saturated soils using newly developed tensile strength measuring apparatus. *Soils and Foundations* 45(6): 103-110.

Tang, G. X. & Graham, J. 2000. A Method for Testing Tensile Strength in Unsaturated Soils. *Geotechnical Testing Journal* 23(3): 377-382.

Trabelsi, H., Jamei, M., Zenzri, H. & Olivella, S. 2012. Crack patterns in clayey soils: Experiments and modeling. *International Journal of Numerical and Analytical Methods in Geomechanics* 36: 1410-1433.

Zeh, R. M. & Witt, K. J. 2007. The Tensile Strength of Compacted Clays as Affected by Suction and Soil Structure. In: T. Schanz (ed), *Experimental Unsaturated Soil Mechanics*: 219-226. Springer Berlin Heidelberg.

ACKNOWLEDGEMENTS

The authors would like to acknowledge Jonathan Murphy and Stefan Frangov for laboratory testing and Stuart Patterson and David Innes for their work in manufacture.